PHYSIK-DEPARTMENT

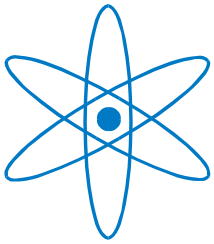

Influences on Structure Formation in Surface-Supported Organic Nanostructures

Dissertation

von

Thomas Sirtl

TECHNISCHE UNIVERSITÄT

MÜNCHEN

TECHNISCHE UNIVERSITÄT MÜNCHEN
Fakultät für Physik
Oskar-von-Miller Lehrstuhl für Wissenschaftskommunikation

Influences on Structure Formation in Surface-Supported Organic Nanostructures

Thomas Sirtl

Vollständiger Abdruck der von der Fakultät für Physik der Technischen Universität München zur Erlangung des akademischen Grades eines

Doktors der Naturwissenschaften
(Dr. rer. nat.)

genehmigten Dissertation.

Vorsitzender: Univ.-Prof. Dr. J. L. van Hemmen

Prüfer der Dissertation:

1. Univ.-Prof. Dr. J. Barth
2. Priv.-Doz. Dr. M. Lackinger, Ludwig-Maximilians-Universität München

Die Dissertation wurde am 29.10.2013 bei der Technischen Universität München eingereicht und durch die Fakultät für Physik am 19.12.2013 angenommen.

Contents

Abstract

In the present study, nanostructures are fabricated on metal or graphite surfaces under ultrahigh vacuum conditions or alternatively, at the solution-solid interface. Structure formation and its dependence on preparation parameters is analyzed by two complementary experimental surface-sensitive techniques, namely, scanning tunneling microscopy and low energy electron diffraction. With the aid of these techniques, details of irregular to highly ordered structures and their underlying intermolecular binding motifs are derived. As building blocks for the synthesis of surface-supported nanostructures, aromatic and polyaromatic organic molecules are utilized, equipped with functional groups (i.e. halogen substituents, nitrile or thiol groups). Various intermolecular binding motifs are discovered in surface-supported nanostructures upon deposition of monomers. Subsequently to deposition of monomers, on-surface reactions can occur. In the order of increasing strength, binding motifs are dispersive interactions, halogen-halogen bonds, hydrogen bonds, metal-organic bonds, organometallic bonds, or covalent bonds. The formation of structures is found to be dependent on expected parameters as the stereochemistry of a monomer or substrate temperature, but also on the monomer coverage on the surface, lattice and material of a substrate, coadsorption of solvent molecules, and deposition rate of monomers.

The expression of the binding motif (hydrogen bonds vs. metal-organic bonds) along with the arrangement of monomers in surface-confined self-assembly of a large trinitrile molecule is shown to be dependent on the substrate material (silver vs. copper), revealing the importance of adatom reactivity and resulting bond strength of metal-organic bonds. Additionally, the structure formation on Cu(111) is kinetically controlled as deduced by experiments with ultralow deposition rates. Here, the deposition rate can account for structure selection.

The effect of coadsorption of solvent molecules on monolayer self-assembly is studied at the fatty acid-graphite interface. Here, solvent molecules from the solvation shell coadsorb with the solute and give rise to kinetically trapped metastable polymorphs. Thermal energy is required for desorption of the coadsorbed solvent molecules and subsequently, a structural phase transition of the monolayer into a thermodynamically more stable phase occurs. These experimental results are underpinned by complementary studies at the vacuum-graphite interface.

Also, the adsorption site of a trithiolate molecule on Cu(111) is determined with subatomic precision. All thiol groups adsorb on hcp threefold hollow sites and all phenyl rings occupy fcc threefold hollow sites. Additionally, intramolecular deformations and substrate relaxations are observed. The reliability of the analysis of this comparatively large adsorbate structure is discussed in the context of recent literature and compared to theoretical structure determination by density functional theory. In order to avoid expensive analyses, the use of markers is discussed as a method of facile adsorption site determination by scanning probe microscopy.

From benzenetrithiol, self-assembled molecular monolayers and layers of atomic sulfur are synthesized on Cu(111). Temperature-induced irreversible and reversible phase transitions in resulting copper-sulfide adlayers are observed. Also, the theoretical simulation of an abundantly observed but not yet structurally solved copper-sulfide phase is supported by experiment.

Kurzdarstellung

Die atomare Konfiguration einer oberflächenbasierten Nanostruktur ist mit den heutigen Methoden noch nicht nach ersten Prinzipien vorhersagbar. Immer noch werden experimentelle Vorleistungen für das Grundverständnis der Strukturbildung benötigt. In diesem Zusammenhang beschreibt die vorliegende Arbeit die Herstellung von Nanostrukturen auf Metall- oder Graphitoberflächen im Ultrahochvakuum oder an der Fest-Flüssig Grenzfläche. Die Einflüsse von Präparationsparametern auf die Strukturbildung werden mit zwei komplementären oberflächensensitiven analytischen Methoden untersucht, der Rastertunnelmikroskopie und der Niederenergetischen Elektronenbeugung. Kombiniert lassen beide Methoden Rückschlüsse auf die präzise Struktur und intermolekulare Bindungen zu, die für die Anordnung der Grundbausteine in einer Struktur verantwortlich sind. Als Ausgangsstoffe zur Herstellung der Nanostrukturen dienen Aromaten, die mit Halogen-, Nitril- oder Thiolgruppen funktionalisiert sind. Auf die Abscheidung der Moleküle folgen oberflächenkatalysierte Reaktionen, die zu einer großen Bandbreite an intermolekularen Bindungstypen führen. Geordnet nach abnehmender Bindungsstärke treten Dispersionskräfte, Halogen-Halogen-, Wasserstoffbrücken-, radikalische und nichtradikalische metallorganische, oder kovalente Bindungen auf. Vielseitig sind ebenso die beobachteten Einflussparameter auf die Strukturbildung, nämlich die Molekülstruktur, der Bedeckungsgrad, das Oberflächenmaterial und -gitter, die Abscheidung von Lösungsmittelmolekülen, die Abscheiderate der Grundbausteine und die Oberflächentemperatur.
Das Material der Oberfläche bestimmt die intermolekularen Bindungen (Wasserstoffbrücken- oder metallorganische Bindungen) in einer Monolage aus Trinitril-Molekülen. Dieser Effekt wird der Reaktivität von Adatomen und der Bindungsstärke der metallorganischen Bindungen zugeordnet. Experimente mit extrem niedriger Abscheiderate weisen zudem die kinetische Kontrolle der Strukturbildung nach.
Die Einflüsse der Ko-Abscheidung von Lösungsmittelmolekülen auf die Strukturbildung werden in Experimenten an der Fest-Flüssig Grenzfläche untersucht. Lösungsmittelmoleküle lagern sich zwischen die Grundbausteine der Struktur und treten erst nach Temperaturerhöhung wieder in die flüssige Phase über. Dabei verändert sich die Anordnung der Grundbausteine irreversibel in eine thermodynamisch günstigere Struktur. Experimente in lösungsmittelfreier Umgebung untermauern die dargestellten Schlussfolgerungen.
Die Bindungsgeometrie eines Trithiol-Moleküls auf einer Kupferoberfläche wird mit subatomarer Genauigkeit durch quantitative Niederenergetische Elektronenbeugung nachgewiesen. Die kovalenten Bindungen zwischen Schwefel- und Kupferatomen sind danach ausschlaggebend für die Strukturbildung. Zusätzlich werden molekulare Deformationen und Relaxationen in den obersten Oberflächenschichten analysiert. Die Zuverlässigkeit der Strukturbestimmung wird mit einer theoretischen Strukturanalyse und einer Literaturübersicht vergleichbarer Studien untermauert. Um die Bestimmung von Adsorptionsplätzen in Zukunft zu erleichtern, wird ein Marker für Rastersondenmikroskopie-Experimente vorgeschlagen.
Trithiolbenzol wird zur Herstellung von Kupfersulfidschichten verwendet. Dabei werden reversible und irreversible temperaturabhängige Strukturumwandlungen beobachtet. Kürzlich erschienene theoretische Strukturbestimmungen der am häufigsten beobachteten Kupfersulfidphase können experimentell bestätigt werden.

Chapter 1

Surface-Supported Nanostructures from Molecular Building Blocks – an Introduction

To date, the research area of surface-supported nanostructures[a] (SSNs) is a fascinating topic of fundamental surface science with promising industrial applications.[1] SSNs are prepared through self-assembly of molecular building blocks on solid surfaces under diverse conditions. These range from clean, utmost defined ultrahigh vacuum (UHV)[2] to highly dynamic solution-solid interfaces[3] to electrolyte-metal interfaces under tunable electrochemical conditions.[4] A tremendous variety of building blocks has been utilized to date, with sizes ranging from diatomic molecules[5] to small, conformationally rigid aromatic molecules[6] to extended, foldable oligomers with atomic masses exceeding 4000 u.[7] Owing to the broadness of available monomers and fabrication strategies, the resulting structures of SSNs are diverse. Examples are densely packed, well ordered monolayers of molecules adsorbed in planar[8,9] or upright[10] fashion, as well as porous networks with varying degree of regularity.[1,11–16]

Scanning tunneling microscopy (STM) is a powerful technique for studying SSNs. STM allows for the submolecularly resolved determination of each intermediate aggregation step that might emerge: single molecules, dimers, oligomers, irregular networks, or long-range ordered monolayers. Frequently, spacing and orientation of adsorbed molecules are derived from STM data along with the most important experimental input for revealing the intermolecular binding motif. In chapter 2, theory and the experimental setup for STM are described. Low energy electron diffraction (LEED), a surface-sensitive diffraction technique, is used complementary to STM in studying SSNs. By LEED, adsorbate lattice parameters of ordered adlayers[b] are derived with high precision along with the relative orientations to the substrate lattice. In particular cases LEED also facilitates a precise surface structure determination including the determination of adsorption sites. In chapter 3 an introduction to LEED theory and the experimental setup is given.

Despite the large efforts in studying SSNs over the last two decades, the detailed reasons for their enormous structural versatility are often only fragmentarily un-

[a] "nanostructure": structure with nanometer-sized dimensions

[b] "adlayer": adsorbed (mono)layer

derstood. Accordingly, an ab initio prediction of structure formation without any experimental input remains impossible to date.[17] Structure Formation of SSNs is mainly determined by the type of interlinks between the building blocks, ranging from weak van der Waals interactions[8,18] to strong covalent bonds.[16,19,20] Chapter 5 depicts representative examples of experimentally observed SSNs, classified by the type of bond that stabilizes the arrangement.

Conceivable applications for SSNs comprise their use as electroactive materials for molecular electronics, transparent electrode materials, membranes with selective permeability, or templates for the growth of three-dimensional (3D) nanostructures.[1] For this, organic materials with high stability, long-range order, low defect density, and tunable electronic properties are required. High stability is achieved by strong interlinks between the monomers, however, the strength of the interlinks hitherto stands in contrast to the degree of ordering. For weak interlinks, long-range order is frequently observed,[3,4,6,12,21,22] whereas domain sizes of regular and covalent SSNs only rarely exceed 40 nm.[20] Furthermore, the desired structural characteristics and tunable electronic properties require a detailed knowledge of the effects of influencing parameters on structure formation in SSNs. The experimental input is also a prerequisite for the advancement of ab initio predictions of SSNs. Within the scope of the present study, various influencing parameters on the formation of SSNs have been revealed and analyzed. A discussion is provided in chapter 6.

The metal-organic coordination bond is a promising type of interlink for the formation of stable and regular SSNs.[11,22] Despite their comparatively high bond strength,[11] metal-organic coordination bonds remain reversible under usual experimental conditions. Bond Reversibility enables curing of defects, and thus is the main reason for the low defect density of metal-coordinated SSNs. Carboxyl-,[23] thiol-,[24] pyridyl-,[23] or nitril-groups[25] are favoured functional groups for metal-organic coordination. Metal-organic networks are either prepared by codeposition of metal atoms and molecular building blocks or by exploiting the adatom[c] gas of specific surfaces to provide metal centers for coordination bonds. Studies of a large polyaromatic trinitrile molecule on single crystal surfaces of silver and copper reveal important influencing parameters on structure formation of metal-coordinated SSNs. These are known parameters as substrate material (or adatom reactivity) and temperature, and a hitherto rarely discussed parameter, the monomer deposition rate. Details are provided in chapter 7 (publication #6).[26]

At the solution-solid interface, solvated adsorbate molecules and excess solvent molecules maintain an adsorption/desorption equilibrium. In contrast to defined UHV conditions, here even more subtle parameters effect structure formation of SSNs. For instance, desorption, readsorption, as well as solvent coadsorption may be considered as influencing variables. Furthermore, solute concentration and type of solvent have an impact on structure formation.[11] Numerous examples of solvent-dependent effects are given in literature,[6,7,27–34] however most publications do not clarify the underlying reasons. Studies of a large polyaromatic trinitrile molecule in different solvents at the solution-graphite interface shed light on a specific case of solvent-dependent polymorphism and irreversible temperature-induced phase transition. In addition to experiments at the solution-solid interface, the analysis is

[c] "adatom": adsorbed atom

extended to the UHV-graphite interface in order to prove the resumptive statement. Based on this combined study it is concluded that here solvent coadsorption and temperature-dependent desolvation are the major influencing parameters. A detailed discussion is given in chapter 8 (publication #8).[35]

Conceivable applications of SSNs comprise active materials connected to metal electrodes via functional groups in molecular electronics. The detailed knowledge of the binding site of the organic molecules - preferably thioles - to electrode surfaces is required for a correct simulation of the contact resistance.[36] Electrode materials are gold or copper, for instance. On that account, an SSN formed by a polyaromatic trithiol molecule is studied on copper, where the adsorption site was hitherto unknown. An atomically precise adsorption site determination of this rather large adsorbate by both theory and experiment is discussed in chapter 9 (publication #7). The crucial reason for the formation of only one of several possible adsorption geometries is attributed to the distinct preference of sulfur atoms for a specific binding site.[37]

Adsorption site determination by LEED requires long-range ordered superstructures with large domain sizes and low sensitivity to electron irradiation. SSNs of functionalized organic molecules most often do not fulfill these requirements. Also by STM, adsorption sites can only very rarely be derived,[38] because barely controllable particular tip conditions and extraordinary thermal stability of the STM need to be achieved. Thus, facile and reliable methods of adsorption site determination of large functional molecules are urgently needed in surface science. In chapter 11, a method for marking a particular adsorption site on the Cu(111) surface is described. Codeposition of the marker next to an SSN promotes the determination of adsorption sites of the respective building blocks in STM images by superimposing the lattices.

In addition, an SSN of an aromatic trithiol molecule with rather small organic backbone is studied on a single crystal surface of copper. The surface chemistry of the self-assembled monolayer and the structures of temperature-induced copper-sulfide phases are analyzed. Here, reversible and irreversible, dissociative and displacive phase transitions are observed. See chapter 10 (publication #9) for results and a discussion. Adsorption characteristics of atomic sulfur on catalytically active materials are important for industrial processes. For instance, sulfur can act as a catalyst poison.[39] The presented experimental results confirm a recently published theoretical study of the most abundantly observed copper-sulfide adlayer which is structurally not solved yet. Also, two rarely observed copper-sulfide phases are examined.

Chapter 2

Scanning Tunneling Microscopy (STM)

STM is an extremely powerful technique for real space structure determination of solid surfaces and interfaces. Periodic as well as non-periodic structures can be imaged with unprecedented spatial resolution. In the present study, STM is used to analyze SSNs of organic adsorbates. For many systems, sub-molecular contrast is routinely obtained, allowing for a statement of molecular orientations and intermolecular bonds. This chapter presents the theoretical basis for STM (section 2.1) and the experimental setup of the predominantly used STMs (section 2.2).

2.1 Theory

The basic principle for STM is quantum mechanical tunneling. It describes the probability of a particle to traverse a potential barrier, even though the energy of the particle is classically insufficient. For STM, the underlying tunneling effect is the transmission of electrons through a potential barrier between two electrodes. One electrode is a metal tip, the other is the sample of interest, namely a metal or graphite crystal with adsorbed molecules. When the electrodes are spaced in tunneling distance ($\sim 0.6\,\mathrm{nm}$)[40] and a voltage (mV - V) is applied between tip and sample, electrons tunnel through the potential barrier into the electrode with lower potential.[41,42]

From a quantum mechanical point of view, electron tunneling in STM can be described as scattering of electron wavefunctions at the surfaces of the tunneling barrier. The amplitudes of the electron wavefunctions decay exponentially into the region of the barrier. If the wavefunctions of both electrodes overlap, tunneling (or in other words, transport of electrons) becomes possible.[42] A model of a tunneling barrier is displayed in figure 2.1. Two electrodes (l, r) are separated by a vacuum gap of width z and a voltage V_T is applied. The tunneling current I_T of electrons from electrode l (wavefunction ψ_l) to electrode r (wavefunction ψ_r) is given by the summation over pairs of electronic states:[40,42,43]

$$I_T \propto \sum_{l,r} f(E_l)[1 - f(E_r + eV_T)]|M_{lr}|^2 \delta(E_l - E_r).$$

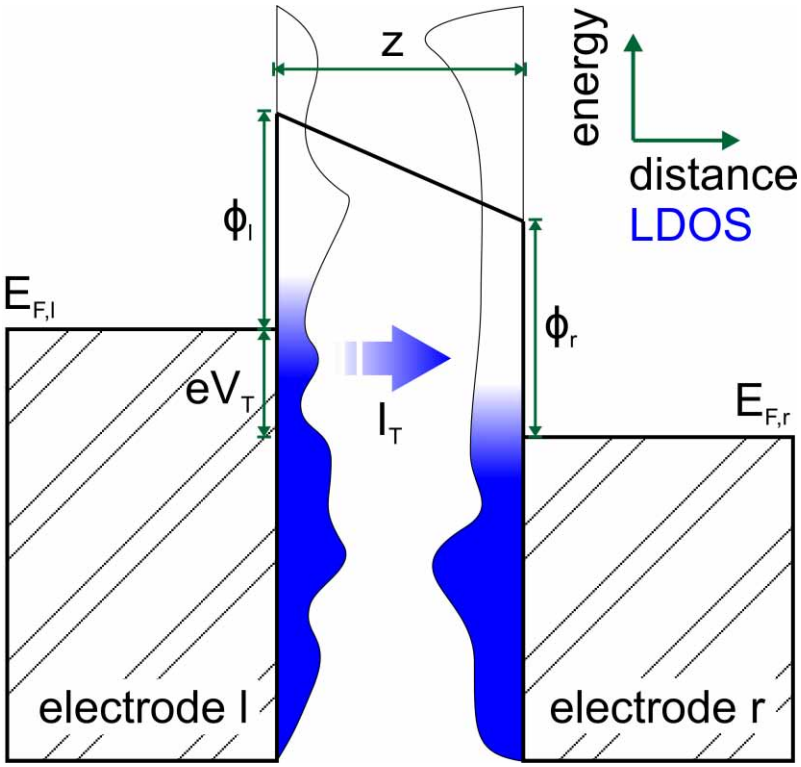

Figure 2.1: Sketch of a one-dimensional (1D) tunneling barrier. $E_{F,i}$, Fermi energy of electrode i; Φ_i, barrier height (work function of the electrode material); I_T, tunneling current; LDOS, local density of states (color gradient indicates occupation by electrons from filled (blue) to empty (white) states); V_T, applied tunneling voltage; z, real space width of the barrier. Adapted from literature.[42,44–48]

Here, $f(E_i)$ is the Fermi function, taking into account the Pauli exclusion principle, i.e. tunneling is only possible from a filled into an empty electronic state. E_i is the energy of ψ_i. The Dirac delta function ensures that only elastic tunneling with constant electron energy takes place. The matrix element M_{lr} gives the probability of the tunneling event by coupling the wavefunctions ψ_l and ψ_r. Assuming the low temperature and low voltage limit, the equation for the tunneling current can be simplified to[42,45]

$$I_T \propto V_T \sum_{l,r} |M_{lr}|^2 \delta(E_l - E_{F,l}) \delta(E_r - E_{F,l}).$$

From this it can be deduced that the tunneling current depends on the density of electronic states of the independent electrodes l and r. The local density of states (LDOS) is visualized in figure 2.1 by an arbitrary distribution.

The matrix element is an integral over the entire surface of the barrier region, here $(\psi_l^* \overrightarrow{\nabla} \psi_r - \psi_r \overrightarrow{\nabla} \psi_l^*)$ is the current operator:[40,49]

$$M_{lr} \propto \int d\overrightarrow{S} (\psi_l^* \overrightarrow{\nabla} \psi_r - \psi_r \overrightarrow{\nabla} \psi_l^*).$$

An estimation of M_{lr} and thus I_T is possible by using plane waves for the sample wavefunctions and an s-wavefunction for the tip (assuming an ideal spherical tip, see figure 2.2 B):[45]

$$I_T \propto V_T D_{tip}(E_F) e^{2kR} \rho(r_0, E_F) \tag{2.1}$$

with $\rho(r_0, E_F) = \sum |\psi_{sample}(r_0)|^2 \delta(E_{sample} - E_F)$ and $|\psi_{sample}(r_0)|^2 \propto e^{-2k(R+z)}$,

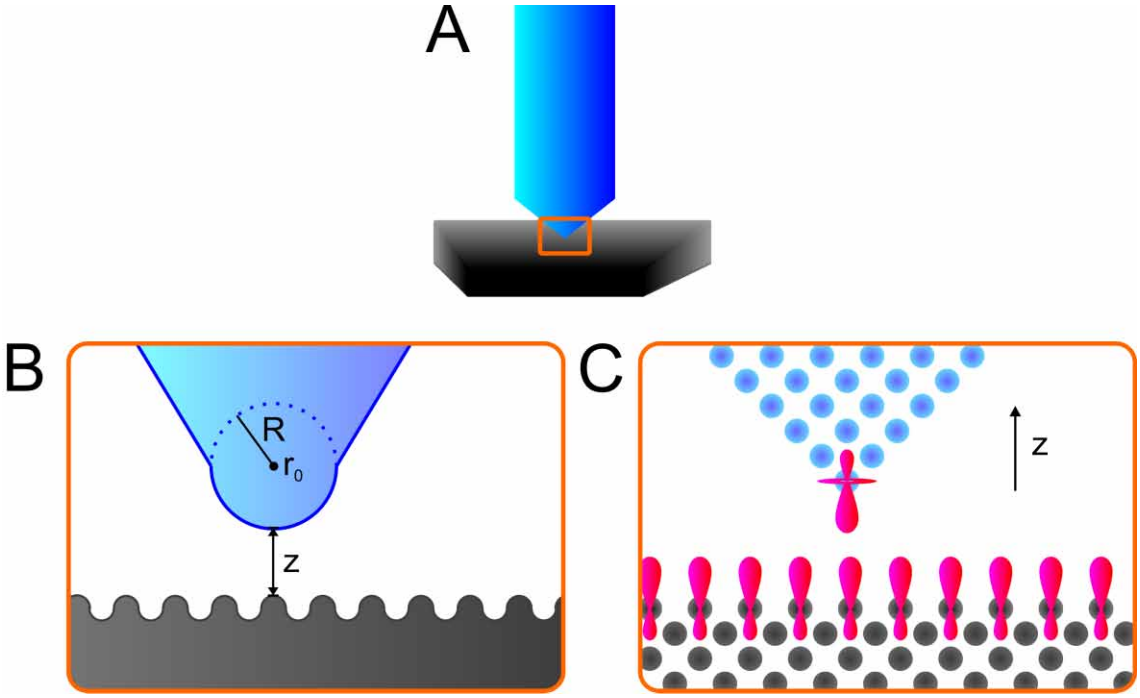

Figure 2.2: Sketches of STM tunneling gaps. (A) Macroscopic picture of a tip approached to a sample. (B) Close-up of the tunneling gap, the tip is represented by a spherical wave and the sample by a plane wave. Adapted with permission from J. Tersoff and D. R. Hamann, *Phys. Rev. Lett.* 50, 1998-2001, 1983. Copyrighted by the American Physical Society.[40] (C) Close-up of the tunneling gap, dangling bond model for the tip (d_{z^2} orbital) and the sample (sp^3 orbitals). Adapted with permission from C. J. Chen, *J. Vac. Sci. Technol. A* 9, 28-34. Copyright 1991, American Vacuum Society.[50]

$$\text{thus} \quad I_T \propto e^{-zk}.$$

Here $D_{tip}(E_F)$ is the density of states of the tip at the Fermi level; k is the decay constant ($k = \hbar^{-1}\sqrt{2m\Phi}$); $\rho(r_0, E_F)$ is the local density of states of the sample at the Fermi level at the position r_0, being the center of the spherical tip; R is the radius of the spherical tip; z is the distance between tip and sample. Formula (2.1) inidicates that the tunneling current is dependend on the tunneling voltage and the local density of states of the tip at the Fermi level. It is furthermore an exponential function of the effective tip radius and the tip-sample distance. This sensitivity to the distance is the origin of the high vertical resolution of STM. In the presented model, the major contribution to STM imaging is the LDOS of the sample or in other words, mainly the properties of the sample are represented by STM images, in the case of a known s-wave tip.[45]

The above stated Tersoff and Hamann theory was first applied to Au(110) and showed good agreement with experiments,[40,43] however numerous experimentally observed characteristics in STM images were left unexplained.[51] Examples are: The model assumes low tunneling biases, which is frequently not the case for semiconductor surfaces, molecular monolayers, or scanning tunneling spectroscopy; chemical forces between tip and sample result from close tip-sample distances, with a significant influence on the wavefunctions of tip and sample - accordingly tip and sample can

not be treated as isolated systems anymore; a contrast measured in STM can change spontaneously while scanning without changing the scanning parameters, resulting in a tremendous enhancement or reduction of lateral resolution. The latter constitutes an experimental indication for a tip dependence. However, the primary drawback of the model is the inability to explain experimentally observed atomic resolution in STM. A reason for that is the oversimplified tip model as an s-wavefunction. Improvements to this issue were achieved for several more sophisticated tip models,[51–55] one of the most promising of these is introduced below.[50]

Figure 2.2 C displays a simplified sketch of the microscopic theory for STM proposed by C. J. Chen.[50,55] Therein, a localized surface state is assumed at the tip apex, in the form of a dangling bond pointing towards the surface, for instance a d_{z^2} atomic orbital. The sample is considered as an array of dangling bonds perpendicularly sticking out of the surface, for instance sp^3 atomic orbitals. Overlapping tip and sample states are thereafter responsible for STM image formation, giving rise to a significantly enhanced lateral resolution like observed experimentally.

This study presents monolayers of mainly π-conjugated (poly)aromatic molecules adsorbed onto metal surfaces or graphite. The discrete gas phase molecular orbitals and the metal wavefunction hybridize upon adsorption, thus the STM image contrast represents the LDOS isosurface of the combined molecule-surface system.[48] An arbitrary LDOS contour is indicated in figure 2.1 in blue. Depending on the strength of interaction and the functional groups of the adsorbate, an adsorbed layer can even become metallic.[56]

The consideration of tip properties in predictions of STM images is feasible with an extension to the elastic-scattering quantum-chemistry (ESQC) method, for instance. For this, the extended Hückel molecular orbital theory is used to calculate molecular orbitals of the tunneling junction of the STM, that is, the "tip-apex-adsorbate-sample" structure. This is done for varying x, y, z coordinates surrounding the tunneling junction. Subsequently, the transfer matrix is calculated from the propagator through the tunneling junction. The transfer matrix then yields the scattering matrix (dependent also on the electron energy) and finally the conductance. Based on the conductance, the STM contrast can be calculated. So, the ESQC method includes atomic and electronic characteristics of adsorbate, substrate, and tip. Therewith, even the atomic structure of an adsorbate can be obtained by fitting a calculated to an experimental STM image.[57]

2.2 Experimental

From the first documented successful vacuum tunneling experiment[58] to state of the art STMs,[59–61] a tremendous development has taken place and is still ongoing. While the first STM was operated in high vacuum and at room temperature,[62] recent STMs work even under extreme conditions such as high temperatures in almost ambient pressure,[59] ultralow temperatures in high magnetic fields,[60] or high scanning speeds in an electrochemical environment.[61] The majority of experiments for the present study was conducted with home-built STMs: one instrument for application in UHV at variable temperatures (subsection 2.2.1), another instrument for *in situ* imaging in solutions (subsection 2.2.2).

2.2.1 Ultrahigh Vacuum Variable Temperature STM

The variable temperature UHV-STM was built by R. Gutzler, S. Kloft, and M. Lackinger as a slightly modified version[46] of the original design by B. C. Stipe and coworkers.[63] In the following a concise description of major components is given, further details are described elsewhere.[46,47,63,64]

An STM scanning unit is mounted in a stainless steel UHV chamber on a vibration-damping optical table. A set of mechanical vacuum pumps, a getter-ion pump, and a titanium sublimation pump maintain a base pressure of 3×10^{-10} mbar. The UHV chamber is equipped with a mass spectrometer, a UHV manipulator, sample and tip preparation facilities, namely an ion sputter gun and an electron beam heater (for crystal preparation parameters, see section 4.3), as well as numerous molecule evaporators such as home-built Knudsen effusion cells[65] or dosing valves. Additionally, the STM scanning unit is attached to a continuous flow cryostat for liquid nitrogen or helium operation. For the present study solely liquid nitrogen was used, yielding minimum sample temperatures of around 80 K.

The STM scanning unit is fixed via three vibration-damping Inconel springs and surrounded by two thermal radiation shields, i.e. gold-coated copper plates. Doors within the radiation shields allow for sample and tip exchange, properly positioned holes enable deposition onto a sample in the STM held at either room temperature or low temperature. The beetle type STM consists of three outer piezo tubes ("carriers"),[66] which carry a sample holder via tungsten spheres on top and perform a coarse approach through a stick-slip mechanism. For this, the sample holder contains three helical ramps. A crystal is mounted at the center of the sample holder. A fourth piezo tube ("scanner")[66] is mounted at the center of the three carriers. It is equipped with an electrochemically etched tungsten tip. Once a sample is in tunneling range, the outer piezos are grounded and the tip movement for all three spatial directions is realized solely by the scan piezo. A feedback loop maintains a constant tunneling current. The tunneling voltage is applied to the sample. The piezo movements are calibrated by imaging atomically resolved single crystal surfaces. Standard commercial electronics and software are used for STM operation and image processing.

2.2.2 Ambient STM

The versatile ambient STM for experiments at the solution-solid interface was designed and constructed by S. Kloft and M. Lackinger. A list of components follows, however detailed descriptions of the setup are reported elsewhere.[67,68]

An STM base plate is located in a metal housing to shield the scanning unit from outside influences. Vibration isolation is accomplished by suspension on three springs, eddy current damping and an optical table as support. A sample holder with a crystal is mounted at the center of the base plate, the tunneling current is measured at the sample by the use of an amplifier. A scanning head is placed on the sample holder. Scanning head and sample holder are made of Super-Invar, an alloy with low thermal expansion, to minimize temperature drift effects. Inside the scanning head, a linear nanopositioner holds a piezo tube with a mechanically cut $Pt_{90}Ir_{10}$ tip. The tunneling voltage is applied to the tip. The linear nanopositioner is used for coarse approach and performs an automated approach using stick-slip procedures. With the

sample in tunneling distance, the driving piezo of the linear positioner is grounded. The piezo tube is used for the scanning motion of the tip in x, y, and z directions. For data processing and STM operation, standard commercial electronics and software are applied. A supplementing resistively heated sample holder is used for studying temperature dependent effects, enabling imaging at elevated temperatures up to 80 °C. For imaging structures at the liquid-solid interface, the STM tip is immersed into a droplet of a solution (cf. section 4.2).

Chapter 3

Low Energy Electron Diffraction (LEED)

The first electron diffraction experiments were reported by C. Davisson and L. H. Germer in 1927.[69] This was the experimental proof of the wave-nature of electrons, as postulated in 1924 by L. de Broglie.[70] Since then, LEED evolved to a surface analysis technique with a wide range of applications. An atomically flat sample is irradiated with a monochromatic electron beam, the electrons are backscattered by the surface, and collected at a fluorescent screen. The energy of the incident electrons can be varied from a few eV to several hundred eV. The striking property of electrons in this energy range is the low mean free path in solids, i.e. the low escape depth, rendering LEED surface-sensistive.[71] Furthermore, at this energy range the wavelength of electrons is in the range of interatomic distances, enabling diffraction (e.g. 0.1 nm at 100 eV).[72,73] In the present study LEED is used to determine size and orientation of surface unit cell meshes (to this end, a single scattering theory is applied: Cf. section 3.1) and for structure determination of not only adsorbate layers but also relaxations in underlying surface layers (thereto, a multiple scattering approach is used: Cf. section 3.2). Section 3.3 describes the experimental setup.

3.1 Kinematic Theory - Single Scattering

3.1.1 Reciprocal Space

The conception of reciprocal space is a helpful tool to understand and interpret diffraction. In three dimensions, the three reciprocal unit cell vectors $\vec{a}_1^*$, $\vec{a}_2^*$, $\vec{a}_3^*$ corresponding to the three real space unit cell vectors $\vec{a}_1$, $\vec{a}_2$, $\vec{a}_3$ of a lattice are defined as[74]

$$\vec{a}_1^* = 2\pi \frac{\vec{a}_2 \times \vec{a}_3}{\vec{a}_1 \cdot (\vec{a}_2 \times \vec{a}_3)} \tag{3.1}$$

$$\vec{a}_2^* = 2\pi \frac{\vec{a}_3 \times \vec{a}_1}{\vec{a}_1 \cdot (\vec{a}_2 \times \vec{a}_3)} \tag{3.2}$$

$$\vec{a}_3^* = 2\pi \frac{\vec{a}_1 \times \vec{a}_2}{\vec{a}_1 \cdot (\vec{a}_2 \times \vec{a}_3)}.$$

Figure 3.1 A depicts a 3D lattice next to the unit cell vectors of real and reciprocal space. For surfaces, the three dimensions of real and reciprocal space reduce to two, because periodicity is only assumed in two dimensions. As LEED is a surface-sensitive technique, mainly the terminating surface layers of a crystal contribute to LEED data. Whereas, for instance, for X-ray diffraction with its large penetration depth the surface can be neglected for 3D structure analysis. There, periodicity is assumed in all three spatial directions.

The two-dimensional (2D) reciprocal unit cell vectors can be derived from equations (3.1) and (3.2), assuming $\vec{a_3}$ perpendicular to $\vec{a_1}$ and $\vec{a_2}$. Equations (3.3) and (3.4) give the resulting 2D reciprocal unit cell vectors, where $\vec{n}$ is the unit vector of the surface normal.[72–74] Figure 3.1 B displays a 2D lattice and the corresponding real and reciprocal unit cell vectors. Figure 3.1 C shows a top view of the 2D lattice.

$$\vec{a_1^*} = 2\pi \frac{\vec{a_2} \times \vec{n}}{|\vec{a_1} \times \vec{a_2}|} \tag{3.3}$$

$$\vec{a_2^*} = 2\pi \frac{\vec{a_1} \times \vec{n}}{|\vec{a_1} \times \vec{a_2}|} \tag{3.4}$$

$$\text{with} \quad \vec{n} = \frac{\vec{a_1} \times \vec{a_2}}{|\vec{a_1} \times \vec{a_2}|}.$$

Using the definition $\vec{a_i} \cdot \vec{a_j^*} = \delta_{ij} = \begin{cases} 0 \text{ if } i \neq j \\ 1 \text{ if } i = j \end{cases}$, the absolute values of the vectors are calculated by[72]

$$|\vec{a_i}| = \frac{1}{|\vec{a_i^*}| \sin\alpha} \quad \text{and} \quad |\vec{a_i^*}| = \frac{1}{|\vec{a_i}| \sin\alpha}. \tag{3.5}$$

Here, $\vec{a_i}$ is at an angle of α to $\vec{a_j}$ (see figure 3.1 C). Any lattice vector in real space can be expressed as a linear combination of base vectors ($\vec{R} = n_1\vec{a_1} + n_2\vec{a_2}$), in reciprocal space as $\vec{k} = h\vec{a_1^*} + k\vec{a_2^*}$ (n_i, h, k: integer numbers).[74]

3.1.2 Diffraction Criteria - Laue Conditions - Ewald Sphere

For a modern LEED apparatus, incident electrons can be assumed to be collimated.[72] Their wavelength λ is given by the de Broglie formula. Here h is the Planck constant, m the electron rest mass, v the velocity of the electrons, and U the electron acceleration voltage.[69] All LEED experiments for this study were carried out with normal incidence and represent elastic scattering (no energy loss).

$$\lambda = \frac{h}{mv} \approx \sqrt{\frac{1.5\ \text{V}}{U}}\ \text{nm} \tag{3.6}$$

Figure 3.2 illustrates the diffraction of electrons (wavevectors $\vec{k}$) on a 1D array of points. Constructive interference of the scattered beams ($\vec{k'}$) occurs, whenever the path difference Δ is an integer multiple of the wavelength:

$$\Delta = d \sin\varphi \stackrel{!}{=} n\lambda \tag{3.7}$$

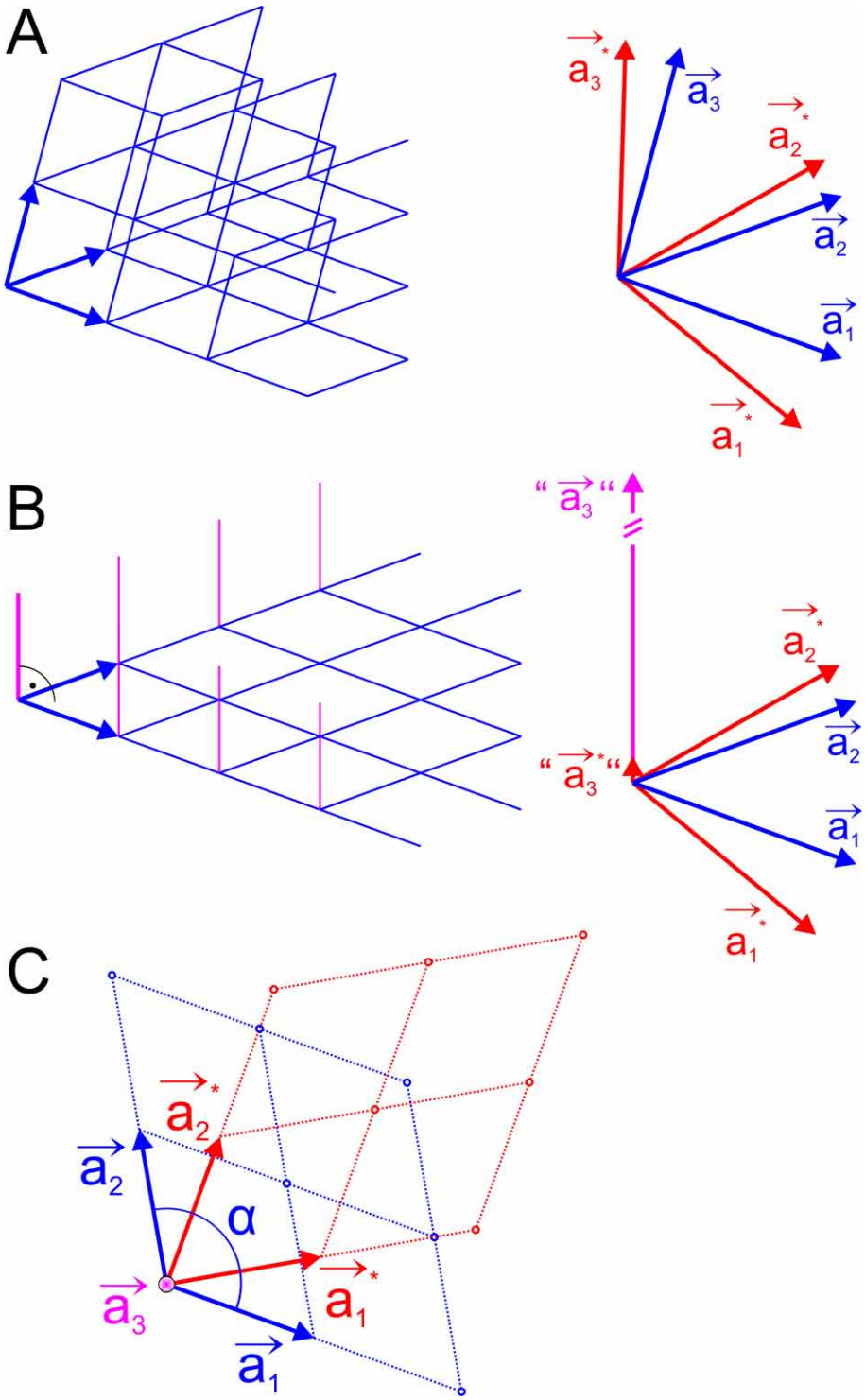

Figure 3.1: Real space and reciprocal space unit cell lattice. (A) 3D and (B,C) 2D periodicity. Blue, real space; red, reciprocal space. Adapted from literature.[72]

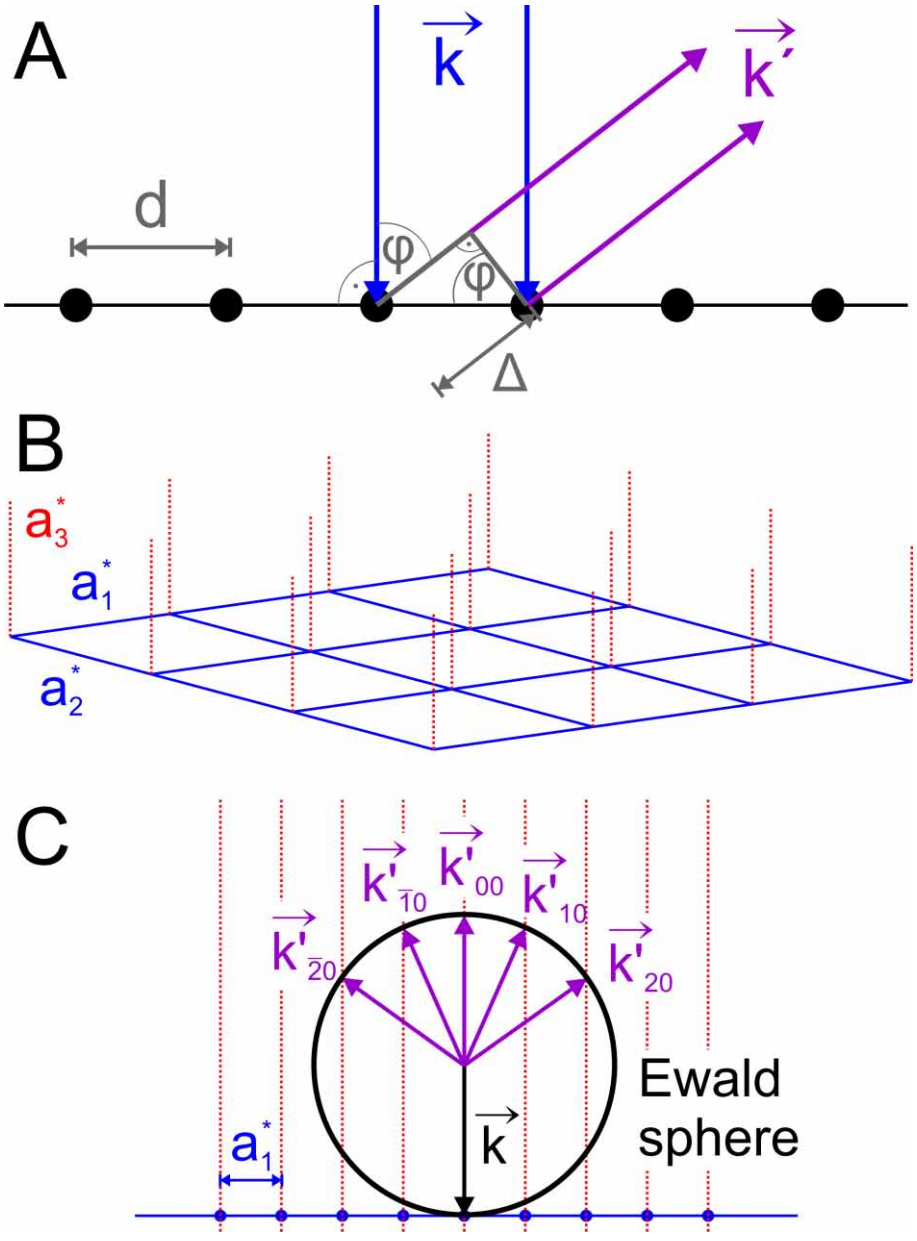

Figure 3.2: Diffraction criteria. (A) Diffraction of a collimated beam ($\vec{k}$) at a periodic array of points in 1D.[74] (B) 2D reciprocal lattice as an array of infinitesimally spaced points in z direction. (C) Section of B along $\vec{a}_1^*$, viewed along $\vec{a}_2^*$. (B-C) Adapted from literature.[73] $\vec{k}_{hk}$, incident beam; $\vec{k}'_{hk}$, diffracted beam.

For a 2D real space lattice as depicted in figure 3.1 B one can assume the third perpendicular "unit cell vector" ("$\vec{a_3}$") to be infinitely long. Hence, due to equation (3.5) the length of the corresponding reciprocal vector "$\vec{a_3^*}$" is infinitely small. Thus, the 2D reciprocal lattice consists of reciprocal lattice rods, as illustrated in figure 3.2 B. A section through this 2D reciprocal structure along "$\vec{a_1^*}$" viewed along "$\vec{a_2^*}$" is displayed in figure 3.2 C, here the 2 Laue conditions for diffraction of indicent electrons with wavevector ($\vec{k}$) are given by:[73]

$$(\vec{k} - \vec{k'}) \cdot \vec{a_1} = 2\pi h \quad \text{and} \quad (\vec{k} - \vec{k'}) \cdot \vec{a_2} = 2\pi k$$

Hence, a vector $\vec{k'}$ fulfils the diffraction criteria by ending on one of the reciprocal lattice rods of infinitely narrow points in reciprocal space, given that $\vec{k}$ ends on the origin of the reciprocal lattice. An illustrative visualisation of this diffraction condition is the Ewald sphere (cf. figure 3.2 C for a section through the Ewald sphere). The radius of the Ewald sphere is $|\vec{k}|$ and depends on the electron energy of the incident beam ($k \sim \sqrt{E_k in}$). With increasing electron energy the Ewald sphere radius and hence the number of beams fulfilling the diffraction criterion increase.

3.1.3 Formation of LEED Reflections

Figure 3.3 displays the formation of LEED reflections. At the LEED screen, constructive interference of diffracted beams is detected by a fluorescent material. From the sketch one can infer:

$$\sin\varphi = \frac{\frac{x}{2}}{r}.$$

Combination with equations (3.6) and (3.7) gives:

$$\sin\varphi = \frac{\frac{x}{2}}{r} = \frac{n\lambda}{d} = \frac{nC\sqrt{\frac{1}{U}}}{d} \quad \Longrightarrow \quad d = \frac{nrK}{x\sqrt{U}}.$$

Here, d is a real space lattice parameter, C and K are constants, n is the diffraction order, r is the radius of the LEED screen with the sample at the center, x is the distance of two equivalent spots on the LEED pattern, and U is the electron acceleration voltage. For the ratio of real space lattice parameters b and a one obtains:

$$\frac{b}{a} = \frac{\frac{n_b rK}{x_b\sqrt{U_b}}}{\frac{n_a rK}{x_a\sqrt{U_a}}} \quad \Longrightarrow \quad \frac{b}{a} = \frac{n_b x_a}{n_a x_b}\sqrt{\frac{U_a}{U_b}} \tag{3.8}$$

Equation (3.8) is helpful for a precise determination of superstructure real space unit cell parameters from LEED data. Spot distances on LEED patterns (x_a, substrate; x_b, superstructure) are measured from two patterns at different electron acceleration energies (U_a, substrate; U_b, superstructure). A literature value for the substrate unit cell parameter a (see section 4.3) can be inserted in order to derive absolute values for superstructure unit cell parameter b using equation (3.8).

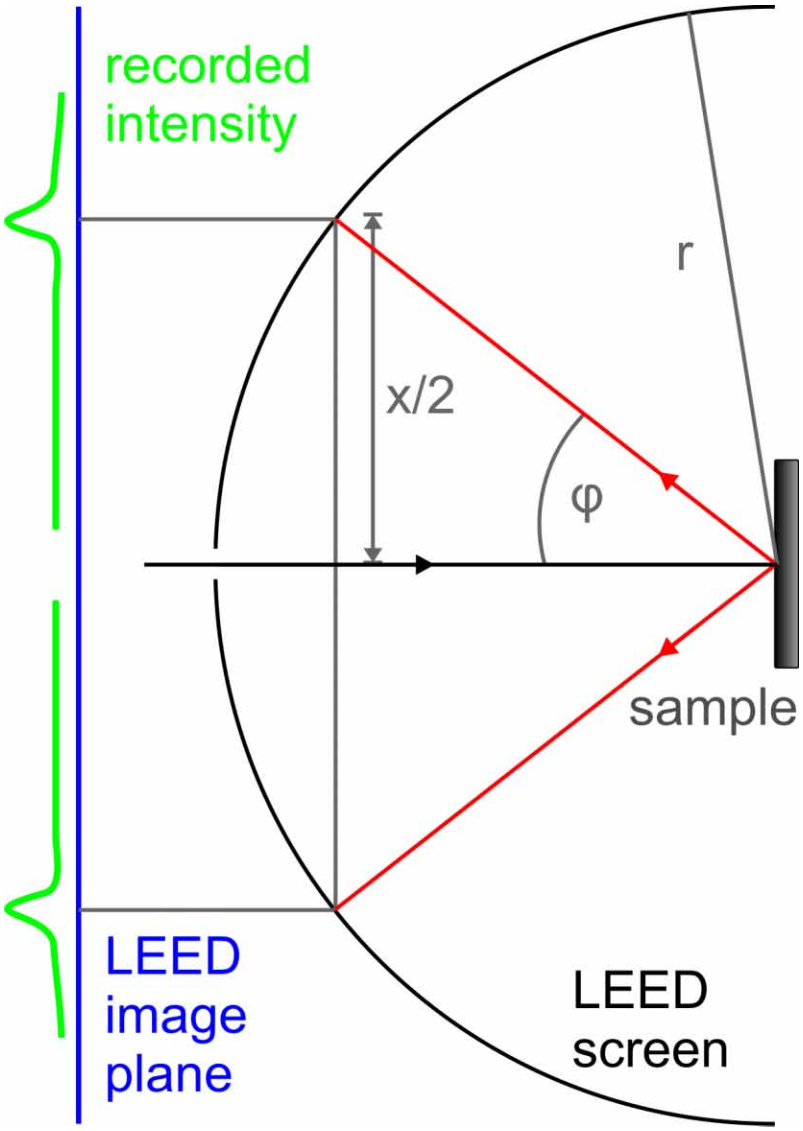

Figure 3.3: Sketch of a LEED experiment and the formation of reflections on the screen and the image plane. Incident beam, black; diffracted beams, red.

3.2 Dynamical Theory - Multiple Scattering

Subsections 3.2.2 - 3.2.7 adapted from literature.[72]

3.2.1 Procedure for LEED Intensity versus Voltage Calculations

In order to derive the adsorbate structure of a monolayer and the topmost substrate layers at the vacuum-solid interface, the LEED intensity of reflections is analyzed with respect to the energy of the incident electron ("LEED-I(V) analysis" or "quantitative LEED analysis"). From a LEED video, i.e. a series of LEED patterns for different electron energy, an intensity versus voltage curve (I(V)-curve) can be extracted for each reflection (hk).[a] On the basis of an initial model for the adsorbate structure, a structure refinement is applied. For this, I(V)-curves are simulated and compared to the experimental I(V)-curves. Subsequently, a fitting procedure optimizes the structure model.[b] In the following, important steps of the calculation are described.

3.2.2 Muffin-Tin Approximation

An atom can be described as a positively charged nucleus and a surrounding electron cloud with negative charge. When another electron approaches an atom, it is influenced by attractive forces and repulsive forces from nucleus and electrons, respectively. The smaller the distance to the nucleus, the larger the attractive force and the smaller the screening by the electron cloud. The forces on the approaching electron with respect to the distance to the atom are described by a potential. An approximation is required in order to describe the potential of a multi-electron atom and even more so of a crystal that is comprised of multiple atoms. Namely, ion-core potentials are used, where the nuclei are surrounded by several fixed electrons and only the outermost electrons are treated as delocalized. Thus, this model describes a crystal as a lattice of ion-cores in a 3D electron gas. For calculation reasons, the ion-core potentials are assumed to be spherical and in between two non-overlapping potential wells the potential is constant. This approach is called muffin-tin approximation, an illustration is given in figure 3.4. The Coulomb potential is given by

$$V_C(r) = \frac{2Z}{r} - U_C(r),$$

where r is the distance from an ion-core, Z is the total nuclear charge, and $U_C(r)$ is the electron contribution derived by the Poisson's equation. The total Coulomb potential at an ion-core is achieved by summation of the atomic potential with contributions from all neighbouring ion-cores, where only spherical symmetric contributions are considered. The region of constant potential between the ion-cores is slightly elevated, ending with a small step at the surface. This is necessary for a conservation of the overall ion-core charge.

[a] For video acquisition and I(V)-curve extraction, the software package EE2010 (M. F. Opheys, http://www.ee2000.de/) is used.

[b] The program LEEDFIT (W. Moritz, M. Gierer, J. Landskron, T. Grünberg, M. Deschauer, Y. Gauthier, J. Rundgren, and H. Over, contact: wolfgang.moritz@lrz.uni-muenchen.de) [75–77] is used for LEED-I(V) analyses.

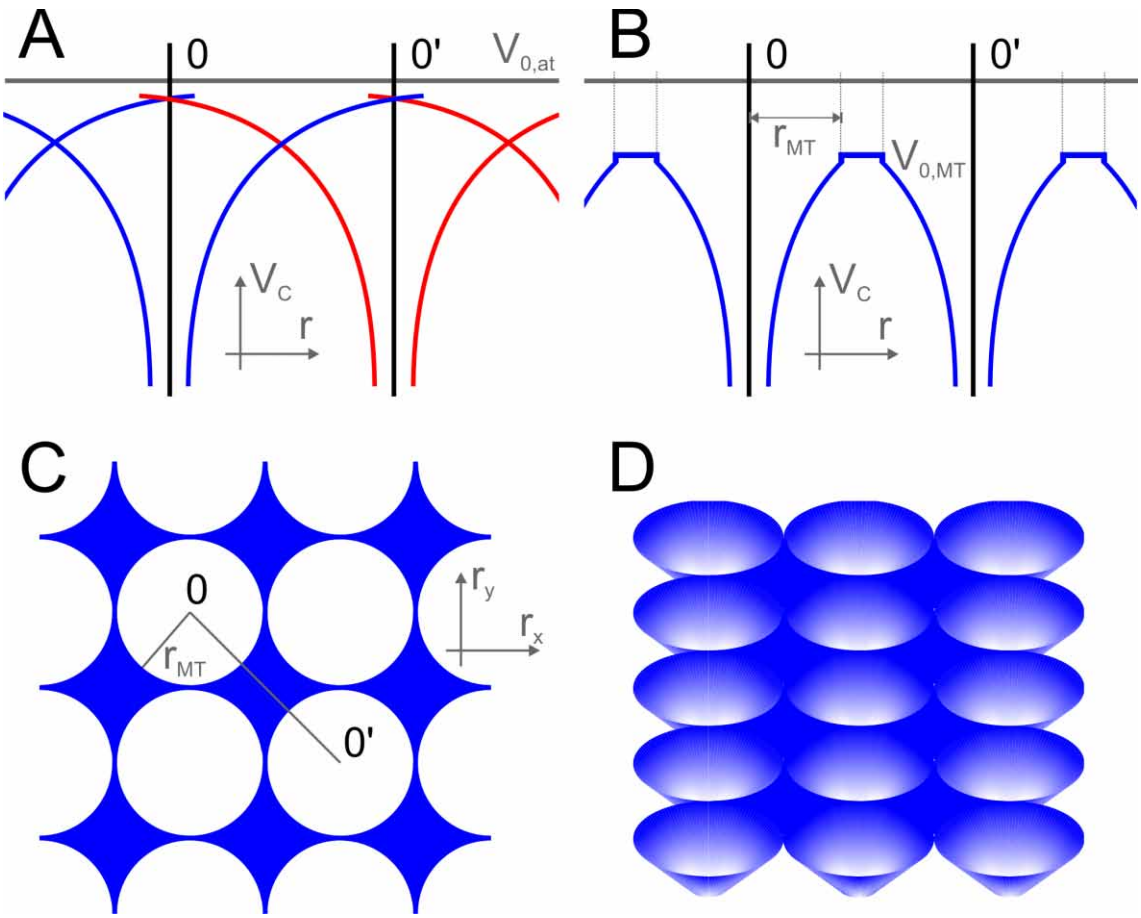

Figure 3.4: Muffin-tin approximation using ion-core potentials. (A) Coulomb potential V_C versus distance r for an array of ion-cores: Blue and red, overlapping potentials of neighbouring ion-cores 0 and 0′; $V_{0,at}$, atomic potential zero. (B) Muffin-tin approximation with muffin-tin radius r_{MT} and muffin-tin zero$V_{0,MT}$. An elevation of the horizontal part of the potential is required for conservation of the overall charge. (C) Top-view on and (D) 3D illustration of the muffin-tin potential of an ion-core layer. (A-C) Reprinted (adapted) with permission from L. J. Clarke, "Surface Crystallography". Copyright 1985 John Wiley & Sons Ltd. [72]

Further contributions to an ion-core potential arise from electron-electron exchange and correlation effects. The exchange term is based on the Pauli principle, that forbids two electrons in the same system to have four equal quantum numbers. In other words, the exchange of two electrons requires antisymmetry of the total wavefunction. A consequence of the exchange term is a forbidden region around each electron, resulting in an actually reduced potential. The correlation term is a consequence of Coulomb repulsion between two electrons. If an incident electron enters an ion-core region, very locally the electron density is decreasing in the surrounding of the incident electron. Thus, the potential is affected by the incident electron, so that the repulsion strength in its vicinity is decreased compared to an undisturbed ion-core potential. Here, two examples for a local approximation to the exchange potential are given, first with J. C. Slater's modification of the Hartree-Fock equations,[78] here $\rho(r)$ is the local electron density:

$$V_X^{\text{Slater}}(r) = -3\sqrt[3]{\frac{3\rho(r)}{8\pi}}.$$

Another related expression was derived by W. Kohn and L. J. Sham from an approach by R. Gaspar:[79,80]

$$V_X^{\text{KSG}}(r) = -\frac{2}{3}V_X^{\text{Slater}}(r).$$

For heavy atoms (starting from transition metals in the sixth period), the additional consideration of relativistic effects for the calculation of the ion-core potential can induce slight improvements compared to non-relativistic approaches. For lighter atoms, due to the low energy of the incident electrons, relativistic effects can be ignored. In the present study, scattering atoms are not belonging in the category of heavy atoms, thus non-relativistic approximations are assumed to be adequate.

3.2.3 Phase Shifts

An incident electron can be described by a wave function Ψ with amplitude a and phase b:

$$\Psi = a \cdot e^{-ib}.$$

Ψ^* is the complex conjugate of Ψ, and $\Psi^* \cdot \Psi = a^2$ is the probability of presence, related to the intensity recorded in LEED. During elastic scattering a is constant. Consequently, elastic electron scattering is sufficiently described by shifts of the wave function phases b. The Schördinger equation is used to associate wave functions to ion-core potentials of the muffin-tin approximation. Due to the spherical symmetry of the potentials V(r), the solution to the wave function can be separated into a product wavefunction with three factors: First and second part of the solution are functions of azimuthal and polar angle, $\Phi_m(\varphi)$ and $\Theta_{lm}(\vartheta)$, respectively. Here, l is the angular quantum number and m is the magnetic quantum number, i.e. the projection of l along the $\vartheta = 0$ and $\varphi = 0$ direction. $\Phi_m(\varphi)$ and $\Theta_{lm}(\vartheta)$ are independent of the scattering potential. With Ω being a solid angle comprised of ϑ and φ, they can

be expressed as a spherical harmonic $Y_{lm}(\Omega)$. $Y_{lm}(\Omega)$ gives rives to the angular distribution of the scattered wave:

$$\text{With} \quad \Phi_m(\varphi) = e^{im\varphi} \quad \text{and} \quad \Theta_{lm}(\vartheta) = P_l(\cos\vartheta) \quad \text{is}$$

$$Y_{lm}(\Omega) = \Phi_m(\varphi)\Theta_{lm}(\vartheta) = P_l(\cos\vartheta)e^{im\varphi}.$$

The third part of the solution is a radial function $R_l(r)$. Here, $\rho = r\sqrt{2}(E - V(r))$ is used for replacing r, $h_l^{(1)}$ is the first kind spherical Hankel function, δ_l is the phase shift, and $s_l(\rho)$ is the scattering amplitude with respect to the phase shift, depicted by a function called S-matrix.

$$R_l(r) = f_l(\rho)r\sqrt{2}(E - V(r))$$

$$\text{with} \quad f_l(\rho) = u_l(\rho) + s_l(\rho) \quad \text{and} \quad s_l(\rho) = \beta_l(e^{2i\delta_l} - 1)h_l^{(1)}$$

With this, calculation of a scattering event is possible for a given ion-core potential and energy of the incident electron by a set of phase shifts for a set of angular quantum numbers l. For a quantification of phase shifts, the Schrödinger equation has to be numerically integrated within the ion-core potential. This is done using the logarithmic derivative L_l and integration to the sphere boundary S:

$$L_l = \frac{f_l'(S)}{f_l(S)} \quad \text{and} \quad \delta_l = \frac{1}{2i}\ln\left(\frac{L_l h_l^{(2)} - h_l'^{(2)}}{h_l'^{(1)} L_l h_l^{(1)}}\right).$$

Here, $h_l^{(2)}$ is the second kind Hankel function. With the above stated equation, the phase shifts can be calculated from the numerical solution of the Schrödinger equation using the scatting potential and the muffin-tin radius. Self-consistent phase shift calculations ("LEED-PS") at the final steps of LEED-I(V) analyses may be implemented to improve the agreement of a fit, as applied and discussed in chapter 9 (publication #7)).[37]

3.2.4 Inner Potential

An additional term is required to cope with contributions to the total potential of a crystal. In the muffin-tin approximation, as background potential the muffin-tin zero (cf. $V_{0,MT}$ in figure 3.4 B) is used, the horizontal part of the potential in-between two spherical potential wells. More effects contribute to the total background potential, rendering the muffin-tin zero an insufficient approximation. Additional effects on the total background potential that is constant over the entire crystal are summarized in the inner potential V_0. Main contributions are listed hereafter.

The work function varies for different crystallographic orientations of a crystal, which is impossible to be considered in the uniform bulk parameter muffin-tin zero. For instance, with increasing corrugation of a face-centered cubic (fcc) crystal surface, the work function decreases. An approach is to simply use tabulated mean work function values as contributions to V_0.

The energy of the incident electron influences the inner potential. Owing to reduced screening effects for higher energy electrons, the height of the ion-core

potential well (determined by the inner potential) thus has to be reduced in order to maintain a constant net repulsion of incident electrons. Calculations result in a variation in V_0 of a few eV within a typical LEED energy range.

Whenever a low energy electron enters a material, also inelastic processes occur involving a loss of energy. However, the LEED setup described in section 3.3 for the most part filters out inelastically scattered electrons by means of a counter voltage. Inelastic processes are for instance excitations of plasmons or phonons. Phonons are lattice vibrations of nuclei in a crystal and are described in subsection 3.2.6, because of their importance for the temperature dependency. Here, plasmons are discussed, being collective oscillations of a free electron gas. There is a low-energy threshold for plasmon excitation, but electrons with energies in the standard LEED range exceed it. On the other hand, the higher the electron energy, the less crucial is the energy loss by plasmon excitations, originating in the increased velocity of the incident electron. Plasmon excitation is phenomenologically included in the inner potential as an incident-energy-dependent imaginary term V_i that is constant for the entire crystal:

$$V_0 = V_r + iV_i.$$

Values of V_i can be determined experimentally on the basis of I(V) beam widths, however, a more convenient method is to guess a value for V_i in the early stages of a LEED-I(V) analysis and include variations of V_i in the final refinement steps.

3.2.5 Multiple Scattering Formalism - Layer Doubling Method

An incident electron is not only scattered one time, but multiple times inside the crystal before it finally exits the surface in the direction to the LEED screen. A multiple scattering formalism is implemented by mathematically slicing a crystal into layers parallel to the surface. Here, a layer is a group of parallel subplanes with one atom per unit cell and short inter-subplanar distance. Incident electrons are scattered by each subplane of the crystal, either in forward (into the crystal) or backward direction. Beams that are scattered in forward direction may be scattered at the next subplane again, either in forward or backward direction. In principle this procedure could be continued infinitely, however, the occurrence of inelastic processes at standard LEED energies drastically limits the penetration depth of electrons and also the number of total scattering events. An elegant method to cope with multiple scattering is the layer doubling approach. First, scattering at one crystal subplane is considered, including all combinations of forward and backward scattering. Subsequently, duplication of the subplane yields scattering characteristics for two subplanes, repeated duplication gives scattering from four subplanes, etcetera. A scattered electron is described by its wavefield at a given distance from the scattering origin, the subplane. Therein contributions of scattering and propagation are included. The scattering wavefields of ion-core planes are described by transmission and reflection matrices $\tau_\alpha^+(K)$ and $\tau_\alpha^-(K)$, applied to wavevector K of a wave scattered at a layer α. With the unit matrix E and the propagation vector P ($^+$, forward; $^-$, backward), the four possible summarized scattering events (T, transmission; R, reflection) on either side of the symmetrical plane, as visualized in figure 3.5 A, are:

$$[T_\alpha^{++}] = [P^+(E + \tau_\alpha^+(K)P^+)]$$

$$[T_\alpha^{--}] = [P^-(E + \tau_\alpha^+(K)P^-)]$$
$$[R_\alpha^{+-}] = [P^+\tau_\alpha^-(K)P^-]$$
$$[R_\alpha^{-+}] = [P^-\tau_\alpha^-(K)P^+].$$

Starting from position a, the beam is either transmitted to position b without scattering (figure 3.5 A, T_α^{++}, left), scattered at the crystal subplane α in forward direction (mathematically described by τ_α^+), or backscattered at α (using τ_α^-). Starting from b, the reverse processes take place analogously.

If a second crystal subplane β is added to α, similar events can occur successively (see figure 3.5 B). For instance, a transmission ($T_{(2)}$) or reflection ($R_{(2)}$) event is described by all possible paths from position a to c or back, respectively. Using a matrix inversion and assuming mirror symmetry between the planes, one obtains:

$$T_{(2)} = T\left(1 - R^2\right)^{-1} T \quad \text{and} \quad R_{(2)} = R + TR\left(1 - R^2\right)^{-1} T$$

According to this, scattering from two neighbouring crystal subplanes ($T_{(2)}$ and $R_{(2)}$) is described solely based on the effects of scattering from one subplane (T and R). This simplification is illustrated in figure 3.5 C. The procedure is repeated, so that scattering from four, eight, 16, or more layers is taken into account.

3.2.6 Temperature Effects

At finite temperatures, the nuclei in a crystal are in motion. Effects are typically the increase of lattice parameters with temperature and enhanced probabilities for inelastic scattering events of incident electrons at phonons. Here, ion-core vibrations are discussed, leading to incoherent scattering, resulting in reduced intensity. Atoms are not totally fixed at their lattice points, but oscillate around their mean position. At surfaces, due to their extremely anisotropic nature, atomic vibrations can be assumed to evolve differently in different directions, hence anisotropic displacement factors can also be included in LEED-I(V) calculations to reach a higher degree of agreement with experimental data.[81] Nevertheless, for optimization of anisotropic displacement factors, an excellent experimental dataset exhibiting high signal to noise ratio is necessary along with an already excellent agreement of experimental and theoretical data. In the present study, this degree of confidence is not reached, thus solely isotropic displacement factors are reasonably optimized.

To yield an illustrative representation of the effects of isotropic atomic displacements Δr, the following assumptions are made: Single scattering[c] of electrons at layers of identical ion-core potentials; averaging over time due to the high frequency of vibrations with respect to standard measurement timeframes; absence of correlations between atomic vibrations; zero velocity for the motion of ion-cores compared to the

[c] An implementation of temperature factors in multiple scattering calculations is given by W. Moritz et al.,[81] for instance.

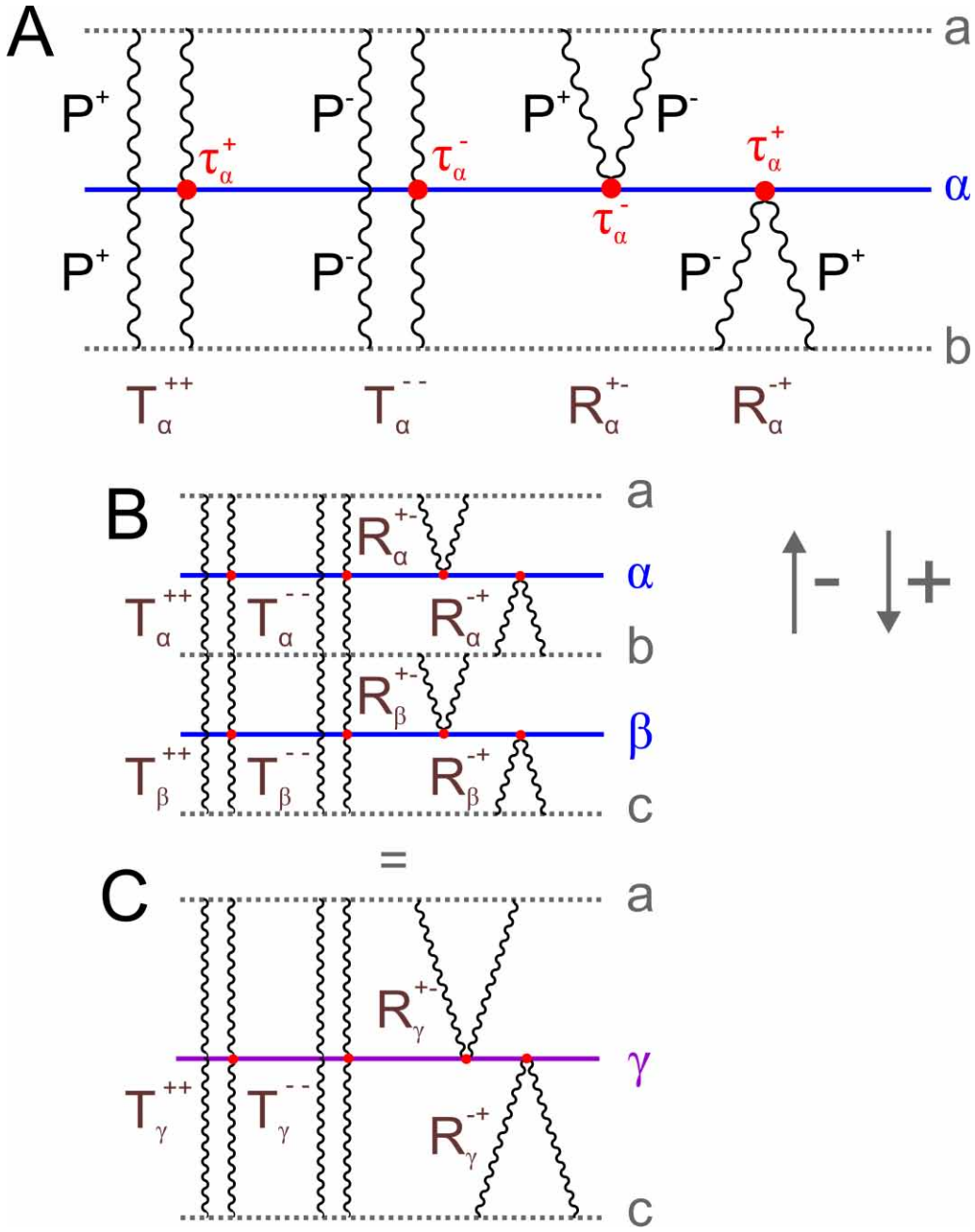

Figure 3.5: Schematic illustration of the multiple scattering formalism using the layer doubling method. (A) Transmission (T) and reflection (R) events between two positions a and b as arrays of propagation vectors (P) in forward (+) and backward (-) direction. Scattering from the crystal subplane (α) is described by scattering matrices (τ). (B) Double layered arrangement with two identical scattering processes from α and β. In the layer doubling formalism, scattering from the two subplanes is described in terms of one novel quasi-subplane γ (C), where from then on the transmission and reflection matrices between positions a and c are referred to (index γ). Reprinted (adapted) with permission from L. J. Clarke, "Surface Crystallography". Copyright 1985 John Wiley & Sons Ltd. [72]

motion of electrons in accord with the Born-Oppenheimer approximation. Therewith, the mean squared atomic displacement $\langle(\Delta r)^2\rangle$ reads:

$$\langle(\Delta r)^2\rangle \approx \sqrt{\left[\frac{9}{mk_B\vartheta_D}\left(\frac{1}{4}+1.642\frac{T^2}{\vartheta_D^2}\right)\right]^2+\left[\frac{9}{mk_B\vartheta_D}\right]^2}.$$

Here, k_B is the Boltzmann constant, ϑ_D is the Debye temperature in Kelvin, and T is the absolute temperature in Kelvin. Hence, the avaraged intensity of a LEED reflection $\langle I\rangle$ is reduced, according to:

$$\langle I\rangle = I_0 \cdot e^{-\frac{2}{6}|\vec{\Delta k}|^2\langle(\Delta r)^2\rangle}.$$

Therein, I_0 is the intensity at absolute zero, i.e. without vibration of the ion-cores and Δk the scattering vector of the electron ($\vec{\Delta k} = \vec{k} - \vec{k'}$). In order to take isotropic atomic displacements into account in a LEED-I(V) analysis, the Debye temperature for each atom or type of atom may be optimized individually.

3.2.7 Pendry's Reliability Factor

The quality of the agreement between theoretical and experimental data needs to be quantified, in order to judge the analysis. In 1980, J. B. Pendry developed a reliability factor (r-factor) for LEED-I(V) analyses,[82] which is to date one of the most frequently used r-factors. Since absolute intensities can be influenced by various parameters during LEED measurements, it is more promising to focus on peak and valley positions in I(V)-curves. Against this background, Pendry's reliability factor (R_P) is based on the logarithmic derivative of the intensity (L(E)), which is the slope in the intensity contour at a certain energy, normalized by the actual energy. R_P is defined as:

$$R_P = \frac{\int \sum_g \left(Y_g, th - Y_g, exp\right)^2 dE}{\int \sum_g \left(Y_g, th + Y_g, exp\right)^2 dE}$$

$$\text{with} \quad Y(E) = \frac{L^{-1}}{L^{-2}+V_i^2} \quad \text{and} \quad L(E) = \frac{I'(E)}{I(E)}.$$

Here, V_i determines the width of the peaks. Usage of R_P has tremendous advantages compared to other r-factors, however it is prone to noise, especially in regions with low signal to noise ratio. To avoid underestimation of the reliability of a simulated curve, particularly the experimental curve may be smoothed carefully at such regions.

The more reliable a fit is, the closer approaches R_P to zero. A typical value for an acceptable fit of a complex adsorbate structure is in the range 0.1 - 0.4, as is discussed in detail in chapter 9 (publication #7).[37] Uncorrelated curves would yield R_P close to unity, anticorrelation would approach a value of 2.0.

Subsections 3.2.2 - 3.2.7 adapted from literature, where further information including sources and original references are available.[72]

3.2.8 Least Squares Optimization

The search for the best fitting model of all symmetry-allowed physically relevant adsorption structures is usually an early stage of structure optimization. Thereby existing experimental results or computational geometry optimizations are typically exploited. Subsequently, a grid search for a valley of R_P in the parameter space of the structure is applied. In a grid search, one or a few parameters are varied independently one after another in predefined steps. Once a reasonable geometry is found with the grid refinement, the actual automated refinement procedure is started, being a least squares optimization.[76,77,83] Therein, the mean-square of the discrepancy between the experimental and theoretical curves is minimized. The derivatives of this function are calculated from the numerically obtained derivatives of the intensity curves by a linear expansion with respect to the free fitting parameters. The best-fit structure is found by iterative minimization of the mean-square deviation as a function of structural and non-structural parameters of the adsorption structure. In order to emphasize the importance of I(V)-peak positions rather than absolute intensity values, Y(E) of Pendry's r-factor can be used as a fitting function as well. The least squares optimization procedure enables computationally efficient structure refinements, since the calculation time scales only linearly with the number of independent fitting parameters.

3.3 Experimental

A LEED setup is mounted in a stainless steel UHV chamber, where a set of mechanical pumps, an ion getter pump, and a titanium sublimation pump maintain a base pressure of 1×10^{-10} mbar. The chamber is equipped with a focusable Ar^+ sputter ion source, a mass spectrometer, and molecule evaporators, namely home-built Knudsen cells[65] and dosing valves (evaporation parameters are listed in section 4.1). The sample is mounted on a manipulator with two orthogonal rotation axis perpendicular to the surface normal. A filament for electron beam heating is mounted close to the rear side of the sample, while the temperature is measured with a thermocouple at the inside (Cu(111)) or at the rear side of the crystal (Ag(111)), and controlled by a Eurotherm[d] temperature controller. For crystal preparation parameters, see section 4.3. The sample holder is fixed to a height-adjustable and rotatable manipulator at the top of the chamber. Height and rotation adjustments are required for alignment of the sample towards preparation facilities and to optimize normal incidence for LEED experiments (beam orientation of the LEED system is fixed). It is also used for the investigation of macroscopically different sample areas. Compensation of the earth's magnetic field (vertical component) is achieved by placing the chamber inside a pair of Helmholtz coils (excitation current ~0.7 A). Sample cooling is carried out by a closed cycle helium cryostat, conducting heat away from the sample holder via a copper rod and a copper strap. For operation of the cryostat, a helium compressor unit is connected via helium high pressure flex lines.

[d] Invensys Systems GmbH, EUROTHERM, Limburg an der Lahn, Germany

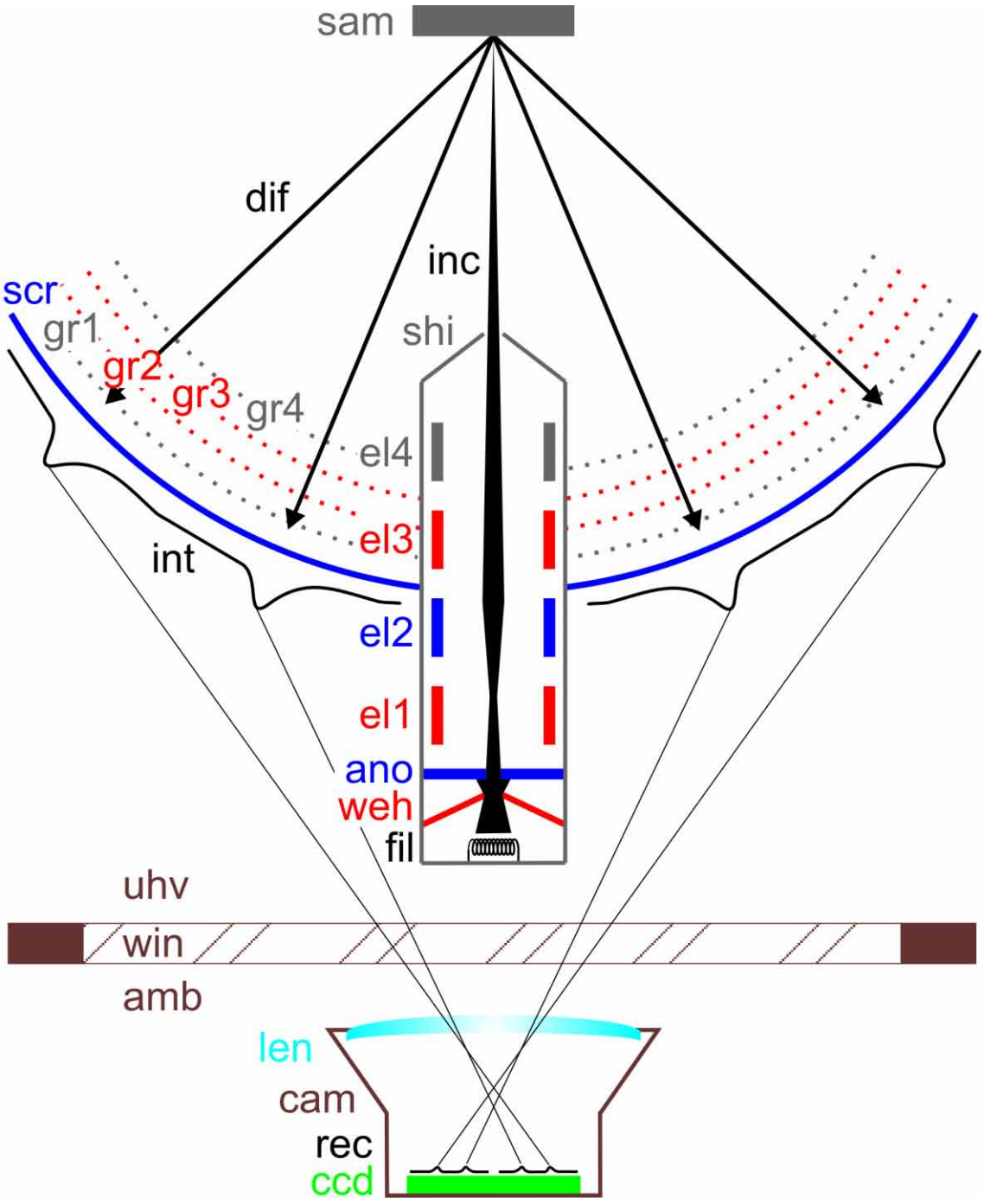

Figure 3.6: Sketch of a LEED setup (not to scale). Color code: grey, grounded; red, negative potential with respect to internal ground; blue, positive potential with respect to internal ground. Abbreviations from top to bottom: sam: sample; dif: diffracted electron beam; inc: incident electron beam; shi: mu-metal shield; scr: screen; gr1-4: grid 1-4; el1-4: electromagnetic lens 1-4; int: fluorescence intensity on the screen; ano: anode; weh: Wehnelt cylinder; fil: filament (cathode); uhv: ultrahigh vacuum side; win: window; amb: ambient pressure side; len: wide angle lens; cam: camera; rec: recorded intensity on the CCD sensor; ccd: CCD sensor. Standard settings for the components are given in table 3.1. Adapted from literature.[84,85]

Table 3.1: Settings for the LEED system (see figure 3.6 for a sketch).[84,85]

component	offset [V]	gain*
anode	+400	0.000
grid 2/3	0	-0.075
electromagnetic lenses 1 and 3	-6	-1.803
electromagnetic lens 2	+10	+1.031
screen	+6000	-1.000
Wehnelt cyclinder	-18	0.000

*related to the electron energy

The LEED system is a Spectaleed[e] four grid optics (see figure 3.6 for a sketch and table 3.1 for settings) and an ErLEED digital[f] control electronics. A focussed electron beam exits the mu-metal housing of an electron gun, thereby the potential difference between filament and internal ground defines the electron energy. A thoriated tungsten filament is used as electron source, applying filament currents of 1.48 A or less for thermionic emission. Emitted electrons are accelerated towards the anode (positive potential with respect to the electron beam, (+)). In between, a Wehnelt cylinder (negative potential with respect to the electron beam, (-)) optimizes the beam shape and acts as a filter. The electron beam is shaped by electromagnetic lenses 1 (-), 2 (+), and 3 (-), and subsequently propagates through a grounded electromagnetic lens 4 and a mu-metal shield onto the sample. The diffracted beams are recorded at the screen. Before the diffracted electrons reach the screen, they are transmitted through a set of four grids. Grid 4, mu-metal shield, and sample are grounded in order to maintain a constant potential between sample and grid. Hence, electrostatic charging and resulting deflection of the beam are reduced. After the diffracted beam passes grid 4, it is filtered by grid 2 or 3 (-) in terms of its energy distribution. The negative counter voltage of grid 2 or 3 is only slightly smaller than the electron energy and repels inelastically scattered electrons. The filtered beam propagates further through another grounded grid 1 and is finally accelerated towards a fluorescent screen (+) where it collides and causes the emission of visible light. The fluorescence intensity is recorded by a charge-coupled device (CCD) camera through a window, using a wide angle lens in order to collect light from the total area of the screen. Coverings around camera and each window of the chamber minimize stray light.

The commercial program EE2010[g] is used for controlling the ErLEED digital electronics, for recording LEED patterns and videos, as well as for I(V)-, I(T)-, and I(t)-curve extraction from LEED videos. The LEED setup can be operated in four modes. Firstly, a constant electron energy or energy steps can be applied. This mode is used at an early stage of preparation in order to check the cleanliness of a surface or the surface coverage of an adlayer structure. Images can be saved at each energy step. Unit cell parameters of unknown superstructures can be derived from LEED patterns of a superstructure in combination with a LEED pattern of a substrate for calibration (using equation 3.8, cf. section 3.1). Also a single LEED pattern displaying substrate and superstructure reflections is sufficient. The software

[e] Omicron NanoTechnology GmbH, Taunusstein, Germany
[f] Specs GmbH, Berlin, Germany
[g] M. F. Opheys, http://www.ee2000.de/

LEEDpat allows for a qualitative comparison of reflection positions to simulated LEED patterns, by applying kinematic theory.[h]

Secondly, the electron energy can be automatically varied in predefined steps. Simultaneous recording of LEED patterns at each step yields an energy-dependent series of LEED patterns. From an I(V)-video, I(V)-curves for each LEED reflection (hk) can be extracted as experimental dataset for LEED-I(V) structure refinements (see section 3.2).

Thirdly, variation of the sample temperature by the temperature controller can be combined with simultaneous recording of LEED patterns in predefined time steps, thereby generating a temperature-dependent video (I(T)-video). During recording of an I(T)-video, the electron energy is kept fixed at a value where the reflections of interest are visible on the screen. I(T)-curves can be extracted from an I(T)-video for each reflection, allowing to derive phase transition temperatures or the temperature range for the stability of a certain phase.

Fourthly, the time-dependent measurement of LEED patterns in predefined time steps without changing sample temperature or electron energy results in an intensity versus time (I(t)) video. An I(t)-video is used for the investigation of beam effects on an adlayer. I(t)-curves can be extracted for each reflection, so that degradation of the reflection intensity can be quantified. This information is useful for the adjustment of an appropriate LEED beam current by variation of the filament current as a compromise between signal intensity and radiation damage.

[h] LEEDpat: LEED pattern analyzer, version 3.0 (2013), K. Hermann and M. A. Van Hove, http://www.fhi-berlin.mpg.de/KHsoftware/LEEDpat/

Chapter 4

Materials

This chapter introduces adsorbates (section 4.1), solvents (section 4.2), and substrates (section 4.3) used for the present study. Respective evaporation or preparation parameters are given for all compounds.

4.1 Adsorbates

Organic molecules with aromatic backbones are used as adsorbates, or in other words as monomers for the fabrication of 2D networks. Adsorbates in solid state (powders) are filled into the evaporator and degassed at the sublimation temperature for several hours prior to deposition. This step is necessary for a complete removal of synthesis byproducts. Thereafter, molecules are kept at elevated temperatures to avoid recontamination. Typical sublimation parameters are listed in the following, along with additional specifications. Sublimation temperatures lower than 100 °C indicate deposition through commercial UHV dosing valves, otherwise home built Knudsen effusion cells[65] are used. Chemical structures of the adsorbates are displayed in figure 4.1.

A; 1,3,5-benzenetricarbonitrile (BCN); CAS 10365-94-3; purity ≥ 97 % (purchased from Synthon);[a] sublimation temperature ∼90 °C (deposition rate $\sim 3 \times 10^{-2}$ monolayer/min).

B; 1,3,5-benzenetrithiol (BTT); CAS 38004-59-0; purity ≥ 98 % (purchased from TCI);[b] subl. temp. ∼35 °C (dep. rate $\sim 7 \times 10^{-2}$ monolayer/min).

C; 1,3,5-triiodobenzene (TIB); CAS 626-44-8; purity not specified (purchased from Sigma-Aldrich);[c] subl. temp. ∼85 °C (dep. rate $\sim 7 \times 10^{-2}$ monolayer/min).

D; 1,3,5-tris(3',5'-dibromophenyl)benzene (TDBB); CAS 29102-67-8; purity not specified (synthesized by M. Schmittel and coworkers);[d] subl. temp. ∼210 °C (dep. rate $\sim 1 \times 10^{-1}$ monolayer/min).

[a] Synthon Chemicals GmbH & Co. KG, Wolfen, Germany
[b] TCI Europe NV, Zwijndrecht, Netherlands
[c] Sigma-Aldrich Chemie Gmbh, Munich, Germany
[d] Group of M. Schmittel, Center of Micro- and Nanochemistry and Engineering, Organische Chemie I, Universität Siegen, Germany

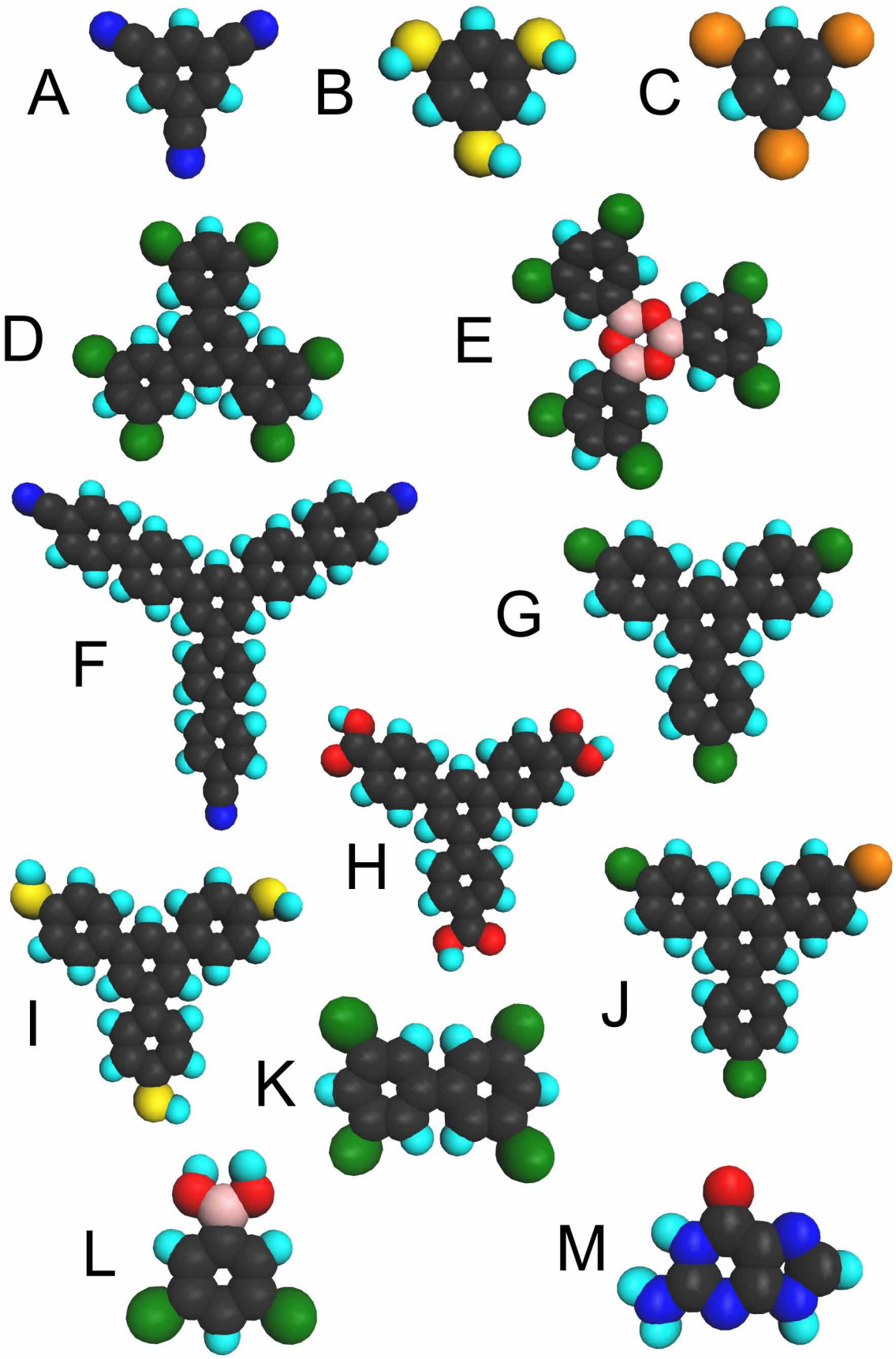
A
B
C
D
E
F
G
H
I
J
K
L
M

E; 1,3,5-tris(3',5'-dibromophenyl)boroxine (TDBPB); purity not specified (synthesized via in-crucible reaction of compound L); subl. temp. ∼190 °C (dep. rate ∼7 ×10^{-2} monolayer/min).[86]

F; 1,3,5-tris(4'-biphenyl-4"-carbonitrile)benzene (BCNB); purity not specified (synthesized by S. Neogi, M. Schmittel, and coworkers);[d] subl. temp. ∼330 °C (dep. rate ∼2.5 ×10^{-2} monolayer/min).[26]

G; 1,3,5-tris(4'-bromophenyl)benzene (TBB); CAS 7511-49-1; purity ≥ 97 % (purchased from Sigma-Aldrich);[c] subl. temp. ∼160 °C (dep. rate ∼1 × 10^{-1} monolayer/min).[64,87]

H; 1,3,5-tris(4'-carboxyphenyl)benzene (BTB); CAS 50446-44-1; purity not specified (synthesized by K. Mahata, M. Schmittel, and coworkers);[d] solely used at the solution-solid interface.[88]

I; 1,3,5-tris(4'-mercaptophenyl)benzene (TMB); purity not specified (synthesized by K. Das, M. Schmittel, and coworkers);[d] subl. temp. ∼145 °C (dep. rate ∼1 ×10^{-1} monolayer/min).[24]

J; 1-(4'-iodophenyl)-3,5-bis(4'-bromophenyl)benzene (IBB); purity not specified (synthesized by M. Schmittel and coworkers);[d] subl. temp. ∼200 °C (dep. rate ∼5 ×10^{-2} monolayer/min).

K; 3,3',5,5'-tetrabromobiphenyl (TBBP); CAS 16400-50-3; purity not specified (purchased from Sigma-Aldrich);[c] subl. temp. ∼65 °C (dep. rate ∼1 ×10^{-1} monolayer/min).

L; 3,5-dibromophenylboronic acid (DBPBA); CAS 117695-55-3; purity not specified (purchased from Sigma-Aldrich);[c] not sublimable (in-crucible reaction to compound E).[86]

M; Guanine, CAS 73-40-5; purity ≥ 98 % (purchased from Sigma-Aldrich);[c] subl. temp. ∼235 °C (dep. rate ∼1 ×10^{-1} monolayer/min).[89]

Figure 4.1 ***(preceding page)*:** Adsorbates as monomers for SSNs. (A) 1,3,5-benzenetricarbonitrile (BCN); (B) 1,3,5-benzenetrithiol (BTT); (C) 1,3,5-triiodobenzene (TIB); (D) 1,3,5-tris(3',5'-dibromophenyl)benzene (TDBB); (E) 1,3,5-tris(3',5'-dibromophenyl)boroxine (TDBPB); (F) 1,3,5-tris(4'-biphenyl-4"-carbonitrile)benzene (BCNB); (G) 1,3,5-tris(4'-bromophenyl)benzene (TBB); (H) 1,3,5-tris(4'-carboxyphenyl)benzene (BTB); (I) 1,3,5-tris(4'-mercaptophenyl)benzene (TMB); (J) 1-(4'-iodophenyl)-3,5-bis(4'-bromophenyl)benzene (IBB); (K) 3,3',5,5'-tetrabromobiphenyl (TBBP); (L) 3,5-dibromophenylboronic acid (DBPBA); (M) Guanine. Color code: boron, rose; bromine, green; carbon, black; hydrogen, turquoise; iodine, orange; nitrogen, blue; oxygen, red; sulfur, yellow.

4.2 Solvents

For self-assembly experiments at the solution-solid interface, low-molecular-weight organic compounds are used as solvents. Figure 4.2 displays chemical structures of the subsequently listed solvents. All solvents are purchased from Sigma-Aldrich.[c] A saturated solution is prepared by mixing adsorbates in solid state (powders) with a liquid solvent and subsequent sonication ($\sim 10\,\text{min}$). Centrifugation results in sedimentation of the excess solute. With a pipette, a droplet ($\sim 5\,\mu\text{L}$) of the clear solution is applied to a pristine crystal surface (for crystal preparation, see subsection 2.2.2).

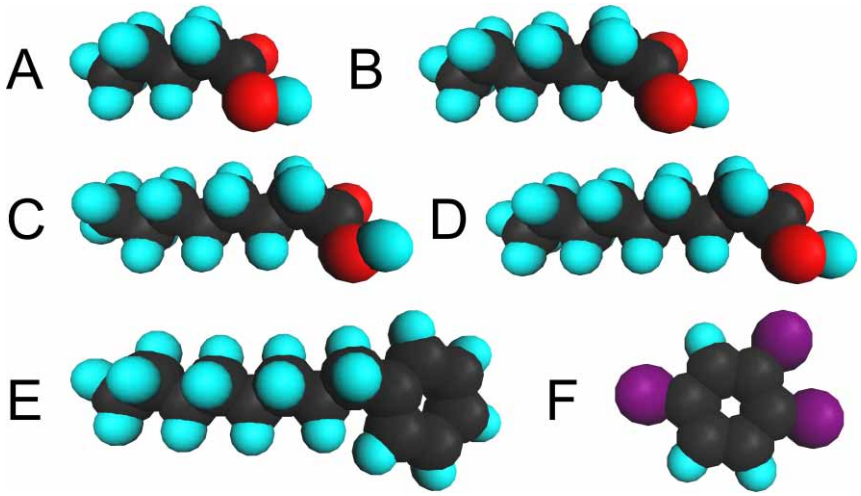

Figure 4.2: Solvents used for experiments at the solution-solid interface. (A) Pentanoic acid (5A); (B) heptanoic acid (7A); (C) octanoic acid (8A); (D) nonanoic acid (9A); (E) 1-phenyloctane; (F) 1,2,4-trichlorobenzene. Color code: carbon, black; chlorine, purple; hydrogen, turquoise; oxygen, red.

A; pentanoic acid (5A); CAS 109-52-4; purity $\geq 99\,\%$.

B; heptanoic acid (7A); CAS 111-14-8; purity $\geq 97\,\%$.

C; octanoic acid (8A); CAS 124-07-2; purity $\geq 98\,\%$.

D; nonanoic acid (9A); CAS 112-05-0; purity $\geq 97\,\%$.

E; 1-octylbenzene; CAS 2189-60-8; purity $\geq 98\,\%$.

F; 1,2,4-trichlorobenzene; CAS 120-82-1; purity $\geq 99\,\%$.

4.3 Substrates

Metal or graphite surfaces are used as substrates for on-surface growth of organic monolayers: Highly oriented pyrolytic graphite (HOPG) in (0001) orientation; silver and copper in (111) orientation. Figure 4.3 displays models of the surfaces. In the following, substrates, preparation parameters, as well as substrate lattice parameters are listed.

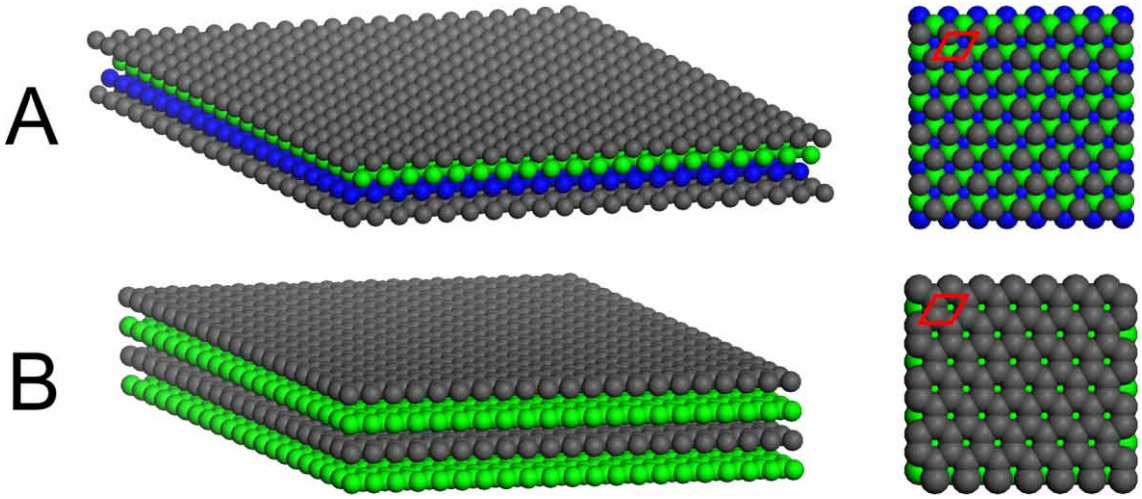

Figure 4.3: Surface structures; left: side view; right: top view; layers are indicated by varying colors; unit cells are overlaid. (A) fcc(111), here: Ag(111), Cu(111; (C) HOPG(0001).

Ag(111); (111) surface of a silver single crystal (figure 4.3 A); purchased from Mateck;[e] plane symmetry group $p3m1$; lattice parameters a = b = 0.2889 ± 0.0001 nm, $\gamma = 120\,°$;[90,91] preparation in UHV by repeated cycles of sputtering (Ne^+ (1 keV) or Ar^+ (2 keV) ions, ∼10 min) and annealing (∼825 K, ∼30 min).

Cu(111); (111) surface of a copper single crystal (figure 4.3 A); grown by P. Gille and coworkers,[f] or purchased from Mateck;[e] plane symmetry group $p3m1$; lattice parameters a = b = 0.2556 nm, $\gamma = 120\,°$;[91,92] preparation in UHV by repeated cycles of sputtering (Ne^+ (1 keV) or Ar^+ (2 keV) ions, ∼10 min) and annealing (∼800 K, ∼30 min).

HOPG(0001); (0001) surface of a highly oriented pyrolytic graphite (HOPG) crystal (figure 4.3 B); purchased from Optigraph;[g] plane symmetry group $p3m1$; lattice parameters a = b = 0.2464 ± 0.0002 nm, $\gamma = 120\,°$;[91,93] preparation in UHV by annealing (∼825 K, ∼2 h); preparation under ambient conditions by cleaving top layers with adhesive tape.

[e] MaTecK Material-Technologie & Kristalle GmbH, Jülich, Germany
[f] Group of P. Gille, Institute for Crystallography, Department for Earth and Environmental Sciences, University of Munich, Germany
[g] Optigraph GmbH, Berlin, Germany

Chapter 5

Intermolecular Bond Types – Examples

In this chapter, the observed SSNs are classified in terms of the intermolecular interactions stabilizing the arrangements of building blocks. Here, the intermolecular interactions are ordered by increasing bond strengths ranging from weak dispersive interactions (section 5.1) to strong covalent bonds (section 5.6).[8,23] Section 5.7 is related to a metal chalcogenide superstructure that was obtained after dissociation of adsorbate C-S bonds. For a list of the utilized monomers, cf. section 4.1.

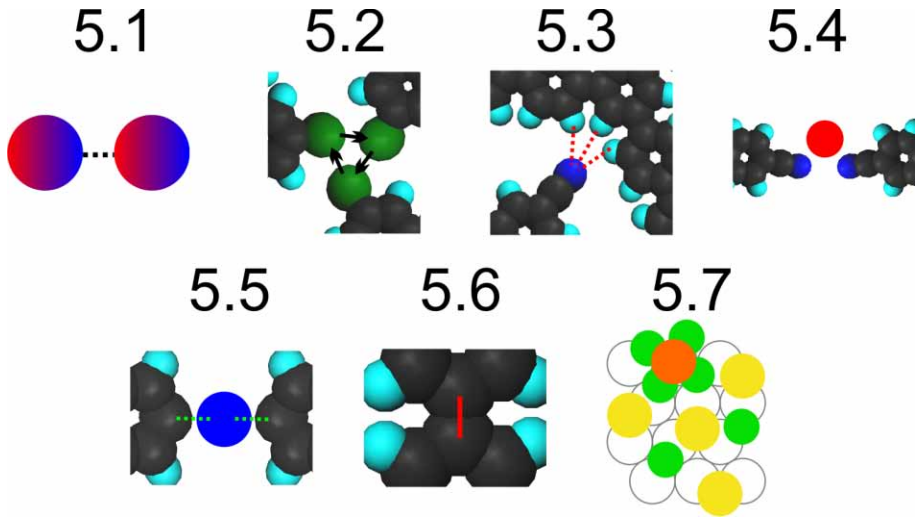

5.1 Dispersive Interactions

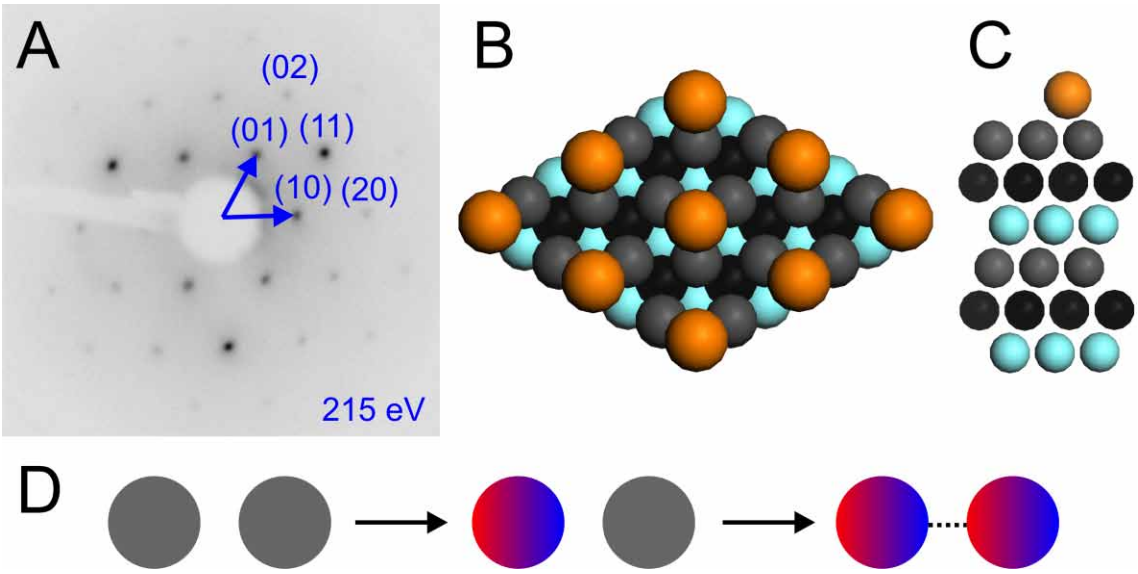

Figure 5.1: Iodine adlayer on Cu(111). (A) LEED pattern acquired at an electron energy of 215 eV with overlaid reciprocal unit cell vectors and reflection indices, belonging to a $\left(\sqrt{3} \times \sqrt{3}\right)$ R30° superstructure. (B,C) Best-fit model of a LEED-I(V) analysis. (B) Top view on 2×2 unit cells; (C) side view of a unit cell; iodine: orange; copper: grey, black, or turquoise. Iodine occupies hcp threefold hollow sites of the Cu(111) surface (cf. chapter 11 (manuscript #10)). P. M. León is acknowledged for support. (D) Sketch of the formation of attractive dispersive interactions between adjacent non-polar atoms. Red and blue areas denote oppositely charged parts. [94]

An iodine monolayer on Cu(111) is prepared by deposition of TIB with the sample held at room temperature. The C-I bonds dissociate upon adsorption. At this point it remains unclear whether the organic remainder desorbs subsequently to the C-I bond dissociation or forms irregular structures that are not detectable by LEED. A conceivable process is the dissociation of only one of the three C-I bonds in TIB upon upright adsorption on Cu(111), followed by an immediate desorption of the diiodobenzene-radical. Split off iodine atoms arrange in a densely packed $\left(\sqrt{3} \times \sqrt{3}\right)$ R30° superstructure (cf. chapter 11 (manuscript #10)). Figure 5.1 presents a LEED pattern and the best-fit surface structure of a LEED-I(V) analysis. Iodine atoms adsorb on hexagonal closed-packed (hcp) threefold hollow sites of the Cu(111) substrate. The rather large interatomic distance of 0.44 nm indicates only weak interatomic interactions within the iodine layer. Iodine atoms occupy similar adsorption sites due to strong adsorbate-substrate interactions, whereas interatomic dispersive interactions account for a high packing density. The interatomic dispersive interaction between neutral atoms is displayed in figure 5.1 D. Dipole formation in the left atom due to spontaneous charge density fluctuations induces another dipole in the right atom, resulting in attractive dipol-dipol interactions. [94]

5.2 Halogen-Halogen Bonds

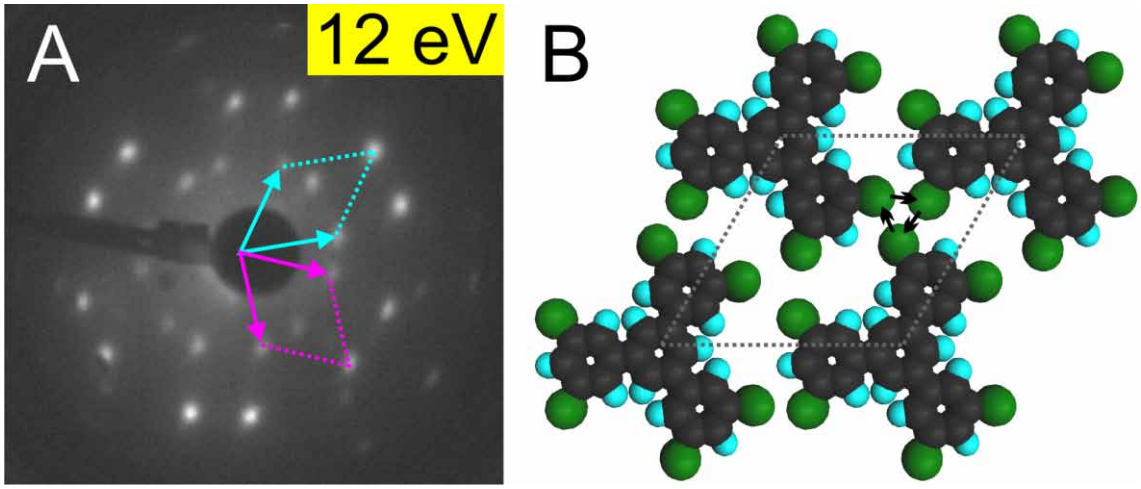

Figure 5.2: Monolayer of TDBB on Ag(111), prepared and analyzed at a substrate temperature of 60 K. (A) LEED pattern acquired at an electron energy of 12 eV with overlaid unit cell vectors of the two domains (lattice parameters: a = 1.49 nm; $\gamma = 120°$; rotation to the substrate unit cell vectors R = ±19°). (B) Tentative model of the molecular arrangement within a unit cell. Halogen-halogen bonds between three TDBB molecules are indicated by arrows.

An example for a 2D network stabilized by halogen-halogen bonds between brominated aromatic molecules is given in figure 5.2. The LEED pattern displays a monolayer of TDBB on Ag(111), deposited and analyzed at 60 K. The LEED-derived space of a unit cell is sufficient for the occupation of one planar adsorbed TDBB molecule. The intermolecular distances indicate halogen-halogen bonds as observed in other SSNs.[64,86,87] Halogen-halogen bonds are formed between three TDBB molecules in circular arrangements of the carbon-halogen bonds. A non-spherical charge distribution results in a positively charged cap at the bromine atom and a negatively charged ring around the C-Br bond. Within the circular arrangement, each positive cap points at a negative ring, and thus an attractive intermolecular bond is formed.[95] Similar binding motifs stabilize monolayers of TDBPB molecules on HOPG(0001) (cf. publication #5),[86] or TBB molecules on Cu(111) at low temperature and on Ag(111) at room temperature (cf. publication #2).[64,87]

5.3 Hydrogen Bonds

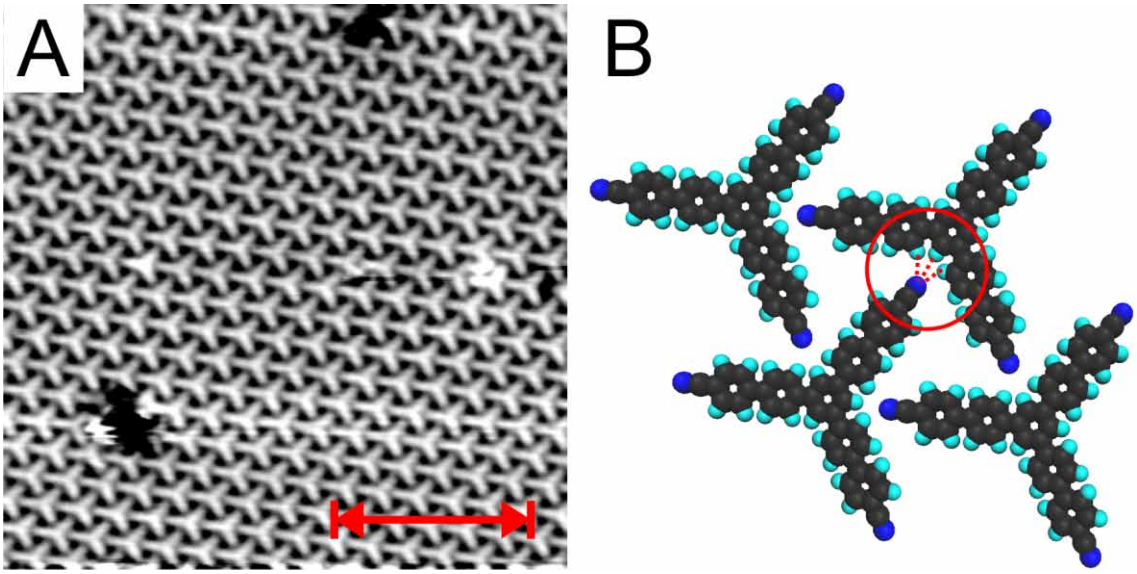

Figure 5.3: Monolayer of BCNB on Ag(111). (A) STM topograph of the α-phase; scale bar 10 nm. (B) Model of the molecular arrangement, stabilized by C ≡ N ··· H – C hydrogen bonds (cf. dashed red lines inside the circle). Reprinted (adapted) with permission from publication #6 (T. Sirtl et al., *J. Am. Chem. Soc.* 135, 691-695). Copyright 2013 American Chemical Society.[26]

An STM image of a network of BCNB molecules on Ag(111) is displayed in figure 5.3 A. The densely packed structure (α-phase) is stabilized by three intermolecular C ≡ N ··· H – C hydrogen bonds per nitrile group, as depicted in figure 5.3 B. Here, hydrogen bonds are dipole-dipole interactions between positively charged hydrogen atoms and the negatively charged nitrogen atom.[26] For further information on BCNB, cf. chapter 7 (publication #6). Similar C ≡ N ··· H – C hydrogen bonds occur in self-assembled monolayers of terphenyl-dicarbonitrile molecules. However, there the hydrogen bond angles differ.[25] Recent ab initio calculations showed that not only one carbon atom but the aromatic ring contributes to the intermolecular bond. Consequently, these bonds are more precisely described as "proton acceptor-ring interactions".[96] A different variant of intermolecular hydrogen bonds is present in monolayers of BTB on HOPG(0001). Here, two C–O ··· H–O–C hydrogen bonds per carboxyl group stabilize the chicken-wire structure.[27] For further information, cf. publication #1.[88]

5.4 Metal-Organic Bonds

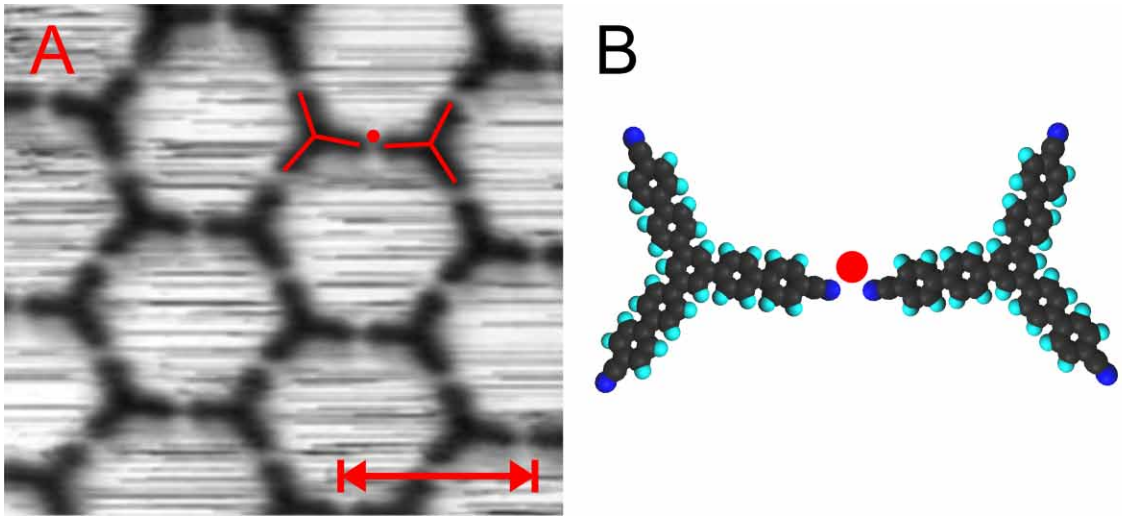

Figure 5.4: Monolayer of BCNB on Cu(111). (A) STM topograph of the β phase with overlaid tripods representing BCNB, scale bar 5 nm. (B) Illustration of the twofold metal-organic (copper-nitrile) bond between two BCNB molecules and a copper adatom (red dot) (cf. chapter 7). Reprinted (adapted) with permission from publication #6 (T. Sirtl et al., *J. Am. Chem. Soc.* 135, 691-695). Copyright 2013 American Chemical Society.[26]

Figure 5.4 A presents a monolayer of BCNB on Cu(111) arranged in the β phase. Metal-organic[a] Copper-nitrile bonds (as depicted in figure 5.4 B) stabilize the structure. Two nitrile groups of adjacent BCNB molecules coordinate to a copper adatom. The electron lone pairs of the nitrogen atoms form attractive coordination bonds with the positively charged copper adatom. The slight tilt off the linear coordination motif in the dimer is an effect of registry to the substrate. For further information, cf. chapter 7 (publication #6).[26]

[a] Here, "metal-organic bonds" refer to bonds between organic ligands and metal atoms or clusters,[97] while carbon-metal bonds are excluded (for carbon-metal bonds, cf. section 5.5).

5.5 Organometallic Bonds

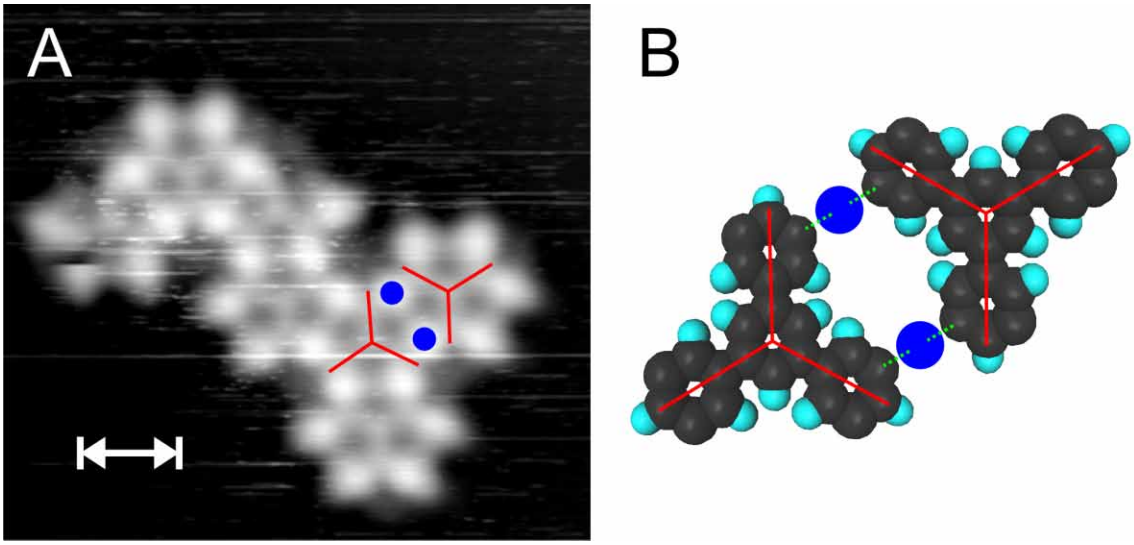

Figure 5.5: Monolayer of TDBB on Ag(111), deposited at room temperature and tempered at 375 K. (A) STM topograph of a protopolymer with intermolecular organometallic (C – Ag – C) bonds. Overlaid tripods represent triphenylbenzene hexa-radicals, blue dots depict silver adatoms. Scale bar 1 nm; scanning parameters – 2.2 V & 50 pA. (B) Sketch of the C – Ag – C bonds between adjacent hexa-radicals (cf. dashed green lines). Analogous organometallic C – Cu – C bonds are found for TBB molecules on Cu(111) (cf. publication #2).[64,87]

An SSN stabilized by intermolecular organometallic bonds[b] is displayed in figure 5.5 A. The deposition of TDBB onto Ag(111) at room temperature and subsequent tempering at 375 K causes the dissociation of the C-Br bonds. Reaction of the remaining triphenylbenzene hexa-radicals with silver adatoms results in the formation of protopolymers. Here, the building blocks are interlinked by organometallic C – Ag – C bonds (see figure 5.5 B). Similar reactions occur in monolayers of TBB molecules on Cu(111) (cf. publication #2).[64,87]

[b] Here, "organometallic bonds" refer to carbon-metal bonds between organic compounds and metal atoms or clusters.[98]

5.6 Covalent Bonds

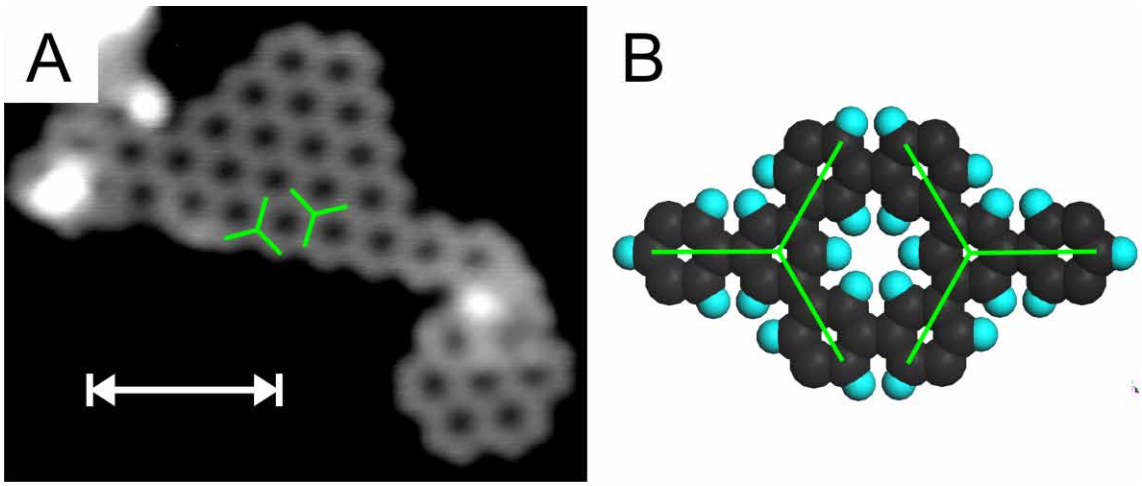

Figure 5.6: Tempered (510 K, 10 min) domain of TDBB on Ag(111). (A) STM topograph (– 2.0 V, 49 pA, scale bar 3 nm) depicting a domain of a 2D COF, comprised of interconnected phenyl rings. (B) Dimer of covalently linked triphenylbenzene hexa-radicals. Green tripods indicate the original monomers.

Covalent bonds are the intramolecular bonds that hold the organic building blocks together. However, covalent bonds are also promising intermolecular connections for an increased stability of an SSN compared to other intermolecular forces. Various types of covalent bonds are conceivable, however, this example depicts covalent C – C bonds in SSNs. Brominated molecules are well known monomers for the synthesis of covalent organic frameworks (COFs), however a drawback is the high defect density of resulting COFs. The stereochemistry of the monomer TDBB was designed for a reduction of defects in resulting COFs, as also discovered for TDBPB molecules.[86] Deposition of TDBB onto Ag(111) held at room temperature and tempering for ten minutes at 510 K causes dissociation of the C-Br bonds and recombination of the resulting triphenylbenzene hexa-radicals to covalently linked hexagonal networks with a lattice parameter of a = 0.8 nm (see figure 5.6). The reaction is similar to TDBPB on Ag(111) (cf. publication #5).[86] The thermal stability of the synthesized COFs was proven by heating the sample up to temperatures of ∼670 K. The defect density of the COF is nearly zero, however the size of synthesized domains is limited to ∼ 5 nm.

5.7 Copper Sulfide Bonds

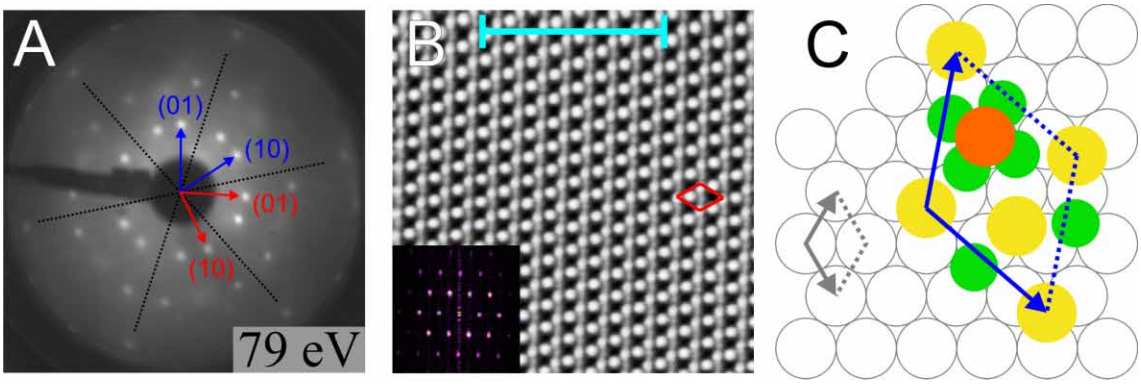

Figure 5.7: Copper sulfide superstructure on Cu(111). (A) LEED pattern of the $\left(\sqrt{7} \times \sqrt{7}\right) \mathrm{R} \pm 19.1°$ superstructure (a = 0.68 nm) acquired at an electron energy of 79 eV. Reciprocal unit cell vectors of the two domains are overlaid (blue and red). Dashed lines indicate high symmetry directions of the substrate. (B) STM topograph and fast Fourier transform (inset). A unit cell is overlaid. Scale bar: 5 nm. (C) Structure model favoured by DFT calculations.[c] The structure comprises a "Cu_4S_3" surface phase atop the copper bulk phase. Copper adatoms: green; sulfur atoms adsorbed on the surface: yellow; sulfur atom adsorbed on top of a copper adatom quartet: orange. Reprinted (adapted) with permission from publication #9 (T. Sirtl et. al, *J. Phys. Chem. C*, DOI:10.1021/jp411084k). Copyright 2014 American Chemical Society. Cf. chapter 10

Deposition of BTT on Cu(111) at room temperature and annealing up to 500 K results in the formation of a copper sulfide superstructure. Thereto, the C-S bonds dissociate and sulfur atoms arrange in a copper sulfide superstructure, while the residual aromatic backbones arrange in irregular networks or desorb from the surface. The underlying bond type of the superstructure is the covalent Cu-S bond. Figures 5.7 A and B display a LEED pattern and an STM topograph of the $\left(\sqrt{7} \times \sqrt{7}\right) \mathrm{R} \pm 19.1°$ copper sulfide superstructure with a lattice parameter of a = 0.68 nm. One out of three favoured models of a density functional theory (DFT) structure optimization[c] is depicted in figure 5.7 C. Here, formally a "Cu_4S_3" surface phase is attached to the bulk phase of Cu(111). This is the only phase whose symmetry is in accord with the experiment. For further information on BTT on Cu(111), temperature-induced copper-sulfide phases, and phase transition temperatures, see chapter 10 (publication #9).

[c] Structure model S9 of a DFT analysis.[99] J. Behler is acknowledged for providing structural data.

Chapter 6

Experimental Parameters for Structure Selection

In this chapter, the influence of synthesis parameters on structure formation in SSNs is analyzed on the basis of experimental observations. In section 6.1, the influences of monomer availability (here: surface coverage) or characteristics (here: functionalization) are described. Substrate properties (here: adatom reactivity or lattice) are discussed in section 6.2. Section 6.3 deals with kinetic effects owing to the preparation procedure (i.e. solvent coadsorption, deposition rate of monomers, or substrate temperature).

6.1 Monomer

6.1.1 Coverage

Table 6.1: Intensity maxima (centers of Gauß fits of I(T)-curve peaks, cf. figure 6.1) of guanine phases on Ag(111) with respect to the deposition time.[89]

deposition time [min]	peak center [K]			
	α	β	γ	δ
6	470	503	530	576
10	484	508	531	≥ 580
15	—*	510	539	592

*α-phase not present for deposition times exceeding 10 min.

Numerous examples of coverage-dependent formations of SSNs are reported in literature.[8,100–102] Here, preliminary results of a coverage-dependent study on guanine at the UHV-Ag(111) interface are presented. Both the formation of structures and the transition temperatures between phases are influenced by the coverage. In figure 6.1, LEED-I(T) results are displayed. For this, guanine was deposited for 10 min onto clean Ag(111). A LEED pattern of a structure called α-phase evolves upon increasing the temperature to ∼450 K. Thus, a preceding disordered phase (hence no LEED pattern) is transformed into an ordered arrangement by the supply of thermal energy. Further increase in temperature results in three consecutive phase transitions into structures termed β-, γ-, and δ-phases. The respective transition temperatures amount to: α- to β-phase at ∼500 K; β- to γ-phase at ∼525 K; γ- to δ-phase at

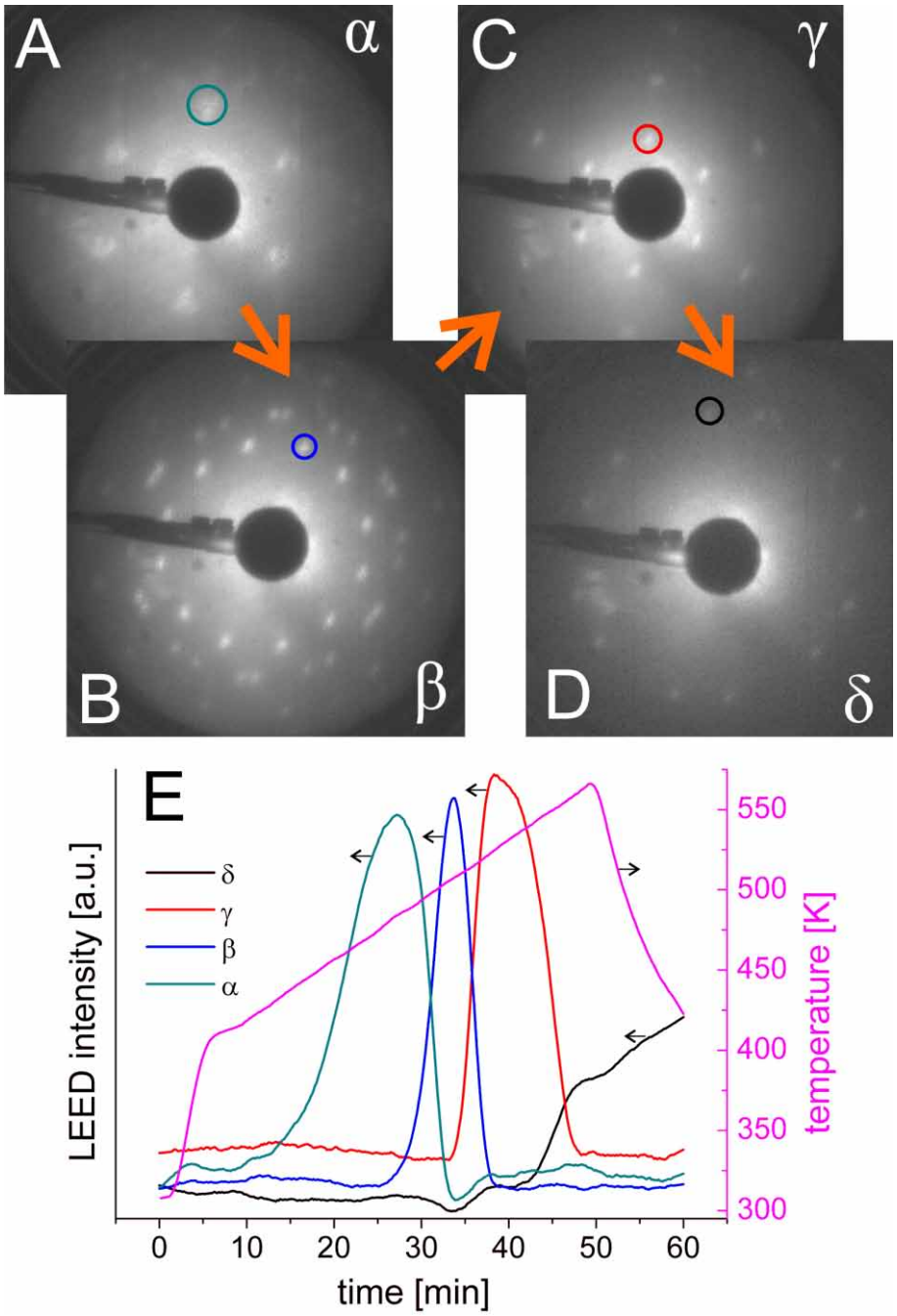

Figure 6.1: Guanine on Ag(111) (deposition time: 10 min). (A-D) Images from a LEED-I(T) video recorded at an electron energy of 15 eV. The LEED patterns represent the intensity maximum of each phase (α, β, γ, δ). For LEED intensity maxima with respect to deposition times, see table 6.1. (E) I(T)-curves corresponding to the LEED spot intensity indicated by circles in (A-D). The temperature profile is overlaid (right axis).[89] S. Bauer is acknowledged for experimental support.

~550 K. Interestingly, depending on the deposition time and thus monomer coverage, the phase transition temperatures shift to higher temperatures. Table 6.1 lists peak centers of I(T)-curves for deposition durations of 6, 10, and 15 min. Accordingly, the temperature of the intensity maximum for each phase increases with the deposition time. However, variations in coverage not only affect the temperature range for the formation of each of the four phases, but even control structure formation in the case of the α-phase. The α-phase is not present for deposition times exceeding 10 min. STM should be applied to determine the arrangement of guanine inside the unit cell. With the help of detailed STM images, structure models can be developed. Structure models provide the basis for the understanding of the origin of the remarkable coverage-dependence of guanine self-assembly on Ag(111).

6.1.2 Functionalization

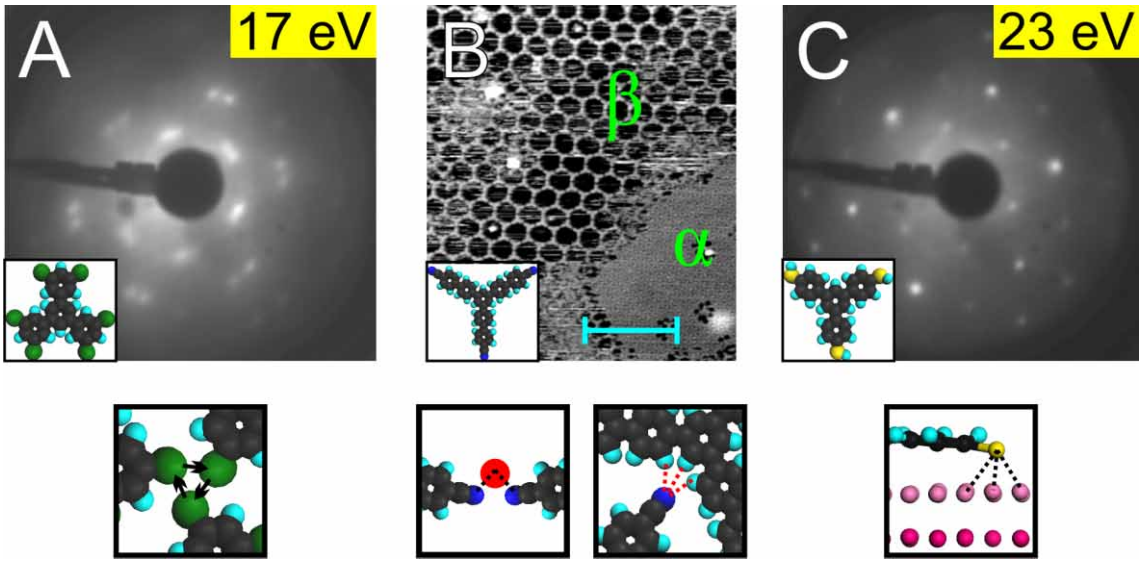

Figure 6.2: SSNs on Cu(111). (A) LEED pattern (electron energy: 17 eV) of a TDBB monolayer, deposited at a substrate temperature of 60 K (top). TDBB molecules (inset) are functionalized with bromine substituents. The emerging densely packed structure is stabilized by halogen-halogen bonds (bottom). (B) STM topograph of a BCNB monolayer, deposited at room temperature (top). BCNB molecules (inset) are functionalized with nitrile groups. Two coexsisting polymorphs are observed, a densely packed α-phase stabilized by hydrogen bonds (bottom, right), and a porous β-phase stabilized by metal-organic bonds (bottom, left). Reprinted (adapted) with permission from publication #6 (T. Sirtl et al., *J. Am. Chem. Soc.* 135, 691-695). Copyright 2013 American Chemical Society.[26] (C) LEED pattern (electron energy: 23 eV) of a TMB monolayer, deposited at the substrate held at room temperature (top). TMB molecules (inset) are functionalized with thiol groups. The emerging structure is stabilized by covalent anchoring of sulfur atoms to substrate atoms (bottom).[24,37] Reproduced by permission of the Owner Societies from publication #7 (T. Sirtl et al., *Phys. Chem. Chem. Phys.* 15, 11054-11060). Cf. chapter 9 and also publication #4.

Functional groups of building blocks considerably account for structural versatility observed in SSNs.[23] In figure 6.2, LEED patterns and an STM topograph, along with corresponding binding motifs of different SSNs are displayed. Here, molecules

with threefold symmetric organic backbones but different types of functional groups form completely divergent structures on Cu(111):

- The following example demonstrates two possible binding motifs based on halogen substituents as functional groups of aromatic adsorbates. A TDBB molecule comprises a triphenylbenzene backbone functionalized with six bromine substituents. TDBB molecules arrange in halogen-halogen bonded, densely packed structures upon deposition on the substrate held at 60 K (cf. figure 6.2 A). Deposition on the substrate held at room temperature results in the dissociation of the C-Br bonds and the formation of organometallic networks (cf. figure 6.10 D,E).
- A BCNB molecule consists of a tris(biphenyl)benzene backbone functionalized with three nitrile groups. Based on two different binding motifs, BCNB molecules form coexisting polymorphs upon deposition at room temperature (cf. figure 6.2 B). Firstly, a densely packed, hydrogen bonded α-phase is observed. Nitrile groups and hydrogen atoms of adjacent molecules form $-C \equiv N \cdots H-C_{aryl}-$ hydrogen bonds. Secondly, a porous, metal-organic β-phase emerges. Nitrile groups of adjacent adsorbates bind to a copper adatom or cluster to form copper-nitrile coordination bonds.[24,26] Cf. chapter 7 (publication #6).
- A TMB molecule comprises a triphenylbenzene backbone functionalized with three thiol groups. Upon deposition at room temperature, the S-H bonds dissociate, and subsequently the resulting TMB-trithiolates arrange in a well ordered monolayer (cf. figure 6.2 C). The structure is mainly stabilized by covalent anchoring of sulfur atoms to copper atoms of the substrate.[37] Cf. chapter 9 (publication #7).

Thus, in these examples, on the same substrate the choice of functionalization of comparable organic backbones significantly influences intermolecular binding motifs and molecular arrangement in SSNs.

6.2 Substrate Material

6.2.1 Lattice

The formation of SSNs is also considerably governed by the relation of the preferred adsorbate lattice to the substrate lattice. Here, adsorbate-adsorbate interactions compete against adsorbate-substrate interactions.[8] The material of a substrate influences the strength of adsorbate-substrate interactions. Also the lattice of a surface is predefined by the surface material. The influence of the substrate lattice on SSN formation decreases with increasing bond strength of the interlink in an SSN. For instance, incommensurability of an SSN lattice to a surface lattice usually implies minor effects of the adsorbate-substrate interactions. Incommensurability is indicated by a Moiré pattern in an STM topograph or by splitting of LEED reflections. In the following, three examples are highlighted, where the substrate lattice and material distinctly influence adsorbed monolayers.

Firstly, self-assembled adlayers of BCNB on Ag(111) are compared to those on Cu(111) (cf. LEED patterns in figure 6.3). The molecular arrangement is

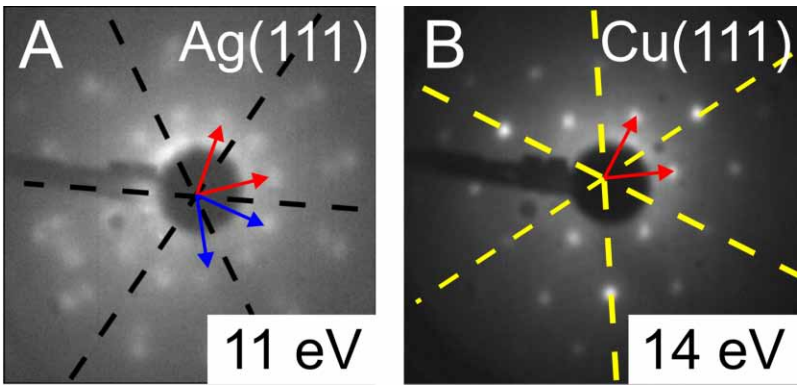

Figure 6.3: LEED patterns of BCNB arranged in the α-phase on (A) Ag(111) (electron energy 11 eV) and (B) Cu(111) (electron energy 14 eV). The registry between adsorbate lattice and substrate lattice causes different superstructure relations of $\left(\sqrt{39} \times \sqrt{39}\right) \mathrm{R} \pm 16°$ on Ag(111) and $\left(4\sqrt{3} \times 4\sqrt{3}\right) \mathrm{R}30°$ on Cu(111). The molecular arrangement is similar for both SSNs. Reciprocal superstructure unit cell vectors are overlaid (arrows), as well as substrate high symmetry directions (dashed lines). Reprinted (adapted) with permission from publication #6 (T. Sirtl et al., *J. Am. Chem. Soc.* 135, 691-695). Copyright 2013 American Chemical Society.[26] Cf. chapter 7.

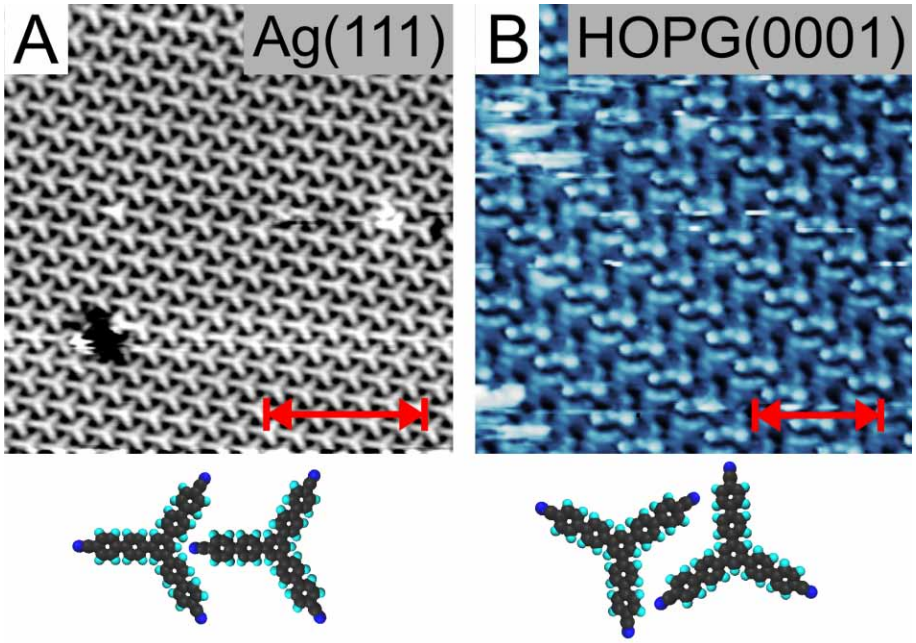

Figure 6.4: STM topographs (top) and binding motifs (bottom) of BCNB monolayers at the UHV-Ag(111) (A) and the UHV-HOPG(0001) (B) interfaces. The substrate material is a conceivable reason for the different molecular arrangements of adsorbed BCNB molecules. (A) Densely packed α-phase. Scale bar 10 nm. Reprinted (adapted) with permission from publication #6 (T. Sirtl et al., *J. Am. Chem. Soc.* 135, 691-695). Copyright 2013 American Chemical Society.[26] Cf. chapter 7. (B) Densely packed γ-phase. Scale bar 5 nm. Reprinted (adapted) with permission from publication #8 (T. Sirtl et al., *ACS Nano* 7(8), 6711-6718). Copyright 2013 American Chemical Society.[35] Cf. chapter 8.

similar for both substrates, that is, densely packed and stabilized by intermolecular hydrogen bonds (α-phase). However, despite the similar arrangements, adsorption sites of BCNB molecules differ on both substrates. The kinematic LEED analysis reveals a $\left(\sqrt{39} \times \sqrt{39}\right) \mathrm{R} \pm 16°$ superstructure on Ag(111), but a $\left(4\sqrt{3} \times 4\sqrt{3}\right) \mathrm{R}30°$ superstructure on Cu(111). No splitting of LEED reflections is observed, thus commensurability of superstructure to substrate lattices is given, as a consequence of a non-negligible influence of the substrate. A conceivable explanation for the difference in superstructure relations is energy minimization by adjustment of the orientation of BCNB molecules (and hence superstructure lattices) to the substrate lattices. Both substrates exhibit trigonal symmetry, but different lattice parameters (cf. section 4.3: $a_{Ag(111)} = 0.289\,\mathrm{nm}$; $a_{Cu(111)} = 0.256\,\mathrm{nm}$). In other words, a densely packed BCNB monolayer (arranged in the α-phase) exhibits a preferred lattice parameter (DFT geometry optimization without contribution of a substrate: $b_{DFT} = 1.81\mathrm{nm}$). Due to the tendency to commensurability, the preferred lattice parameter is varied by the substrate to the different substrates. As a result, the lattice parameter of the α-phase is larger on silver ($b_{Ag} = 1.80\mathrm{nm}$) compared to copper ($b_{Cu} = 1.77\mathrm{nm}$) and also the orientation of BCNB molecules differs, as indicated by the different superstructure relations.[26]

Not only the orientation of a superstructure with respect to the substrate is influenced by the substrate registry, but also the molecular arrangement itself. An example for this is a study of BCNB self-assembly at the UHV-Ag(111) and the UHV-HOPG(0001) interfaces (cf. STM topographs in figure 6.4). On Ag(111), the α-phase with head-to-tail arrangement of BCNB molecules emerges, whereas on HOPG(0001) under similar experimental conditions, a dimer-row structure (ε-phase) forms. Both the α- and the ε-phases are stabilized by up to three $-\mathrm{C} \equiv \mathrm{N} \cdots \mathrm{H} - \mathrm{C}-$ hydrogen bonds per nitrile group, however, the bond angles differ. Based on the absence of Moiré patterns in the STM topographs, commensurability between superstructure and substrate lattices is assumed. A conceivable factor for the formation of different structures in these two examples is the substrate material and its effect on the type and strength of adsorbate-substrate interactions.[26,35] For further information on BCNB, cf. chapters 7 and 8 (publications #6 and #8).

In the case of weak intermolecular forces, an SSN is largely determined by adsorbate-substrate interactions. Then, especially for rather large organic adsorbates, long-range order in SSNs is only achieved under certain conditions. That is, the molecular symmetry, the intramolecular distances, and the positions of functional groups match to the substrate defined adsorption sites. For instance, TMB molecules in self-assembled monolayers on Cu(111) simply need to slightly deform in order to meet the above stated requirements. Immediately upon adsorption, the S-H bonds dissociate, thus TMB molecules are deprotonated. Subsequently, TMB-trithiolates arrange in a densely packed structure based on covalent anchoring of the thiolate groups to the copper surface. Long-range ordered structures with only one rotational domain are formed. In figure 6.5, the LEED-I(V) optimized adsorption structure is displayed. Based on the rather large $-\mathrm{S} \cdots \mathrm{H} - \mathrm{C}-$ distances within the monolayer, a stabilization of the arrangement by hydrogen bonds can be excluded. Hence, the dominating interactions are covalent S-Cu bonds with the substrate. Thiolate groups exhibit preferred adsorption sites on Cu(111), thus an optimization of the structure in terms of total energy requires the occupation of the same preferred adsorption

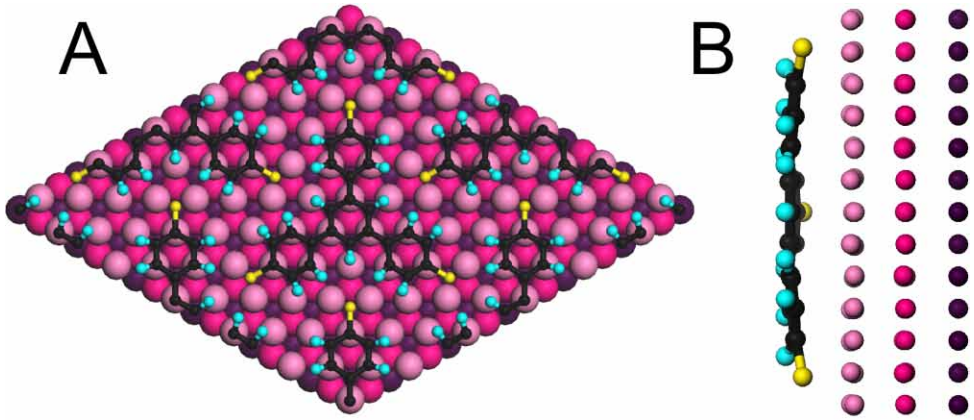

Figure 6.5: (A) Top view and (B) side view on the LEED-I(V) best fit structure of TMB on Cu(111). The registry between the preferred adsorption sites of the adsorbate and the substrate lattice coincide to such an extent that only this adsorption geometry is found. Reproduced by permission of the Owner Societies from publication #7 (T. Sirtl et al., *Phys. Chem. Chem. Phys.* 15, 11054-11060).[37] Cf. chapter 9 and publication #4.[24]

sites by all three thiolate groups of TMB-trithiolate molecules. This is possible by a suitable orientation of the adsorbates with respect to the substrate lattice. In the actual geometry, all sulfur atoms are found to be located above hcp threefold hollow sites and all phenyl rings above fcc threefold hollow sites. Obviously, the good match between adsorbate geometry and Cu(111) surface mesh results in the formation of this particular SSN.[37] For further information, cf. chapter 9 (publication #7).

6.2.2 Adatom Reactivity

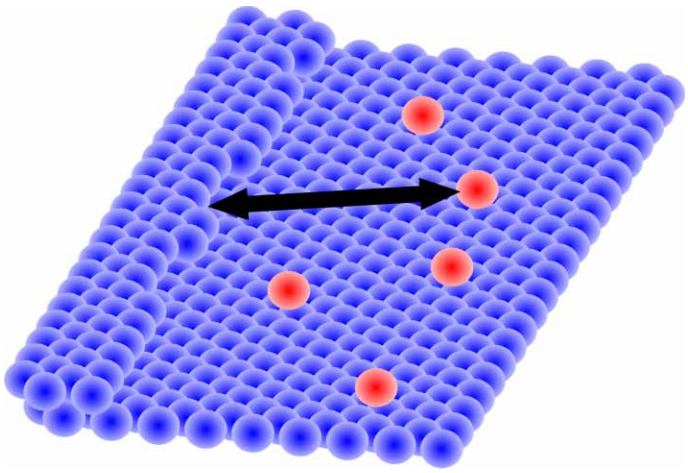

Figure 6.6: Sketch of the adatom gas of an fcc(111) surface. Red: adatoms; blue: surface atoms. The arrow indicates detachment of an adatom from a step edge or attachment of an adatom to a step edge.

The surface material not only affects the aforementioned substrate lattice and the catalytic activity of a surface (as known for TBB on Ag(111) vs. Cu(111), cf. publication #2),[64,87], but also the reactivity of adatoms. On metal surfaces an adatom gas is present, comprised of highly mobile adsorbed metal atoms. Adatoms detach from step edges and attach to step edges, so that the average adatom density reaches an equilibrium value. A sketch of the adatom gas on an fcc(111) surface is depicted in figure 6.6. In order to study the influence of adatom reactivity,

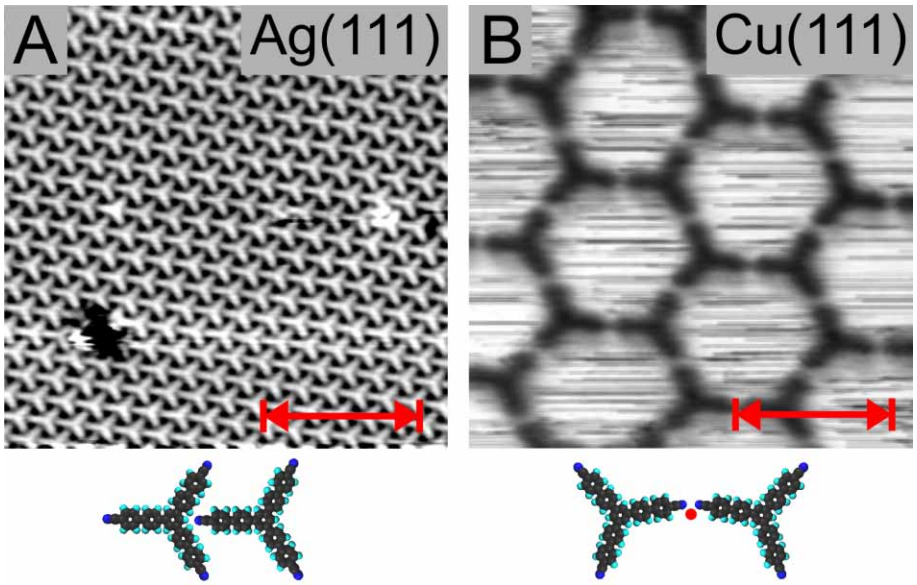

Figure 6.7: STM topographs (top) and binding motifs (bottom) of BCNB on Ag(111) (A) and Cu(111) (B). In (A) the densely packed, hydrogen bonded α-phase is present, in (B) the porous, metal-organic β-phase, stabilized by copper-nitrile coordination bonds involving copper adatoms. The reactivity of silver adatoms is insufficient for the formation of coordination bonds. Scale bars: (A) 10 nm; (B) 5 nm. Reprinted (adapted) with permission from publication #6 (T. Sirtl et al., *J. Am. Chem. Soc.* 135, 691-695).[26] Copyright 2013 American Chemical Society. Cf. chapter 7.

surface self-assembly of BCNB molecules at the UHV-Ag(111) interface is compared to self-assembly at the UHV-Cu(111) interface. In figure 6.7, STM topographs and binding motifs are displayed. Despite similar preparation conditions, different structures are observed: In the case of Ag(111), a densely packed, hydrogen bonded structure (α-phase) is present, whereas in the case of Cu(111) additionally a porous network stabilized by metal-organic coordination bonds (β-phase) emerges. Thus two significantly different binding motifs are present. The metal-organic bond is formed by coordination of copper adatoms to two nitrile groups. Also on the Ag(111) surface the adatom gas exhibits a similar density compared to Cu(111), however metal-organic bonds have never been observed on Ag(111). Reasons might be differences in adatom reactivity and bond strength of the respective -CN-metal-NC- bonds (indicated by DFT-derived bond dissociation energies: Ag-CN, 0.30 eV; Cu-CN, 0.90 eV). Accordingly, silver adatoms are too unreactive for the formation of a stable silver-nitrile bond at room temperature, whereas copper-nitrile bonds are readily created.[26] For further information, cf. chapter 7 (publication #6).

6.3 Kinetic Effects

6.3.1 Solvent Coadsorption

A key factor for SSN formation arises from the competition of thermodynamic versus kinetic effects.[17] The transition into the thermodynamically most favourable structure is often kinetically hindered. One conceivable origin of the entrapment blockade

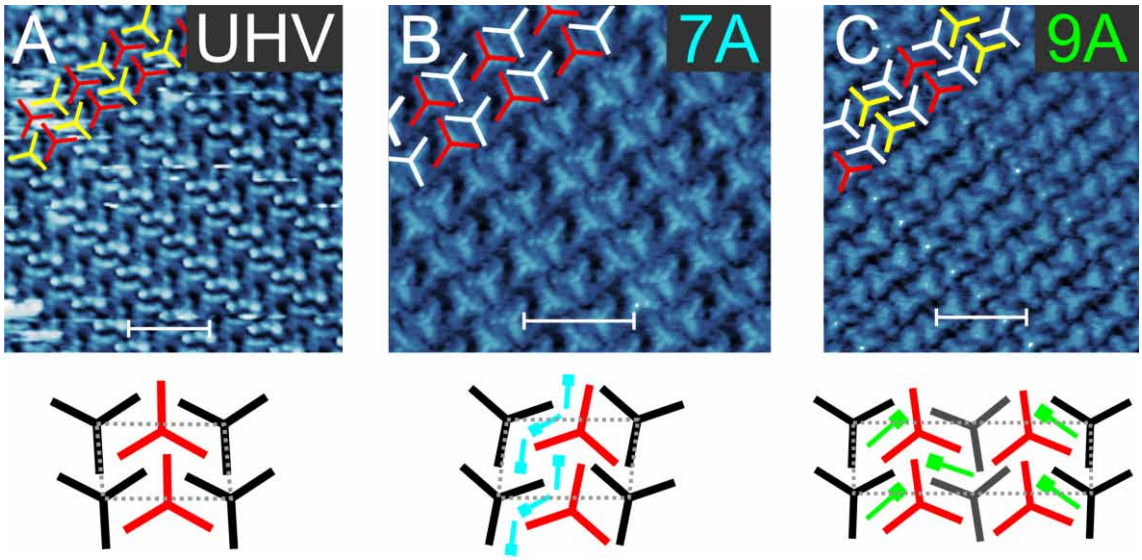

Figure 6.8: STM topographs (top) and structure models (bottom) of BCNB at the (A) UHV-, (B) 7A-, and (C) 9A-graphite interface. BCNB molecules are arranged in (A) the ε-phase, (B) the γ-phase, and (C) the δ-phase. The adsorption of solvated BCNB molecules (B,C) promotes coadsorption of solvent molecules. Scale bars 5 nm. Reprinted (adapted) with permission from publication #8 (T. Sirtl et al., *ACS Nano* 7(8), 6711-6718). Copyright 2013 American Chemical Society.[35] Cf. chapter 8.

is solvent coadsorption. Figure 6.8 illustrates the effect of solvent coadsorption on surface self-assembly of BCNB molecules on HOPG(0001): At the UHV-graphite interface (A), the most densely packed structure observed on graphite is formed, that is, the ε-phase; at the heptanoic acid-graphite interface (B) the γ-phase emerges; at the nonanoic acid-graphite interface (C) the δ-phase is found. Gaps between BCNB molecules that are only present in the γ-phase and the δ-phase are most likely filled with coadsorbed solvent molecules, stabilizing the rather loose packing. Supply of thermal energy by heating to 70 °C results in a transformation of both metastable phases into the ε-phase. The ε-phase does not seem to contain solvent molecules, because it exhibits no sufficiently large gaps between BCNB molecules. This is also supported by the fact that solvent-free synthesis in UHV also facilitates formation of the ε-phase. Thus, solvent coadsorption kinetically prevents BCNB molecules from the formation of the thermodynamically most favourable structure. Coadsorbed solvent molecules may arise from the solvation shell around dissolved BCNB molecules, present in the solution prior to adsorption.[35] For further information on solvent coadsorption in BCNB monolayers, cf. chapter 8 (publication #8).

6.3.2 Deposition Rate

Another kinetic influencing variable on the formation of intermolecular bonds in SSNs is the deposition rate of building blocks. Conventional deposition rates for SSNs are in the order of 0.1 monolayer/min. The experimental study of BCNB self-assembly at the UHV-Cu(111) interface sheds light on this hitherto sparsely attended parameter. Two polymorphs are observed for BCNB deposition on Cu(111) at room temperature, stabilized by two different types of intermolecular bonds: The densely packed α-phase,

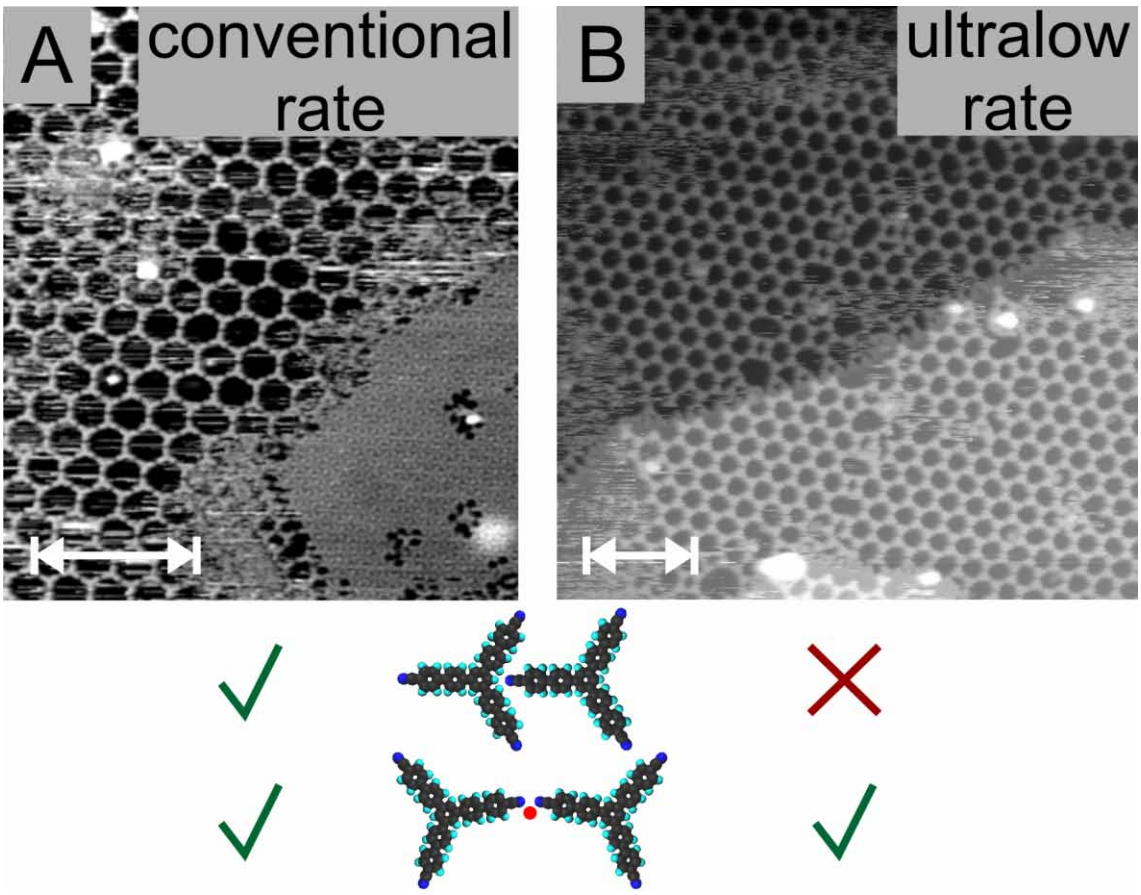

Figure 6.9: STM topographs (top) and binding motifs (bottom) of BCNB on Cu(111), prepared with conventional (A) or ultralow (B) deposition rate. In (A) both a densely packed, hydrogen bonded α- and a porous, metal-organic β-phase arise; in (B) only the β-phase emerges. Scale bars: 20 nm. Reprinted (adapted) with permission from publication #6 (T. Sirtl et al., *J. Am. Chem. Soc.* 135, 691-695).[26] Copyright 2013 American Chemical Society. Cf. chapter 7.

stabilized by hydrogen bonds between BCNB molecules in head-to-tail arrangement; and the porous β-phase with intermolecular copper-nitrile bonds. Respective STM topographs and binding motifs are given in figure 6.9. Preparation with a conventional deposition rate ($\sim 2.5 \times 10^{-2}$ monolayer/min) facilitates formation of both polymorphs in coexistence, whereas an ultralow deposition rate of $\sim 2.5 \times 10^{-4}$ monolayer/min results in exclusive formation of the β-phase. In other words, the deceleration of the deposition by a factor of 100 can be used for a selection of the type of intermolecular bond, along with a selection of the molecular arrangement. Here, the deposition rate influences the kinetics of structure formation. At the onset of the deposition, BCNB molecules find sufficient copper adatoms to form the metal-coordinated β-phase. However, formation of the copper-nitrile bonds consumes adatoms. From this moment on, a particular ratio turns the scale, that is, the ratio of deposition rate to the rate of adatom replenishment from step edges. A predominance of molecule deposition – as in the case of the conventional rate – leads to a lack of copper adatoms on the surface. As a consequence, arriving BCNB molecules then arrange in the hydrogen bonded α-phase. A subsequent transition of the α-phase into the β-phase is kinetically blocked. An STM topograph with coexisting α-phase and β-phase is depicted in figure 6.9 A. On the other hand, with a sufficiently high adatom replenishment rate – as in the case of the ultralow deposition rate – a sufficient amount of copper adatoms is available for exclusive formation of the β-phase. A corresponding STM topograph is depicted in figure 6.9 B.[26] Further information is given in chapter 7 (publication #6).

6.3.3 Temperature

The balance between kinetic and thermodynamic control of an SSN formation is significantly influenced by the temperature of the substrate.[17] An example for thermodynamic control in SSNs is given in publication #1.[88] Here, self-assembled monolayers of BTB molecules at the fatty acid-graphite interface are investigated. At room temperature, a porous phase is the thermodynamically most favoured structure (for nonanoic acid as solvent). The porous structure is stabilized by solvent molecules, incorporated in the pores. Whereas at temperatures above 55 °C the coadsorbed solvent molecules desorb from the surface and the BTB molecules rearrange in order to form a densely packed phase. The reversibility of this phase transition underlines its thermodynamic origin.

On the other hand, the increase in substrate temperature also enables transitions from metastable to thermodynamically more stable phases that are kinetically hindered at room temperature. A striking observation hereby is the irreversibility of the phase transition. An example for a kinetic control is found for self-assembly of BCNB molecules on HOPG(0001). Here, thermal energy is required to overcome a kinetic barrier that arises from coadsorbed solvent molecules.[35] See subsection 6.3.1 or chapter 8 (publication #8) for further information.

Likewise, interesting kinetically controlled temperature-induced phase transitions occur in guanine self-assembly on Ag(111) (cf. figure 6.1 and table 6.1 in subsection 6.1.1).[89] In this example, the supply of thermal energy after deposition at room temperature results in up to four irreversible phase transitions: From a disordered state into the α-phase; from the α-phase successively into the β-, γ-, and

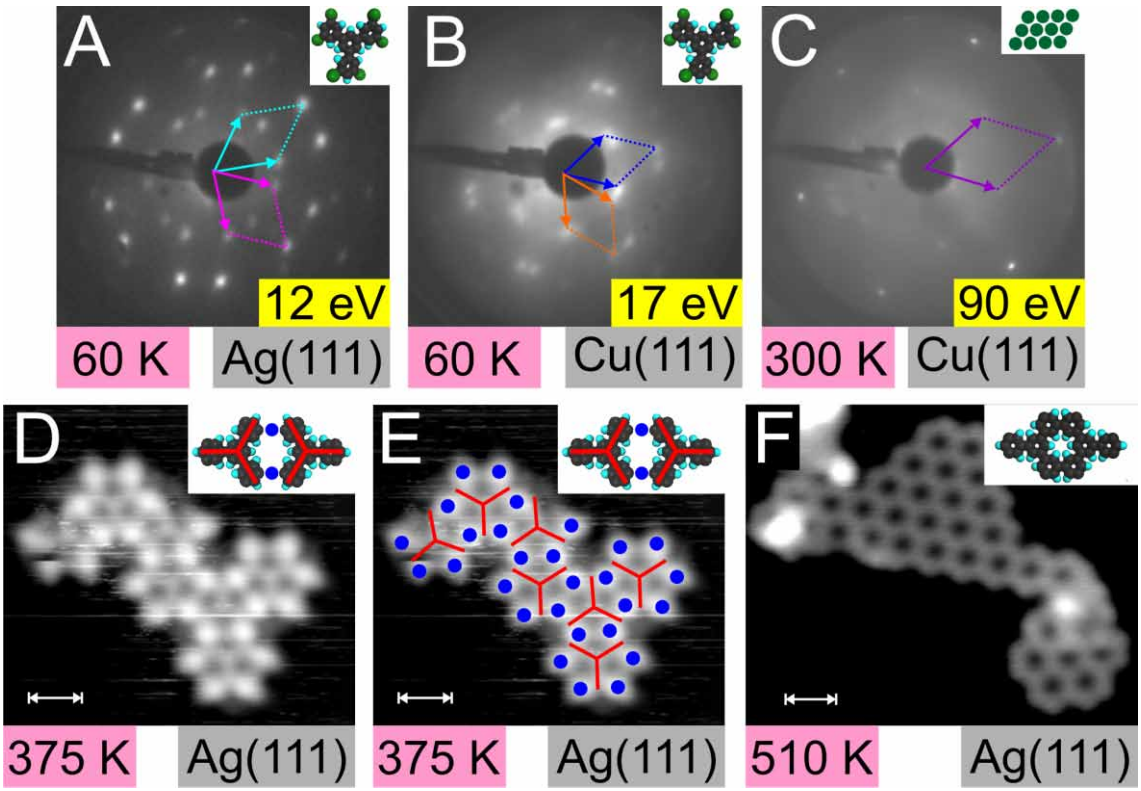

Figure 6.10: LEED patterns (A-C) and STM topographs (D-F) of TDBB adlayers. The respective substrate is indicated in the lower right corner of each image and the annealing or recording temperature is given in the lower left corner; the inset hints at the molecular or atomic arrangement; the electron energy for a LEED pattern is displayed in a yellow box; reciprocal unit cells are overlaid; blue circles in (D,E) depict silver adatoms; STM scale bars correspond to 1 nm. Deposition of TDBB at a substrate temperature of 60 K results in self-assembly of intact molecules, with trigonal unit cell parameters of a = 1.49 nm [a = 1.45 nm] and rotation angle of superstructure to substrate lattice of R = ±19° [R = ±25°] on Ag(111) (A) [Cu(111) (B)]. Upon room temperature deposition, the C-Br bonds are dissociated and the split off bromine atoms arrange in a $\left(\sqrt{3} \times \sqrt{3}\right)$ R30° superstructure on Cu(111) (C). The residual triphenylbenzene hexa-radicals form organometallic networks upon tempering at 375 K (D,E) and COFs upon annealing at 510 K (F). Here, results on a Ag(111) substrate are shown, but SSN formation is similarly observed on Cu(111). Scanning parameters: – 2.2 V, 50 pA (D-E); – 2.0 V, 68 pA (F). Analogous reactions occur for TDBPB on Ag(111) (cf. publication #5). [86]

δ-phases. However, so far the origin of these phase transitions remains unexplained. Further studies with complementary techniques to LEED might enable structure simulations of the observed phases. Detailed knowledge of the molecular arrangement of guanine in each structure might provide a conceivable explanation for their temperature-induced transformations.

In the context of heterogeneous catalysis, not rearrangement of adsorbates is relevant, but the dissociation of intramolecular bonds in adsorbates. Bond cleavage is the basis of on-surface reactions. For instance, halogen atoms are promising functional groups for the synthesis of 2D COFs.[19,103] For TBB molecules on Cu(111), the intermediate stage between intact molecules and COFs are organometallic networks termed protopolymers.[a] In this example, the substrate temperature determines whether a molecule stays intact upon adsorption or the C-Br bond is already cleaved. At 80 K, the deficit in thermal energy prevents C-Br bond cleavage. Whereas at 300 K, C-Br bond cleavage and subsequent formation of protopolymers is readily observed. See publication #2.[87]

Similar results are obtained for SSNs of TDBB on Ag(111) and Cu(111). LEED patterns and STM topographs of temperature-dependent experiments are displayed in figure 6.10. At low substrate temperatures (∼60 K), self-assembly of presumably unreacted TDBB molecules is observed (A,B). The unit cell size fits well to a structure of planar adsorbed, halogen-halogen bonded molecules (cf. the tentative model in figure 5.2 B). Again, an increase of substrate temperature results in dissociation of the C-Br bonds. Split-off bromine atoms then arrange in a densely packed layer on the surface, that is, a $\left(\sqrt{3} \times \sqrt{3}\right)$ R30° superstructure on Cu(111) (C). Additionally, tiny domains of protopolymers (D,E) are revealed by STM, whereas they are undetectable by LEED due to the low coverage. Triphenylbenzene hexa-radicals (from C-Br bond dissociation of TDBB) combine with silver adatoms from the free adatom gas to form protopolymers. Upon further annealing (∼510 K) silver adatoms can be expelled from the organometallic bond, enabling formation of covalent C-C bonds. Thus, a 2D COF emerges (F). Similar reaction mechanisms are observed on Ag(111) and on Cu(111). See publication #5 for a related study.[86]

Analogous structural transitions are observed in self-assembled monolayers of IBB on Ag(111). The C-I and C-Br bonds dissociate upon adsorption at room temperature. Resulting triphenylbenzene triple-radicals form disordered organometallic networks with silver adatoms. Tempering at ∼100 °C yields porous but still rather irregular networks stabilized by C-Ag-C bonds. In figure 6.11 A, an STM topograph and the binding motif of this structure are depicted. The molecular arrangement is similar to the aforementioned structure of TBB molecules on Cu(111) (cf. publication #2).[64,87] Again, silver adatoms can be expelled from the organometallic bond by the supply of thermal energy. So, tempering at ∼200 °C yields small domains of 2D COFs (cf. figure 6.11 B).

Preliminary results on TBBP self-assembly on Cu(111) are a final example of a temperature-controlled C-Br bond cleavage. Corresponding LEED patterns are shown in figure 6.12. Deposition of TBBP on Cu(111) at 50 K and annealing to 175 K results in the coexistence of two polymorphs. In LEED, two patterns are observed at different macroscopic locations on the sample. Unit cell parameters amount to a = b = 0.97 nm (A) and a = b = 0.87 nm (B). By translating the

[a] "protopolymers": "radical-metal coordination complexes or networks"[64,87]

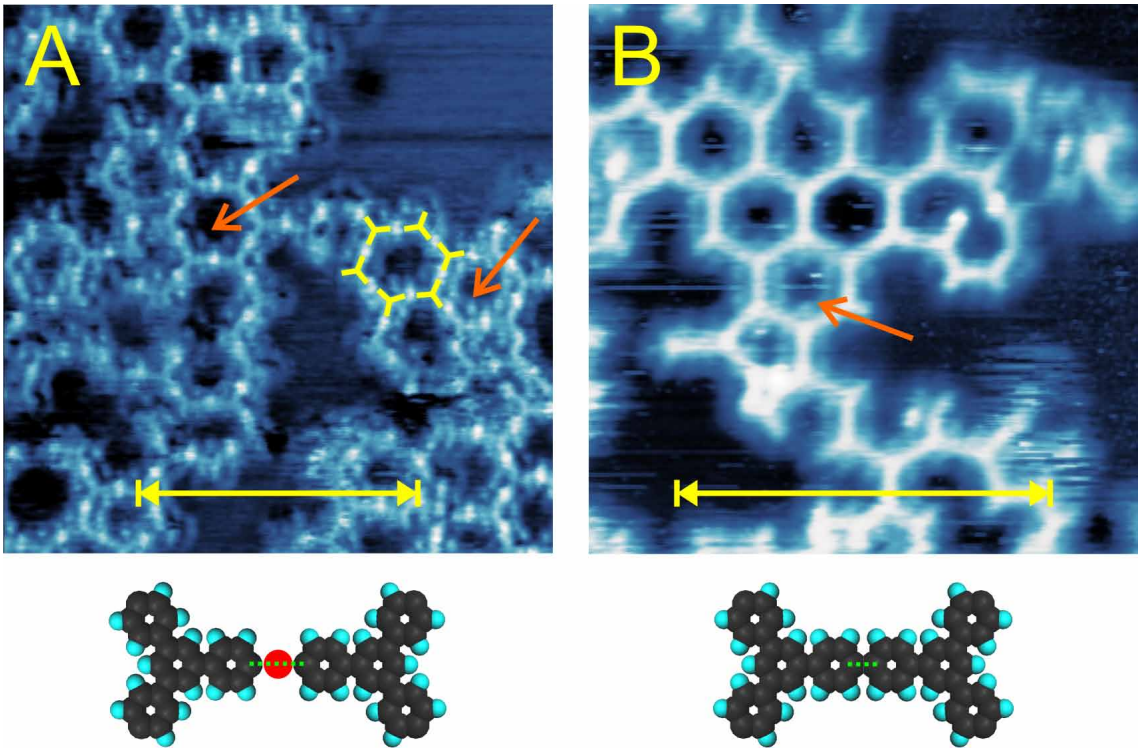

Figure 6.11: STM topographs (top) and binding motifs (bottom) of IBB on Ag(111). (A) Deposition of IBB onto the substrate held at room temperature and subsequent tempering at ∼100 °C for 5 min results in rather irregular, porous networks (inter-pore distance: ∼2.7 nm) stabilized by organometallic (C-Ag-C) bonds. Silver adatoms in the C-Ag-C bond are visible in the STM image as bright dots between tripodally shaped triphenylbenzene triple-radicals (cf. overlaid yellow tripods). (B) Tempering at ∼200 °C for 5 min yields small domains of porous COFs with a pore distance of ∼2.3 nm. Split-off halogen atoms are trapped within the pores, examples are indicated by arrows. Scanning parameters: (A) 100 mV & 200 pA; (B) 700 mV & 98 pA. Scale bars: 10 nm.

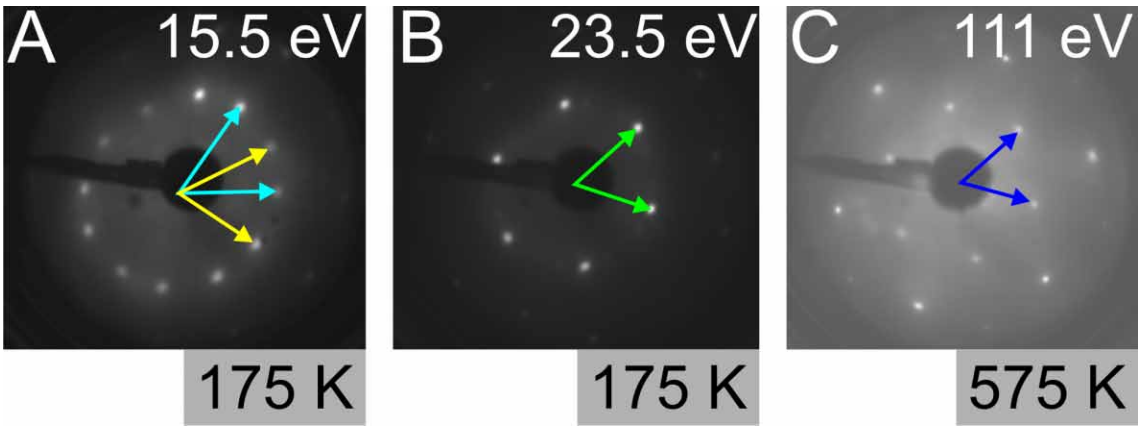

Figure 6.12: LEED patterns of TBBP on Cu(111), deposited at 50 K and recorded at 175 K (A,B), or deposited at 300 K and recorded at 575 K (C). Electron energies are depicted in the upper right corner. At low temperature, self-assembly of intact molecules is observed (A,B). The trigonal lattice parameter amounts to a = 0.97 nm [a = 0.87 nm] (A) [(B)]; the rotation angle of superstructure to substrate lattice is R = ±15 ° [R = 30 °]. At elevated temperatures the C-Br bonds are dissociated. Then, in LEED solely the $\left(\sqrt{3} \times \sqrt{3}\right)$ R30° bromine superstructure is observed (C). [104]

sample, different positions on the sample are irradiated by the incident electron beam and contribute to LEED data. The fact that the area within the electron beam diameter ($\sim 0.5\,\mathrm{mm}^2$) is mainly covered by either of the two polymorphs hints towards the existence of extremely large domains. This assumption is supported by the sharpness of the LEED reflections. Thus, most likely TBBP molecules are intact at this stage. C-Br bond dissociation occurs, like in the other examples, upon annealing. Here, a sharp pattern of a $\left(\sqrt{3} \times \sqrt{3}\right)$ R30° bromine superstructure emerges at a sample temperature of ∼575 K.[104] Due to the lack of long range order or low surface coverage, the fate of the aromatic backbone cannot be clarified by the LEED analysis. To this end, examinations with complementary surface-sensitive techniques are necessary. In particular, STM is required for the investigation of the molecular arrangement within a unit cell.

Also the dissociation of other types of intramolecular bonds is triggered by supplying thermal energy, i.e. increasing the substrate temperature. In figure 6.13, the LEED-I(T) analysis of BTT on Cu(111) is displayed. Similar to their larger homologue TMB, BTT molecules deprotonate upon adsorption. For studies of TMB on Cu(111), see publications #4 and #7 (chapter 9).[24,37] Subsequently to deprotonation, BTT molecules arrange in a metal-organic structure. Increase in substrate temperature results in dissociation of the C-S bonds, accompanied with an irreversible phase transition from the metal-organic α-phase (A,G) to the β-phase (C) at ∼300 K. In the β-phase, sulfur atoms form a $\left(\sqrt{3} \times \sqrt{3}\right)$ R30° superstructure on Cu(111), however the detailed structure (i.e., the asymmetric unit) of the adlayer is under discussion.[99] The fate of the benzene triple-radicals remains unclear at this stage. In the following, solely phase transitions within the copper-sulfide adlayer are analyzed. Continued supply of thermal energy results in a transition into the γ-phase at ∼462 K, exhibiting a $\left(\sqrt{7} \times \sqrt{7}\right)$ R ± 19.1° superstructure lattice (D). The γ-phase disappears at ∼640 K and reappears after cool down at ∼600 K (F,H). Additionally, an incommensurate phase termed δ-phase appears after cool down (at ∼467 K) (F,H). Thus, in this example of BTT or sulfide adlayers, both irreversible and reversible phase transitions are observed, along with dissociative or displacive reconfigurations. For further information on BTT, see chapter 10 (publication #9).

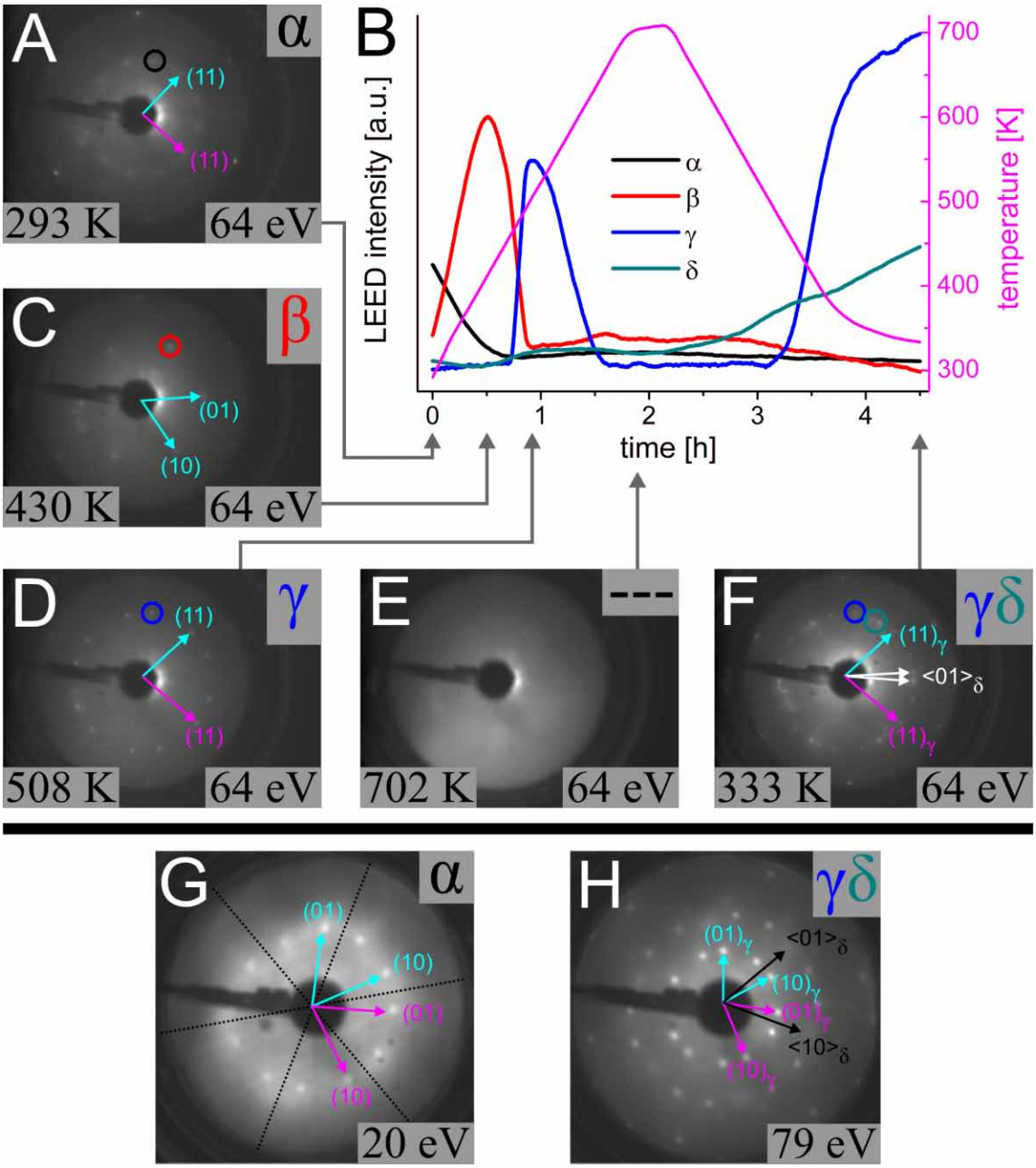

Figure 6.13: LEED results of BTT on Cu(111). (A-F) LEED-I(T) analysis with I(T)-curves (B) of temperature-dependent evolution of α-, β-, γ-, and δ-phase and corresponding LEED patterns ((A), α-phase, (C), β-phase, (D) γ-phase, (F) superposition of γ- and δ-phase) at an electron energy of 64 eV. Deposition of BTT on Cu(111) results in a molecular superstructure (α-phase) with a trigonal lattice parameter of a = 0.91 nm and a rotation to substrate unit cell axes of R = ±13.9 °. First order reflections of the two domains are displayed in (G) at an electron energy of 20 eV. Annealing results in a phase transition to the β-phase (trigonal, a = 0.41 nm, R = 29.5 °), due to dissociation of the C-S bond and an arrangement of the sulfur atoms in a $\left(\sqrt{3} \times \sqrt{3}\right)$ R30° superstructure.[105] At higher temperatures the γ-phase is formed (trigonal, a = 0.64 nm, R = 19.2 °), a copper-sulfide adlayer with $\left(\sqrt{7} \times \sqrt{7}\right)$ R ± 19.1° superstructure relation to the substrate (see (H) for first order reflections).[99,105]. Upon a further increase in temperature, the γ-phase disappears and reappears after cooling down, together with the δ-phase. Reprinted (adapted) with permission from publication #9 (T. Sirtl et. al, *J. Phys. Chem. C*, DOI:10.1021/jp411084k). Copyright 2014 American Chemical Society. Cf. chapter 10.

Chapter 7

Control of Intermolecular Bonds by Deposition Rates at Room Temperature: Hydrogen Bonds versus Metal Coordination in Trinitrile Monolayers

Thomas Sirtl,[ab] Stefan Schlögl,[ab] Atena Rastgoo-Lahrood,[ab] Jelena Jelic,[c] Subhadip Neogi,[d] Michael Schmittel,[d] Wolfgang M. Heckl,[abe] Karsten Reuter,[c] and Markus Lackinger.[abef] Reprinted (adapted) with permission from *Journal of the American Chemical Society* 135, 691-695, **2013**.

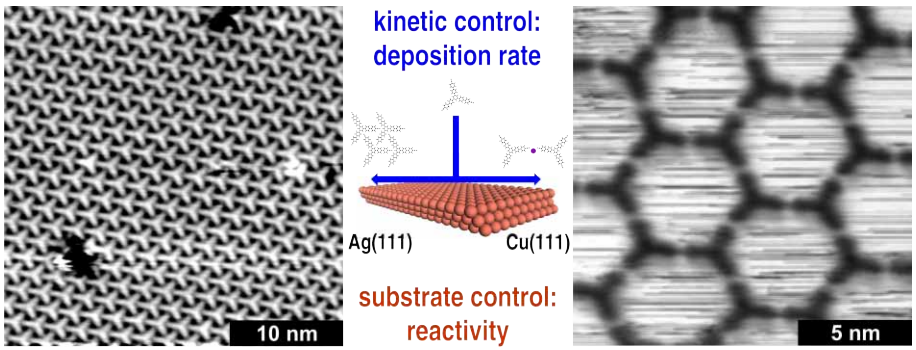

[a] Department of Physics, Technische Universität München, James-Franck-Str. 1, 85748 Garching, Germany
[b] Center for NanoScience (CeNS), Schellingstr. 4, 80799 Munich, Germany
[c] Department of Chemistry, Technische Universität München, Lichtenbergstr. 4, 85747 Garching, Germany
[d] Center of Micro- and Nanochemistry and Engineering, Organische Chemie I, Universität Siegen, Adolf-Reichwein-Str. 2, 57068 Siegen, Germany
[e] Deutsches Museum, Museumsinsel 1, 80538 Munich, Germany
[f] Corresponding author; e-mail: markus@lackinger.org; web: www.2d-materials.com

7.1 Abstract

Self-assembled monolayers of 1,3,5-tris(4'-biphenyl-4"-carbonitrile)benzene, a large functional trinitrile molecule, on the (111) surfaces of copper and silver under ultrahigh vacuum conditions were studied by scanning tunneling microscopy and low-energy electron diffraction. A densely packed hydrogen-bonded polymorph was equally observed on both surfaces. Additionally, deposition onto Cu(111) yielded a well-ordered metal-coordinated porous polymorph that coexisted with the hydrogen-bonded structure. The required coordination centers were supplied by the adatom gas of the Cu(111) surface. On Ag(111), however, the well-ordered metal-coordinated network was not observed. Differences between the adatom reactivities on copper and silver and the resulting bond strengths of the respective coordination bonds are held responsible for this substrate dependence. By utilizing ultralow deposition rates, we demonstrate that on Cu(111) the adatom kinetics plays a decisive role in the expression of intermolecular bonds and hence structure selection.

7.2 Introduction

Self-assembled organic monolayers are promising candidates for the development of novel materials with tremendous options.[22] Many of their properties decisively depend on the type of intermolecular bond that stabilizes the monolayer.[106] The bond type is mostly predetermined by functionalization but may additionally be influenced by kinetic effects. For instance, temperature can affect structure formation because of activation barriers.[87,107] Among the different non-covalent intermolecular bonds that can stabilize monolayers, not only is metal coordination the strongest,[23] but thiolate-copper coordination bonds, for example, can also offer strong intermolecular electronic coupling as required for molecular electronic applications.[24]

Formation of metal-coordination bonds requires both electron-donating ligands and metal centers. For surface-supported systems, the latter can be supplied either by metal deposition or by the adatom gas of a metal surface. Deposition of extrinsic metal centers facilitates chemical variability, while network formation with intrinsic metal centers offers facile preparation. Carboxylates and thiolates are suitable anionic ligands for coordinative bonds,[24,106,108,108] while nitrogen in hetero-cycles (e.g., pyridine or other azines) or nitriles are among the favored neutral ligands.[23,25,106,109] In contrast to thiol and carboxyl groups, where the formation of metal-coordinated networks requires additional thermal activation,[24,106,108] nitrile coordination is readily observed at room temperature with an onset around 180 K.[107]

For many correspondingly functionalized molecules, the type of intermolecular bond can be changed by supplying coordination centers. A good example therefore are dinitriles on Ag(111).[8,23,25,110,111] Additional deposition of cobalt atoms induces a change from hydrogen bonding to metal coordination, accompanied by structural reorganization.

Besides temperature, the competition between molecular flux onto the surface and diffusion on the surface can also play a decisive kinetic role in determining the structure. An experimental example is given by Li and Lin,[112] who observed structurally different pyridyl-porphyrin monolayers upon variation of the deposition rate.

However, all of these structures were stabilized by the same type of intermolecular bond (i.e., copper coordination), and no change of bond type was induced.

Here we studied the self-assembly of the large functional molecule 1,3,5-tris(4'-biphenyl-4"-carbonitrile)benzene (BCNB) on both Cu(111) and Ag(111). These surfaces were chosen as substrates because they exhibit two-dimensional adatom gases that are comparable in mobility[113] but differ in reactivity.[87,114] To study the influence of the above-mentioned kinetic competition on the formation of adatom-coordinated trinitrile networks, experiments were conducted with variation of the deposition rate over two orders of magnitude.

7.3 Experimental Details

BCNB monolayers were characterized by scanning tunneling microscopy (STM) and low-energy electron diffraction (LEED) in ultrahigh vacuum (UHV). STM data were acquired with a home-built beetle-type scanning tunneling microscope driven by an SPM100 controller from RHK. The topographs were processed by a mean value filter. All of the images were obtained at room temperature at a base pressure below 3×10^{-10} mbar. The Ag(111) and Cu(111) single-crystal surfaces were prepared by cycles of Ne^+ ion sputtering at 1 keV and electron-beam annealing at 550 °C for 30 min. Thorough calibration of the microscope with atomically resolved topographs of Cu(111) allowed lattice parameters and distances to be derived with an accuracy of 5 %.

LEED experiments were performed in a separate UHV chamber at a base pressure below 1×10^{-10} mbar. The LEED optics (Omicron NanoTechnology GmbH) were controlled by electronics from SPECS Surface Nano Analysis GmbH. The Ag(111) and Cu(111) surfaces were prepared by Ar^+ ion sputtering at 2 keV and subsequent electron-beam annealing at 550 °C for 30 min. The deposition parameters were similar to those for the STM experiments. LEED patterns were acquired at a sample temperature of ∼60 K. The software LEEDpat3 was used for geometric simulations.

BCNB (see the Figure 7.1 inset for its molecular structure and section 7.7 for its synthesis) was deposited from a home-built Knudsen cell[65] and thoroughly outgassed prior to deposition. The substrates were held at room temperature. The crucible temperature was varied between 280 and 330 °C, resulting in deposition rates between $\sim 2.5 \times 10^{-4}$ and $\sim 2.5 \times 10^{-2}$ monolayer/min, respectively. To determine the BCNB sublimation rate as a function of crucible temperature and to verify the long-term stability of the sublimation, a Knudsen cell equipped with a quartz crystal microbalance was used (cf. section 7.7).

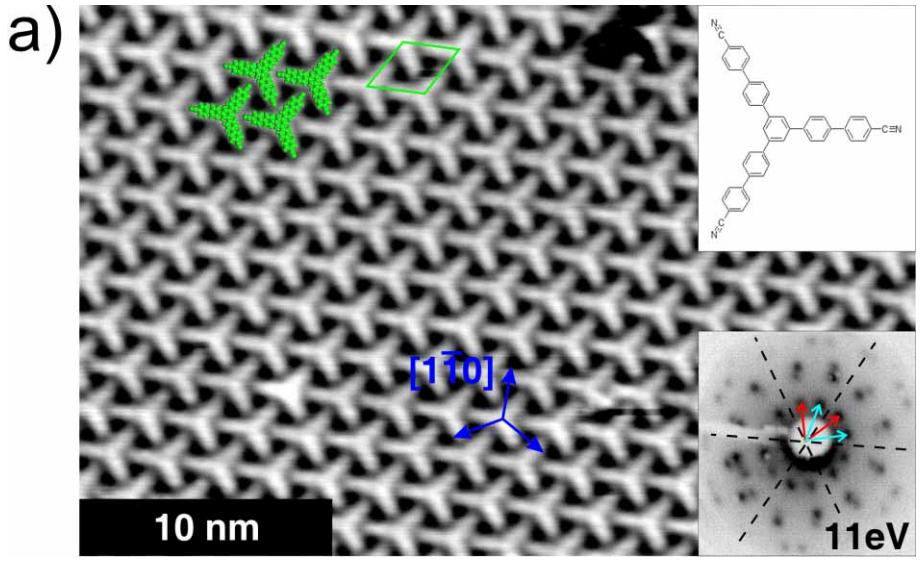

Figure 7.1: STM topograph (+1.61 V, 100 pA) of the densely packed $\left(\sqrt{39} \times \sqrt{39}\right)$ R ± 16° BCNB superstructure on Ag(111). Molecules are overlaid, and the unit cell is indicated by green lines. The structure of BCNB is shown in the upper inset. The lower inset shows the LEED pattern. The two rotational domains are marked by red and turquoise arrows (cf. section 7.7). Dashed lines indicate high-symmetry substrate directions.

7.4 Results and Discussion

On Ag(111), BCNB self-assembles into long-range-ordered, densely packed monolayers with $p31m$ symmetry. Both STM and LEED consistently revealed a $\left(\sqrt{39} \times \sqrt{39}\right)$ R± 16° super-structure with a lattice parameter of 1.80 nm (Figure 7.1). The existence of two rotational domains is evident in the LEED pattern depicted in the lower inset (cf. section 7.7). The identification of the molecular arrangement is unambiguous since the threefold contour of BCNB is clearly recognizable and the STM-derived size is in excellent agreement with the optimized geometry of the isolated BCNB molecule (cf. section 7.7). On the basis of the dense packing of BCNB, additional constituents can be excluded. From the molecular arrangement, it is concluded that the dominant interactions are C≡N···H-C hydrogen bonds, as similarly observed in surface self-assembly[107,110,115] and bulk crystals[116,117] of carbonitriles. The nitrile groups are in close proximity to three phenyl hydrogen atoms. Density functional theory (DFT) calculations of two isolated molecules gave a center-to-center distance of 1.81 nm (cf. section 7.7). The extremely small deviation from the experiment (1.80 nm) indicates a minor substrate influence and justifies the comparison with gas-phase calculations. The closest N···H distances (260 pm) are consistent with hydrogen-bond lengths in comparable bulk crystals (250 - 260 pm).[116,117] BCNB deposition with a rate of $\sim 2.5 \times 10^{-2}$ monolayer/min onto Cu(111) yielded two polymorphs, both with $p31m$ symmetry. The overview STM image in Figure 7.2 a illustrates the coexistence of both a densely packed α phase and a porous β phase. The lattice parameter and molecular arrangement of the α phase on Cu(111) are comparable to those on Ag(111). The commensurate $\left(4\sqrt{3} \times 4\sqrt{3}\right)$ R30° superstructure on Cu(111) (cf. the Figure 7.2 a inset for the LEED pattern and cf. section 7.7) exhibits a slightly smaller lattice parameter of 1.77 nm and only one rotational domain. According to

the similarities with the structure on Ag(111), it is concluded that the α phase on Cu(111) is likewise stabilized by similar intermolecular C≡N···H-C hydrogen bonds.

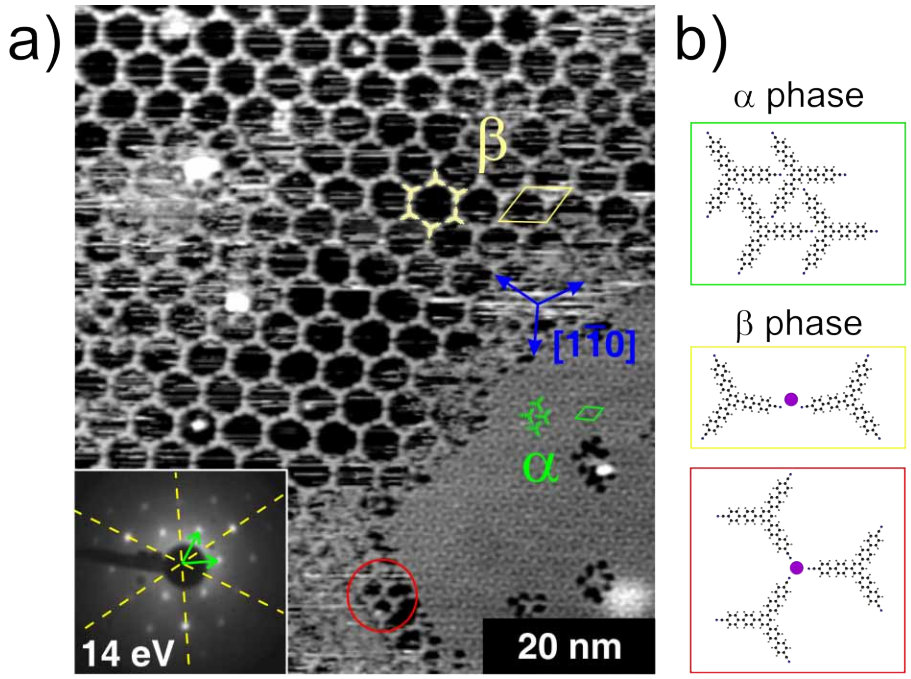

Figure 7.2: (a) STM topograph (+ 2.09 V, 80 pA) of a BCNB monolayer on Cu(111) deposited at a rate of ∼2.5 ×10^{-2} monolayer/min. The inset shows the LEED pattern (cf. section 7.7), in which arrows indicate the reciprocal unit cell vectors of the α phase and dashed lines mark high-symmetry substrate directions. (b) Tentative binding models of the α (green) and β (yellow) phases; threefold coordination (red) was also occasionally observed, but only in isolated arrangements.

The pores of the β phase are arranged on a hexagonal lattice, and the unit cell contains two molecules. The streaky features observed within some but not all of the pores arise from entrapped mobile species, either excess molecules or adatoms. Similar observations have been reported for various porous systems.[110,118–121] Two different epitaxial relations to the substrate were found, namely, $\left(11\sqrt{3} \times 11\sqrt{3}\right)$ R30° and 19 × 19 superstructures having almost identical lattice parameters (4.87 and 4.86 nm, respectively). Generally, the emergence of a porous polymorph already hints at stronger intermolecular bonds. From the rather large center-to-center distance of 2.8 nm between adjacent molecules, direct interactions via intermolecular hydrogen bonds can a priori be excluded. A detailed view of the β phase furthermore revealed an arrangement where the molecular lobes are not aligned with the long diagonal of the unit cell but are slightly tilted by ±9 ° (Figure 7.3). In most dimeric binding motifs, the two molecules tilt in the same direction (i.e., one molecule tilts clockwise and the other counterclockwise). Tilts can occur in both directions and occur in segregated domains (cf. section 7.7).

On the basis of the intermolecular arrangement, we propose that BCNB molecules are interconnected by coordination bonds between the nitrile groups and copper adatoms. This hypothesis is further substantiated by occasionally observed adatom-related contrast features in the STM images, the results of DFT calculations, and the good match with an epitaxial model, as detailed in the following. In accordance

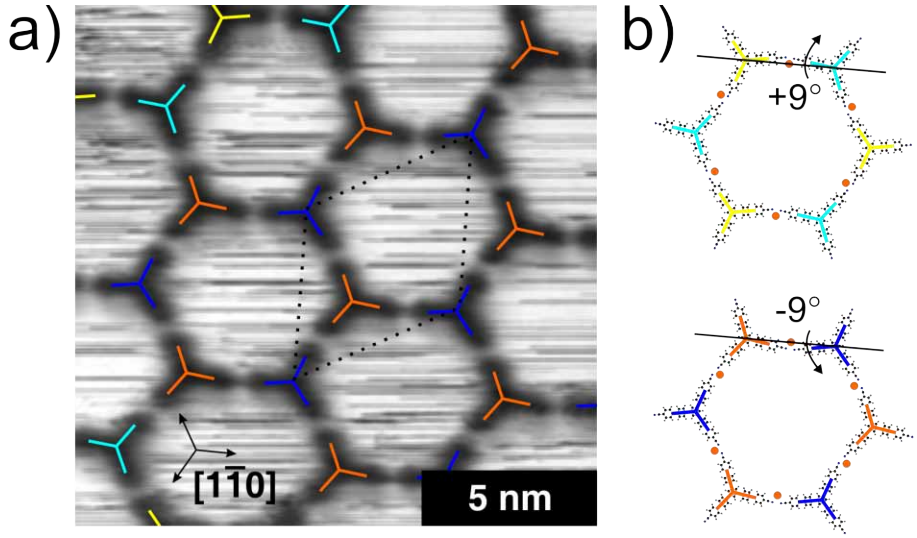

Figure 7.3: β phase of BCNB on Cu(111). (a) Close-up STM topograph (1.41 V, 80 pA) with overlaid tripods. The colors encode the different tilts of ±9 °. (b) Tentative models. C, gray; Cu, orange; H, white; N, blue.

with most other experiments on copper-coordinated networks, the copper atoms are normally not resolved by STM.[122–128] This invisibility of obviously present coordination centers in STM images has also been reported for many other metal-coordinated networks, such as Co-coordinated nitriles[23,25,111,129] and is attributed to an electronic effect.[130] Nevertheless, occasionally for peculiar tip conditions, distinct topographic maxima were observed in the β phase at the proposed positions of the copper coordination centers (i.e., midway between two BCNB molecules; see section 7.7). Moreover, in these images, the BNCB molecules appear with diminished apparent height, indicating a tip that is sensitive to electronic states in a different energy range. Because of their positions, these topographic maxima are unambiguously identified as the coordinating copper adatoms. Similar signatures of coordinating adatoms in the STM contrast have been reported for Cu-benzoate complexes on Cu(110).[131]

In the β phase, copper adatoms coordinate two nitrile groups. Threefold coordination, the major binding motif in Co-coordinated nitrile networks[23,25,111] and hitherto-known Cu-coordination,[107] was only rarely observed in isolated arrangements (Figure 7.2). However, for surface-supported metal-coordinated networks, unusual coordination with lower coordination numbers seems to be the more general case.[108,123,132] This can be rationalized by the special environment of these surface-supported systems. On the one hand, there is the restriction to a planar geometry due to the surface confinement, and on the other hand, there is an additional electronic influence of the metal surface due to charge transfer and screening by free electrons.[123,132] DFT calculations were performed to derive optimal bond lengths for copper-nitrile coordination and to find explanations for the tilt in the intermolecular bonds. For a full account of surface effects, it is also important to include the copper substrate. However, because of the large system size, the DFT calculations had to be restricted to benzonitrile as a representative model system. As depicted in Figure 7.4 a, energy minimization of two benzonitrile molecules coordinated to one

copper adatom resulted in a straight bond with the adatom stably adsorbed in a threefold hollow site. The N-Cu bond length is 1.92 nm, and the copper adatom resides 0.200 nm above the topmost copper layer and 0.121 nm below the benzene rings. The DFT calculations revealed a global energy minimum for the benzene rings oriented along the $\langle 1\bar{1}0 \rangle$ high-symmetry direction of the substrate and a further, only slightly less stable local minimum for alignment in the bisecting $\langle 11\bar{2} \rangle$ direction.

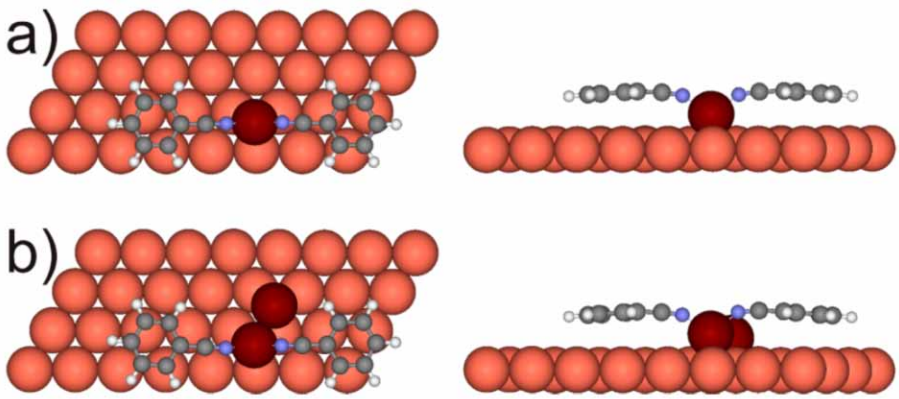

Figure 7.4: DFT geometry optimization of two benzonitrile molecules coordinated to copper adatoms (represented by dark-red spheres). Left: top views (i.e., parallel to [111]). Right: side views (i.e., parallel to [112]). Only one copper substrate layer is depicted, but three layers were considered in the calculation. (a) Coordination to one copper adatom in a threefold hollow site. (b) Coordination to one copper adatom in a threefold hollow site with a further copper adatom in an adjacent site.

Since DFT geometry optimization yielded a straight bond, the experimentally observed tilt cannot be explained by intrinsic properties of the chosen model system. In an alternative approach, a second copper adatom was placed adjacent to the coordinating copper atom, likewise in a threefold hollow site. The optimized geometry is depicted in Figure 7.4 b. Addition of a second adatom actually results in a tilt of the bond angle by 6 °, thereby offering a possible explanation.

Although the DFT simulations of the model systems included direct substrate effects, conceivable registry effects could arise for the full BCNB molecule that could be relevant for the β phase. Nevertheless, an optimal N-Cu bond length of 0.192 nm in the adsorbed system was deduced from the DFT calculations, and there is a clear confirmation that copper adatoms have a strong preference for threefold hollow sites. The fairly large unit cell of the β phase contains two BCNB molecules and three copper adatoms. When the above-stated requirements are considered, it becomes clear that the substrate registry does not allow for a straight bond configuration. To keep C≡N-Cu coordination bonds within 5 % of the optimized length and guarantee threefold hollow sites for all adatoms, the β phase has to adapt to the substrate lattice in the energetically most efficient way, which involves tilting the BCNB molecules with respect to each other. A tentative model of the β phase that includes all of the requirements and the experimental tilt angle into account is presented in Figure 7.5.

To obtain insights into the growth kinetics, experiments were conducted with ultraslow deposition, wherein a surface coverage of one monolayer was accomplished in 67 h. On Cu(111), this resulted in the exclusive formation of the β phase, thereby hinting at a kinetic origin of the polymorphism. A representative STM image is

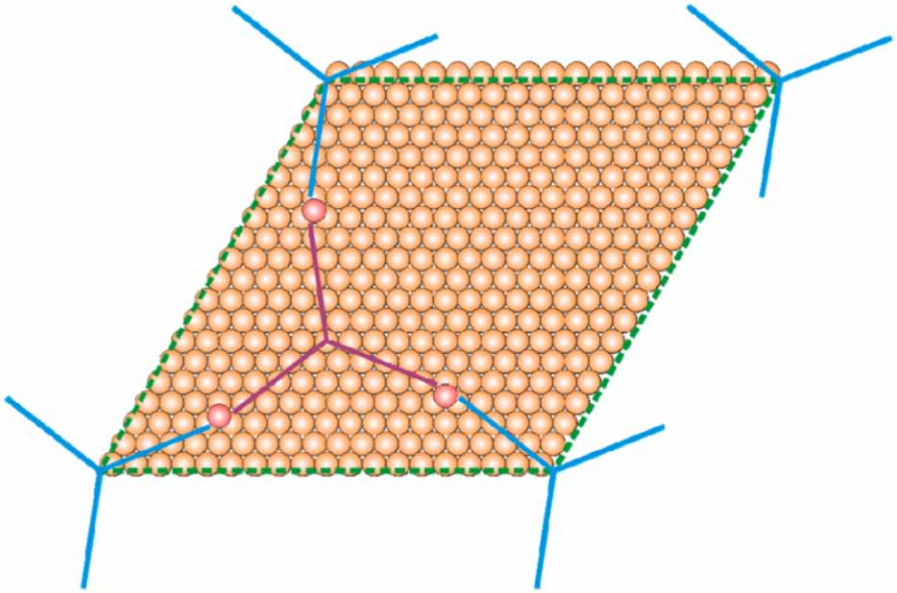

Figure 7.5: Tentative model of the β phase on Cu(111). The dashed green lines indicate the 19×19 unit cell. For clarity, the BCNB molecules are represented by tripods. This model considers the experimental tilt angle and the preference of copper adatoms for threefold hollow sites. All C≡N-Cu bonds are within 5 % of the DFT-derived optimal bond length of 0.192 nm. The three coordinating copper adatoms are located on the same sublattice (cf. section 7.7).

presented in Figure 7.6 a. Irrespective of the low deposition rate, a similar tilt angle between the BCNB molecules was observed, pointing to an equilibrium effect. Occasionally, the STM images also showed a parallel side-by-side arrangement of two dimers, an example of which is highlighted in Figure 7.6 a. However, these uncommon coordination schemes are grouped along a line and thus are attributed to an antiphase domain boundary. Interestingly, similarly slow deposition onto Ag(111) still resulted in the densely packed polymorph, yet with a notably extended domain size, as illustrated in Figure 7.6 b.

We thus assign the polymorphism on Cu(111) to a kinetic effect, namely, the availability of Cu adatoms. Upon deposition of BCNB, formation of the β phase consumes Cu adatoms and thus depletes the density of the adatom gas below its equilibrium value. If the progressive consumption of Cu adatoms caused by further deposition of BCNB molecules is faster than adatom replenishment from step edges, the availability of Cu centers for coordination bonds decreases. The absence of Cu adatoms leads to the realization of the second best option in terms of intermolecular bonds, namely, the hydrogen-bonded α phase.

This picture is supported by the experiments on Cu(111) with ultraslow deposition, which resulted in the exclusive formation of the β phase. When the BCNB deposition rate is so low that the equilibrium density of the adatom gas is not perturbed, Cu centers are constantly available, and the preferred formation of Cu coordination bonds is not hampered by kinetic limitations. In contrast, the insufficient reactivity of Ag adatoms at room temperature leads to the exclusive formation of the hydrogen-bonded structure on Ag(111), even for ultraslow deposition. On this less reactive surface, the slow deposition affects only the nucleation and growth kinetics, resulting in extended domains of the densely packed hydrogen-bonded phase.

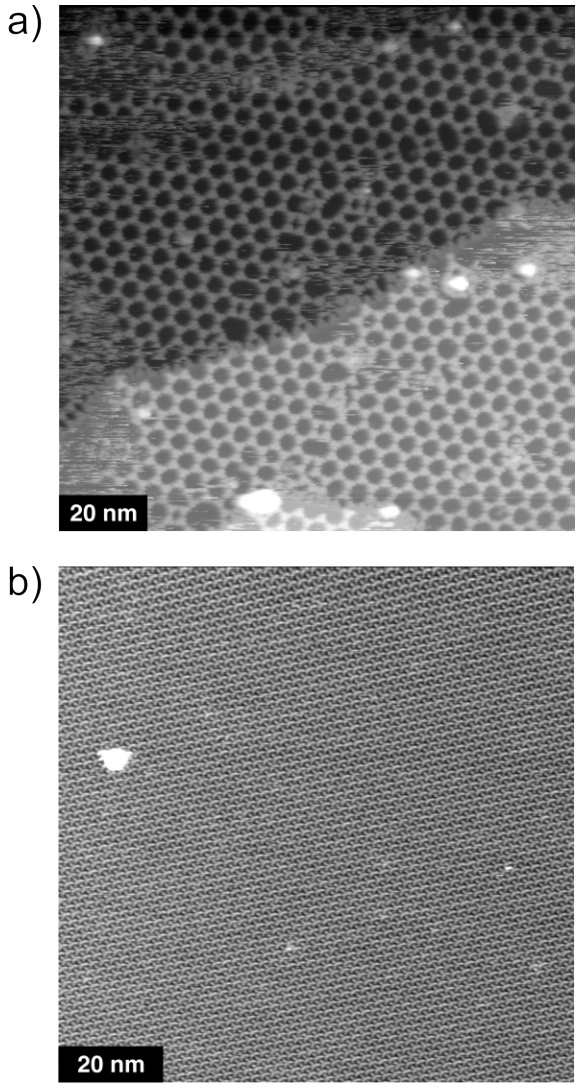

Figure 7.6: (a) STM topograph (+ 2.01 V, 39 pA) of BCNB on Cu(111). The monolayer was prepared by ultraslow deposition ($\sim 2.5 \times 10^{-4}$ monolayer/min), which exclusively yielded the porous β phase. The dashed circle highlights a parallel side-by-side arrangement of dimers, and the dashed line indicates a domain boundary. (b) STM topograph (– 0.19 V, 40 pA) of BCNB on Ag(111). The monolayer was similarly prepared by ultraslow deposition ($\sim 8.3 \times 10^{-4}$ monolayer/min). However, on Ag(111) no change of intermolecular bond type was induced. The α phase was observed exclusively but with a notably increased domain size.

This striking difference between Cu(111) and Ag(111) can be explained by the lower bond dissociation energy (BDE) of C≡N-Ag vs C≡N-Cu coordination bonds. The BDE of two benzonitrile molecules coordinated either by one Cu atom or one Ag atom for isolated arrangements was evaluated by DFT calculations. The BDE for the copper case amounts to 0.90 eV per benzonitrile molecule, which is substantially higher than the value of 0.30 eV in the case of silver. Accordingly, Ag-coordinated BCNB networks might be stable only at lower temperature, although under those conditions the adatom density and mobility become the limiting factors for the formation of metal-coordinated networks.

7.5 Conclusion

The deposition-rate-dependent self-assembly of BCNB on Ag(111) and Cu(111) demonstrates the importance of both substrate and kinetic effects for the expression of a specific type of intermolecular bond. Two types of intermolecular bonds dominate in BCNB monolayers, namely, hydrogen bonds and metal-coordination bonds with adatoms. Their emergence can be controlled by the choice of substrate, a well-known effect that is in the case of metal coordination mostly related to the adatom reactivity and the bond strength of the respective coordination bonds. Moreover, here we discovered that the deposition rate is also effective in deliberately selecting the type of intermolecular bond and thus controlling the structure. A qualitative study of these kinetic effects allows for a basic understanding of growth kinetics and polymorph selection in the abundantly employed formation of metal-organic networks through adatom coordination.

7.6 Acknowledgment

Funding by the Fonds der Chemischen Industrie (T.S.), the Nanosystems-Initiative-Munich Cluster of Excellence, the Alexander von Humboldt Foundation (S.N.), and the Elitenetzwerk Bayern (S.S.) and discussions with Debabrata Samanta are gratefully acknowledged.

7.7 Supporting Information

Synthesis and Characterization of BCNB

Synthesis of 1,3,5-Tris(4'-biphenyl-4"-carbonitrile)-benzene (BCNB): A 100 mL three-neck round-bottomed flask was loaded with 1,3,5-tri(p-bromophenyl) benzene[133] (0.30 g, 0.55 mmol), 4-cyanophenylboronic acid (0.29 g, 1.98 mmol), and anhydrous THF (30 mL). Under a nitrogen atmosphere, $Pd(PPh_3)_4$ (39 mg, 6 mol %) and aqueous K_2CO_3 (2.46 g, 9 mmol) were added. The mixture was stirred at 80 °C for 24 h under N_2 and evaporated to dryness. Chloroform (50 mL) and a 50 % brine solution were added to the dark solid, then the layers were separated. The chloroform layer was isolated, dried over sodium sulphate, and evaporated to dryness. Column chromatography over silica gel, eluting with ethyl acetate/hexane (1:8), yielded the pure product as a white solid in 70 % yield. Melting point 246 °C; ^{1}H nuclear magnetic resonance (NMR) (400 MHz, THF-d_8) δ = 8.04 (s, 3 H, a-H), 7.97 (d, 6H,

^3J = 8.4 Hz, e-H), 7.92 (d, 6H, ^3J = 8.8 Hz, [b/c]-H), 7.87 (d, 6H, ^3J = 8.4 Hz, d-H), 7.83 (d, 6H, ^3J = 8.8 Hz, [b/c]-H); ^{13}C NMR (400 MHz, CD_2Cl_2) δ = 145.2, 142.0, 141.4, 138.9, 133.1, 128.3, 128.1, 127.9, 125.6, 119.2, 111.5; IR (KBr) ν 3469, 3031, 2225, 1604, 1494, 1442, 1390, 1271, 1178, 1111, 1004, 816, 781 cm^{-1}; Anal. Calcd. for $C_{45}H_{27}N_3$: C, 88.64; H, 4.46; N, 6.89. Found: C, 88.35; H, 4.56; N, 6.77.

^{1}H and ^{13}C NMR were recorded on a Bruker Avance 400 MHz spectrometer using the deuterated solvent as the lock and its protiated remainder as the internal reference. NMR measurements were carried out at 298 K. The following abbreviations were utilized to describe peak patterns: s = singlet and d = doublet. The numbering of the carbon atoms of the molecular formula is only used for the assignments of the NMR signal and is not in accordance with the IUPAC nomenclature rules. The melting point was measured on a Büchi SMP-20 and the infrared spectrum on a Varian 1000 FT-IR instrument. Elemental analysis measurement was done using a EA 3000 CHNS.

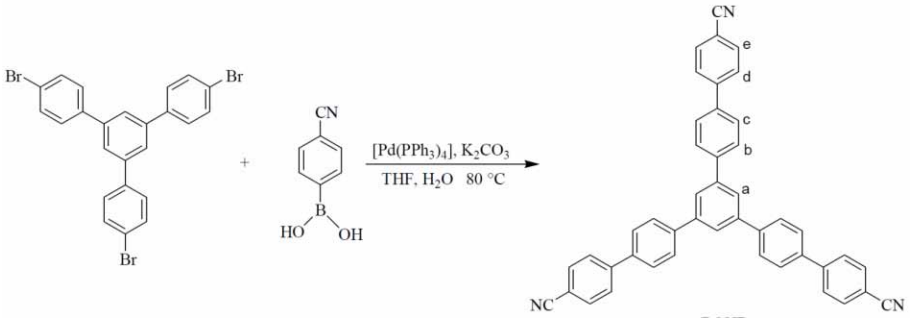

Figure 7.7: Synthesis of 1,3,5-tris(4'-biphenyl-4"-carbonitrile)-benzene (BCNB).

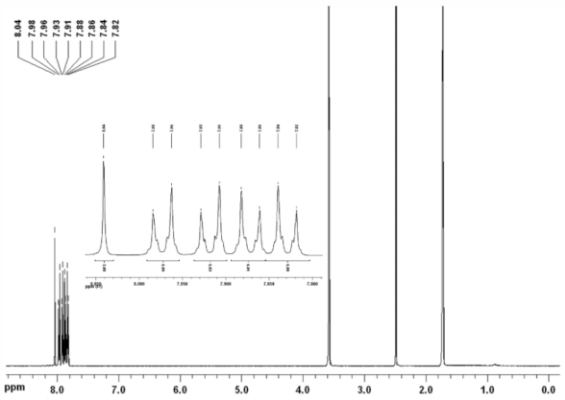

Figure 7.8: ^{1}H NMR spectrum (400 MHz, THF-d_8, 298 K) of BCNB. Inset shows the splitting in the aromatic region.

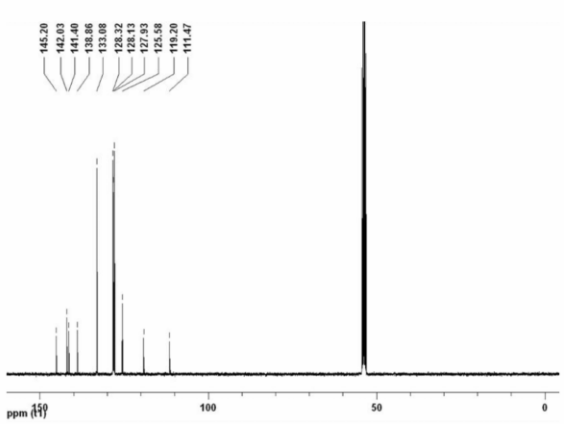

Figure 7.9: ^{13}C NMR spectrum (400 MHz, DCM-d_2, 298 K) of BCNB

BCNB Sublimation Rate

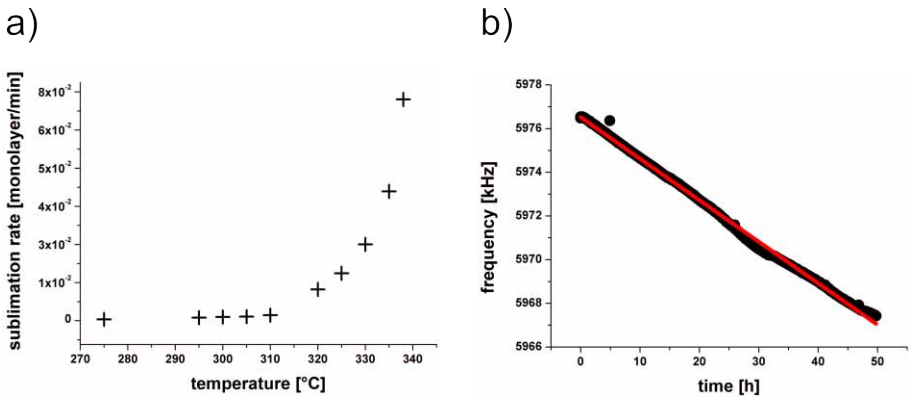

Figure 7.10: The sublimation rate of BCNB was measured with a quartz crystal microbalance that is integrated into the shutter of the Knudsen-cell.[65] a) Sublimation rate of BCNB vs. crucible temperature of the Knudsen-cell. STM images were used for coverage calibration. b) Resonant frequency of the quartz crystal vs. time measured over 50 h at a constant crucible temperature of 280 °C. Black dots: experimental results; red line: linear fit. A linear decrease of the resonant frequency over time indicates a constant effusion rate.

LEED: Experiment and Geometric Simulation

Figure 7.11 depicts experimental and simulated LEED patterns of a $\left(\sqrt{39} \times \sqrt{39}\right)$ R$\pm$ 16° superstructure on Ag(111) (a-c) and a $\left(4\sqrt{3} \times 4\sqrt{3}\right)$ R30° superstructure on Cu(111) (d-f).

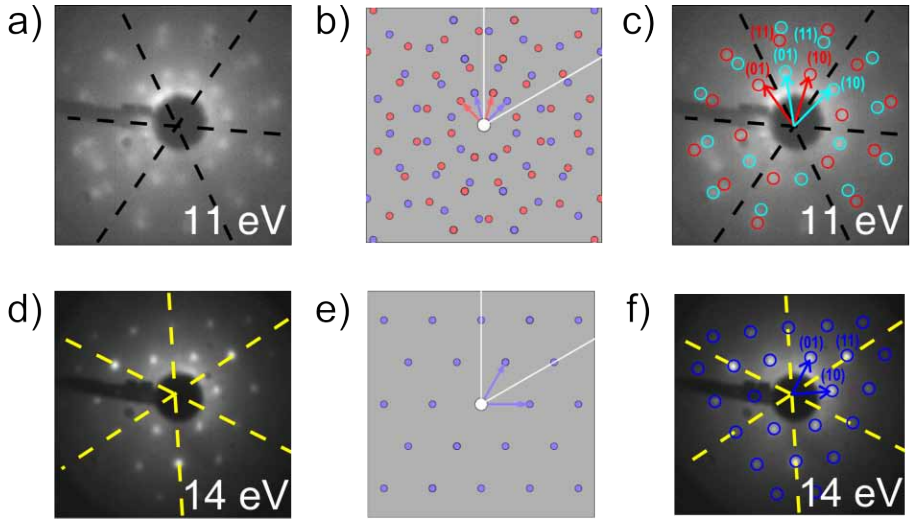

Figure 7.11: Experimental and simulated LEED patterns of BCNB on Ag(111) (a-c) and Cu(111) (d-f). Dashed lines indicate high symmetry directions of the substrates, respectively. a) LEED pattern (electron energy: 11 eV) of the BCNB α phase on Ag(111) exhibiting two equivalent rotational domains of a $\left(\sqrt{39} \times \sqrt{39}\right)$ R ± 16° superstructure. b) Simulated LEED pattern of a $\left(\sqrt{39} \times \sqrt{39}\right)$ R ± 16° superstructure. The two rotational domains are marked by red and blue dots, respectively. c) Similar LEED pattern as in a) with overlaid results of the geometric LEED simulation. Red and turquoise arrows illustrate the reciprocal unit cell vectors of the two rotational domains, respectively. d) LEED pattern (electron energy: 14 eV) of the BCNB α phase on Cu(111) exhibiting a $\left(4\sqrt{3} \times 4\sqrt{3}\right)$ R30° superstructure. e) Simulated LEED pattern of a $\left(4\sqrt{3} \times 4\sqrt{3}\right)$ R30° superstructure. f) Similar LEED pattern as in d) with overlaid results of the geometric LEED simulation. Blue arrows illustrate the reciprocal unit cell vectors.

Density Functional Theory (DFT) Calculations

Entire BCNB Molecules without Substrate

The Gaussian 03 package was used for DFT calculations and geometry optimizations of isolated BCNB and hydrogen bonded BCNB dimers, i.e. without explicit consideration of the substrate.[134] Owing to the extended size of BCNB and the large lattice parameter of the β phase (4.9 nm), full consideration of the substrate would result in an extremely large number of atoms (∼800 for only two substrate layers). Since treating such a large system is computationally too expensive, the substrate was not explicitly taken into account for the first part of the DFT calculations. Yet, all atomic positions of the molecules were fixed in their Z-coordinates to mimic planar adsorption. No further constraints were applied to X- and Y-coordinates. For all calculations standard convergence criteria were used. Although these simplified model calculations only roughly approximate the substrate's influence, benchmark values for intermolecular distances that are characteristic for a specific type of intermolecular bond can nevertheless reliably be derived.

Isolated BCNB The geometry of an isolated BCNB molecule was optimized in order to obtain intramolecular distances for a valid size comparison with the STM data. A hybrid B3LYP functional[135] was used in combination with a Pople type

basis set 6-31G with six Gaussian cores for the X dimension and three and one valence orbitals for the Y and Z dimension.[136] Optimized structure and computed distances are shown in Figure 7.12.

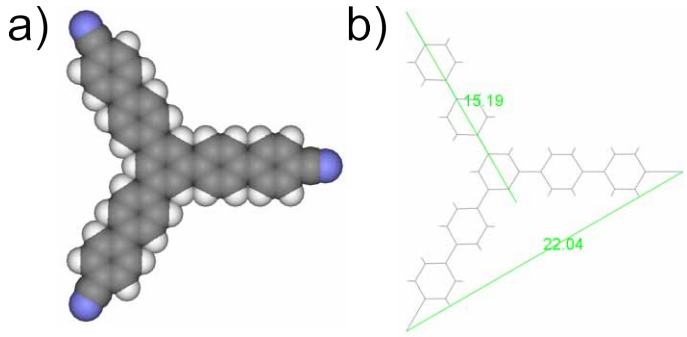

Figure 7.12: a) DFT geometry optimized structure of a single BCNB molecule in the gas phase, important distances are indicated in b). All distances are given in Å (hydrogen: white, carbon: grey, nitrogen: blue).

Hydrogen Bonded Dimer In a next step, the geometry of a hydrogen bonded BCNB dimer was optimized. A B3LYP hybrid functional[135] was used in combination with the similar Pople type basis set 6-31G as in 7.7. For the starting geometry, the molecules were prearranged in a head-to-tail arrangement as experimentally observed. Optimized structure and computed distances are shown in Figure 7.13.

Figure 7.13 illustrates the DFT result for a BCNB dimer of the densely packed α phase. The corresponding theoretical lattice parameter of 1.81 nm (corresponding N-N distance as marked in b)) is in excelent agreement with the experimental lattice parameter of 1.80 nm on Ag(111) and 1.77 nm on Cu(111). The slightly smaller experimentally observed distance is due to adsorbate-substrate interactions, that are not included in these DFT calculations. Three N···H distances are small enough to facilitate hydrogen bonds, namely the three marked distances in figure 7.13 b: 0.30 nm, 0.26 nm, 0.26 nm. At least two of the three corresponding N···H distances are in good agreement with experimental findings of similar hydrogen bond lengths (0.24 nm - 0.26 nm).[116,117]

Model System: Adatom Coordination of Benzonitrile on Cu(111)

In order to capture substrate effects further DFT calculations were conducted for a model system consisting of two adatom coordinated benzonitrile molecules on Cu(111). These DFT calculations were performed with the CASTEP code[137] using the PBE functional[138] together with the dispersion correction scheme developed by Tkatchenko and Scheffler.[139] Core electrons were described by Vanderbilt ultrasoft pseudo potentials,[140] while the valence electrons were treated by a plane wave basis set with a cutoff energy of 450 eV. The surface was represented in a supercell geometry, with three layer Cu slabs (with an optimized lattice parameter of 3.626 Å) and a vacuum separation exceeding 10 Å.

An initial set of calculations addressed the binding of a single benzonitrile molecule to a Cu adatom situated in a most favorable hollow site. For this, we

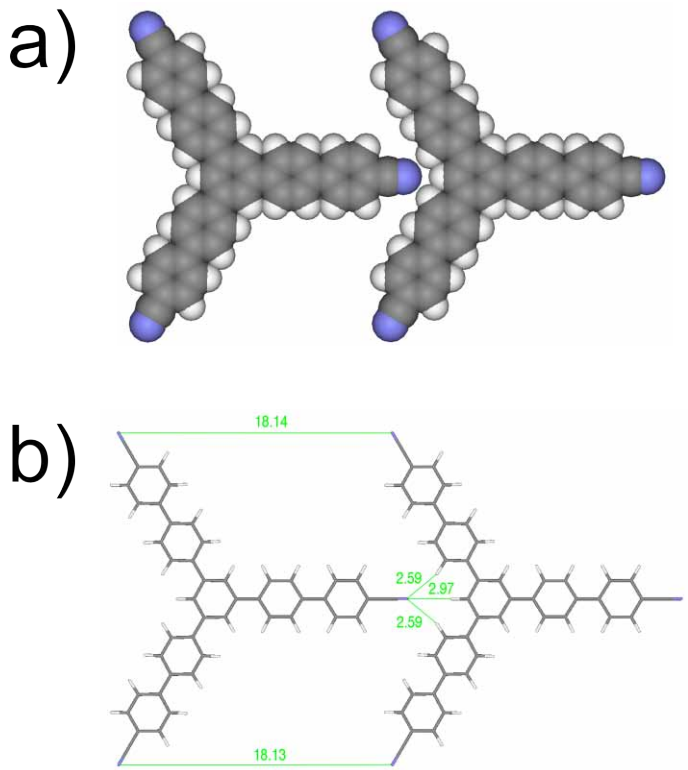

Figure 7.13: a) DFT geometry optimized structure of a hydrogen bonded BNCB dimer (in the gas phase) - the main motif of the α phase; significant distances are marked in b). All distances are given in Å (hydrogen: white, carbon: grey, nitrogen: blue).

employed a (4×4) surface unit-cell and a 2×2×1 Monkhorst-Pack[141] k-point grid. Full geometry optimization starting from different initial geometries (and keeping the bottom two Cu layers fixed at their ideal bulk positions) led to a most stable final structure in which the axis of the benzonitrile molecule is oriented along a line of close-packed Cu surface atoms and with the molecule lying almost parallel to the surface. In particular, there was no kink in the adsorption geometry, i.e. the Cu adatom, the coordinating N atom, and the center of the phenyl moiety fall along one line in the projection. A second identified, slightly less stable (∼0.1 eV) geometry also exhibits this bonding behavior, but the molecular axis now points half way between two close-packed Cu rows.

Ensuing calculations then addressed the bonding of two benzonitrile molecules to the Cu adatom, and were correspondingly performed in an enlarged (4×8) surface unit-cell and a 2×2×1 Monkhorst-Pack grid. Addition of the second benzonitrile molecule when only one Cu adatom is present does not have any influence on the molecular orientation. The two molecules simply orient in opposite directions. The same behavior was also found for the energetically less stable second configuration.

A kink in the adsorption configuration was only observed after addition of a second Cu adatom in a nearest-neighbor hollow site. In the resulting geometry, one benzonitrile molecule is now slightly displaced in the direction of the extra Cu adatom. The configuration is such that the molecular axes of the benzonitrile molecules exhibit a kink angle of 6.2 °. Similar observations were made for the second,

less stable configuration, where a kink angle of 4 ° resulted after addition of the second Cu adatom.

Additional STM Topographs

Epitaxial Relations of BCNB Monolayers on Cu(111)

Figure 7.14 exemplifies the epitaxial relations of BCNB monolayers on Cu(111). The porous polymorph occurs in a $\left(11\sqrt{3} \times 11\sqrt{3}\right)$ R30° as well as a 19×19 superstructure. However, for the densely packed polymorph only a $\left(4\sqrt{3} \times 4\sqrt{3}\right)$ R30° superstructure is found.

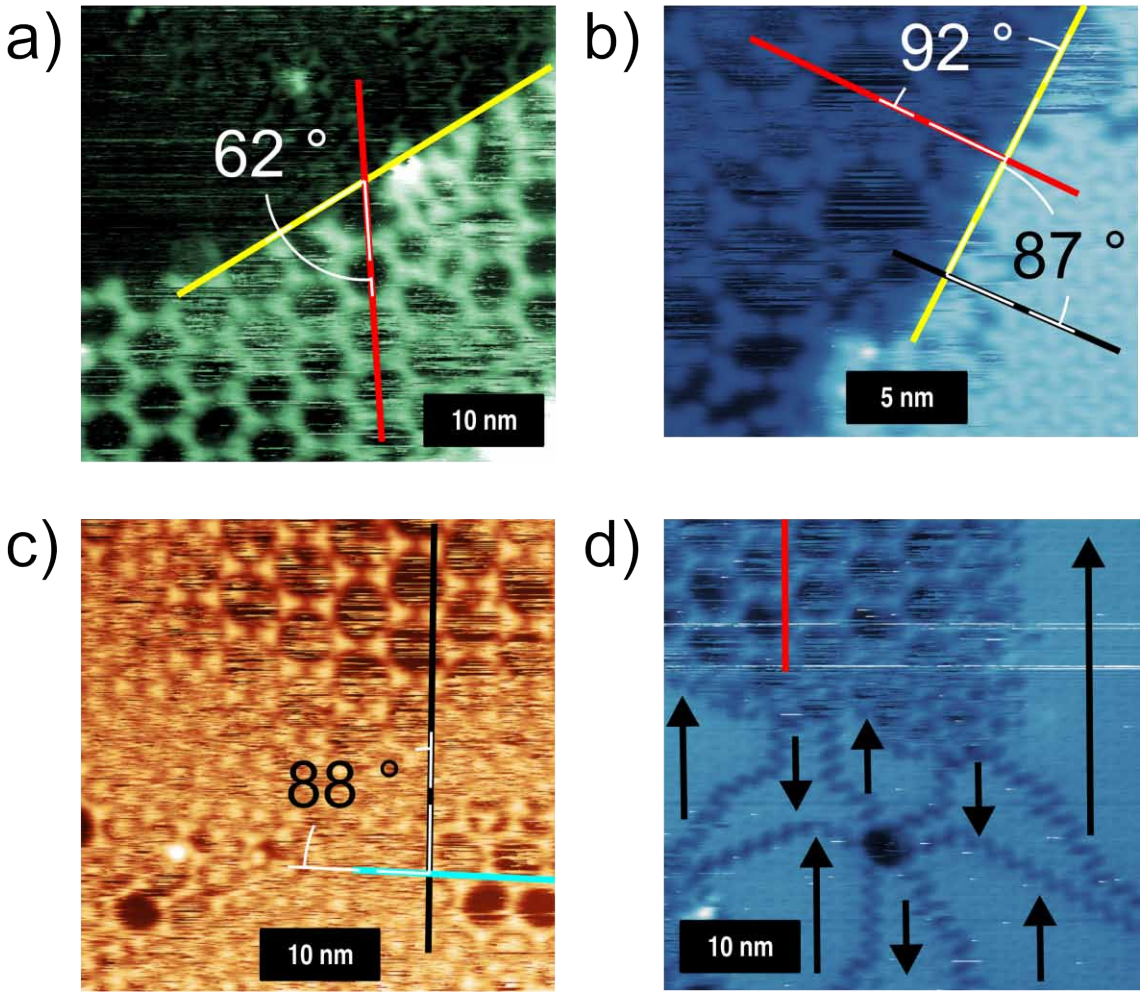

Figure 7.14: Selected STM topographs of BCNB monolayers on Cu(111), deposited with $\sim 2.5 \times 10^{-2}$ monolayer/min. These images were used to derive the epitaxial relations of the adsorbate layer. a) 19×19 superstructure of the porous β phase. The rotational angles of adsorbate to substrate unit cell axes amount to 0 °, 60 °, 120 °. One unit cell axis of the β phase is indicated by the red line. It is at an angle of ∼60 ° to the straight substrate step-edge (yellow line), which runs parallel $[1\bar{1}0]$ for fcc (111) surfaces. Tunneling parameters: +1 V, 75 pA. b) Porous (left part, lower terrace) and densely packed α phase (right part, upper terrace) with unit cell axes rotated by approximately 90 ° with respect to the step-edge (yellow line). Corresponding epitaxial relations for α and β phase are $\left(11\sqrt{3} \times 11\sqrt{3}\right)$ R30° and $\left(4\sqrt{3} \times 4\sqrt{3}\right)$ R30°, respectively. Tunneling parameters: +1.70 V, 70 pA. c) Co-existence of the two epitaxial relations ($\left(11\sqrt{3} \times 11\sqrt{3}\right)$ R30° and 19×19) for the porous β phase, verified by one unit cell axis at an angle of approximately 90 ° with respect to the other (black and turquoise lines). Tunneling parameters: + 2.11 V, 50 pA. d) Coexisting porous (upper left corner) and densely packed polymorph (rest of the image). The densely packed α phase consists of eight domains. The red line indicates one unit cell vector of the porous polymorph, the black arrows indicate unit cell vector of the densely packed polymorph, all in parallel alignment. The densely packed domains exhibit the same unit cell orientations, but differ in the azimuthal orientation of BCNB molecules. For illustration the arrows point in different directions. Tunneling parameters: + 1.44 V, 56 pA.

Domain Formation in the Beta Phase

Figure 7.15 displays an overview image of a BCNB monolayer on Cu(111). The possible tilt directions of BCNB molecules are color coded. Additionally their domain structure is visualized.

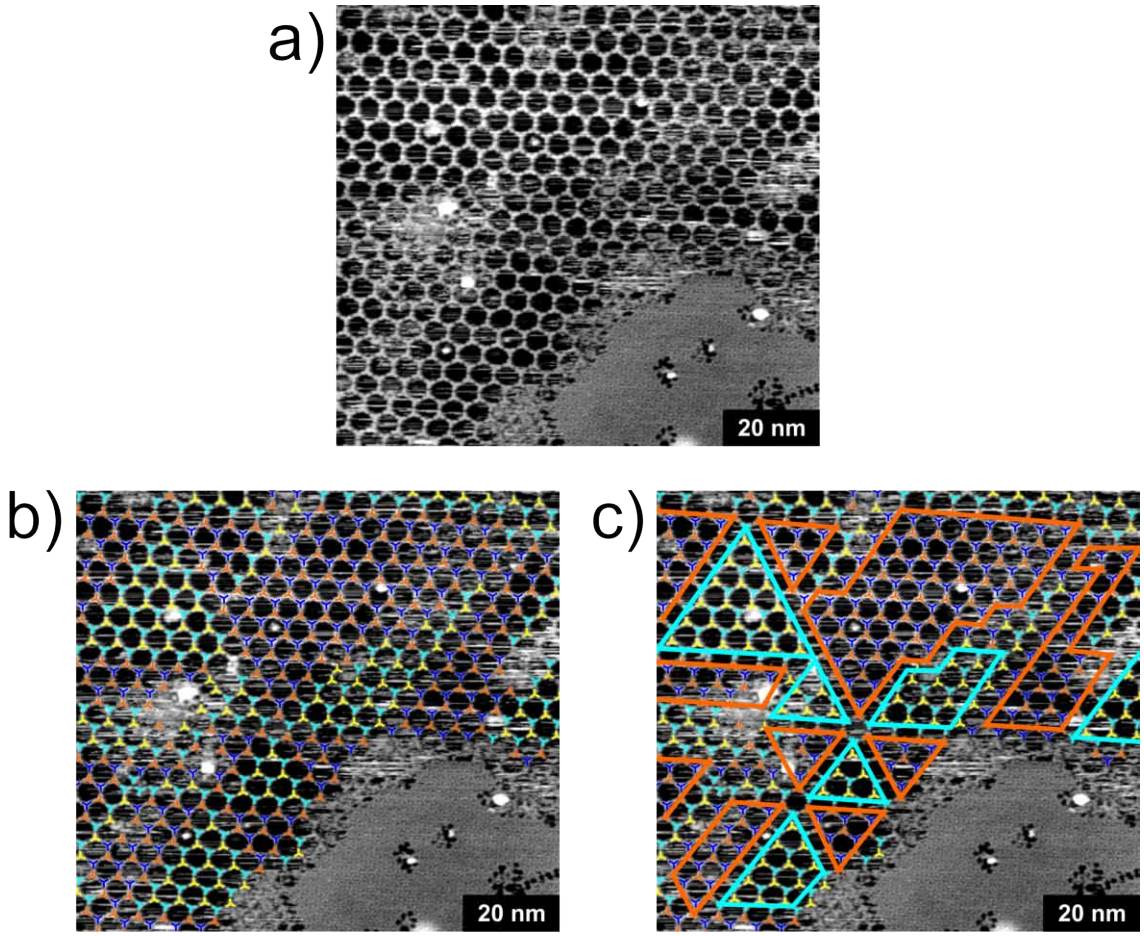

Figure 7.15: STM topograph ($+2.09$ V, 80 pA) of a BCNB monolayer on Cu(111) prepared with a deposition rate of $\sim 2.5 \times 10^{-2}$ monolayer/min (same image as in main manuscript) showing the co-existence of α and β phase. a) Overview image. b) Same image with overlaid colored tripods for visualization of the tilt direction. c) As in b) but with additionally indicated domain boundaries. Yellow and turquoise tripods form one observed domain (boundaries are marked by turquoise solid lines), whereas orange and blue tripods form the other observed mirror domain (boundaries are marked by orange solid lines).

Adatom Signatures in the Beta Phase

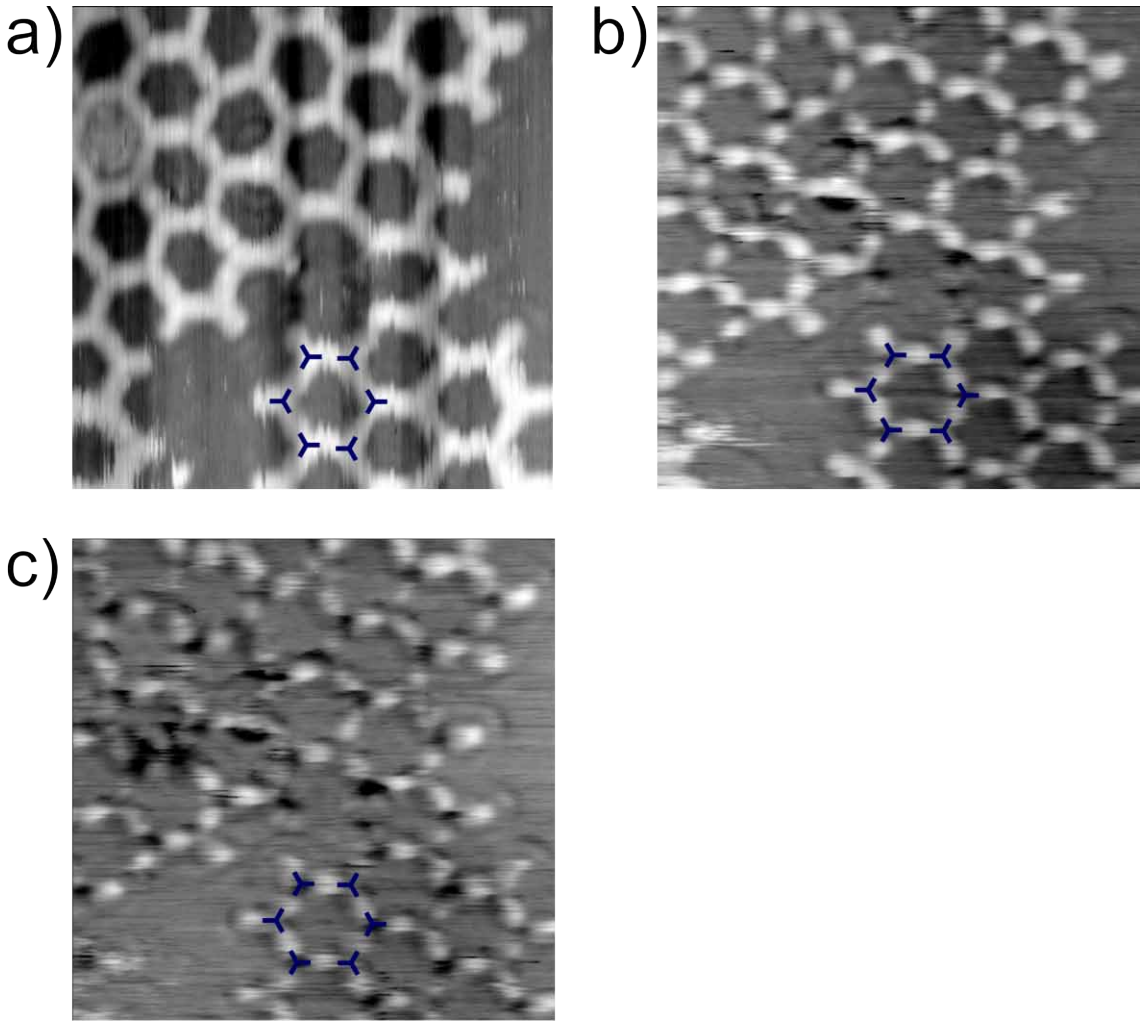

Figure 7.16: Series of STM topographs of the β phase on Cu(111) (all 25×25 nm^2). The same area was successively imaged. Characteristic changes in the STM contrast were observed for different tunneling voltages, but also over time, most likely due to tip changes. BCNB molecules are indicated by the overlaid blue tripods. a) Initial STM contrast dominated by the contour of BCNB molecules (+ 1.11 V, 56 pA, Δt = 0 min). b) Changed STM contrast; the BCNB molecules appear less bright, while the regions of the coordination bonds between the BCNB molecules, where the adatoms are located appear still bright. (+ 0.77 V, 60 pA, Δt = 24 min). c) Significantly changed STM contrast; the apparent height of the BCNB molecules is considerably diminished, while the contrast is dominated by the signature of the adatoms between two BCNB molecules (+ 0.77 V, 59 pA, Δt = 33 min). A similar adatom related contrast feature was also observed for Cu-benzoate complexes on Cu(110).[131]

Tentative Model of the Beta Phase on Cu(111)

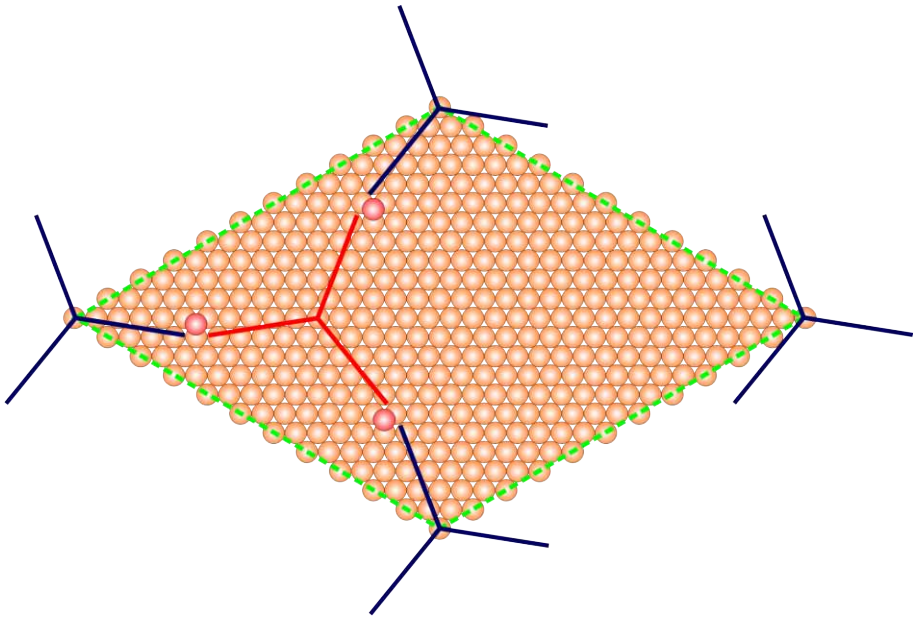

Figure 7.17: Tentative model of the β phase on Cu(111), the dashed green lines indicate the $\left(11\sqrt{3} \times 11\sqrt{3}\right)$ R30° unit cell (analogous to Figure 5 of the main manuscript).

Chapter 8

Solvent-Dependent Stabilization of Metastable Monolayer Polymorphs at the Liquid-Solid Interface

Thomas Sirtl,[ab] Wentao Song,[ab] Georg Eder,[ab] Subhadip Neogi,[c] Michael Schmittel,[c] Wolfgang M. Heckl,[abd] and Markus Lackinger.[abde] Reprinted (adapted) with permission from *ACS Nano* 7(8), 6711-6718, 2013.

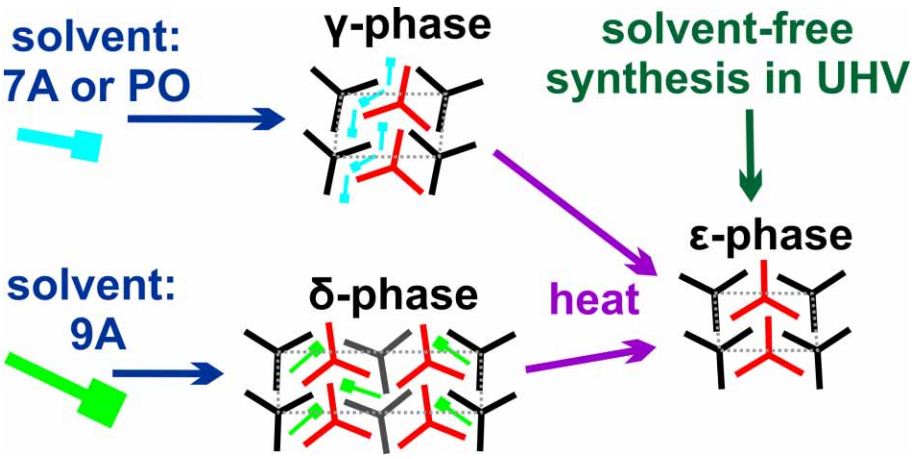

[a] Department of Physics, Technische Universität München, James-Franck-Str. 1, 85748 Garching, Germany
[b] Center for NanoScience (CeNS), Schellingstr. 4, 80799 Munich, Germany
[c] Center of Micro- and Nanochemistry and Engineering, Organische Chemie I, Universität Siegen, Adolf-Reichwein-Str. 2, 57068 Siegen, Germany
[d] Deutsches Museum, Museumsinsel 1, 80538 Munich, Germany
[e] Corresponding author; e-mail: markus@lackinger.org; web: www.2d-materials.com

8.1 Abstract

Self-assembly of 1,3,5-tris(4'-biphenyl-4"-carbonitrile)benzene monolayers was studied at the liquid-solid interface by scanning tunneling microscopy. Application of different fatty acid homologues as solvents revealed a solvent-induced polymorphism. Yet, tempering triggered irreversible phase transitions of the initially self-assembled monolayers, thereby indicating their metastability. Interestingly, in either case, the same thermodynamically more stable and more densely packed monolayer polymorph was obtained after thermal treatment, irrespective of the initial structure. Again, the same densely packed structure was obtained in complementary solvent-free experiments conducted under ultrahigh vacuum conditions. Thus, self-assembly of metastable polymorphs at room temperature is explained by adsorption of partially solvated species under kinetic control. The irreversible phase transitions are induced by thermal desolvation, that is, desorption of coadsorbed solvent molecules.

8.2 Introduction

Surface-supported self-assembled monolayers have been extensively studied over the past decade, due to their chemical and structural versatility, ranging from densely packed to porous two-dimensional structures.[3,11,21] Monolayer topologies are foremost determined by the chemical structure of the molecular building blocks, where type and stereochemical arrangement of functional groups decisively control intermolecular binding. However, the emergence of different monolayer polymorphs of a compound on the same surface already indicates an important influence of more subtle parameters, especially for self-assembly at the liquid-solid interface. Among those, solute concentration, temperature, and type of solvent were identified as being most important. In particular, solvent-induced polymorphism plays an important role because it is abundant, but its reasons are in most cases not clear.[142] For instance, a solvent-specific stabilization of certain monolayer structures is well-known for aromatic carboxylic acids,[6,27–31] foldable oligomers,[7] porphyrins,[32] or long-chain-substituted aromatic molecules.[33,34]

Different theoretical approaches such as Monte Carlo simulations,[143–146] molecular dynamics,[147] and thermodynamic models[17,88,100,148,149] were pursued to understand monolayer formation and selection processes. For the latter, it is assumed that the experimentally observed structures correspond to thermodynamic equilibrium. At the liquid-solid interface, this fundamental assumption is underpinned by experimental evidence for a dynamic equilibrium between dissolved and adsorbed molecules.[17,147] This phenomenon is unique for liquid-solid interfaces being the consequence of a drastically lowered desorption barrier due to solvation of the desorbed species in the supernatant liquid phase. An experimental manifestation of this dynamic equilibrium is the adaptation of the adsorbed monolayer structure to concentration changes in the liquid phase. For instance, transitions from a densely packed to a porous phase were observed for various compounds upon dilution.[14,29,100,148,150] Reversible temperature-driven phase transitions, likewise between a porous and a densely packed monolayer polymorph, provide further evidence for thermodynamical control.[88] Accordingly, thermodynamic models were successfully applied to understand structure selection in the concentration-dependent self-assembly of

annulene, oligopyridine, and tricarboxylic acid monolayers[14,100,148,151] and the composition-dependent formation of binary tricarboxylic acid monolayers.[149]

Despite the utility of thermodynamical descriptions, counterexamples prove that an observed self-assembled monolayer structure does not necessarily represent a thermodynamically fully equilibrated situation.[17,147,150] In general, it remains difficult to experimentally decide whether a structure is the thermodynamically most favorable polymorph. A common method to disprove thermodynamic equilibrium is tempering, where irreversible phase transitions indicate conversion of metastable into equilibrium structures. For instance, upon heating of alkane-substituted hexabenzocoronene monolayers on Au(111), three subsequent phase transitions with a progressive increase in packing density were reported.[152] Similarly, thermally triggered irreversible phase transitions were observed in monolayers of polyaromatic molecules on graphite.[151,153] These findings are commonly explained by kinetic entrapment of the initial monolayer in a metastable state, and tempering provides the required activation energy for conversion into a thermodynamically more stable structure.

We present a study of monolayer self-assembly of the comparatively large polyaromatic trinitrile molecule 1,3,5-tris(4'-biphenyl-4"-carbonitrile)benzene (BCNB; see the inset to Figure 8.1a for molecular structure) at the liquid-solid interface, which targets the competition between kinetically and thermodynamically governed structure formation for larger compounds. By using fatty acid homologues as solvents, two different polymorphs were identified on graphite at room temperature. Yet, both polymorphs are irreversibly converted into the same, more densely packed monolayer by a thermal treatment, thereby indicating the metastability of both initial structures. In an attempt to unambiguously attribute this to solvent effects, complementary studies were carried out in a solution-free, utmost defined ultrahigh vacuum (UHV) environment.

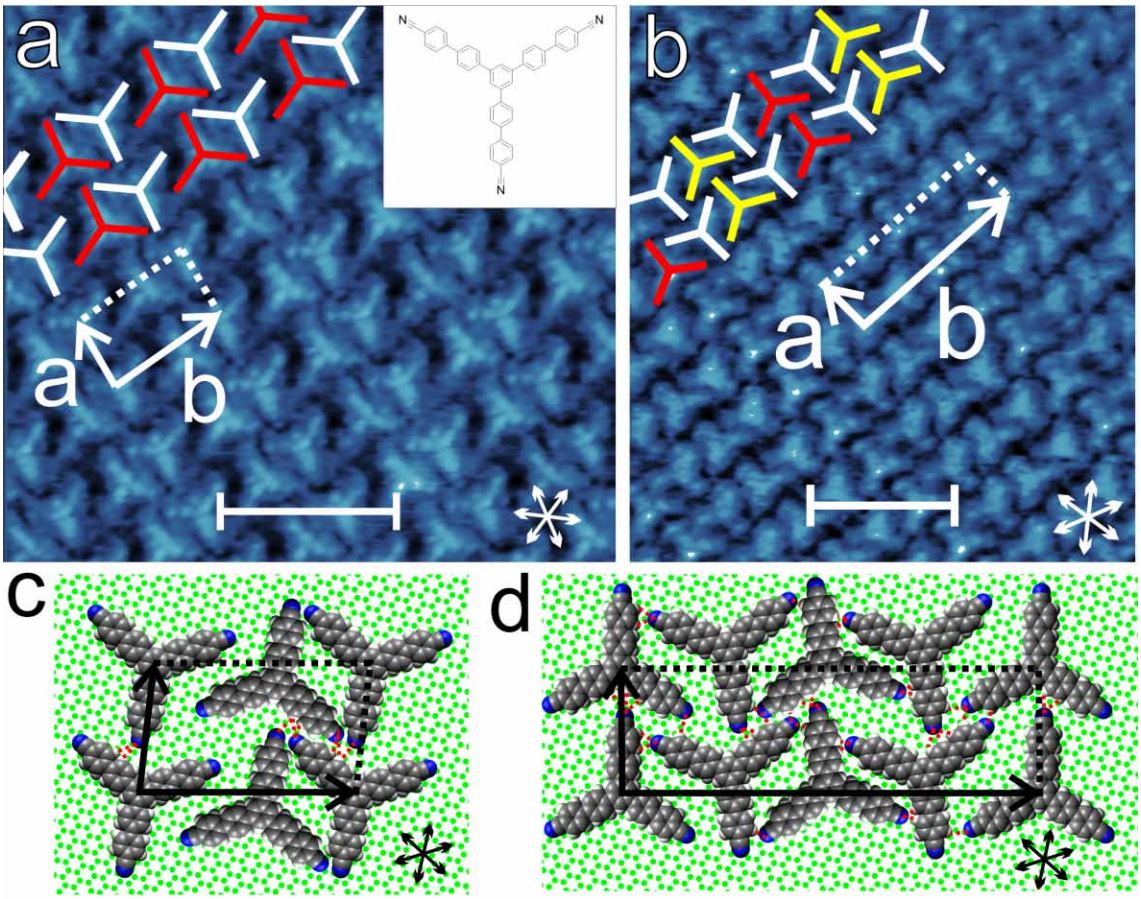

Figure 8.1: (a) STM image of the BCNB γ-phase at the heptanoic acid-graphite interface (56 pA, − 0.35 V). Inset: Molecular structure of BCNB. (b) STM image of the BCNB δ-phase at the nonanoic acid-graphite interface (40 pA, − 1.3 V). (c) Tentative model of the γ-phase. (d) Tentative model of the δ-phase. In (a) and (b), overlaid tripods symbolize BCNB molecules, and the unit cell vectors are denoted by arrows. Scale bars correspond to 5 nm. Arrows in the lower right corner indicate ⟨1000⟩ directions of graphite. The tentative models in (c) and (d) are based on the closest commensurate superstructures. DFT geometry-optimized BCNB molecules were used for the models and positioned according to the STM data (carbon atoms of BCNB, gray; carbon atoms of the graphite surface, green; hydrogen, white; nitrogen, blue). Conceivable intermolecular hydrogen bonds are indicated by dotted lines.

8.3 Results and Discussion

At the heptanoic acid-graphite interface, a self-assembled well-ordered BCNB monolayer termed γ-phase was observed. A representative STM image is shown in Figure 8.1a. From split images, lattice parameters of $a = 2.1 \pm 0.1$ nm, $b = 3.6 \pm 0.1$ nm, and $\gamma = 85 \pm 3°$ and an angle of $18 \pm 1°$ between the $\vec{a}$ vector of the superstructure and the graphite ⟨1000⟩ direction were determined. Within the experimental error, the BCNB lattice is consistent with a commensurate superstructure given by $\begin{pmatrix} 8 & -1 \\ 11 & 16 \end{pmatrix}$. Further evidence for commensurability is provided by the absence of a Moiré pattern as normally observed for incommensurate superstructures on graphite. BCNB adsorbs planarly and each unit cell contains a pair of oppositely oriented molecules, as unambiguously concluded from the appearance of BCNB in the STM images. Adjacent molecules have similar orientation along a, whereas they are alternatingly oriented along $\vec{b}$. Moreover, the nearest neighbor BCNB distances in this direction are alternating between 1.5 nm and 2.0 nm, allowing the dimers to be distinguished. Accordingly, the structure can be viewed as rows of stacked dimers running along $\vec{a}$ that are separated by small, but clearly recognizable, gaps. A tentative model of the BCNB dimer row structure is presented in Figure 8.1c. Owing to the large contact area between planarly adsorbed BCNB and graphite, the monolayer is to a large extent stabilized by molecule-substrate interactions. Additionally, the dimers bind through intermolecular $C \equiv N \cdots H - C$ hydrogen bonds, as indicated in Figure 8.1c. Formation of intermolecular hydrogen bonds was previously reported for BCNB on Ag(111) and Cu(111)[26] and is also well-known from other carbonitriles on surfaces[107,110,115] or in bulk crystals.[116,117] Further attractive electrostatic contributions might arise from so-called proton acceptor-ring interactions, as recently proposed in a theoretical ab initio study.[96] At this point, however, it remains unclear what causes and determines the spacing between the dimers.

At the nonanoic acid-graphite interface, a different and more complex BCNB monolayer polymorph termed δ-phase was observed. A representative STM image is depicted in Figure 8.1b, showing BCNB to be adsorbed in a planar fashion. Similar to the γ-phase, the orientation of adjacent BCNB molecules is equal along $\vec{a}$ and alternates along $\vec{b}$. Yet, along $\vec{b}$, the structure does not simply consist of equally spaced dimers, but exhibits a more complex stacking sequence that also comprises single molecules or trimers, again separated by small gaps. An example for the most frequently observed monomer-trimer-monomer sequence is depicted in Figure 8.1b. The corresponding unit cell contains four molecules and the underlying lattice parameters of $a = 2.0 \pm 0.1$ nm, $b = 6.7 \pm 0.3$ nm, and angle of $87 \pm 2°$ can again be mapped on a commensurate superstructure given by $\begin{pmatrix} 7 & -2 \\ 21 & 31 \end{pmatrix}$. A tentative model of the δ-phase is depicted in Figure 8.1d. Again, for the closely spaced BCNB molecules, stabilization by intermolecular $C \equiv N \cdots H - C$ hydrogen bonds is proposed. The BCNB nearest neighbor distances in a monomer-trimer-monomer sequence amount to 1.9 nm…1.6 nm…1.6 nm…1.8 nm. Thus, the intratrimer distance in the δ-phase (1.6 nm) is similar to the intradimer distance in the γ-phase (1.5 nm), and also the intertrimer (1.8 – 1.9 nm) and interdimer (2.0 nm) distances are comparable for

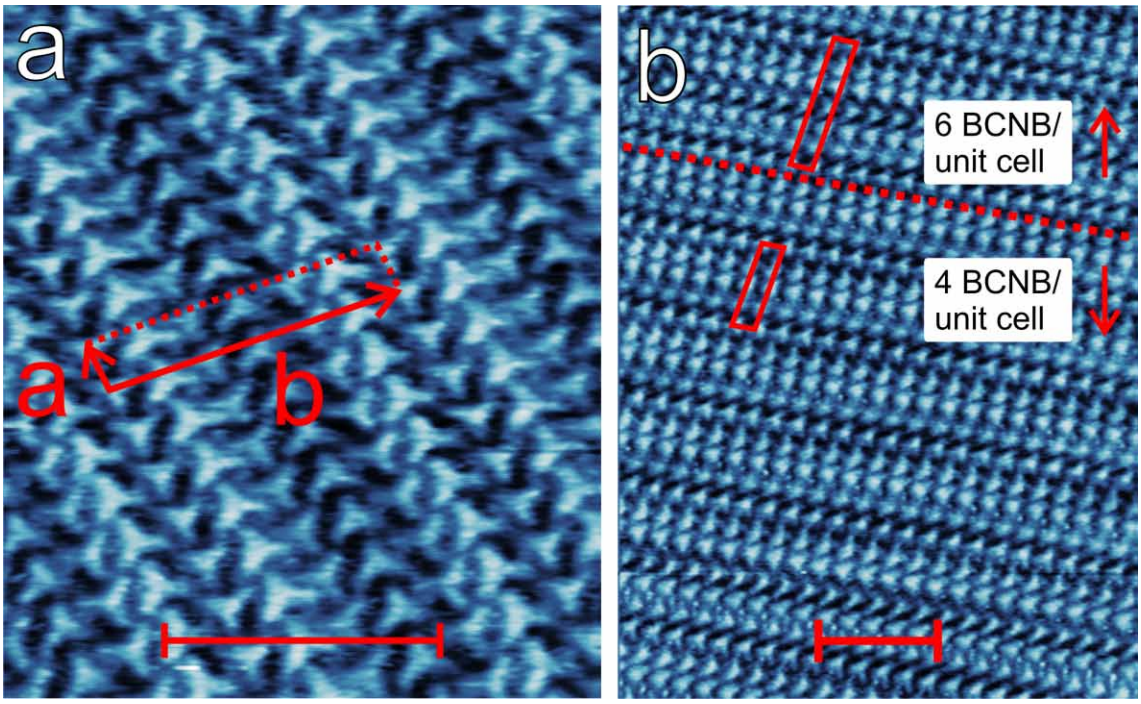

Figure 8.2: STM images of BCNB monolayers at the nonanoic acid-graphite interface. (a) Close-up of a variant of the δ-phase, exhibiting a monomer-dimer-monomer-dimer-monomer stacking sequence along $\vec{b}$. The unit cell vectors are indicated; $\vec{b}$ is elongated as compared to the most frequently observed δ-phase, and a unit cell contains six BCNB molecules (50 pA, − 0.50 V). (b) Overview image depicting different stacking sequences within one domain of the δ-phase (65 pA, − 1.2 V). Scale bars correspond to 10 nm.

the two phases. Occasionally, also more complex stacking sequences were observed for BCNB at the nonanoic acid-graphite interface, for instance, a monomer-dimer-monomer-dimer-monomer sequence, where the molecular orientation in successive monomer rows alternates (Figure 8.2). The corresponding unit cell containing six molecules is even larger with lattice parameters of $a = 2.1 \pm 0.2$ nm, $b = 9.7 \pm 0.6$ nm, and an angle of $89 \pm 4°$. Different stacking sequences can also occur within the same domain; an example is depicted in Figure 8.2b.

Lattice parameters of all monolayer structures are summarized in Table 1. Interestingly, the spacing of similarly oriented molecules in rows parallel to $\vec{a}$ is quite similar for the γ-phase and the δ-phase, indicating a preferred distance between equally oriented stacked molecules and also a certain degree of analogy between these structures. Further experiments with pentanoic and octanoic acid as well as 1-phenyloctane (cf. figure 8.6) as solvents also yielded the γ-phase, rendering the δ-phase unique for nonanoic acid.

To explore whether the solvent-specific polymorphs represent the thermodynamically most favorable structures, experiments were conducted on thermally treated samples. For both polymorphs self-assembled at room temperature, thermal treatment at 70 °C for 10 min results in irreversible phase transitions. Interestingly, irrespective of the initial structure, the same structure termed ε-phase emerges after tempering either the γ- or δ-phase. STM images of the ε-phase obtained from the two different initial structures are depicted in Figure 8.3b,c. Also tempering of

Table 8.1: Lattice Parameters of All Experimentally Observed BCNB Monolayer Polymorphs

phase	lattice parameters				surface packing desity	
	a (nm)	b (nm)	$\sphericalangle$a, b	$\sphericalangle$b, g	(BCNB/nm^2)	(BCNB/unit cell)
γ	2.1 ± 0.1	3.6 ± 0.1	$85 \pm 3°$	$18 \pm 1°$	0.27 ± 0.02	2
γ^{a}	2.1^{a}	3.5^{a}	$84°^{a}$	$18°^{a}$	0.27^{a}	2
δ	2.0 ± 0.1	6.7 ± 0.3	$87 \pm 2°$	$18 \pm 2°$	0.30 ± 0.02	4
δ^{a}	2.0^{a}	6.7^{a}	$89°^{a}$	$18°^{a}$	0.30^{a}	4
δ^{ext}	2.1 ± 0.2	9.7 ± 0.6	$89 \pm 4°$	$19 \pm 4°$	0.29 ± 0.04	6
ε	2.0 ± 0.1	3.2 ± 0.1	$88 \pm 2°$	$20 \pm 2°$	0.31 ± 0.02	2
ε^{UHV}	1.9 ± 0.1	3.3 ± 0.1	$82 \pm 2°$		0.32 ± 0.01	2
ε^{a}	1.9^{a}	3.3^{a}	$86°^{a}$	$19°^{a}$	0.32^{a}	2

[a] Lattice parameters of the closest commensurate superstructures; a and b, absolute lengths of the unit cell vectors; $\sphericalangle$a, b, angle between a and b; $\sphericalangle$b, g, smallest angle between b and a graphite $\langle 1000 \rangle$ direction; δ^{ext}, additional variant of this phase with extended unit cell; ε^{UHV}, experimental results at the vacuum-graphite interface.

the γ-phase prepared in 1-phenyloctane yielded the ε-phase (cf. figure 8.6). The ε-phase was characterized either by STM after *ex situ* heating and after the samples had cooled or additionally during *in situ* heating by STM imaging at an elevated temperature of 70 °C (in nonanoic acid, cf. figure 8.5) without finding any differences. The unit cells of all ε-phases obtained under different conditions are identical within experimental error.

The irreversible phase transitions clearly indicate the higher thermodynamic stability of the ε-phase, hence the metastability of both γ- as well as δ-phase. A conversion of the metastable phases at room temperature without any additional thermal activation was never observed, not even in long-term experiments with prolonged exposure times of up to 1 week.

Lattice parameters of the ε-phase amount to 2.0 ± 0.1 nm, 3.2 ± 0.1 nm, and $88 \pm 2°$ and are again consistently reproduced by a commensurate superstructure given by $\begin{pmatrix} 8 & 1 \\ 5 & 15 \end{pmatrix}$. BCNB molecules are again adsorbed planarly in the ε-phase, and the unit cell contains two molecules. Both the a lattice parameter and the orientation with respect to the graphite substrate are again comparable to the two metastable polymorphs. Similar to the γ- and δ-phases, adjacent BCNB molecules are oriented equally along $\vec{a}$ and alternatingly along $\vec{b}$. In contrast to the other phases, BCNB molecules are now evenly spaced with close proximity and the small gaps that were observed in the metastable polymorphs disappeared. BCNB nearest neighbor distances amount to 1.6 – 1.7 nm, comparable to the intradimer distance in the γ-phase (1.5 nm) and the intratrimer distances in the δ-phase (1.6 nm). This also leads to a smaller b lattice parameter of 3.3 nm in the ε-phase as compared to 3.5 nm of the γ-phase. Likewise, intermolecular C $\equiv$ N $\cdots$ H – C hydrogen bonds contribute to the stabilization of the ε-phase. However, the closer packing and the absence of gaps implicate enhanced possibilities for intermolecular hydrogen bonds as compared to the room temperature phases. Accordingly, each of the nitrile groups in the ε-phase is involved in a stabilization of the structure via intermolecular hydrogen bonds.

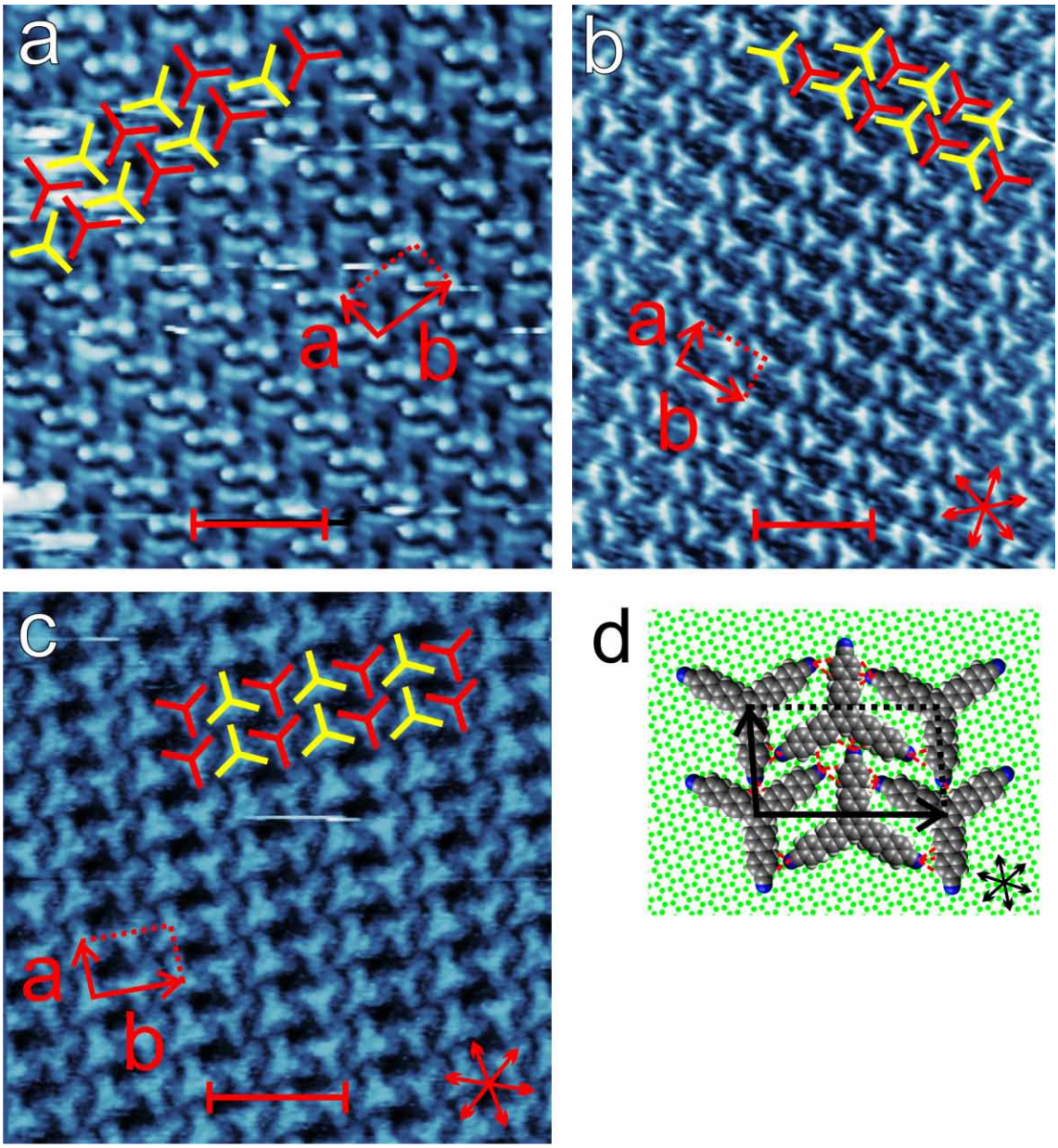

Figure 8.3: (a) STM image of the BCNB ε-phase at the vacuum-graphite interface (50 pA, + 1.1 V). (b,c) STM images of *ex situ* tempered (70 °C; 10 min) samples with (b) nonanoic acid and (c) heptanoic acid: (b) 35 pA, − 1.3 V; (c) 36 pA, − 0.95 V. In both cases. the BCNB ε-phase was observed. (d) Tentative model of the ε-phase. Overlaid tripods in (a-c) indicate BCNB molecules, and the unit cell vectors $\vec{a}$ and $\vec{b}$ are marked. Scale bars correspond to 5 nm. Arrows denote ⟨1000⟩ directions of graphite.

Moreover, the ε-phase is the polymorph with the smallest unit cell, and thus features the highest surface packing density. A similar trend (i.e., higher packing densities of the final structures) was commonly observed for irreversible phase transitions of surface-supported monolayers.[151–153] Decreased intermolecular distances offer an enthalpic advantage through stronger intermolecular bonds. Accordingly, in many cases, more densely packed monolayer polymorphs are thermodynamically more favorable.[17,147] Significant enthalpic contributions also arise from molecule-surface

interactions that increase with packing density. Of course, structural changes that are associated with higher packing densities may also affect or even impair intermolecular bonds. However, the enthalpy change due to intermolecular bonds can be inferior in relation to the adsorption enthalpy, in particular, for large molecules. An instructive example therefore is the large tricarboxylic acid 1,3,5-tris(carboxybiphenyl)benzene, the monolayer structure of which is a compromise in favor of an increased packing density rather than optimized intermolecular hydrogen bonds.[14]

We interpret the observed irreversible phase transitions from two distinct solvent-dependent monolayer polymorphs to a single solvent-independent structure as conversion of metastable polymorphs into thermodynamic equilibrium. Tempering provides the required energy to overcome the activation barrier. Additional experiments were carried out to substantiate the irreversibility of the phase transitions. If the phase transitions were reversible, γ- and δ-phases would be the thermodynamically preferred phases at room temperature. Accordingly, the ε-phase would only be observable at room temperature because it is kinetically trapped; that is, the rate of back-conversion is too slow. To support our hypothesis, graphite samples were immersed into solution, heated to 70 °C, and cooled at an extremely low rate of 6.2×10^{-3} °C min^{-1} to facilitate a possible back-conversion. However, even with these extremely low cooling rates, the ε-phase prevailed, providing further indications that it actually is the thermodynamically more stable monolayer structure (cf. figure 8.7).

In the light of the many examples for solvent-induced polymorphism, it is remarkable that none of the initial room temperature polymorphs represents thermodynamic equilibrium. The solvent-dependent stabilization of different metastable polymorphs suggests a solvent-specific influence. One open question, however, is whether the solvent is the actual cause for the initial formation of metastable monolayer polymorphs. We address this intricate question by complementary experiments, where we study self-assembly of BCNB monolayers without any solvent in an utmost defined and clean environment. To this end, BCNB was deposited by thermal sublimation onto graphite under ultrahigh vacuum conditions and characterized *in situ* by STM. A representative STM image acquired at room temperature is shown in Figure 8.3a. Both lattice parameters and arrangement of BCNB are similar to the ε-phase observed at the liquid-solid interface. Based on the STM results and the equality of the unit cells, we conclude that vacuum deposition yields the same ε-phase as obtained from the thermally activated conversion of metastable γ- and δ-phases at the liquid-solid interface, respective images are shown in Figure 8.3b,c.

Apparently, the solvent directs the initial self-assembly toward metastable structures, giving rise to questions about the origin of this phenomenon. Given that both metastable phases are less densely packed than the stable ε-phase and exhibit gaps between otherwise densely packed rows of molecules, we propose that solvent coadsorption stabilizes both γ- and δ-phase. Solvent coadsorption is a well-known effect for self-assembly at the liquid-solid interface.[142] For instance, heptanoic acid solvent molecules were found to coadsorb in an upright geometry around coronene solute molecules on Au(111).[154] Their upright adsorption is mediated by strong interaction of the carboxyl groups with the metal substrate. On weakly interacting graphite surfaces, a different picture emerges: aliphatic solvent molecules as heptanol[155] or undecanol[156,157] were found to coadsorb planarly in an all-trans conformation in networks of isophthalic acid derivatives on graphite. For self-assembly

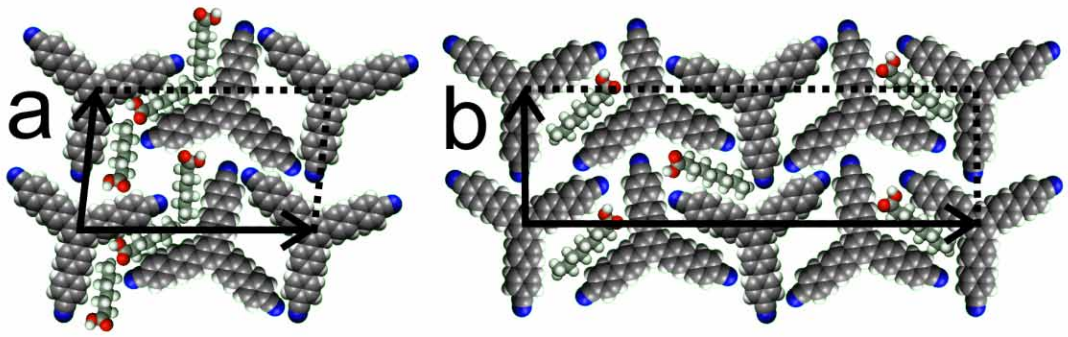

Figure 8.4: Tentative models for coadsorption of fatty acid solvent molecules in a hypothetical all-trans conformation. (a) Three heptanoic acid molecules per unit cell in the γ-phase. (b) Three nonanoic acid molecules per unit cell in the δ-phase. MM geometry-optimized molecular structures were used for solvents (carbon, gray; hydrogen, white; nitrogen, blue; oxygen, red). Unit cells are indicated by arrows and dashed lines.

of melamine structures in fatty acids, 12 solvent molecules bind radially to melamine hexamers by hydrogen bonds in an all-trans conformation, and the length of their alkane tails determines the lattice parameter.[158] Both the γ- and δ-phases provide enough void space for planarly adsorbed solvent molecules in the inter-row gaps, as illustrated in Figure 8.4a, where the uncovered area of the γ-phase can be filled with up to three heptanoic acid molecules per unit cell. An analogous tentative model for nonanoic acid coadsorption in the δ-phase is displayed in Figure 8.4b, where up to three nonanoic acid molecules can be coadsorbed in each unit cell. In the STM data, the solvent molecules cannot be clearly resolved, in accord with other studies.[6,31,88,159–165] Thus, no conclusions can be drawn on the precise adsorption geometry or conformation of the solvent molecules. Nevertheless, the tentative models clearly demonstrate that both metastable phases provide enough void space for solvent. On the other hand, the dense packing of the ε-phase does not facilitate solvent coadsorption, suggesting that it is a pure BCNB monolayer without any solvent contribution.

Solvation properties governed by the strength of interactions between solvents and solutes are discussed to be significant parameters for monolayer structure selection.[33,163,164] In solution, BCNB molecules are solvated by fatty acid molecules with the strongest solvent-solute interaction arising from hydrogen bonding between carboxylic acid and nitrile groups. The similar observations realized with the nonprotic solvent 1-phenyloctane suggest that the type of solute-solvent interaction is not decisive. We propose that upon adsorption on graphite BCNB molecules only partially desolvate, so that the solvent molecules in the remaining solvation shell become likewise adsorbed on the surface. In this mixed solvent-solute adsorbate, the solvation shell prevents direct contact between adjacent BCNB molecules, thus giving rise to metastable polymers with the observed gaps between molecular rows. In the UHV experiments, that is, in the absence of solvent molecules, no solvation shell impedes close contact, and the thermodynamically more favorable ε-phase self-assembles directly.

Obviously, thermal energy at room temperature is not sufficient for a full desolvation of the adsorbed BCNB molecules, while higher temperatures initiate this irreversible entropy-driven process. Accordingly, the origin of this activation barrier is the favorable interaction of coadsorbed solvent molecules with both the graphite substrate and the stably adsorbed BCNB molecules. Once the solvent molecules have desorbed, the molecule-molecule interaction is increased by decreasing the mutual distance and thereby closing the inter-row gaps. A similar mechanism was proposed for coronene derivatives on Au(111), where solvent desorption already sets in at 25 °C.[152] The proposed straightforward mechanism for this desolvation-induced displacive phase transition is supported by the striking analogies between all polymorphs. Both the a lattice parameters and the orientation of the BCNB superstructures with respect to graphite are similar for all structures within experimental error. In addition, the relative orientations of adjacent molecules – equal along $\vec{a}$ and alternating along $\vec{b}$ – are a common feature of all polymorphs. Consequently, the phase transition requires neither substantial structural changes as for instance the reorientation of molecules nor desorption or diffusion of BCNB molecules but is consistent with the model proposed above, where just the intermolecular gaps are closed by a comparatively small displacement of the molecules after complete desolvation.

The UHV experiments on graphite reveal remarkable differences to BCNB self-assembly on Ag(111) and Cu(111). On both metal surfaces, a trigonal, densely packed polymorph termed α-phase with one molecule per unit cell and almost similar lattice parameters of 1.80 and 1.77 nm was observed.[26] This structure appears ideal since its higher symmetry reflects the BCNB symmetry, and also, its packing density of 0.36 molecules/nm^2 is probably the highest achievable with planar adsorption. Accordingly, the different topology and the lower packing density of the ε-phase on graphite (0.32 molecules/nm^2) hints toward a substrate registry effect that would rather be expected for strongly interacting metal surfaces than for weakly interacting graphite.

8.4 Conclusion

At first sight, self-assembly of interfacial BCNB monolayers appears to be a further ordinary case of solvent-induced polymorphism. Despite its abundance, the origins of this phenomenon are in most cases not even qualitatively understood. On a fundamental level, it is often not clear whether different solvents affect the thermodynamical equilibrium or kinetically trap the system in a metastable state. By means of straightforward tempering experiments, we demonstrate that in the case of BCNB monolayers none of the initially self-assembled polymorphs corresponds to a fully thermodynamically controlled situation. For all different solvents, irreversible phase transitions lead to the same final monolayer, strongly suggesting that this is the thermodynamically most favorable polymorph. The two observed metastable polymorphs are less densely packed than the final structure due to small gaps between otherwise compact rows of monomers, dimers, or trimers. In principle, two possible reasons are conceivable for these in terms of molecule-molecule interactions' unfavorable gaps, either a substrate registry effect or solvent coadsorption. A clear distinction based on the STM data is not possible because the coadsorbed solvent

molecules cannot be discerned. In order to nevertheless resolve this question, the studies at the liquid-solid interface were complemented by experiments in a solvent-free ultrahigh vacuum environment, where the same structure was found as after tempering the initial structures. From this, we conclude that self-assembly of the less densely packed polymorphs is not caused by substrate registry effects but by solvent coadsorption, even though clear signatures of solvent molecules were not identified in the STM data. Solvent coadsorption is attributed to incomplete desolvation when the BCNB molecules are adsorbed on graphite. Thus partially solvated BCNB molecules adsorb on the surface, preventing direct molecule-molecule contact. The energetic barrier for the desorption of solvent molecules (i.e., full desolvation of the adsorbed BCNB molecules) cannot be overcome at room temperature, thus kinetically trapping metastable monolayer polymorphs.

On the basis of the present study, we conclude that even for highly dynamic self-assembly at the liquid-solid interface, the observed polymorph is not necessarily the thermodynamically most favorable structure. In particular, for less densely packed phases that are not obviously driven by the optimization of intermolecular bonding, simple *ex situ* tempering is an appropriate measure to reveal metastability of monolayer polymorphs. An important step toward a fundamental understanding of self-assembly of surface-supported structures from liquids is to recognize and understand solvent effects. Here, we demonstrate that studying the same system in a solvent-free environment (i.e., under UHV conditions) is a powerful combination.

8.5 Materials and Methods

Synthesis details as well as the density functional theory optimized geometry of isolated BCNB (chemical abstract name: [1,1':4',1":3",1"':4"',1""-quinquephenyl]-4,4""-dicarbonitrile, 5"-(4'-cyano[1,1'-biphenyl]-4-yl)-) are reported elsewhere.[26] Molecular mechanics (MM) simulations were utilized for geometry optimization of fatty acid solvent molecules (Dreiding force field). BCNB monolayers were prepared on highly oriented pyrolytic graphite (HOPG, grade ZYB, Optigraph GmbH, Germany) both at the liquid-solid and the vacuum-solid interface and characterized by scanning tunneling microscopy (STM). All given tunneling voltages refer to the sample. STM topographs were drift corrected and processed by a mean value filter. STM experiments at the liquid-graphite interface were carried out with a home-built microscope operated by an ASC 500 control electronics (attocube Systems AG, Germany). Split images displaying both the adsorbate and graphite lattice within one frame were used for a precise determination of superstructure matrices.[101] Saturated solutions were prepared by mixing an excess of BCNB with 1 mL of the respective solvent (pentanoic acid, purity $\geq$ 99%; heptanoic acid, $\geq$ 97%; octanoic acid, $\geq$ 98%; nonanoic acid, $\geq$ 97%; 1-phenyloctane, $\geq$ 98%; all from Sigma-Aldrich), sonicating for 10 min, and subsequent centrifugation for 5 min. Samples were prepared by pipetting 5 µL of solution onto freshly cleaved HOPG. STM images were acquired with a mechanically cut Pt/Ir (90/10) tip immersed into the liquid. Samples were tempered at 70 °C either *in situ* with a home-built, resistively heated sample holder or *ex situ* in a preheated oven. During *in situ* heating, the temperature was measured at the bottom of the HOPG crystal with a thermocouple and controlled by a temperature controller (Eurotherm 2416, Invensys Inc., USA). STM images were

acquired at elevated temperatures after thermal equilibration of the STM. *Ex situ* tempered samples were investigated after cooling. For both heating methods, the liquid phase was still present after tempering.

STM experiments at the vacuum-graphite interface were performed with a home-built beetle-type STM operated by an SPM-100 control electronics (RHK Technology Inc., USA). STM topographs were acquired with electrochemically etched tungsten tips at room temperature at a base pressure below 3×10^{-10} mbar. The HOPG crystal was prepared by electron-beam annealing at 600 °C for several hours. Thoroughly outgassed BCNB was deposited from a home-built Knudsen cell at a crucible temperature of 340 °C.[65] A relatively slow monolayer deposition over 90 min promotes self-assembly of the thermodynamically most stable structure.

8.6 Acknowledgment

We gratefully acknowledge financial support by the Nanosystems Initiative Munich (NIM) and the Fonds der Chemischen Industrie (FCI) (T.S.), as well as the Chinese Scholarship Council (W.S.), the Hanns-Seidel-Stiftung (G.E.), and the Alexander von Humboldt Stiftung (S.N.). We are indebted to Dr. Kingsuk Mahata for initial synthetic work.

8.7 Supporting Information

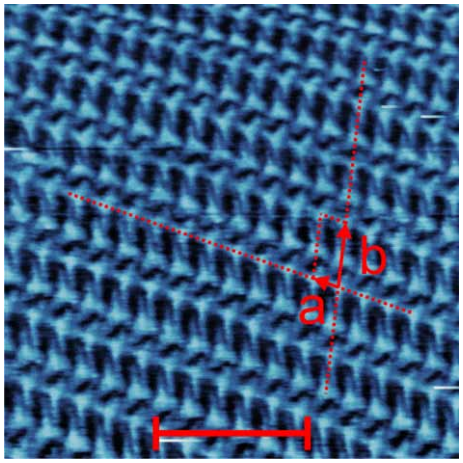

Figure 8.5: STM imaging during *in situ* heating: STM topograph of a BCNB monolayer at the 9A-graphite interface. This image was acquired at a sample temperature of ∼70 °C. The image has not been drift corrected, but the uniform intermolecular spacing along the direction is a clear indication for the ε-phase. Tunneling parameters: −1.5 V, 50 pA; the scale bar corresponds to 10 nm.

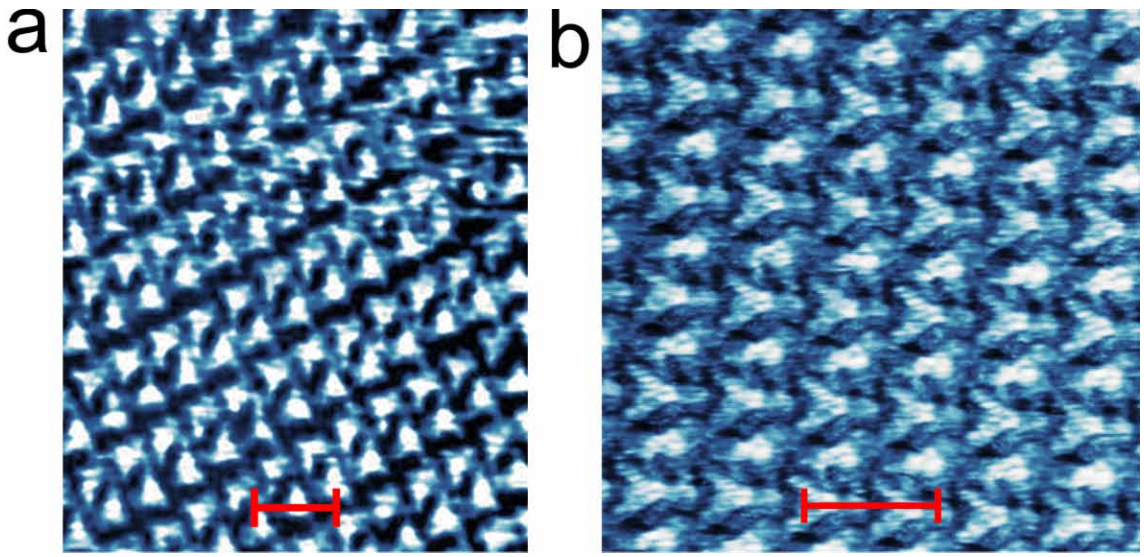

Figure 8.6: BCNB monolayers at the phenyloctane-graphite interface: STM topographs of BCNB monolayers at the 1-phenyloctane-graphite interface: (a) before and (b) after *ex situ* heating the sample at ∼70 °C for 10 min. Before tempering rows of dimers separated by small gaps can clearly be recognized that indicate the γ-phase, whereas after tempering the ε-phase with uniform intermolecular spacing emerges. In addition to the similar topology and appearance, the lattice parameters of both γ-phase and ε-phase in 1-phenyloctane are equal to those obtained in fatty acid solvents. Tunneling parameters: (a) 0.9 V, 30 pA; (b) 1.0 V, 29 pA; scale bars correspond to (a) 4.0 nm and (b) 3.0 nm.

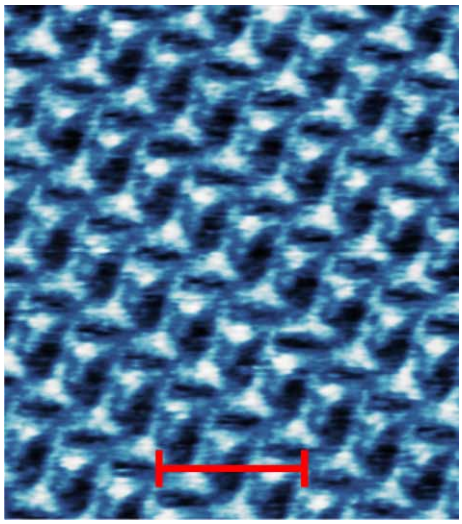

Figure 8.7: Experiments with ultralow cooling rate: STM topograph of a BCNB monolayer at the heptanoic acid-graphite interface. In order to substantiate the irreversibility of the phase transition from γ-phase to ε-phase, the sample was immersed into solution, first heated to 70 °C and then cooled down to room temperature over a timespan of 135 hours, corresponding to an ultraslow cooling rate of $\sim 8.6 \times 10^{-3}$ °Cmin^{-1}. The sample was then *ex situ* characterized by STM. The ε-phase prevailed and no back conversion was observed and. Tunneling parameters: − 0.90 V, 30 pA; the scale bar corresponds to 5.0 nm.

Chapter 9

Adsorption Structure Determination of a Large Polyaromatic Trithiolate on Cu(111): Combination of LEED-I(V) and DFT-vdW

Thomas Sirtl,[ab] Jelena Jelic,[c] Jörg Meyer,[c] Kalpataru Das,[d] Wolfgang M. Heckl,[abe] Wolfgang Moritz,[f] John Rundgren,[g] Michael Schmittel,[d] Karsten Reuter,[c] and Markus Lackinger.[abeh] Reprinted from *Physical Chemistry Chemical Physics* 15, 11054-11060, **2013** - Reproduced by permission of the PCCP owner societies.

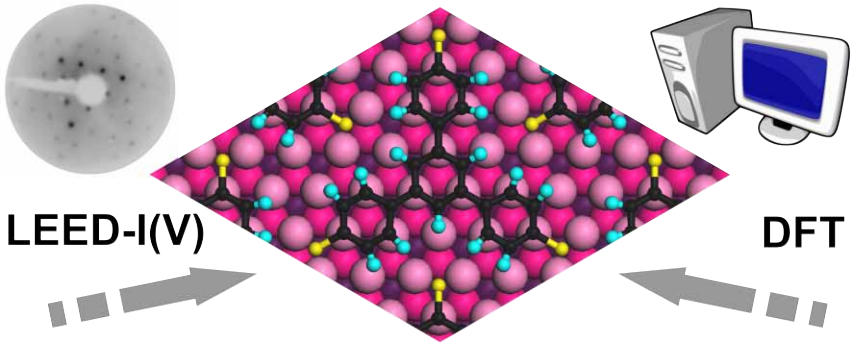

[a] Department of Physics, Technische Universität München, James-Franck-Str. 1, 85748 Garching, Germany
[b] Center for NanoScience (CeNS), Schellingstr. 4, 80799 Munich, Germany
[c] Department of Chemistry, Technische Universität München, Lichtenbergstr. 4, 85747 Garching, Germany
[d] Center of Micro- and Nanochemistry and Engineering, Organische Chemie I, Universität Siegen, Adolf-Reichwein-Str. 2, 57068 Siegen, Germany
[e] Deutsches Museum, Museumsinsel 1, 80538 Munich, Germany
[f] Department of Earth and Environmental Sciences, Ludwig-Maximilians-University, Theresienstr. 41, 80333 Munich, Germany
[g] Department of Theoretical Physics, KTH Royal Institute of Technology, SE-106 91 Stockholm, Sweden
[h] Corresponding author; e-mail: markus@lackinger.org; web: www.2d-materials.com

9.1 Abstract

The adsorption geometry of 1,3,5-tris(4-mercaptophenyl)benzene (TMB) on Cu(111) is determined with high precision using two independent methods, experimentally by quantitative low energy electron diffraction (LEED-I(V)) and theoretically by dispersion corrected density functional theory (DFT-vdW). Structural refinement using both methods consistently results in similar adsorption sites and geometries. Thereby a level of confidence is reached that allows deduction of subtle structural details such as molecular deformations or relaxations of copper substrate atoms.

9.2 Introduction

The atomically precise structure determination of large functional organic adsorbates on surfaces is a challenging task in surface science. Abundantly used scanning tunneling microscopy (STM) yields unit cell parameters for molecular superstructures with a typical accuracy of 5 %. Normally it is also possible to deduce the azimuthal orientation of larger adsorbates with respect to the surface. However, already the determination of adsorption sites can become intricate.[38] Under favourable circumstances estimation of adsorption heights and molecular deformations may be feasible by STM,[166] however a precise quantification remains impossible with this technique. Such details are important for a fundamental understanding of the interactions and properties of adsorbed molecules though. For instance deformations can affect the aromaticity of conjugated molecules and also change electronic properties that are decisive for applications.[56]

A corresponding, more quantitative determination of the internal adsorption geometry has been to date the realm of diffraction methods. Vertical adsorption distances are accessible by X-ray standing wave (XSW) experiments.[167,168] However, besides the lack of lateral resolution, a further drawback of XSW is that for a specific element in comparable chemical surrounding only averaged height data can be obtained. This restriction does not apply to quantitative low energy electron diffraction, LEED-I(V), which is furthermore an experimentally much less elaborate technique.[169] Here the intensities of unique reflections in a LEED experiment are recorded as a function of electron energy. A prerequisite for this diffraction technique is the availability of long-range ordered monolayers, and owing to the elaborate nature of the scattering simulations application of the technique was hitherto restricted to smaller, conformationally rigid adsorbates like dinitrogen,[170] carbon monoxide,[5] formic acid,[171] cyanide,[172] glycine,[173] thiouracil,[81] benzyne,[174] or benzene.[175–180] LEED-I(V) analyses of larger adsorbates to date have been rare, examples being studies on graphene[181] and C_{60} fullerenes.[182]

Recent advances in computer power and simulation software greatly alleviate this restriction to smaller adsorbates, and thus offer the prospect of atomically precise surface structure determination also of technologically most relevant larger functional molecules. In the present study we illustrate this with LEED-I(V) calculations that were performed with an update of the LEEDFIT code,[75–77] which was parallelised and allowed interatomic distances as constraints in the least squares optimisation. A further improvement was the introduction of dynamic phase shift calculations

(LEED-PS), where during the structure refinement the changes in phase shifts due to changes in structural parameters and bond lengths are considered by self-consistent recalculation.

On the theoretical side this development finds its counterpart in the advent of numerically most efficient dispersion-correction approaches to density-functional theory (DFT-vdW).[139,183,184] At essentially zero additional computational cost, these approaches augment the predictive capability of prevalent semi-local DFT functionals with an account of van der Waals interactions, which are known to play a decisive role in determining the structure and stability of organic molecules on solid surfaces.[139,183–191]

With the present study we demonstrate how the increased performance of both LEED and DFT simulations provides access to surface structural data of complex molecules at sub-atomic precision by studying 1,3,5-tris(4-mercaptophenyl)-benzene (TMB) monolayers on Cu(111). Thiol-functionalized molecules are promising candidates for linkers in molecular electronics and their interaction with metal surfaces is of great interest.[192] On reactive surfaces at room temperature, monothiols deprotonate into thiolates, and on Cu(111) the sulfur head group binds covalently at threefold hollow sites.[193] To date the exact adsorption site of TMB has not been unambiguously identified despite its obvious relevance for the formation of metal-organic coordination networks,[22] i.e. it is not clear how the preference for a specific bonding site of the sulfur head groups is matched with the given geometric arrangement of the three thiolate groups in TMB.

9.3 Experimental Section

Sample preparation was carried out under ultra-high vacuum by thermal sublimation of TMB onto Cu(111) held at room temperature. Synthesis details of TMB were published elsewhere.[24] LEED experiments were conducted at a sample temperature of 50 K (cf. section 9.7). The LEED-I(V) analysis includes 22 unique reflections at normal incidence with electron energies between 11 eV and 200 eV, resulting in a cumulative energy range of 2766 eV. The I(V)-curves were averaged over symmetrically equivalent reflections. The degradation of the reflection intensity during data acquisition due to radiation damage was below 20 %. It is noteworthy that the experimentally used electron beam current is a compromise between a sufficiently high signal to noise ratio and low radiation damage.

Phase shifts were derived from a crystal potential obtained by superposition of atomic charge densities. The energy dependent self-energy of the scattered electron was used in the optimisation of non-overlapping muffin-tin radii for the atoms of the crystal while minimizing the potential step between the muffin-tin spheres.[194,195] The same method has been previously applied for oxide surfaces.[196,197] The optimisation of muffin-tin radii results in a different radius for every combination of atom, crystal, and scattering energy. The phase shifts were therefore iteratively recalculated in the final structure refinement step. The influence of the different methods of phase shift calculation on the structural results will be discussed in a separate paper.

In the final refinement iterations anisotropic atomic displacement parameters were used for the adsorbed molecule.[198] The results show an enhanced rms-amplitude of 0.2 - 0.3 Å compared to 0.05 Å of the substrate atoms, which may be caused by thermal vibration and static displacement due to desorbed hydrogen or other defects. The displacement parameters exhibit large error bars and are not discussed in detail here, because no temperature dependent measurements have been made.

9.4 Results and Discussions

Previous STM and LEED experiments of TMB on Cu(111) with a similar sample preparation procedure yielded a $\left(3\sqrt{3} \times 3\sqrt{3}\right)$ R30° superstructure with a lattice parameter of 13.3 Å and 27 copper atoms per unit cell in the first layer.[24] From the STM data a fairly large domain size and a low defect density were inferred, rendering the system ideal for surface diffraction studies. The structure exhibits p31m symmetry with one molecule per unit cell and TMB appeared with threefold symmetric submolecular STM contrast. Hence, the likewise threefold symmetric TMB is centred on a threefold symmetric adsorption site, i.e. either fcc or hcp threefold hollow sites or on top. This assumption is also consistent with the observed LEED pattern.

Considering the given $p31m$ symmetry, the asymmetric unit comprises 10 atoms in the adlayer (Figure 9.1 c). Six distinct adsorption geometries, where the TMB lobes are aligned with a mirror line, are consistent with the above stated symmetry requirements. All adsorption geometries are listed in Table 9.1. Interestingly, the TMB molecule is almost commensurate with the Cu(111) lattice in two respects. In the given azimuthal orientation all four phenyl rings as well as all three peripheral thiolate head groups can simultaneously occupy equivalent adsorption sites without imposing large stress on the molecule.

For both LEED structure refinement and DFT calculations all six adsorption geometries of Table 9.1 were considered. LEED structure refinement was carried out in the asymmetric unit, i.e. applying symmetry constraints, while the DFT calculations were conducted without any symmetry constraints. LEED structure refinement was realized in a two-step process. For an initial evaluation of all six structures, constraints

Table 9.1: LEED-I(V) and DFT results for the six symmetry-allowed adsorption geometries of TMB on Cu(111)

TMB adsorption site			LEED-I(V)	DFT	DFT-vdW[a]
#	Sulfur	Phenyl	R_P	ΔE/eV	ΔE/eV
1	On top	fcc	0.74[b]	+1.11	+1.05
2	On top	hcp	0.73[b]	—[d]	—[d]
3	fcc	On top	0.60[b]	—[d]	—[d]
4	fcc	hcp	0.53[b] (0.32)[c]	0	0
5	hcp	On top	0.81[b]	—[d]	—[d]
6	hcp	fcc	0.75[b]	+0.55	+1.40

[a] Using a dispersion correction scheme developed by Tkatchenko and Scheffler.[139] [b] Copper atoms fixed. [c] More elaborate refinement of the best-fit model. [d] Not optimised until full convergence was achieved.

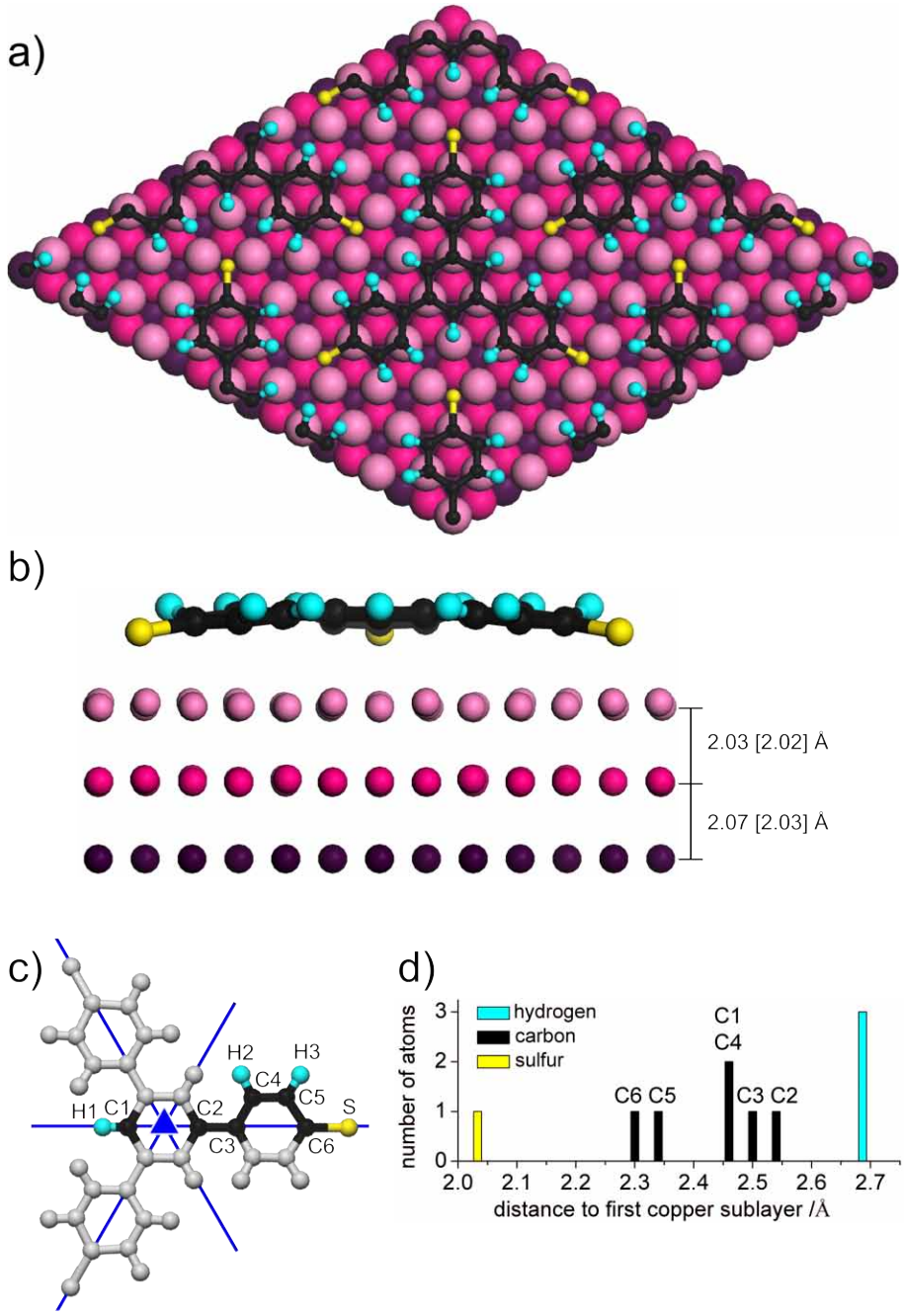

Figure 9.1: Optimised structure of TMB on Cu(111). (a) Top-view of 2×2 unit cells. (b) Side-view of one molecule and three copper layers. Mean distances are depicted for the first three copper layers (the values in parentheses refer to DFT). (c) Asymmetric unit of TMB (colored). All other atom coordinates (grey) are generated by the symmetry operations of C_3v (blue lines, mirror planes; blue triangle, three-fold symmetry axis). (d) Vertical atom distances in the asymmetric unit of TMB, referring to the mean height of the first copper sublayer (LEED-I(V) derived values, for DFT values cf. Table 9.4 and Figure 9.5).

for intramolecular distances of TMB were applied (cf. Table 9.2), and three substrate layers were considered. Layer distances, vertical and lateral atom coordinates of TMB were first optimised consecutively, and simultaneously in the final step. Pendry's R-factor (R_P) is used to evaluate the agreement between experimental and theoretical I(V) curves.[82] This first step resulted in the unambiguous identification of the actual adsorption site. After identifying the correct model, a more elaborate refinement was performed. To this end, firstly, vertical distances between TMB and three copper sublayers were optimised. Secondly, all atom coordinates of TMB, subsequently of first and second layer copper atoms, were optimised. Since Cu(111) is well known to feature a free adatom gas,[24] with many examples for interference with self-assembly of organic structures,[87] two conceivable structures with copper adatoms were considered in addition to those listed in Table 9.1. Firstly, a structure where each thiolate group binds to clusters of three adatoms was tested, however the best R_P achieved was 0.9 (cf. Figure 9.7 a). Secondly, a structure was tested, where interstitial copper adatoms are adsorbed in the gaps between TMB molecules (cf. Figure 9.7 b). An occupation of 100 % led to an R_P value of 0.6, whereby optimisation of the occupation factor together with a full structure refinement of all other parameters led to a local minimum with $R_P = 0.42$ at an occupancy of 30 % and only marginal modification of the molecule geometry. Ultimately, all adatom containing structures were discarded, because the corresponding R_P values are significantly larger than that of the best fit model without copper adatoms (vide infra).

Among the six competing structural models without adatoms (cf. Table 9.1), structure 4 is unambiguously preferred, in which the three thiolate groups bind to fcc threefold hollow sites and the four phenyl rings reside on hcp threefold hollow sites. Adsorption of phenyl rings on threefold hollow sites is common and was also reported for benzene on Co(0001),[176] Ni(111),[177] and Ru(0001).[179,180] As evident from the model presented in Figure 9.1 a, with the given azimuthal orientation of TMB every other carbon atom resides on top of copper. In the LEED results this preference for structure 4 is primarily expressed by the lowest resulting R_P value of 0.32 (cf. Table 9.1). Furthermore, only optimisation of structure 4 yielded physically reasonable results. Although the alternative structural model 3 exhibited initially a comparable R_P value, the corresponding LEED optimised geometry showed unreasonable distortions of the molecule (cf. Figure 9.4).

Experimental and calculated I(V)-curves of fully optimised model 4 are in good agreement (Figure 9.2), as indicated by an overall R_P of 0.32. We note here that the remaining misfit between the measured and calculated I(V) curves may be partially explained by inadequacy of the muffin-tin approximation used in the multiple scattering formalism. R_P dropped from 0.35 to 0.32 when using the dynamic phase shift adaptation algorithm while the atom positions remained within the error limits of 0.10 - 0.15 Å. Also if the two weakest beams - exhibiting a relatively low signal to noise ratio - are excluded, the R_P value can be further improved to 0.28 without any significant changes in the structure. Nevertheless, the structure discussed in the following is derived from all experimental I(V) curves.

It is commonly agreed that R_P values below 0.2 indicate an excellent agreement between experimental and theoretical I(V) curves, whereas values above 0.3 are interpreted as mediocre fits. Excellent refinements yielding very low R_P values in the range 0.11 - 0.24 were reported for complex inorganic surface structures

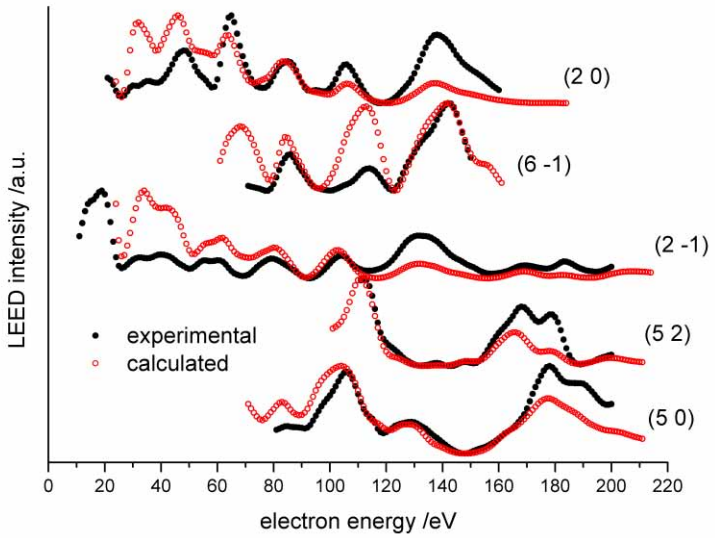

Figure 9.2: Selected experimental and theoretical LEED-I(V) curves for the best-fit model 4 (vertically offset for clarity). Reflection indices are given in brackets. The complete dataset is provided in Figure 9.3.

such as CoO(111),[199] GaN(0001),[200] and $BaFe_2As_2$(001)[201] as well as surface alloys or metal superstructures on metals like Pb/Ni(111),[202] Sn/Ni(110),[203] Sn/Ni(111),[204] Sb/Cu(110),[205] and Au/Pd(100).[206] Moreover, relatively simple atomic superstructures could also be refined with high accuracy, examples comprise hydrogen on Ir(110),[207] (R_P = 0.10) and halogens on metal surfaces such as Cl/Ru(0001)[208] and Br/Pt(110)[209] with R_P = 0.19 and 0.23, respectively. LEED structure refinement was also successfully carried out for sulphide or oxide adlayers like O/V(110),[210] MnO/Ag(100),[211] S/Ir(100),[212] O/Pt/Cu(100),[213] V_2O_3/Pd(111),[214] S/Au(110),[215] O/Cu(210),[216] resulting in R_P of 0.11 - 0.36. Excellent R_P values of around 0.15 - 0.22 were also obtained for smaller organic adsorbates such as dinitrogen/NaCl(100),[170] carbon monoxide/Pt(110),[5] formic acid/TiO_2(110),[171] cyanide/Ni(110),[172] and glycine/Cu(110).[173]

In this respect, R_P values of 0.27 and 0.29 for thiouracil/Ag(111)[81] and benzyne/Ir(100)[174] seem to indicate a less perfect agreement, but are the state of the art for medium-sized molecules on metal surfaces. Even for a comparatively small and rigid molecule like benzene on Co(0001),[176] Ni(111),[177] Co($10\bar{1}0$),[178] and Ru(0001)[179,180] relatively large R_P values of 0.26 - 0.37 were reported. In the literature R_P values of up to 0.40 are thus still considered as reasonable fits for larger adsorbate molecules. In particular for organic superstructures with large unit cells such as graphene[181] or molecules with many atoms such as C_{60} fullerenes on Ag(111)[182] R_P values of 0.29 and 0.36 were obtained. Several reasons may contribute to such typically higher R_P values for organic adlayers. On the theoretical side, we demonstrate for the present system that dynamic adaptation of the phase shifts already leads to a significant improvement of R_P from 0.35 to 0.32. Further-

more, for complex structures with large unit cells the commonly made assumptions, i.e. the muffin-tin approximation, isotropic displacement factors, and the neglect of correlations in the displacement factors, might be oversimplifications. In addition, on the experimental side, several reasons might account for lower R_P values. Organic adlayers are much more prone to radiation damage. In addition, low signal to noise ratios of weak reflections also lead to higher R_P values as shown here, where exclusion of the two weakest beams further improves R_P from 0.32 to 0.28. Moreover, structural defects in the adlayer as grain boundaries further infer the quality of the experimental data set. In LEED-I(V) analyses in general not the same level of agreement can be reached as it is the standard in kinematic refinements for example in X-ray diffraction. As mentioned before, this results from several approximations used in the multiple scattering theory, namely the phenomenological description of inelastic processes by an optical potential, the neglect of correlations in the atomic displacement parameters, and the muffin tin model for single atom scattering. Also defects play a more significant role for surfaces than for bulk samples. Therefore mainly the peak positions are compared in the I(V) curves and an R-factor of $R_P = 0.32$ is fully acceptable for structure optimisation of a large adsorbate.

The six considered adsorption geometries were also optimised in DFT calculations, using the semi-local Perdew-Burke-Ernzerhof functional.[137,138] In order to evaluate the significance of van der Waals contributions in a structure that is dominated by covalent anchoring of the thiolate groups, the calculations were conducted with and without dispersion correction.[139,190] Only three out of the initial six structures were refined until full convergence was achieved. The other three alternative structures were discarded at an earlier stage of the calculation, when the last geometry optimisation steps only led to minor energetic improvements and it became clear that these structures cannot energetically compete anymore with the three more favourable structures (cf. section 9.7). The resulting energy differences of these three remaining fully optimised structures are listed in Table 9.1. In perfect agreement with the LEED results, structure 4, where the phenyl rings are centred at hcp sites and sulphur binds to fcc sites, yields the lowest energy, both in the calculations with and without dispersion-correction. We take this as an indication for the reliability of the obtained energetic ordering, even though absolute binding energies of prevalent dispersion-corrected DFT approaches are known to be severely impaired at metal surfaces by electronic screening effects.[191]

Intriguingly, the agreement of both independent techniques is not only restricted to the adsorption site (sulfur: fcc, phenyl: hcp), but also extends to most intricate structural details of the adsorption geometry. In the model depicted in Figure 9.1 the optimised LEED and DFT structures cannot be distinguished by the naked eye. LEED derived vertical distances for each atom of the asymmetric unit of TMB are summarised in Figure 9.1 d. In addition to the deprotonation, TMB undergoes obvious structural changes upon adsorption. In the gas phase TMB is propeller-shaped due to steric hindrance between the σ-bonded phenyl rings, whereas in the adsorbed state this tilt is not present anymore. It is noteworthy that for a structure simulation within the plane space group $p31m$, the chiral character of the propeller shape cannot be retained. However, a LEED structure refinement without any symmetry constraints likewise results in untwisted phenyl rings, in accordance with the DFT results.

In the following discussion of structural details quoted bond lengths and interatomic distances always refer to the LEED optimised structure, while DFT derived values are given in parentheses. Besides the removal of the propeller shape, a further prominent intra-molecular deformation in TMB is caused by the short sulfur-copper distance, indicating covalent bonds to the copper substrate. Sulfur is located above fcc hollow sites, but in a slightly asymmetric position closer to a twofold bridge site with a similar distance to the two closer Cu atoms. The S-Cu distances amount to 2.64 [2.63] Å and 2.36 [2.37] Å, respectively. At least, the lower bond lengths are in good agreement with covalent S-Cu distances in CuS (2.19 - 2.38 Å)[217] and Cu2S (2.18 - 2.90 Å).[218] The copper atoms of the first layer adjacent to sulfur are lifted by 0.10 [0.07] Å with respect to the mean height of copper in the first layer (cf. Table 9.5). These substrate relaxations can be seen as a consequence of covalent bond formation, as similarly found for tetracyanoquinodimethane (TCNQ) on Cu(100).[219]

Also the organic backbone exhibits further slight deformations. The height of the carbon atom C6 (cf. Figure 9.1 for numbering) is lower as a consequence of the downward bending of the sulfur atoms. This may result in a degradation of aromaticity, as induced by bond elongation and alternation,[220] as well as out-of-plane deformation,[221] with concomitant consequences for bonding properties in metal-organic networks. Both the central and peripheral phenyl rings are slightly distorted, as compared to the C-C bond length of 1.40 Å in benzene.[222] The outer phenyl rings exhibit deviating nearest neighbour C-C distances in the range of 1.39 - 1.49 [1.41 - 1.43] Å. The hydrogen atoms in TMB are bent up with respect to the mean height of the carbon atoms, as also reported for benzene on Co(0001).[176] The next nearest neighbour C-C distance in the inner phenyl ring of TMB of 1.43 [1.42] Å is slightly elongated with respect to the gas phase [1.40 Å] (cf. Table 9.3). This can be explained by stretching of TMB in order to simultaneously optimise all S-Cu bonds. This stretching is also noticeable in the C6-S distance. The value of the adsorbed molecule of 1.76 [1.79] Å is larger than in the gas phase [1.73 Å] (cf. Table 9.3). Hence, stretching of the C6-S bond can be understood as a compromise between an optimal S-Cu bond length, without the necessity to reduce the distance between the aromatic system and the copper surface below its equilibrium value. The overall dimension of adsorbed TMB is slightly expanded, as indicated by intramolecular S-S or C1-S distances of 13.09 [13.02] Å or 9.03 [8.98] Å, compared to 13.00 Å or 8.91 Å for the optimised trithiolate in the gas phase, respectively (cf. Table 9.3).

Intermolecular S$\cdots$H1 and S$\cdots$H2 distances of 3.23 [3.32] Å and 2.85 [2.91] Å are comparatively large, thus intermolecular hydrogen bonds do not appear as an important contribution to the stabilisation of the structure.[223]

It is also very instructive to compare optimised DFT structures obtained with and without dispersion correction. Including van der Waals interactions results in a significantly lower distance between the phenyl rings and the copper surface, i.e. the mean height of carbon decreases from 2.76 Å to 2.35 Å. This diminished adsorption height is in better agreement with the LEED result of 2.43 Å. Yet, neglecting the screening of van der Waals interactions through the free electrons of the metal support leads to overbinding as compared to the experimental results. Nevertheless,

the present results suggest that conventional dispersion corrected DFT-vdW yields more accurate results even on metal surfaces.

9.5 Conclusions

We presented a combined experimental and theoretical structure refinement of the large trithiolate TMB on Cu(111). Out of six initially considered symmetry-allowed structures, the same model was clearly favoured by both LEED-I(V) and DFT. Both methods independently result in an adsorption geometry, where all sulfur atoms bind to fcc threefold hollow sites and all phenyl rings reside on hcp threefold hollow sites with every other carbon atom atop copper. This finally settles the question as to the preferred adsorption site of this molecule. In addition both techniques yield a wealth of further structural details. The sulfur atoms are significantly moved down in order to establish covalent bonds with copper atoms. Sulfur does not adopt a fully symmetric position in the threefold hollow site, but remains closer to a twofold bridge site. The two adjacent copper atoms are also lifted from the substrate plane. Deformations of the organic backbone affect the planarity and the carbon-carbon distances in the phenyl rings. The remarkable agreement in these structural features obtained using the two independent methods supports the conclusion that adsorption geometries of complex functional molecules can be accessed with sub-atomic precision. Besides the obvious power in the combination of the two techniques, the low experimental effort of LEED-I(V) experiments in comparison to synchrotron-based structural techniques is particularly appealing.

9.6 Acknowledgment

This work was supported by the Nanosystems-Initiative Munich (NIM) funded by the Deutsche Forschungsgemeinschaft. T.S. acknowledges financial support from the Fonds der Chemischen Industrie (FCI).

9.7 Electronic Supplementary Information

Experimental Details Low-Energy-Electron-Diffraction

Low-Energy-Electron-Diffraction (LEED) experiments were carried out under ultra-high vacuum (UHV) conditions with a base pressure below 1×10^{-10} mbar. A SPECTALEED 4-grid optics (Omicron NanoTechnology GmbH) was used in combination with an ErLEED digital electronics (SPECS Surface Nano Analysis GmbH). During LEED experiments the sample was cooled to approximately 50 K. LEED-I(V) videos were recorded with a SensiCam CCD camera (PCO AG).

The software package EE2010 (Dr. Michael F. Opheys, http://www.ee2000.de/) was used for data acquisition and extraction of I(V) curves. Structure optimization by dynamic LEED calculations was performed with the home written LEEDFIT software. [75–77]

Cu(111) single crystal surfaces were prepared by cycles of Ar^+ ion sputtering at 2 keV and subsequent e-beam annealing at 820 K for 15 min. The synthesis of TMB and monolayer deposition is described elsewhere. [24]

Calculational Details Density Functional Theory

All density functional theory (DFT) calculations were performed with the plane-wave based code CASTEP[137] using library ultrasoft pseudopotentials[140] and the generalized gradient approximation (GGA) functional due to Perdew, Burke, and Ernzerhof (PBE)[138] to treat electronic exchange and correlation. Long-range dispersive interactions were included on a semi-empirical level through the dispersion-correction scheme suggested by Tkatchenko and Scheffler.[139]

The molecule-surface system was modeled in supercell geometries, using four layer thick Cu slabs (at optimized PBE lattice constant of 3.626 Å), a vacuum region exceeding 20 Å, and a $\left(3\sqrt{3} \times 3\sqrt{3}\right)$ surface unit-cell. Full geometry optimizations of the two topmost slab layers and all molecular degrees of freedom were performed with the BFGS algorithm[139] implemented in CASTEP with a default convergence threshold on the maximum absolute ionic-force component of 0.05 eV/Å. In the initial screening of adsorption sites some of the geometry optimizations were stopped when the last geometry steps led to energetic improvements on the order of 10 meV and it became clear that the structure would be far less favorable than the best adsorption site models tested. At the employed plane-wave kinetic-energy cutoff of 450 eV and reciprocal space integration using $(2 \times 2 \times 1)$ Monkhorst-Pack grids[141] the relative energies of the different optimized structures were converged within 0.05 eV.

Gas phase molecules - the protonated trithiol and the fully deprotonated trithiolate - were also treated in supercell geometries. In order to model "isolated" molecules, a orthorhombic unit cell of $(20 \times 30 \times 20$ Å$)$ dimension with Γ-point sampling and the same plane-wave kinetic-energy cutoff of 450 eV was employed.

Constraints for LEED-I(V) Structure Optimization

Table 9.2: Constraints for intramolecular bonds in the trithiolate as used for the initial LEED-I(V) structure optimization.

atoms	distance /pm		
	minimum	maximum	optimum
C→C, next neighbor	140	170	154
C→C, next nearest neighbor	250	280	267
C→C, diagonal	280	320	308
C→S, next neighbor	160	200	181
C→S, next nearest neighbor	270	310	290
C→H, next neighbor	100	130	115
C→H, next nearest neighbor	210	250	233

Experimental vs. Calculated I(V)-Curves

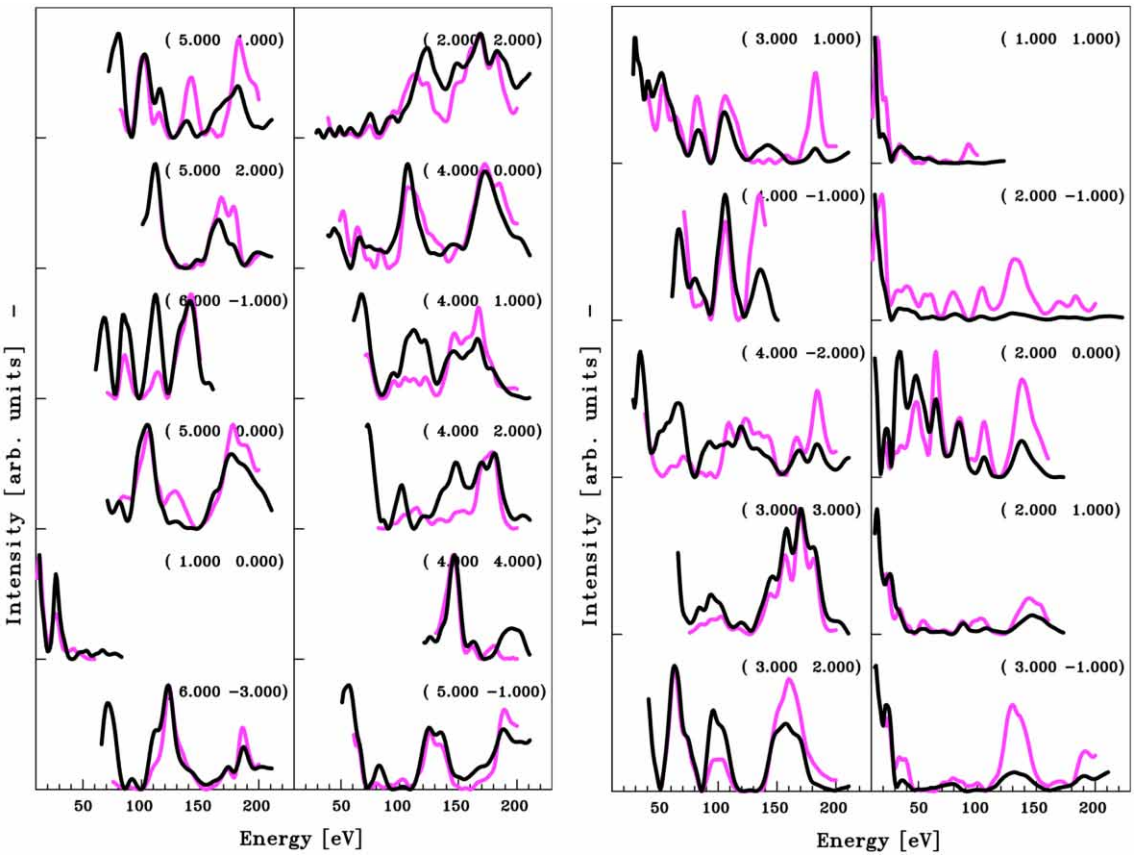

Figure 9.3: Experimental vs. calculated I(V) curves. Complete dataset of 22 independent experimental (pink) and calculated (black) LEED-I(V) curves for the best-fit model (S: fcc, phenyl: hcp), offset for clarity. Indices are given in brackets.

LEED Optimization Results for Competing Models

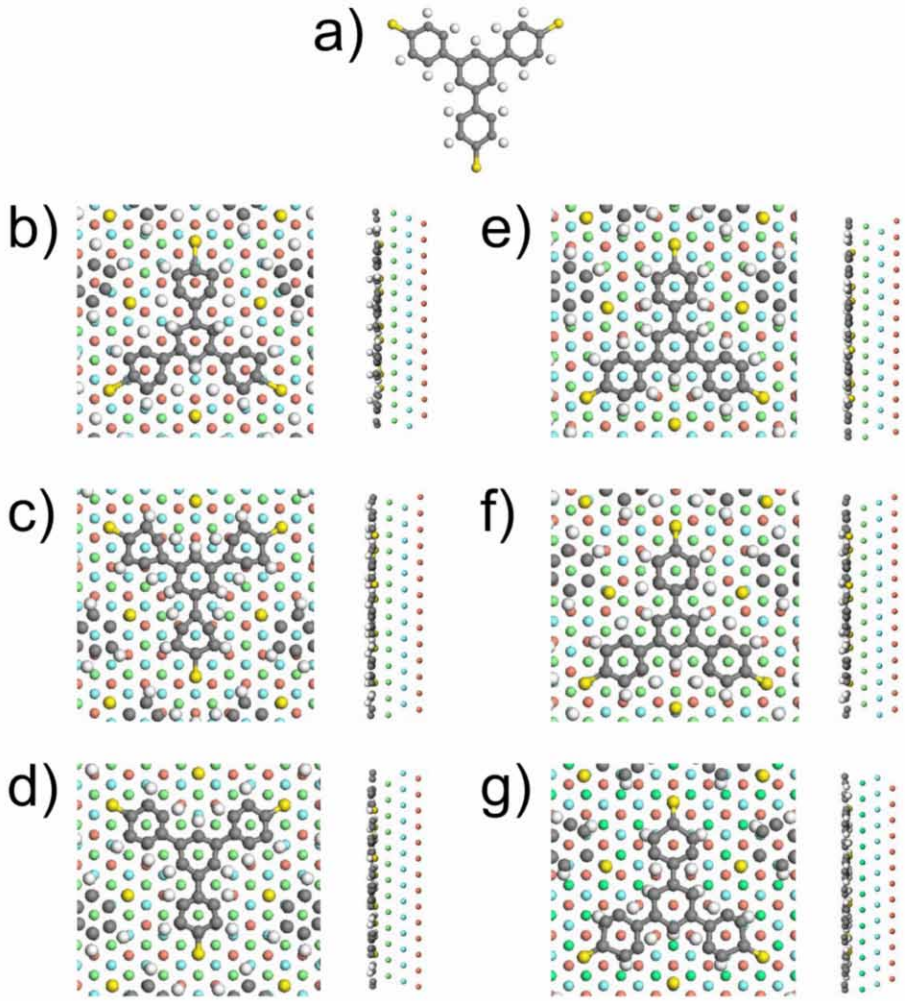

Figure 9.4: LEED optimization results for competing models. (a) Initial structure of TMB, i.e. before LEED structure optimization. (b)-(g) top- and side-view on the LEED optimized structures for all six symmetry-allowed adsorption geometries: (b) model 1, S: on top, phenyl: fcc; (c) model 2, S: on top, phenyl: hcp; (d) model 3, S: fcc, phenyl: on top; (e) model 4, S: fcc, phenyl: hcp; (f) model 5, S: hcp, phenyl: on top; (g) model 6, S: hcp, phenyl: fcc.

Intramolecular distances in TMB

Table 9.3: Intramolecular distances in TMB. Comparison of DFT optimized structures of isolated TMB and the corresponding deprotonated trithiolate in the gas phase, as well as DFT optimized structures of the adsorbed trithiolate without or with dispersion correction, and LEED-optimized structure.

atoms	distance /pm				
	DFT				LEED-I(V)
	isolated trithiol	isolated trithiolate	TMB on Cu(111) without vdW	TMB on Cu(111) with vdW	
C1-C2	140	140	141	142	143
C2-C3	148	147	148	147	150
C3-C4	141	141	142	143	149
C4-C5	138	139	141	141	139
C5-C6	142	142	141	142	143
C6-S	170	173	178	179	176
C1-H1	108	109	108	109	113
C2-H2	109	109	110	109	110
C3-H3	109	109	109	109	110
S→S	1294	1300	1298	1302	1309
C1→S	885	891	895	898	903

Adsorption Heights: DFT without and with Dispersion Correction vs. LEED

Table 9.4: Adsorption heights: Z-coordinates (in pm) of all adsorbate atoms with respect to the mean height of the upmost copper layer.

atom	DFT (without vdW)	DFT (with vdW)	LEED-I(V)
H1	303	248	270
H2	282	259	269
H3	247	237	269
C1	304	242	246
C2	304	243	254
C3	291	240	251
C4	276	238	246
C5	250	228	232
C6	233	217	228
S	198	200	201
mean all C-atoms	276	235	243
mean all atoms	269	235	247

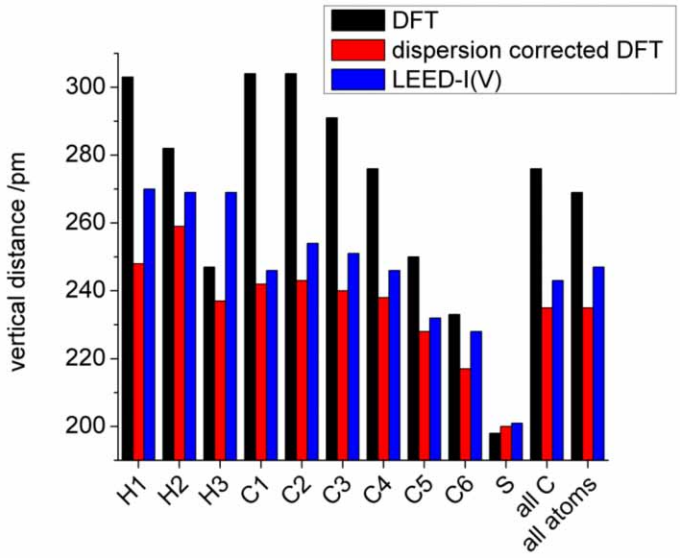

Figure 9.5: Visualization of the Z-Coordinates of Table 9.4.

Z-Coordinates of Selected Copper Atoms

Table 9.5: Z-coordinates for selected copper atoms. LEED-I(V) and dispersion corrected DFT derived distances of selected sublayer copper atoms with respect to the mean height of the respective layer in pm. For copper atom labels cf. Figure 9.6.

Atom	LEED-I(V)	DFT-vdW
Cu1	+10	+7
Cu2	-1	-3
Cu3	+3	-1
Cu4	-2	-1

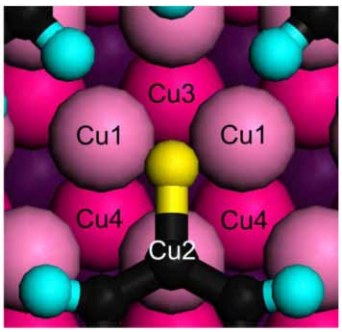

Figure 9.6: Labeling of selected copper atoms, displayed in Table 9.5.

Adatom-Based Models

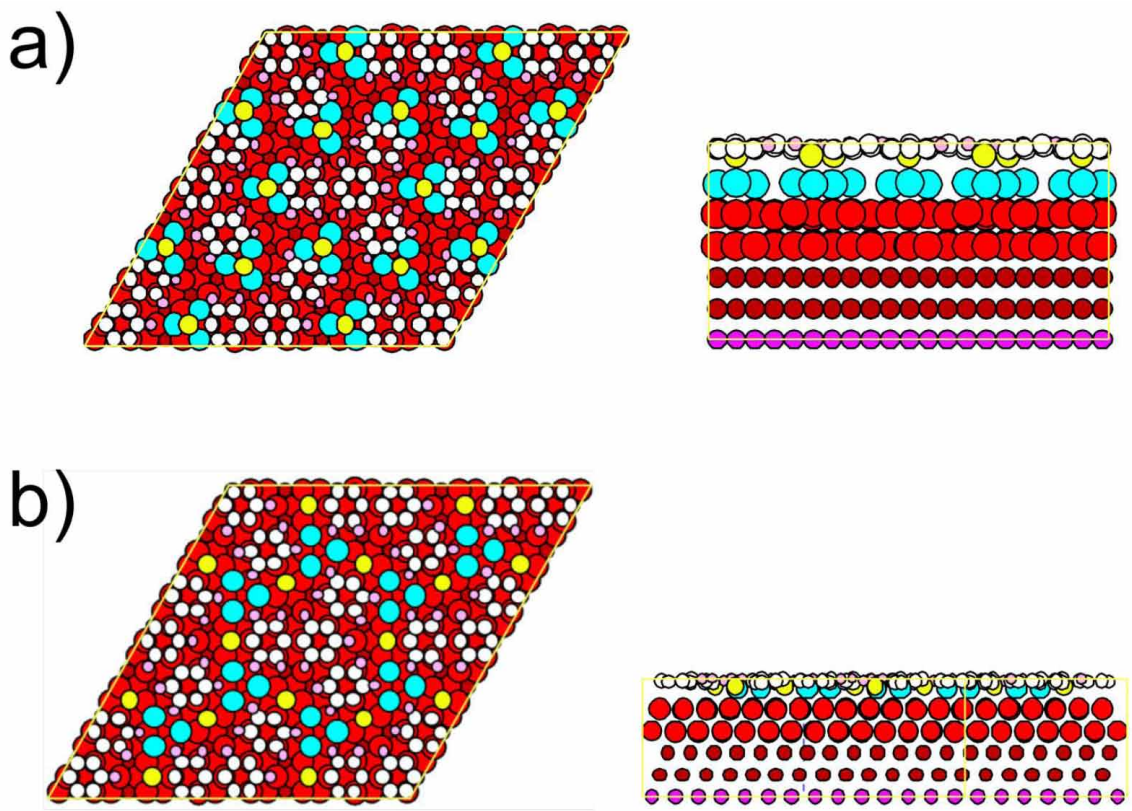

Figure 9.7: Adatom-based models, considered for the LEED-I(V) analysis. (a) adatom interlayer and (b) interstitial adatoms.

Chapter 10

From Benzenetrithiolate Self-Assembly to Copper-Sulfide Adlayers on Cu(111): Temperature-Induced Irreversible and Reversible Phase Transitions

Thomas Sirtl,[ab] Matthias Lischka,[ab] Atena Rastgoo-Lahrood,[ab] Johanna Eichhorn,[ab] Thomas Strunskus,[c] Wolfgang M. Heckl,[abd] and Markus Lackinger.[abde]
Reprinted (adapted) with permission from *The Journal of Physical Chemistry C*, DOI:10.1021/jp411084k, **2014**.

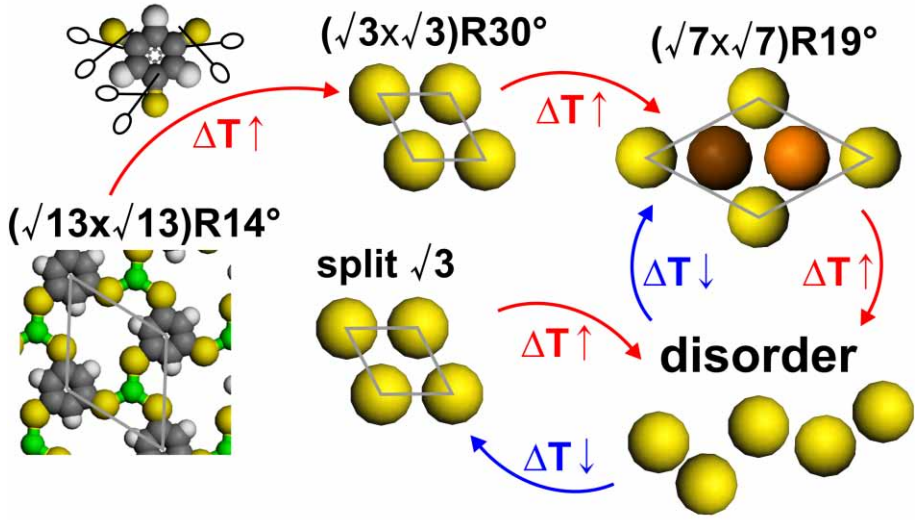

[a] Department of Physics, Technische Universität München, James-Franck-Str. 1, 85748 Garching, Germany
[b] Center for NanoScience (CeNS), Schellingstr. 4, 80799 Munich, Germany
[c] Institute for Materials Science - Multicomponent Materials, Christian-Albrechts-Universität zu Kiel, Kaiserstr. 2, 24143 Kiel, Germany
[d] Deutsches Museum, Museumsinsel 1, 80538 Munich, Germany
[e] Corresponding author; e-mail: markus@lackinger.org; web: www.2d-materials.com

10.1 Abstract

Self-assembly and thermally activated surface chemistry of 1,3,5-benzenetrithiol (BTT) on Cu(111) are studied under ultrahigh vacuum conditions by different complementary surface sensitive techniques. Low energy electron diffraction (LEED) patterns acquired at room temperature and during subsequent heating reveal irreversible phase transitions between in total four different long-range ordered phases termed α-phase to δ-phase. X-ray photoelectron spectroscopy (XPS) of the different phases facilitates to identify major chemical changes for the first phase transition from α- to β-phase, whereas in the succeeding phase transitions no significant chemical shifts are observed anymore. The structural characterization of each phase is carried out by high resolution scanning tunneling microscopy (STM) and adsorption geometries of the phenyl rings were derived from C 1s near edge X-ray absorption fine structure (NEXAFS). Combination of the results from this array of experimental techniques leads to a consistent picture of the various phases and underlying processes. Upon room temperature deposition, BTT fully deprotonates and planar adsorbed molecules self-assemble into an ordered monolayer. With a temperature onset of 300 K the carbon-sulfur bonds start dissociating, resulting in a copper sulfide superstructure, whereas the organic remainders form disordered structures. Further heating converts an initial metastable and rarely observed $\left(\sqrt{3} \times \sqrt{3}\right) \mathrm{R} \pm 30°$ copper sulfide superstructure into the more stable and well-known $\left(\sqrt{7} \times \sqrt{7}\right) \mathrm{R} \pm 19°$ polymorph.

10.2 Introduction

The chemistry of thiolates on metal surfaces was the subject of numerous studies over the last decades, owing to the wide range of conceivable technological implications and applications for thiolate adlayers.[99,224,225] For instance, self-assembled thiolate monolayers (SAMs) are used in molecular optoelectronic devices,[226] as protective coatings,[227] or for chemical sensing, e.g. in combination with gold nanoparticles.[228] For all these applications, the metal-organic interface is extremely important, thus detailed fundamental knowledge about the structures, bond formation, and surface reactions on metals is crucial. Most of the previous work is focused on gold surfaces,[225] hence a comparison to more reactive surfaces is particularly interesting.

On the other hand, the adsorption of atomic sulfur on metals is vitally important for a variety of industrial processes. For instance, sulfur can poison catalysts,[39] whereas copper-sulfide nanoparticles are used for medical imaging.[229] The connection between thiolate monolayers and sulfide adlayers on copper is the preparation protocol for the latter. Sulfur adlayers on Cu(111) are prepared either by deposition and subsequent decomposition of H_2S,[105] or by thermally activated C-S bond dissociation of adsorbed thioles.[230] The stoichiometric variability known from copper sulfide minerals with Cu:S ratios ranging from 1:2 to 2:1 finds its surface counterpart in the various polymorphic copper sulfide phases reported for Cu(111).[99] Observed superstructures comprise $\left(\sqrt{3} \times \sqrt{3}\right) \mathrm{R} \pm 30°$, $\left(\sqrt{7} \times \sqrt{7}\right) \mathrm{R} \pm 19°$, $\begin{bmatrix} 4 & 1 \\ -1 & 4 \end{bmatrix}$,[105] $\left(\sqrt{43} \times \sqrt{43}\right) \mathrm{R} \pm 7.5°$, $\begin{bmatrix} 4 & 0 \\ -3 & 6 \end{bmatrix}$, $\begin{bmatrix} 5 & -1 \\ -3 & 8 \end{bmatrix}$, and $\begin{bmatrix} 3 & 3 \\ -9 & 16 \end{bmatrix}$.[231–233] Formation of the

respective phases was found to depend on coverage and substrate temperature, however, for the greater part the detailed structures are not resolved. For the most common $\left(\sqrt{7} \times \sqrt{7}\right) \mathrm{R} \pm 19^{\circ}$ copper sulfide superstructure on Cu(111) an elaborate theoretical density functional theory (DFT) study compares various proposed structural models, but the energy differences between three favored structures are too small to unambiguously resolve this question.[99]

In the present study we report on self-assembly and surface chemistry of 1,3,5-benzenetrithiol (BTT) on Cu(111). Thermally activated structural changes are studied by means of variable temperature low energy electron diffraction (LEED) experiments which allow for a direct observation of phase transitions. For BTT on Cu(111) LEED reveals the emergence of four different ordered phases between room temperature and 700 K. The structure analysis of each phase is carried out by scanning tunneling microscopy (STM) and augmented by C 1s near edge x-ray absorption fine structure (NEXAFS) studies. X-ray photoelectron spectroscopy (XPS) is employed for a chemical characterization of the different phases.

10.3 Experimental

LEED and STM experiments were carried out in separate ultrahigh vacuum (UHV) chambers with a base pressure below 3×10^{-10} mbar. Cu(111) single crystal surfaces were prepared by cycles of 2 keV-Ar^{+} (LEED) or 1 keV-Ne^{+} (STM) sputtering, and electron beam annealing at $\sim$550 °C. 1,3,5-Benzenetrithiol (BTT, CAS: 38004-59-0; purity $\geq$98 %; purchased from TCI Europe) was deposited via a precision leak valve onto clean Cu(111) held at room temperature. To increase the BTT partial pressure to $\sim 1 \times 10^{-9}$ mbar the compound is heated to a temperature of 35 - 45 °C.

For LEED experiments, a SPECTALEED 4-grid optics (Omicron NanoTechnology GmbH) was used and controlled by an ErLEED electronics (SPECS Surface Analysis GmbH). LEED patterns were recorded with a SensiCam CCD camera (PCO AG) and analyzed with the software package EE2010 (M. F. Opheys; www.ee2000.de). For a precise temperature measurement, a type K thermocouple was mounted inside a bore in the Cu(111) crystal and the surface temperature was controlled by a temperature controller (Invensys Systems GmbH). During LEED measurements at elevated temperature, the filament of the heater - located at the rear side of the sample - was resistively heated. Proper shielding minimizes stray light from the glowing filament.

STM data were acquired with a home-built beetle-type instrument controlled by an SPM100 controller (RHK Technology Inc.). STM topographs were processed by a mean value filter. Given tunneling voltages refer to the sample. STM topographs were recorded at room temperature unless stated otherwise. For low temperature experiments the STM was cooled by a liquid nitrogen flow cryostat to 80 K. The geometry of BTT as used for molecular overlays to the STM images was optimized by molecular mechanics (MM) simulations using the Dreiding force field.

NEXAFS and XPS measurements were carried out in a Prevac UHV system at the HESGM beamline at Helmholtz-Zentrum Berlin. The UHV system is equipped with a preparation chamber allowing sputtering and heating of the sample as well as LEED analysis. The sample preparation was similar to STM and LEED experiments. NEXAFS spectra were acquired in the analysis chamber using a self-built double

channel plate detector in partial electron yield mode. Carbon 1s and sulfur 2p XP spectra were acquired with a Scienta SES 100 electron analyser at normal electron emission with an excitation energy of 400 eV and a pass energy of 50 eV. The binding energy of Cu $3p_{3/2}$ at 75.0 eV was used as an internal standard.[234] The S 2p spin-orbit doublets were fitted with two Gaussians of equal width, applying a fixed intensity ratio of 1:2 and a fixed energy separation of 1.2 eV.

10.4 Results

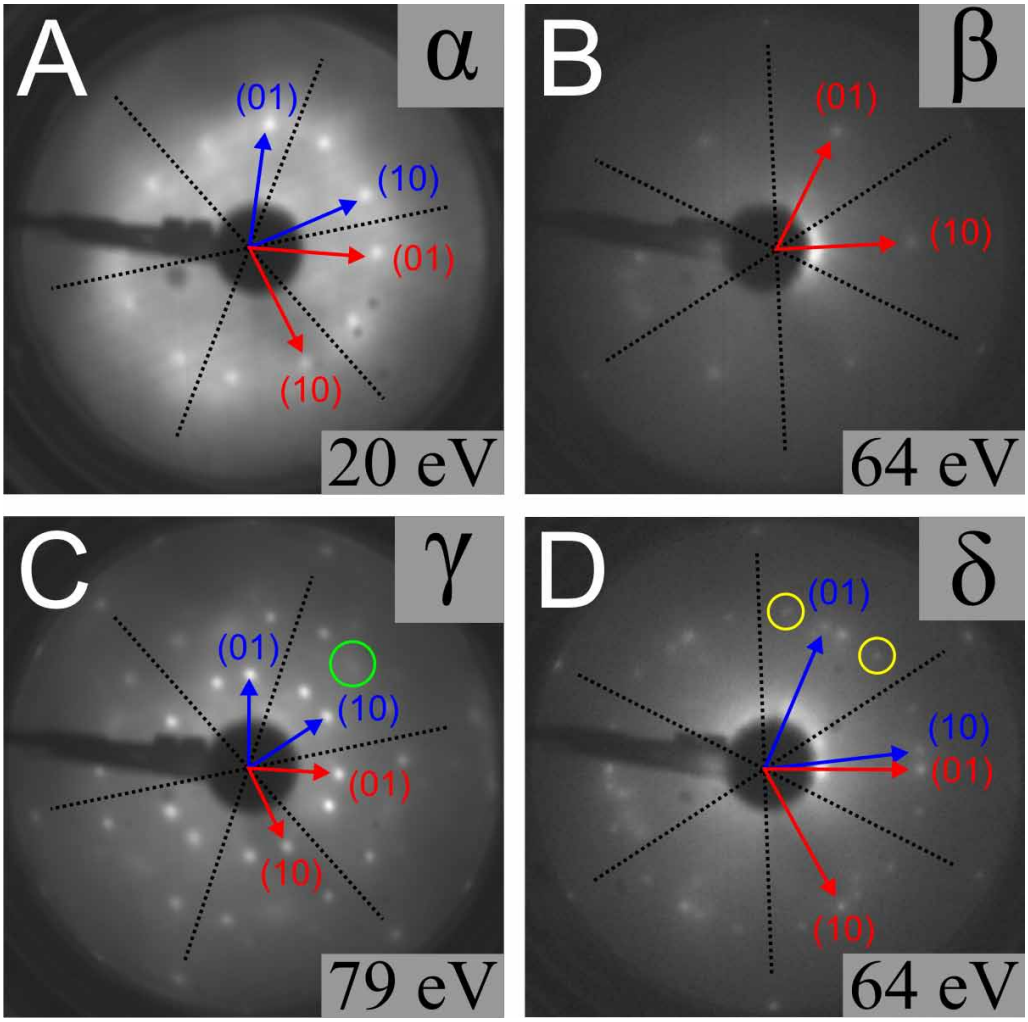

Figure 10.1: LEED patterns obtained from BTT on Cu(111); the respective phases are indicated in the upper right, the electron energies in the lower right corners. Structural parameters are summarized in Table 10.1. (A) α-phase obtained after room temperature deposition. (B) β-phase obtained at a substrate temperature of 430 K. (C / D) Sample tempered to 700 K; the LEED patterns were acquired after cooling down again to room temperature. (C) γ-phase. The green circle marks a diffuse side phase (δ-phase). (D) δ-phase with rather diffuse diffraction pattern. Yellow circles indicate second order reflections of the γ-phase. (A-D) Arrows depict reciprocal unit cell vectors; indices of first order reflections are given in parentheses; dashed lines indicate high symmetry directions of Cu(111).

Room temperature deposition of BTT onto Cu(111) yields a well-ordered structure with trigonal symmetry termed α-phase. From the LEED pattern depicted in Figure 10.1 A the α-phase is identified as a commensurate $\left(\sqrt{13} \times \sqrt{13}\right) \mathrm{R} \pm 19°$ superstructure, corresponding to a lattice parameter of 0.92 nm. Structural parameters of all observed phases are listed in Table 10.1. The temperature evolution of the adlayer was monitored by acquiring LEED patterns while the sample was heated from 300 K up to 700 K and subsequently cooled down again to room temperature. The duration for the whole temperature profile was 4.5 h. The electron energy was held constant at 64 eV, and LEED patterns were captured every 10 s and merged into a LEED vs. T video.

Increasing the substrate temperature to ∼430 K resulted in an irreversible phase transition and formation of a new ordered $\left(\sqrt{3} \times \sqrt{3}\right) \mathrm{R} \pm 30°$ superstructure termed β-phase, the corresponding LEED pattern is shown in Figure 10.1 B. At ∼500 K a second phase transition and emergence of a new $\left(\sqrt{7} \times \sqrt{7}\right) \mathrm{R} \pm 19°$ superstructure termed γ-phase was observed, the corresponding LEED pattern is shown in Figure 10.1 C. Upon further heating the sample, the LEED pattern faded at ∼640 K, indicating the instability of the γ-phase. After subsequently cooling down from 700 K to room temperature the LEED pattern depicted in Figure 10.1 D reveals formation of a new δ-phase at a temperature onset of ∼600 K. The δ-phase possesses hexagonal symmetry, and two rotational domains can be recognized. However, unambiguous assignment to a commensurate superstructure is not possible. Upon further cooling the δ-phase was preserved, and in addition at on onset temperature of ∼470 K also the γ-phase that was already observed during heating reemerged. The phase co-existence of γ- and δ-phase remained stable until room temperature. A striking difference between those two phases is the sharpness of the γ-phase LEED reflections as opposed to the rather diffuse reflections of the δ-phase, indicating relatively large well-ordered domains of the γ-phase. The absence of a LEED pattern above ∼640 K indicates the loss of long-range order, but since γ- and δ-phase reappeared at lower temperature substantial thermal desorption of the adsorbates can be excluded. All phase transitions between ordered phases are irreversible.

Table 10.1: Structural parameters of all observed phases.

	α-phase	β-phase	γ-phase	δ-phase
a, b (nm)	0.91 ± 0.02	0.41 ± 0.06	0.64 ± 0.02	0.40 ± 0.03
∢a, b (°)	120 ± 1	120 ± 1	120 ± 1	120 ± 1
R (°)*	± 14 ± 1	± 30 ± 1	± 19 ± 1	± 27 ± 1
comm.**	$\left(\sqrt{13} \times \sqrt{13}\right)$ R ± 13.9°	$\left(\sqrt{3} \times \sqrt{3}\right)$ R ± 30°	$\left(\sqrt{7} \times \sqrt{7}\right)$ R ± 19.1°	—

* R: rotation to substrate lattice; ** comm.: closest commensurate superstructure relation

For a precise determination of the phase transition temperatures intensity vs. temperature (I(T)) curves were extracted from the LEED vs. T video. Thereto, intensities were integrated and corrected for background light (e.g. stray light from the filament) over rectangles centered at the positions of unique reflections of each phase for each of the ∼1600 LEED patterns of the video. The integrated intensity is a measure for the coverage of the respective phase at the respective sample temperature. The resulting I(T) curves of all phases are shown in Figure 10.2 and Table 10.2 summarizes the extracted peak onset and extinction temperatures, respectively.

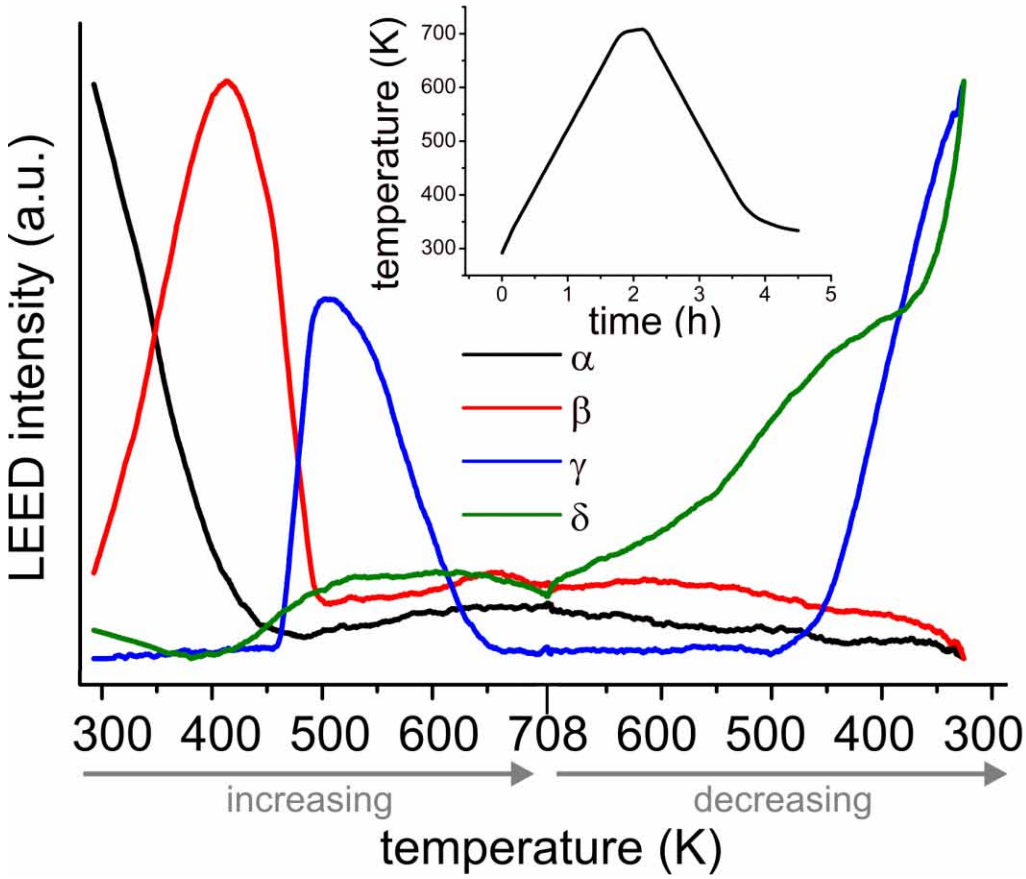

Figure 10.2: LEED reflection intensities vs. substrate temperature (LEED-I(T)) curves. Details are explained in the text body. LEED intensities of the observed phases are corrected for background light, smoothed, and normalized. The inset depicts the underlying temperature vs. time profile.

These curves clearly show a very narrow temperature range for phase co-existence and the decreasing amount of the previous phase along with the increasing amount of the successive phase suggest a conversion from the one into the other.

Table 10.2: Temperature ranges of the observed phases (cf. figure 10.2).

temperature (K)	α-phase	β-phase	γ-phase	δ-phase
onset	< 290*	300	462	600**
disappearance	415	492	640	—
reappearance	—	—	467**	—

* precise onset unknown, experiment started at room temperature;
** while cooling down after heating to 700 K

Table 10.3: Binding energies (BE) and peak intensities (I) from fitted XP spectra.

	C 1s		S $2p_{3/2}$	
	BE (eV)	I (cts)	BE (eV)	I (cts)
α-phase	284.2	7.0×10^6	162.2	3.6×10^6
	284.7	5.6×10^6		
β-phase	284.2	3.8×10^6	162.2	0.6×10^6
	284.7	2.8×10^6	161.5	2.0×10^6
	283.6	4.1×10^6		
γ-phase	284.4	8.5×10^6	161.5	2.0×10^6

For a clear recognition of temperature-induced chemical changes, XPS data of C 1s and S 2p core levels were acquired for as deposited and thermally treated samples, spectra are summarized in Figure 10.3 and Table 10.3. For the α-phase the C 1s spectra can be separated into two chemically shifted peaks centered at 284.2 eV and 284.7 eV binding energy and a peak area ratio of 46:54. These C 1s binding energies accord with aromatic carbon atoms bound to hydrogen and sulfur, respectively.[235,236] The S 2p spectrum of the α-phase shows a spin orbit doublet that arises from only one chemically distinct sulfur species. The S $2p_{3/2}$ binding energy of 162.2 eV is in accord with thiolates on copper.[236] XPS data of slightly heated samples, i.e. the β-phase, exhibit significant shifts of both C 1s and S 2p as compared to the α-phase, and the shifted S $2p_{3/2}$ binding energy of 161.5 eV is consistent with copper sulfides.[237] In the XP spectra of the β-phase small amounts of sulfur with thiolate binding energies (cf. fit in Figure 10.3) suggest that the dissociation reaction has not fully proceeded yet. Upon continued heating the sulfur is fully dissociated, but no significant changes are observed anymore, suggesting that no further substantial chemical alterations occur in the subsequent phase transition from β- to γ-phase.

In addition, NEXAFS spectra were acquired for different incidence angles for both α- and β-phase, the results are summarized in Figure 10.4. The NEXAFS spectra of the α-phase are dominated by resonance that can be assigned to a C1s → π* transition. From the angle dependence a flat adsorption geometry with an angle between substrate and aromatic system of $20\,^\circ \pm 10\,^\circ$ is deduced.

While LEED experiments facilitate a precise superstructure determination and - as shown above - allow stating exact transition temperatures, determination of the

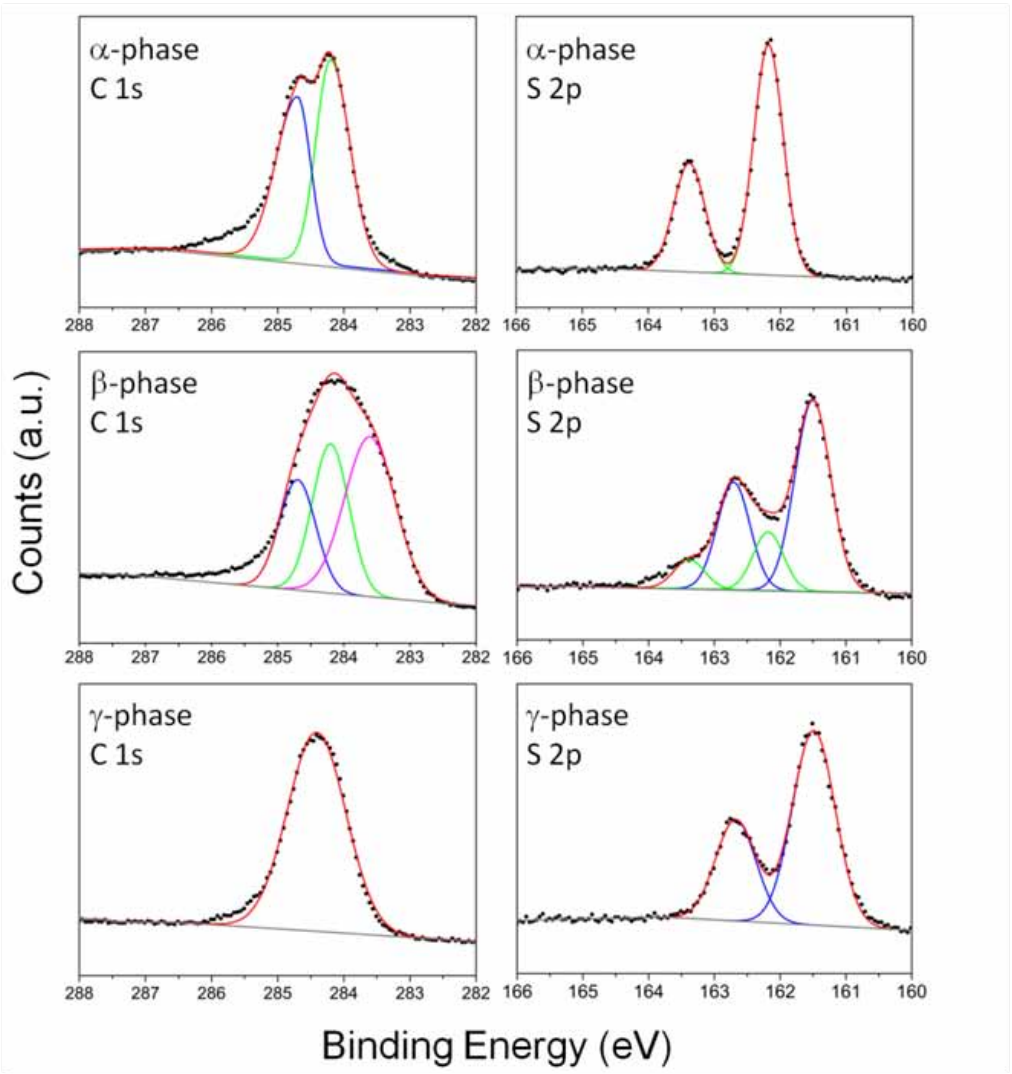

Figure 10.3: XP spectra of the C 1s and S 2p regions of α-, β- and γ-phase. Dots indicate raw data, solid lines represent fits. The experimental spectra were fitted with Gaussians and were normalized at 296 eV and 174 eV, respectively. Binding energies and peak intensities are summarized in Table 10.3.

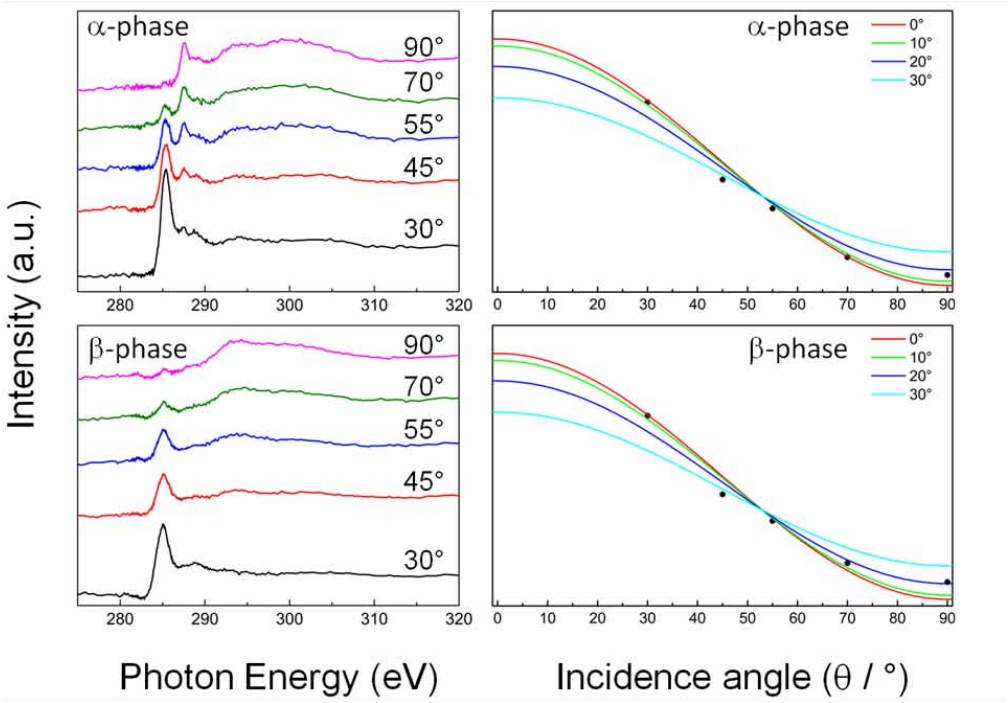

Figure 10.4: C 1s NEXAFS of α- and β-phase: The left column shows the normalized and background corrected spectra obtained for five different angles of incidence (with respect to the surface, i.e. 90 ° corresponds to normal incidence). The right column shows intensity vs. incidence angle plots for the first resonance corresponding to a C 1s $\rightarrow \pi^*$ transition; the colored solid lines serve as guide to the eye, and are theoretical curves for different inclination angles of the aromatic core with respect to the surface, evaluated for an X-ray polarization of $P = 0.92$.

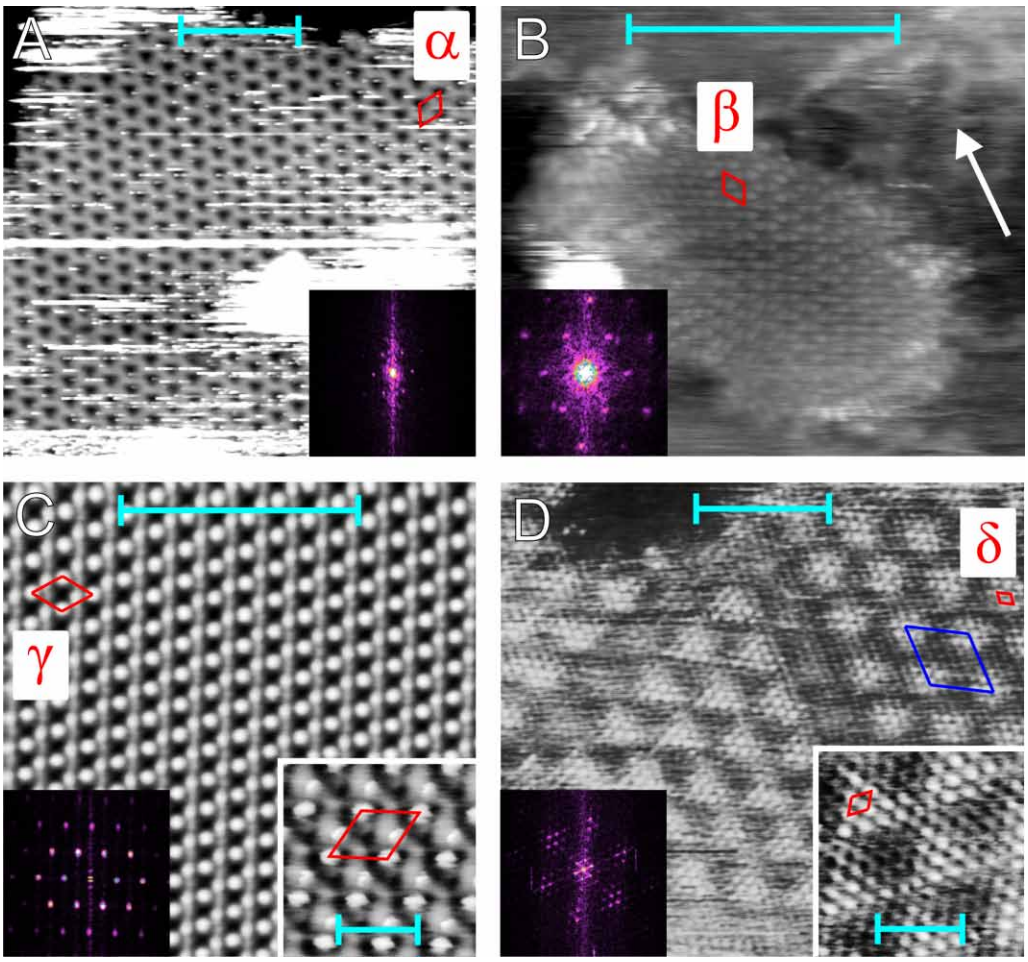

Figure 10.5: STM topographs of all phases on Cu(111) (all $10 \times 10\,\mathrm{nm}^2$). Insets show the corresponding Fast Fourier Transforms (FFT). (A) α-phase prepared by deposition on the sample held at room temperature (experimental lattice parameters: a = b = (1.0 ± 0.1)nm; ◁a, b = 116° ± 8°). (B-D) Recorded at room temperature after tempering the sample at ∼520 K for ∼30 min. (B) Small domains of the β-phase; (exp.: a = b = (0.42 ± 0.03)nm; ◁a, b = 114° ± 9°). (C) Long-range ordered γ-phase covering 85 % of the surface; (exp.: a = b = (0.66 ± 0.03)nm; ◁a, b = 116° ± 5°). Inset on the right: close-up. (D) δ-phase appearing with a pronounced Moiré pattern; (next neighbor distance of adjacent protrusions (red): (0.42 ± 0.04)nm; Moiré unit cell (blue): a = b = (2.0 ± 0.1)nm; ◁a, b = 116° ± 7°). Inset on the right: close-up. Tunneling parameters: (A) 500 mV, 52 pA (B) –3 mV, 98 pA; (C) main image: –2 mV, 296 pA; inset: –2 mV, 1 nA; (D) main image and inset: 2 mV, 1 nA. Scale bars: 5 nm (main images); 1 nm (inset in C); 2 mV (inset in D).

atomic structure is elaborate and not possible in all cases. To bridge this gap, high resolution STM images of all respective phases were acquired. An STM image of the α-phase obtained directly after deposition of BTT onto Cu(111) held at room temperature is depicted in Figure 10.5 A. After tempering the sample at ∼520 K for ∼30 min and subsequent cooling down to room temperature, three structures were found to coexist. Approximately ∼85 % of the surface were covered with a long-range ordered structure (Figure 10.5 C), whose lattice parameters correspond to the γ-phase. Additionally, small islands of the β-phase appeared (Figure 10.5 B). Thirdly, a structure with a pronounced Moiré pattern in the STM contrast is observed (Figure 10.5 C). This phase is assigned to the δ-phase, because the next neighbor distances of adjacent protrusions in STM are in good agreement with the LEED results. Based on the combined LEED, STM, XPS results structural models are proposed for all phases and conceivable driving forces for the phase transitions are discussed.

10.5 Discussion

α-phase

The XPS binding energies of S 2p are in accordance with thiolates on copper,[236] indicating deprotonation of the thiol groups into thiolate groups and formation of covalent bonds to the Cu(111) surface. Moreover, occurrence of only one chemically distinct S 2p signature suggests that all sulfur atoms equivalently bind to the substrate. This already points out to a flat adsorption geometry as similarly and independently inferred from NEXAFS. Furthermore, the C 1s XPS data and the sharp π* resonance in NEXAFS indicate intact benzene rings with half of the carbon atoms bound to thiolate groups.

Accordingly, the α-phase is identified as a self-assembled monolayer of deprotonated but otherwise intact TBB molecules with their molecular plane parallel to the surface. This flat adsorption geometry stands in vast contrast to the upright adsorption of benzenethiolate on Cu(100).[238] Evidently, favorable interactions between the additional thiolate groups and the copper substrate pin the aromatic core down. Under this restriction each unit cell can accommodate only one molecule. The STM topograph in Figure 10.5 A shows a regular and slightly porous structure that can consistently be matched with metal-coordinated networks, where thiolate groups are coordinated by copper adatoms. Figure 10.6 A presents a tentative model of the structure and Figure 10.6 B exemplifies the perfect match by means of a scaled overlay with a close-up STM topograph. The pores coincide, the protrusions are centered at the adatom positions, and even slight indentations appear at the center of each phenyl ring. According to the proposed model, three thiolate groups are coordinated by one copper adatom. This model yields a sulfur-copper bond length of ∼250 pm. This bond length is in good agreement with 1,3,5-tris(4-mercaptophenyl)benzene (TMB) monolayers on Cu(111) (236 – 264pm)[37] and in the same range as observed in copper sulfide minerals (CuS: 219 – 238pm;[217] Cu_2S: 218 – 290pm).[218] The coordinating copper adatoms originate from the free adatom gas present on Cu(111). Similarly, metal-organic networks based on copper-thiolate coordination bonds were observed on Cu(111) upon slightly tempering TMB monolayers to ∼150 °C.[24] On

the other hand, for nitriles on Cu(111) formation of metal-coordinated networks was already observed at room temperature,[26,107] clearly demonstrating a sufficient density of copper adatoms already at room temperature. The necessity of tempering in the case of TMB monolayers suggests that thermal activation might be required to enhance the mobility of this rather large trithiolate molecule.

Although the proposed metal-coordinated network perfectly matches with the STM data, this structural model cannot unambiguously be verified, not even with all analytical techniques applied here. An alternative structure without coordinating adatoms where all thiolate groups directly bind to the copper substrate cannot be excluded but does not agree so well with the data (cf. Figure 10.7).

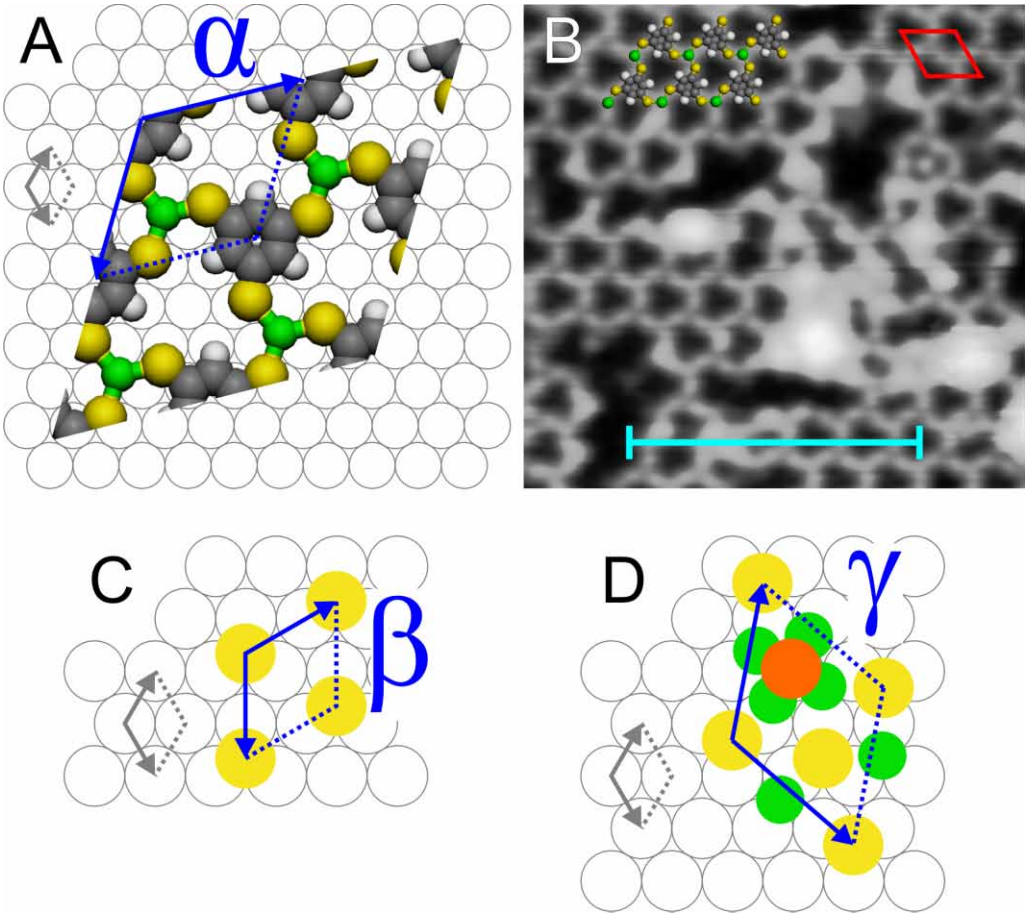

Figure 10.6: Tentative models of the experimentally observed phases, grey circles represent topmost atoms of the Cu(111) surface. (A) α-phase: BTT derived trithiolate molecules form a metal-organic network stabilized by S-Cu coordination bonds with copper adatoms (green). Carbon: dark grey; hydrogen: white; sulfur: yellow; (B) Close-up STM topograph of the α-phase, recorded at ∼80 K. The unit cell is indicated by red lines and the structural model is overlaid to scale. Tunneling parameters: 550 mV, 83 pA; scale bar: 5 nm. (C) β-phase: in this tentative model sulfur atoms are adsorbed on threefold hollow sites (best model of a recent DFT study by Seema et al.)[99]. (D) γ-phase: copper sulfide surface phase with three sulfur atoms per unit cell. Here, structure "S9" is displayed;[99] see main text for details. Copper adatoms: green; sulfur atoms adsorbed on the surface: yellow; sulfur atom adsorbed on top of a copper adatom quartet: orange.

β-phase

The supply of thermal energy irreversibly converts the α-phase into the β-phase (onset of the transition: ∼300 K; cf. Table 10.2). Already the unit cell size of the $\left(\sqrt{3} \times \sqrt{3}\right)$ R ± 30° superstructure precludes the flat adsorption geometry of the α-phase. However, XPS provides the most informative data, where pronounced chemical shifts in S 2p indicate dissociation of carbon-sulfur bonds. Thus the phase transition from α to β is not merely a rearrangement of intact molecules, but driven by dissociation and accompanied by major chemical changes. This dissociation separates the original trithiolate molecule into two chemical species, i.e. the sulfur atoms and the organic remainder. The high affinity of sulfur to copper renders formation of a copper sulfide structure most likely, and a $\left(\sqrt{3} \times \sqrt{3}\right)$ R ± 30° superstructure was already observed upon deposition and subsequent decomposition of H_2S on Cu(111).[105] STM topographs of the β-phase show small domains, however, the contrast cannot be intuitively interpreted. This rather uncommon copper sulfide structure has not been resolved by experimental techniques, yet a conceivable structure model - clearly favored by a DFT analysis - is depicted in Figure 10.6 C. Here, a unit cell contains one sulfur atom, adsorbed on a threefold hollow site.[99]

LEED does not give any hint as to the fate of the organic remainder, since no ordered structure is being formed. However, XPS indicates that carbon is still present on the surface and even the π* resonance is still observable in NEXFAS, indicating the continued existence of aromatic rings in a flat adsorption geometry. STM topographs, however, only show irregular structures next to islands of the β-phase (cf. arrow in Figure 10.5 B) that could originate from the organic remainder. Yet, higher resolution could not be obtained and no unambiguous conclusion is possible at this stage.

γ-phase

Upon further heating, the β-phase is irreversibly converted into the γ-phase at a temperature of ∼462 K. XPS of S 2p indicate that no further chemical changes occur. Thus, the γ-phase is similarly a copper sulfide surface, albeit with a significantly altered structure. Although the $\left(\sqrt{7} \times \sqrt{7}\right)$ R ± 19° superstructure is well-known for atomic sulfur on Cu(111), its detailed atomic structure has not been determined yet and is discussed controversially.[99] Different structure models were proposed by Prince,[239] Domange and Oudar,[105] Saidy and Mitchell,[240] and Foss et al.[241] Most studies agree that the $\left(\sqrt{7} \times \sqrt{7}\right)$ R±19° superstructure is not merely comprised of adsorbed sulfur, but also features interspersed copper atoms. This requires a major structural reorganization of the surface accompanied by substantial mass transport for which thermal activation becomes necessary. A recent DFT study tackles the question of the precise atomic structure by screening and optimizing a large number of prevalent structural models.[99] Although, based on an energetic ordering, some structures appear less likely, a clear decision between three competing models with very similar energies is not possible. One of the favored structures exhibits trigonal symmetry with three sulfur atoms per asymmetric unit adsorbed at hcp and fcc threefold hollow sites as well as an on top site. Additionally, three copper adatoms are located within the sulfur adlayer. Another favorable candidate for the superstructure also exhibits trigonal symmetry and consist of Cu_3S_3 clusters

adsorbed on the surface. The third favorable structure exhibits $p1$ symmetry, where three sulfur atoms are adsorbed onto hcp and fcc threefold hollow sites and on top of a Cu_4 cluster. A model of this least symmetric structure is depicted in Figure 10.6 D.

Based on the LEED results a clear distinction is not possible. Further evidence also on the symmetry of the respective structure can, however, come from STM. The high resolution image depicted in Figure 10.5 C exhibits $p1$ symmetry, i.e. only translational and no rotational or mirror symmetry. Interestingly, all but one structure of the DFT study exhibit higher symmetry with at least three-fold rotational symmetry, while one of the energetically preferred structures has $p1$ symmetry.[99] Based on this agreement, we postulate that the γ-phase as the well-known copper-sulfide $\left(\sqrt{7} \times \sqrt{7}\right) \mathrm{R} \pm 19°$ superstructure is similar to the least symmetric structure originally proposed by Foss et al. (cf. Figure 10.6 D).[241]

At these high temperatures required for formation of the γ-phase the aromatic rings are already decomposed. This hypothesis is supported by XP spectra that show a shift of the C 1s peak to 284.4 eV, indicating amorphous carbon on the surface.[242]

δ-phase

Upon cooling down from 700 K, the δ-phase emerged (onset ∼600 K). The δ-phase features the highest temperature stability and relatively small lattice parameters of $a = b = (0.40 \pm 0.03)$ that are similar to those of the β-phase within experimental error. The pronounced Moiré pattern in the STM topograph indicates non-equivalent adsorption sites within the large unit cell. A comparable LEED pattern as obtained for the δ-phase (Figure 10.1 D) was already reported in literature and referred to as a "split $\sqrt{3}$ pattern".[39] In this study, H_2S was deposited onto clean Cu(111), whereas upon heating two copper-sulfide phases (a "complex" pattern and the well-known $\left(\sqrt{7} \times \sqrt{7}\right) \mathrm{R} \pm 19°$ superstructure) are converted into the "split $\sqrt{3}$" phase at a temperature of 460 – 470K. Thereby, the exact conversion temperature depends on the coverage. However, no description of the atomic structure is given. Also on the basis of the present study it remains highly speculative to propose a structure model, but the relatively high formation temperature may be explained by an onset of sulfur diffusion into the bulk.

10.6 Summary

Self-assembly and thermally induced surface chemistry of BTT on Cu(111) is studied by different complementary surface science techniques. Upon room temperature deposition, the thiol groups of BTT become deprotonated into thiolate groups that act as covalent anchors. NEXAFS indicates flat adsorption of the aromatic core, and in accord with the STM data the long-range ordered α-phase is assigned to a metal-coordinated network based on thiolate copper-coordination bonds. Two subsequent irreversible transitions into β- and γ-phase, respectively, are observed by means of LEED experiments while the sample is heated. Fading of the LEED pattern above 640 K indicates the loss of long-range order. XPS aided in identifying both β- and γ-phase as copper sulfide adlayers, whereby the metastable β-phase with a $\left(\sqrt{3} \times \sqrt{3}\right) \mathrm{R} \pm 30°$ superstructure is irreversibly converted into the well-known more stable $\left(\sqrt{7} \times \sqrt{7}\right) \mathrm{R} \pm 19°$ superstructure upon supply of thermal energy. Interestingly,

when cooling down again first a new δ-phase that has not been observed during heating, i.e. temperature increase, emerged at 600 K, accompanied by reappearance of the already known γ-phase at 467 K. STM images of the δ-phase exhibit a contrast with a pronounced Moiré pattern. However, from the STM data a detailed structure cannot be inferred. The STM data of the γ-phase exhibits p1 symmetry only. Although a recent DFT study could not unambiguously clarify the structure of the $\left(\sqrt{7} \times \sqrt{7}\right) \mathrm{R} \pm 19^{\circ}$ superstructure, only one of the three favored structures exhibits similar symmetry as the STM image. Based on this coincidence, we propose that the superstructure corresponds to the least symmetric structure originally proposed by Foss.[241]

In summary, we demonstrate that only the combination of diffraction, microscopy, and spectroscopy has the potential to provide a detailed picture of the BTT surface chemistry on Cu(111). Especially, the LEED vs. T experiments are relatively straightforward, but allow gaining valuable insights into the kinetics and critical temperatures for phase transitions in surface adlayers.

10.7 Acknowledgment

The Deutsche Forschungsgemeinschaft (LA1842/4) and the Nanosystems-Initiative-Munich cluster of excellence are thankfully acknowledged for financial support. T. Si. acknowledges the Fonds der Chemischen Industrie (FCI) for financial support. We thank Helmholtz-Zentrum Berlin for the allocation of synchrotron radiation beamtime and M.L. and J.E. thankfully acknowledge traveling support. We are indebted to Jörg Behler and coworkers for providing data of copper sulfide structures.

10.8 Supporting Information

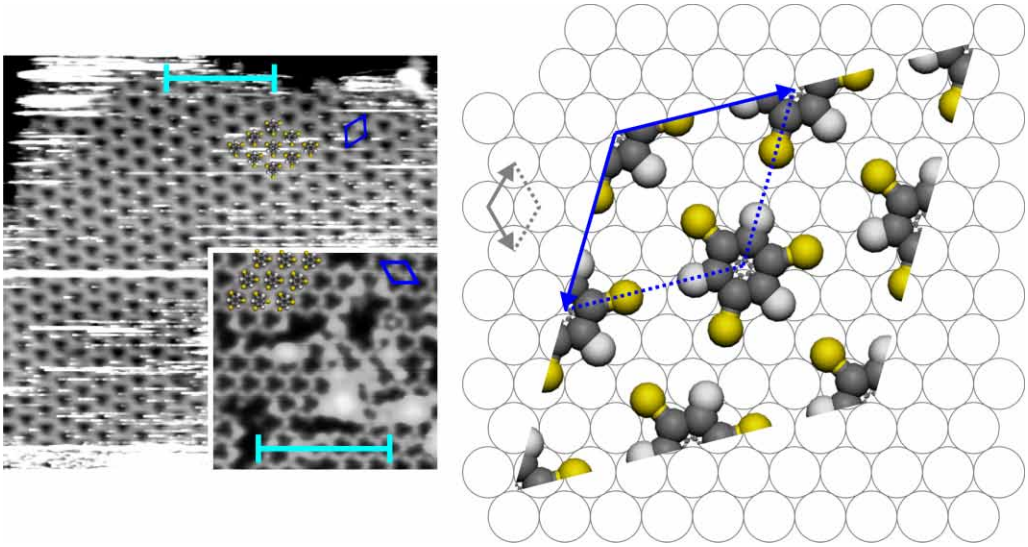

Figure 10.7: STM topographs from Figure 10.5 A and Figure 10.6 B of the manuscript (left) and alternative structure model for the α-phase (right). BTT molecules (overlaid in the STM images) are arranged in head-to-tail configuration. BTT molecules are geometry optimized by force field calculations and depicted to scale. This structure model includes no copper adatoms and is analogue to self-assembly of TMB molecules on Cu(111).[24,37]

Chapter 11

Adsorption Site Marker for hcp Threefold Hollow Sites on Cu(111)

Thomas Sirtl,[ab] Paula M. León,[c] Wolfgang Moritz,[d] Wolfgang M. Heckl,[abe] and Markus Lackinger.[abef] *In preparation.*

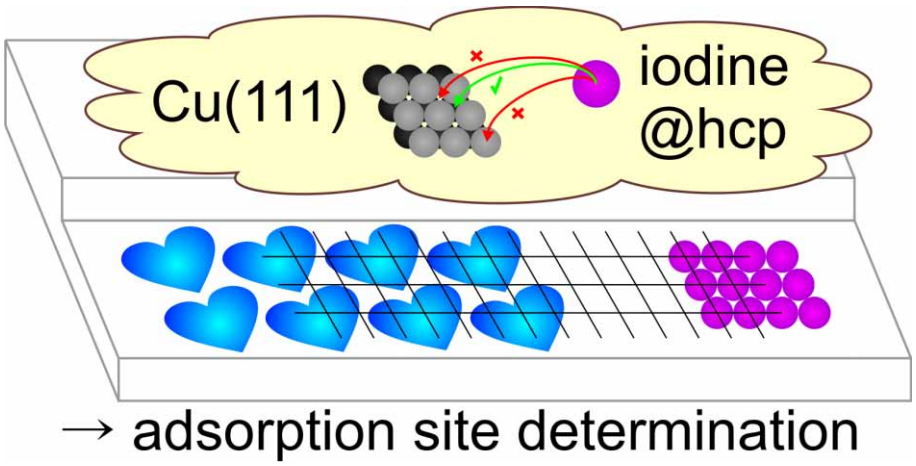

[a] Department of Physics, Technische Universität München, James-Franck-Str. 1, 85748 Garching, Germany
[b] Center for NanoScience (CeNS), Schellingstr. 4, 80799 Munich, Germany
[c] Faculty of Physics, University of Valencia, Calle del Doctor Moliner 50, 46100 Burjassot, Valencia, Spain
[d] Department of Earth and Environmental Sciences, Ludwig-Maximilians-University, Theresienstr. 41, 80333 Munich, Germany
[e] Deutsches Museum, Museumsinsel 1, 80538 Munich, Germany
[f] Corresponding author; e-mail: markus@lackinger.org; web: www.2d-materials.com

11.1 Abstract

We present a straighforward method to use atomically adsorbed iodine as an adsorption site marker for scanning probe microscopy (SPM) experiments on Cu(111). The iodine adsorption site is initially determined by a low energy electron diffraction intensity versus voltage measurement (LEED-I(V)). The application of the marker in SPM enables adsorption site determination of large adsorbates via co-deposition of the marker adjacent to the adsorbate of interest and superimposing the lattices in the SPM image.

11.2 Introduction

Adsorption sites of functional molecules on metal surfaces are the basis for a correct description of contact resistences and electron transport properties.[36] Accordingly, adsorption sites are most relevant for the application of organic nanostructures in molecular electronics devices. Adsorption sites can in principle be determined by low energy electron diffraction intensity versus voltage measurements (LEED-I(V)), however, for this purpose long-range ordered surface phases with large domain sizes and low sensitivity to electron beam damage are required. Self-assembled or on-surface synthesized structures of functionalized organic molecules most often do not fulfill these requirements. Under favorable instances, adsorption sites on the topmost layer can also be derived by scanning tunneling microscopy (STM).[38] For that, adsorbate and substrate lattices are imaged next to each other in one topograph. However, from STM experiments no inferences can be drawn about adsorption sites with respect to subjacent substrate layers. Also, adsorption site determination with respect to the topmost substrate layer by STM is rare because barely controllable particular tip conditions and extraordinary thermal stability of the STM need to be achieved. These premises render the conventional adsorption site determination by STM intricate and leave the success to chance. Thus, facile and reliable methods of adsorption site determination are urgently needed in surface science.

We propose using atomic iodine as a marker for a specific adsorption site on the Cu(111) surface. Codeposition of the marker adjacent to the determined structures enables adsorption site determination of the respective building blocks by superimposing the lattices in SPM images. Due to the ease of imaging iodine adlayers, such experiments can be facilitated at room temperature. Noteworthy, iodine adlayers are fabricated with iodinated precursor molecules instead of toxic pure iodine.

11.3 Experimental

Iodine monolayers are prepared by deposition of 1,3,5-triiodobenzene (TIB; Sigma-Aldrich;[g] CAS: 626-44-8) through a leak valve. The molecule reservoir is heated to ∼85 °C to increase the vapour pressure of TIB. Cu(111) is prepared by cycles of Ar^+ ion sputtering (2 keV) and electron beam annealing (∼550 °C). The periodicity of the superstructures is confirmed by LEED and the adsorption site is determined with the help of LEED-I(V) calculations. A SPECTALEED 4-grid optics[h] was used

[g] Sigma-Aldrich Chemie Gmbh, Munich, Germany
[h] Omicron NanoTechnology GmbH

and controlled by an ErLEED digital electronics[i]. A SensiCam[j] CCD camera is used for recording videos; the software package EE2010[k] facilitates I(V)-curve extraction. I(V)-curves are simulated and compared to the experiment with the home written software package LEEDFIT.[75–77,194,195] The experimental dataset comprises nine independent beams at normal incidence within the energy range of 50 - 500 eV, corresponding to a cumulative energy range of 2564 eV. Symmetrically equivalent reflections are averaged and normalized by the energy dependent beam current. The reliability factor developed by J. B. Pendry (R_P) is used to quantify the agreement of experimental and theoretical I(V)-curves.[82]

11.4 Results and Discussion

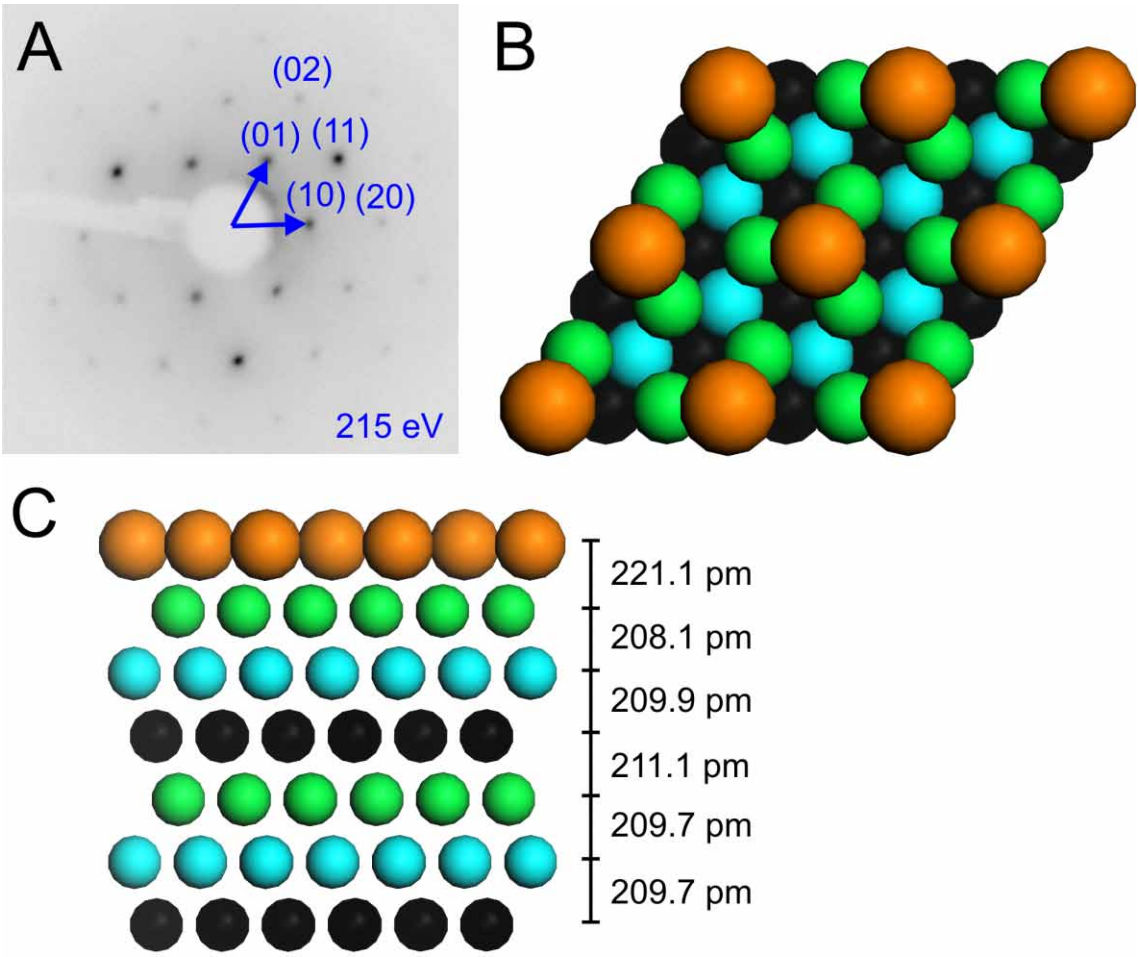

Figure 11.1: Iodine $\left(\sqrt{3} \times \sqrt{3}\right)$R30° superstructure on Cu(111). (A) LEED pattern acquired at an electron energy of 215 eV. Reciprocal unit cell vectors and reflection indices are marked. (B) Top view and (C) side view on 2 × 2 unit cells of the LEED-I(V)-derived adsorption geometry. Iodine atoms adsorb on hcp threefold hollow sites. Layer distances are displayed; orange: iodine; green, blue, black: ABCABC-stacked copper layers.

[i] SPECS Surface Analysis GmbH
[j] PCO AG
[k] M. F. Opheys, www.ee2000.de

Table 11.1: Distances of iodine to adjacent atoms.

adjacent atom	I (top layer)	Cu (2. layer)	Cu (3. layer)	Cu (4. layer)
distance [pm]	427.4	266.1*	429.2	655.9

* in perfect agreement with previous SEXAFS studies (266 ±2 pm).[243]

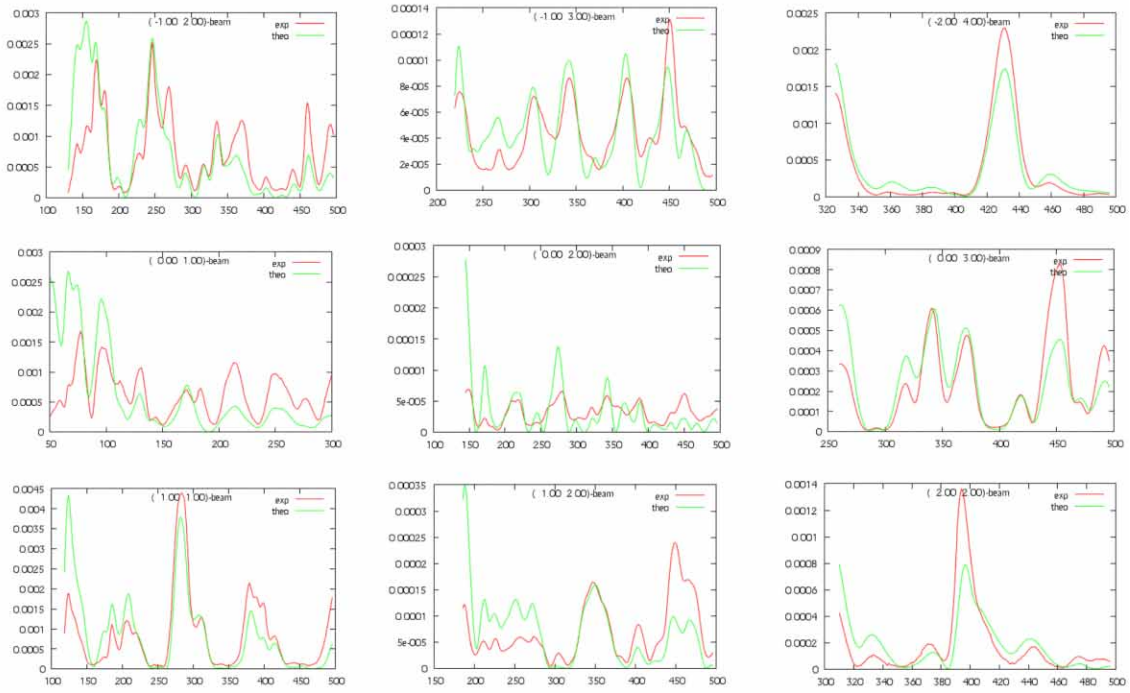

Figure 11.2: Experimental (red) and theoretical (green) I(V)-curves for the best-fit geometry of iodine on Cu(111). The indices in parentheses refer to superstructure reflections. The overall Rp amounts to 0.25.

Upon adsorption of TIB the C-I bonds dissociate and the split off iodine atoms arrange in a $\left(\sqrt{3} \times \sqrt{3}\right)$ R30° superstructure as already known from literature (figure 11.1 A).[243] Threefold hollow sites could be determined as adsorption sites of iodine atoms by surface extended X-ray-absorption fine structure (SEXAFS) measurements. However, the type of threefold hollow sites could not be derived, that is, hcp or fcc. No further reflections aside from the iodine superstructure and the Cu(111) substrate are observed in the LEED patterns. Thus, a conclusion about the organic remainder is not possible. In principle, desorption or on-surface reactions are feasible.

The unit cell size of the iodine superstructure allows for the accommodation of only one iodine atom per unit cell. Three adsorption sites are consistent with the observed symmetry of the LEED pattern and accordingly considered as initial structures for the LEED-I(V) analysis. The structure models comprise the two models proposed by SEXAFS experiments (iodine atoms adsorbed at fcc threefold hollow sites or at hcp threefold hollow sites) and by way of comparison, iodine atoms at on top sites. Unambiguously, the adsorption at hcp threefold hollow sites is the clearly favored after structure refinement ($R_p = 0.25$) over the fcc threefold hollow sites ($R_p = 0.38$) and the top sites ($R_p = 0.63$). In figure 11.2 theoretical and

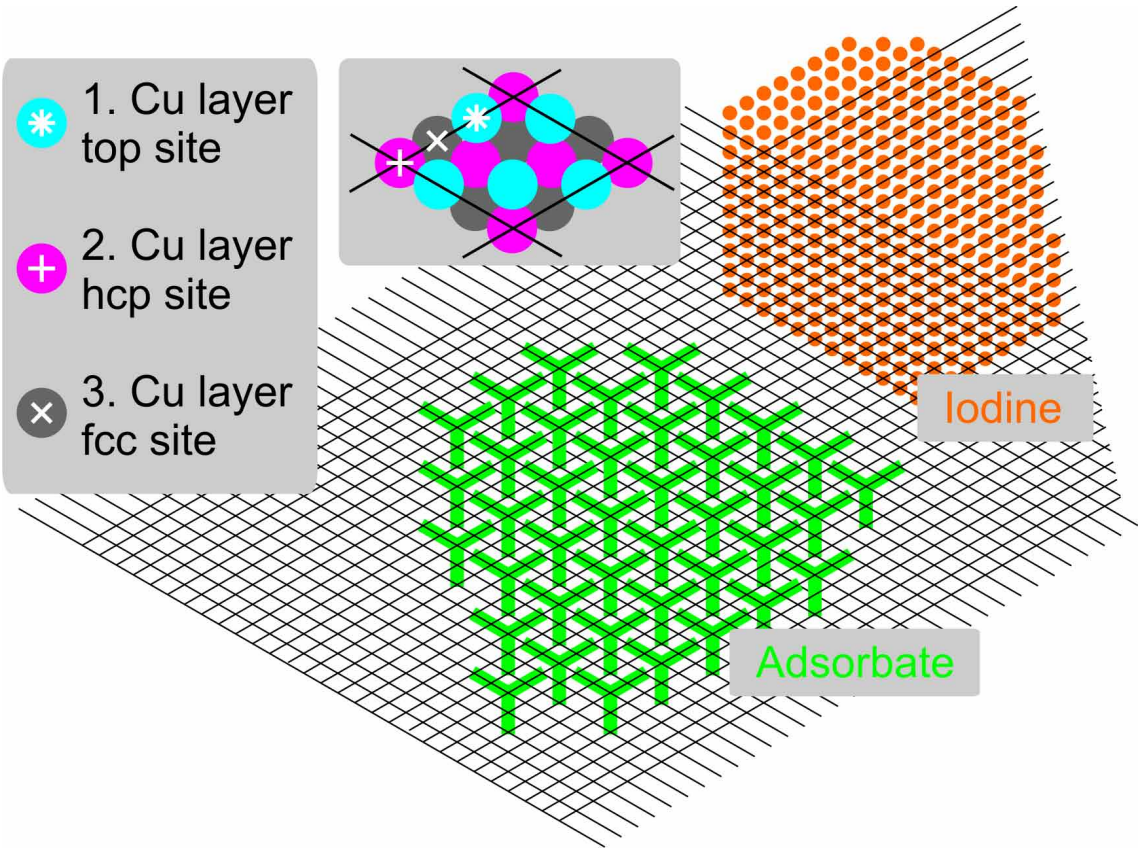

Figure 11.3: Postulated method of adsorption site determination by codeposition of molecular building blocks and iodine atoms: Sketch of an SPM topograph displaying separate domains of adsorbed iodine atoms (orange circles) and molecular adsorbates (green tripods). Superimposing a grid with the periodicity of the iodine superstructure enables the adsorption site determination of the molecular adsorbate. The inset highlights high symmetry adsorption sites at the Cu(111) surface within a unit cell of the iodine superstructure (top site (turquoise), hcp (pink), or fcc (grey) threefold hollow site). However, top sites or fcc threefold hollow sites cannot be determined unambiguously with this technique.

experimental I(V)-curves of the best-fit geometry are depicted. Figures 11.1 B and C illustrate the optimized structure. Table 11.1 presents atomic distances of iodine atoms to adjacent atoms.

Detailed knowledge of the adsorption site of atomic iodine on Cu(111) can be exploited for studying the adsorption geometries of other adsorbates including large molecules. Thereto, a submonolayer of the aimed adsorbate is deposited onto the substrate. The coverage should be 25 - 50 %, so that a sufficient amount of the pristine substrate is left for the codeposition of the marker. As for the LEED experiments of the pure iodine layer, the marker can be deposited in the form of an aromatic molecule functionalized with iodine substituents (e.g. TIB). The catalytically split off iodine atoms arrange in a densely packed structure unless they mix or react with the analyzed adsorbate which is unlikely because adsorbed iodine atoms exhibit low reactivity. Once the drift of the SPM is minimized and the two superstructures are imaged in one SPM topograph, the lattice of the iodine adlayer can be superimposed to the adsorbate domain. Here, intersections between the unit cell axes mark hcp threefold hollow sites. The principle is illustrated in a schematic SPM image in figure 11.3. Hcp threefold hollow sites can be determined with high accuracy, whereas fcc threefold hollow sites, bridge sites or top sites can only be distinguished with the help of complementary data as obtained in split images.[101] Alternatively, another marker could be used. For instance, atomic oxygen is proposed to adsorb onto Cu(111) fcc threefold hollow sites in a recent DFT study.[244]

11.5 Acknowledgment

T.S. acknowledges the Fonds der Chemischen Industrie (FCI) for financial support.

Chapter 12

Conclusion

Structurally diverse surface-supported nanostructures are fabricated on single crystal surfaces under various conditions. They are analyzed in terms of their molecular arrangement and especially their underlying intermolecular interactions. The observed bond types comprise dispersive interactions, halogen bonds, hydrogen bonds, metal-organic bonds, organometallic bonds, and covalent bonds:

- Apart from strong adsorbate-substrate bonds, **dispersive interactions** stabilize an iodine monolayer on Cu(111). Interatomic dispersive interactions are based on attractive interactions between a spontaneous dipole and an induced dipole.
- **Halogen-halogen bonds** are the underlying forces in self-assembly of hexabrominated polyaromatic molecules (TDBB) on Ag(111) and Cu(111). Around each bromine substituent, the charge distribution is non-spherical. The resulting dipoles account for an attractive circular arrangement of the bromine groups of adjacent molecules.
- On Ag(111) and Cu(111), **hydrogen bonds** are present in monolayers of polyaromatic molecules functionalized with nitrile groups (BCNB). As a consequence thereof, the molecules arrange in a densely packed structure with head-to-tail configuration.
- BCNB monolayers on Cu(111) are stabilized by **metal-organic** (i.e. copper-nitrile) **bonds**. Hereto, nitrile ligands bind to copper adatoms from the free adatom gas on the surface. Owing to the molecular geometry, a porous network arises.
- TDBB molecules form **organometallic bonds** on Cu(111). Supply of thermal energy results in the dissociation of C-Br bonds subsequently to the adsorption of TDBB molecules. Resulting triphenylbenzene hexa-radicals react with copper adatoms to organometallic networks (so called protopolymers).
- **Covalent** C-C **bonds** are the most stable of all observed bond types, where strictly speaking these are intrapolymeric rather than intermolecular bonds. Small domains of covalent organic frameworks are synthesized by TDBB, adsorbed onto Cu(111) or Ag(111). The required activation energy is provided by the supply of thermal energy.

The formation of intermolecular bonds and the resulting structure of the molecular arrangement in surface-supported nanostructures strongly depend on various controllable experimental parameters. As a consequence, experimental parameters can be exploited to control intermolecular interactions and the smart balancing of different preparation parameters even facilitates structure selection. Important examples of studied influencing parameters are:

coverage — Self-assembled monolayers of guanine are shown to be influenced by the coverage of the substrate. As a low energy electron diffraction (LEED) study infers, a disordered phase sequentially transforms into four well-ordered phases upon thermal treatment. This phenomenon is only present for low coverages, whereas a higher coverage results in the emergence of only three phases. Also, the temperatures of the phase transitions are slightly coverage-dependent.

functionalization — Self-assembly of polyaromatic molecules is well known to significantly depend on the functionalization of the monomers. Also in the presented examples, the type of functional group predefines the binding motif and accordingly the molecular arrangement: Brominated molecules (TDBB) arrange in densely packed networks stabilized by halogen-halogen bonds on Cu(111) at low temperature, whereas at room temperature C-Br bonds dissociate and organometallic networks are formed. Nitrile molecules (BCNB) are densely packed and weakly hydrogen-bonded on Ag(111) and Cu(111). Additionally, a porous, metal-coordinated structure is found on Cu(111), see below for the influence of the substrate. The arrangement of thiolated molecules (TMB) on Cu(111) is dominated by covalent S-Cu bonds from sulfur atoms of TMB to copper atoms of the substrate.

substrate material and lattice — Effects of the substrate on structure formation are discovered in surface self-assembly of large trinitrile molecules (BCNB). BCNB molecules on Ag(111) arrange in a similar molecular arrangement as on Cu(111), that is, the densely packed α-phase. However, the monolayers exhibit different superstructure relations to the substrates. This is attributed to the differences in substrate lattice parameters and the energy minimization of the adsorption structure by optimizing the adsorption site on each surface. Thereby the superstructure lattice parameters can be varied within a certain range without disturbing the stability of the molecular arrangement. Interestingly, although similarly prepared, BCNB molecules arrange in a different structure on HOPG(0001), namely, the ε-phase. Comparison to the two latter substrates reveals substrate registry as a conceivable reason. This is suprising, since usually adsorbate-substrate interactions of organic adsorbates are weaker on graphite compared to metals. The examples show that the substrate lattice can control orientations of adsorbates, along with bond angles in intermolecular hydrogen bonds.

A further example for an adlayer governed by substrate registry is a self-assembled monolayer of trithiol molecules (TMB) on Cu(111). Here, the adsorption site is determined by LEED-I(V) with subatomic precision. Among six symmetry allowed competing adsorption structures, one adsorption geometry is clearly favored, that is, where all sulfur atoms occupy hcp threefold hollow sites (asymmetrically, near bridge sites) and all phenyl rings are above fcc threefold

hollow sites. Slight molecular deformations and substrate relaxations are also derived from theory and experiment. The coincidence of the stereochemistry of TMB with the preferred adsorption sites on the substrate results in well-ordered domains. In the context of the LEED-I(V) analysis, the standard reliability factor developed by J. B. Pendry (R_P) is discussed for structures of large organic adsorbates. In a literature survey structure refinements with R_P up to 0.4 are found as reliable fits for larger adsorbates.

adatom reactivity of a substrate — The material of a surface determines the reactivity of adatoms. Adatoms are highly mobile metal atoms (e.g. from step edges) that form an adsorbed gas phase on a metal surface. The dependence of structure formation on the reactivity of adatoms is highlighted in self-assembly of trinitrile molecules (BCNB) on the Ag(111) surface compared to the Cu(111) surface. Copper adatoms react with nitrile groups of BCNB to form stable copper-nitrile coordination bonds in metal-organic networks. However, silver adatoms on Ag(111) are less reactive and the resulting bond strength of silver-nitrile bonds is insufficient for the stabilization of a metal-organic network. Instead, solely a hydrogen-bonded structure is observed.

solvent coadsorption — Coadsorption of solvent molecules is shown to be the reason for the emergence of metastable polymorphs in self-assembled monolayers of trinitrile molecules (BCNB) at the fatty acid-graphite interface. Two solvent-dependent polymorphs are observed: a dimer-row structure (γ-phase) in small-chain fatty acids and phenyloctane versus a trimer-monomer-row structure (δ-phase) in nonanoic acid. Both phases exhibit gaps between rows of BCNB molecules, providing sufficient space for the coadsorption of solvent molecules. Temperature dependent transitions of both phases into the more densely packed ε-phase support the assumption of an initial stabilization by solvent coadsorption: The structures are destabilized by desorption of the solvent molecules from the gaps between BCNB molecules. The hypothesis of solvent-incorporation as underlying mechanism for the formation of the γ- and δ-phases is confirmed by the immediate formation of the ε-phase under solvent-free ultrahigh vacuum conditions.

deposition kinetics — The study of monomer deposition rate reveals a hitherto neglected influence on the formation of intermolecular bonds in surface-supported nanostructures. Self-assembled monolayers of trinitrile molecules (BCNB) are deposited onto Cu(111) with either standard ($\sim 2.5 \times 10^{-2}$ monolayer/min) or ultralow ($\sim 2.5 \times 10^{-4}$ monolayer/min) deposition rates. Application of the standard rate results in the coexistence of a hydrogen bonded α-phase and a metal-organic β-phase. Bond formation is attributed to kinetic effects where the deposition rate competes against the adatom replenishment rate. This statement is underpinned by experiments with the ulralow rate, where solely the metal-organic phase is observed. Thus, the lower the molecular deposition rate, the higher is the probability that a sufficient number of adatoms is available to form copper-nitrile bonds.

temperature — Last but not least, the temperature of the substrate is mentioned as a highly important parameter for structure formation, owing to its impact

on both thermodynamics and kinetics. By variation of the substrate temperature, it is possible to reversibly toggle between porous and densely packed polymorphs of tricarboxyl molecules (BTB) on graphite. Here, both phases are thermodynamically favoured. Also irreversible temperature-dependent phase transitions are observed when activation barriers can be overcome, such as in monolayers of BCNB on HOPG(0001) or guanine on Ag(111). Temperature also controls the onset of on-surface reactions, such as C-Br bond cleavage in monolayers of tri-brominated molecules (TBB) on Cu(111). At low temperatures molecules remain intact, whereas at elevated temperatures bond dissociation occurs. Similar observations are made for other halogenated compounds as tetra-brominated biphenyl (TBBP) on Cu(111) and hexa-brominated molecules (TDBB) on Ag(111) and Cu(111). Furthermore, temperature-induced dissociation of C-S bonds in self-assembled monolayers of trithiol molecules (BTT) are analyzed. Upon adsorption at room temperature, molecules stay intact, but sulfur is cleaved off after the increase of substrate temperature. Interestingly, three copper-sulfide phases emerge successively upon tempering. Subsequently to the dissociation of the C-S bonds, irreversible transitions occur in the copper-sulfide phases. Also, a reversible phase transition of the most abundantly studied copper-sulfide phase ($\left(\sqrt{7} \times \sqrt{7}\right) \mathrm{R} \pm 19.1°$) is observed at elevated temperature.

The results presented in this study broaden the understanding of nanostructure formation at single crystal surfaces on the basis of novel materials and parameters. It is urgently required to enlarge the knowledge base of influencing variables in order to facilitate the bottom-up design and synthesis of two-dimensional materials for technological applications. Smartly designed surface-supported nanostructures can be applied in versatile fields, once their synthesis is reliable on a grand scale. Based on the knowledge of fundamental influencing variables on structure formation, also highly specialized structural and electronic properties may be realized in nanostructures. It is essential to study influences on structure formation both under ultrahigh vacuum and ambient conditions to bridge the gap between laboratory conditions and preparation parameters in hypothetical industrial scale productions. In this context, the range of substrates for the fabrication of functional two-dimensional nanostructures should be expanded to more industry-relevant materials, as glasses or polycrystalline matter. As an alternative strategy, mechanisms for a non-destructive transfer of adsorbed nanostructures from surfaces might be a promising topic in the future.

List of Abbreviations

1D	one-dimensional
2D	two-dimensional
3D	three-dimensional
5A	pentanoic acid
7A	heptanoic acid
8A	octanoic acid
9A	nonanoic acid
adatom	adsorbed atom
adlayer	adsorbed (mono)layer
Ag(111)	(111) surface of a silver crystal
BCN	1,3,5-benzenetricarbonitrile
BCNB	1,3,5-tris(4'-biphenyl-4"-carbonitrile)benzene
BDE	bond dissociation energy
BTB	1,3,5-tris(4'-carboxyphenyl)benzene
BTT	1,3,5-benzenetrithiol
CCD	charge coupled device
COF	covalent organic framework
Cu(111)	(111) surface of a copper crystal
DBPBA	3,5-dibromophenylboronic acid
DFT	density functional theory
DFT-vdW	DFT with dispersion correction
ESI	electronic supplementary information
fcc	face-centered cubic ≡ cubic close-packed
FFT	fast Fourier transform
hcp	hexagonal close-packed
HOPG	highly oriented pyrolytic graphite
HOPG(0001)	(0001) surface of an HOPG crystal
IBB	1-(4'-iodophenyl)-3,5-bis(4'-bromophenyl)benzene
I(t)	intensity versus time
I(T)	intensity versus temperature
I(V)	intensity versus voltage
LEED	low energy electron diffraction
LEED-I(V)	LEED intensity versus voltage analysis; ≡ quantitative LEED analysis
nanostructure	structure with nanometer-sized dimensions
NEXAFS	near edge X-ray absorption fine structure
NMR	nuclear magnetic resonance
SEXAFS	surface extended X-ray-absorption fine structure

SSN	surface-supported nanostructure
STM	scanning tunneling microscope/microscopy
TBB	1,3,5-tris(4'-bromophenyl)benzene
TBBP	3,3',5,5'-tetrabromobiphenyl
TDBB	1,3,5-tris(3',5'-dibromophenyl)benzene
TDBPB	1,3,5-tris(3',5'-dibromophenyl)boroxine
TIB	1,3,5-triiodobenzene
TMB	1,3,5-tris(4'-mercaptophenyl)benzene
UHV	ultrahigh vacuum
XPS	X-ray photoelectron spectroscopy

List of Figures

References

[1] J. Sakamoto, J. van Heijst, O. Lukin, and A. D. Schlüter, "Two-dimensional polymers: Just a dream of synthetic chemists?," *Angew. Chem. Int. Edit.*, vol. 48, no. 6, pp. 1030–1069, 2009.

[2] S. Mohnani and D. Bonifazi, "Supramolecular architectures of porphyrins on surfaces: The structural evolution from 1d to 2d to 3d to devices," *Coord. Chem. Rev.*, vol. 254, pp. 2342 – 2362, 2010.

[3] S. De Feyter and F. C. De Schryver, "Self-assembly at the liquid/solid interface: Stm reveals," *J. Phys. Chem. B*, vol. 109, no. 10, pp. 4290–4302, 2005. PMID: 16851494.

[4] T. H. Phan and K. Wandelt, "Molecular self-assembly at metal-electrolyte interfaces," *Int. J. Mol. Sci.*, vol. 14, no. 3, pp. 4498–4524, 2013.

[5] S. Karakatsani, Q. Ge, M. Gladys, G. Held, and D. A. King, "Coverage-dependent molecular tilt of carbon monoxide chemisorbed on pt(110): A combined leed and dft structural analysis," *Surf. Sci.*, vol. 606, pp. 383 – 393, 2012.

[6] M. Lackinger, S. Griessl, W. M. Heckl, M. Hietschold, and G. W. Flynn, "Self-assembly of trimesic acid at the liquid-solid interface - a study of solvent-induced polymorphism," *Langmuir*, vol. 21, no. 11, pp. 4984–4988, 2005. PMID: 15896040.

[7] Y.-T. Shen, N. Zhu, X.-M. Zhang, K. Deng, W. Feng, Q. Yan, S. Lei, D. Zhao, Q.-D. Zeng, and C. Wang, "A foldamer at the liquid/graphite interface: The effect of interfacial interactions, solvent, concentration, and temperature," *Chem.-Eur. J.*, vol. 17, no. 25, pp. 7061–7068, 2011.

[8] A. Kühnle, "Self-assembly of organic molecules at metal surfaces," *Curr. Opin. Colloid Interface Sci.*, vol. 14, no. 2, pp. 157 – 168, 2009.

[9] R. Gutzler, S. Lappe, K. Mahata, M. Schmittel, W. M. Heckl, and M. Lackinger, "Aromatic interaction vs. hydrogen bonding in self-assembly at the liquid-solid interface," *Chem. Commun.*, vol. 0, pp. 680–682, 2009.

[10] S. Seo and H. Lee, "Thermal-processing-induced structural dynamics of thiol self-assembly in solution," *J. Phys. Chem. C*, vol. 115, no. 31, pp. 15480–15486, 2011.

[11] H. Liang, Y. He, Y. Ye, X. Xu, F. Cheng, W. Sun, X. Shao, Y. Wang, J. Li, and K. Wu, "Two-dimensional molecular porous networks constructed by surface assembling," *Coord. Chem. Rev.*, vol. 253, pp. 2959 – 2979, 2009.

[12] D. Bonifazi, S. Mohnani, and A. Llanes-Pallas, "Supramolecular chemistry at interfaces: Molecular recognition on nanopatterned porous surfaces," *Chem.-Eur. J.*, vol. 15, no. 29, pp. 7004–7025, 2009.

[13] M. Lackinger and W. M. Heckl, "A stm perspective on covalent intermolecular coupling reactions on surfaces," *J. Phys. D: Appl. Phys.*, vol. 44, no. 46, p. 464011, 2011.

[14] J. F. Dienstmaier, K. Mahata, H. Walch, W. M. Heckl, M. Schmittel, and M. Lackinger, "On the scalability of supramolecular networks - high packing density vs optimized hydrogen bonds in tricarboxylic acid monolayers," *Langmuir*, vol. 26, no. 13, pp. 10708–10716, 2010.

[15] J. Eichhorn, S. Schlogl, B. V. Lotsch, W. Schnick, W. M. Heckl, and M. Lackinger, "Self-assembly of melem on ag(111)-emergence of porous structures based on amino-heptazine hydrogen bonds," *CrystEngComm*, vol. 13, pp. 5559–5565, 2011.

[16] J. F. Dienstmaier, D. D. Medina, M. Dogru, P. Knochel, T. Bein, W. M. Heckl, and M. Lackinger, "Isoreticular two-dimensional covalent organic frameworks synthesized by on-surface condensation of diboronic acids," *ACS Nano*, vol. 6, no. 8, pp. 7234–7242, 2012.

[17] R. Gutzler, L. Cardenas, and F. Rosei, "Kinetics and thermodynamics in surface-confined molecular self-assembly," *Chem. Sci.*, vol. 2, pp. 2290–2300, 2011.

[18] M. Lackinger, S. Griessl, W. M. Heckl, and M. Hietschold, "Coronene on ag(111) investigated by leed and stm in uhv," *J. Phys. Chem. B*, vol. 106, no. 17, pp. 4482–4485, 2002.

[19] R. Gutzler, H. Walch, G. Eder, S. Kloft, W. M. Heckl, and M. Lackinger, "Surface mediated synthesis of 2d covalent organic frameworks: 1,3,5-tris(4-bromophenyl)benzene on graphite(001), cu(111), and ag(110)," *Chem. Commun.*, vol. 0, pp. 4456–4458, 2009.

[20] J. F. Dienstmaier, A. M. Gigler, A. J. Goetz, P. Knochel, T. Bein, A. Lyapin, S. Reichlmaier, W. M. Heckl, and M. Lackinger, "Synthesis of well-ordered cof monolayers: Surface growth of nanocrystalline precursors versus direct on-surface polycondensation," *ACS Nano*, vol. 5, no. 12, pp. 9737–9745, 2011.

[21] S. De Feyter and F. C. De Schryver, "Two-dimensional supramolecular self-assembly probed by scanning tunneling microscopy," *Chem. Soc. Rev.*, vol. 32, pp. 139–150, 2003.

[22] J. V. Barth, "Molecular architectonic on metal surfaces," *Annu. Rev. Phys. Chem.*, vol. 58, no. 1, pp. 375–407, 2007. PMID: 17430091.

[23] L. Bartels, "Tailoring molecular layers at metal surfaces," *Nat. Chem.*, vol. 2, no. 2, pp. 87–95, 2010.

[24] H. Walch, J. Dienstmaier, G. Eder, R. Gutzler, S. Schloegl, T. Sirtl, K. Das, M. Schmittel, and M. Lackinger, "Extended two-dimensional metal-organic frameworks based on thiolate-copper coordination bonds," *J. Am. Chem. Soc.*, vol. 133, no. 20, pp. 7909–7915, 2011.

[25] U. Schlickum, F. Klappenberger, R. Decker, G. Zoppellaro, S. Klyatskaya, M. Ruben, K. Kern, H. Brune, and J. V. Barth, "Surface-confined metal-organic nanostructures from co-directed assembly of linear terphenyl-dicarbonitrile linkers on ag(111)," *J. Phys Chem. C*, vol. 114, no. 37, pp. 15602–15606, 2010.

[26] T. Sirtl, S. Schloegl, A. Rastgoo-Lahrood, J. Jelic, S. Neogi, M. Schmittel, W. M. Heckl, K. Reuter, and M. Lackinger, "Control of intermolecular bonds by deposition rates at room temperature: Hydrogen bonds versus metal coordination in trinitrile monolayers," *J. Am. Chem. Soc.*, vol. 135, no. 2, pp. 691–695, 2013.

[27] L. Kampschulte, M. Lackinger, A.-K. Maier, R. S. K. Kishore, S. Griessl, M. Schmittel, and W. M. Heckl, "Solvent induced polymorphism in supramolecular 1,3,5-benzenetribenzoic acid monolayers," *J. Phys Chem. B*, vol. 110, no. 22, pp. 10829–10836, 2006.

[28] N. T. N. Ha, T. G. Gopakumar, and M. Hietschold, "Polymorphs of trimesic acid controlled by solvent polarity and concentration of solute at solid-liquid interface," *Surf. Sci.*, vol. 607, pp. 68 – 73, 2013.

[29] G. M. Florio, K. A. Stiso, and J. S. Campanelli, "Surface patterning of benzenecarboxylic acids: Influence of structure, solvent, and concentration on molecular self-assembly," *J. Phys. Chem. C*, vol. 116, no. 34, pp. 18160–18174, 2012.

[30] X. Zhang, Q. Chen, G.-J. Deng, Q.-H. Fan, and L.-J. Wan, "Structural diversity of a monodendron molecule self-assembly in different solvents investigated by scanning tunneling microscopy: From dispersant to counterpart," *J. Phys. Chem. C*, vol. 113, no. 36, pp. 16193–16198, 2009.

[31] Y. Li, Z. Ma, G. Qi, Y. Yang, Q. Zeng, X. Fan, C. Wang, and W. Huang, "Solvent effects on supramolecular networks formed by racemic star-shaped oligofluorene studied by scanning tunneling microscopy," *J. Phys. Chem. C*, vol. 112, no. 23, pp. 8649–8653, 2008.

[32] T. Takami, U. Mazur, and K. Hipps, "Solvent-induced variations in surface structure of a 2,9,16,23-tetra-tert-butyl-phthalocyanine on graphite," *J. Phys. Chem. C*, vol. 113, no. 40, pp. 17479–17483, 2009.

[33] X. Miao, L. Xu, Z. Li, and W. Deng, "Solvent-induced structural transitions of a 1,3,5-tris(10-ethoxycarbonyldecyloxy)benzene assembly revealed by scanning tunneling microscopy," *J. Phys. Chem. C*, vol. 115, no. 8, pp. 3358–3367, 2011.

[34] L. Xu, X. Miao, B. Zha, and W. Deng, "Self-assembly polymorphism: Solvent-responsive two-dimensional morphologies of 2,7-ditridecyloxy-9-fluorenone by scanning tunneling microscopy," *J. Phys. Chem. C*, vol. 116, no. 30, pp. 16014–16022, 2012.

[35] T. Sirtl, W. Song, G. Eder, S. Neogi, M. Schmittel, W. M. Heckl, and M. Lackinger, "Solvent-dependent stabilization of metastable monolayer polymorphs at the liquid-solid interface," *ACS Nano*, vol. 7, no. 8, pp. 6711–6718, 2013.

[36] J. Reichert, R. Ochs, D. Beckmann, H. B. Weber, M. Mayor, and H. v. Löhneysen, "Driving current through single organic molecules," *Phys. Rev. Lett.*, vol. 88, p. 176804, Apr 2002.

[37] T. Sirtl, J. Jelic, J. Meyer, K. Das, W. M. Heckl, W. Moritz, J. Rundgren, M. Schmittel, K. Reuter, and M. Lackinger, "Adsorption structure determination of a large polyaromatic trithiolate on cu(111): combination of leed-i(v) and dft-vdw," *Phys. Chem. Chem. Phys.*, vol. 15, pp. 11054–11060, 2013.

[38] A. Kraft, R. Temirov, S. K. M. Henze, S. Soubatch, M. Rohlfing, and F. S. Tautz, "Lateral adsorption geometry and site-specific electronic structure of a large organic chemisorbate on a metal surface," *Phys. Rev. B*, vol. 74, p. 041402, Jul 2006.

[39] C. T. Campbell and B. E. Koel, "H2s/cu(111): A model study of sulfur poisoning of water-gas shift catalysts," *Surf. Sci.*, vol. 183, pp. 100–112, 1987.

[40] J. Tersoff and D. R. Hamann, "Theory and application for the scanning tunneling microscope," *Phys. Rev. Lett.*, vol. 50, pp. 1998–2001, Jun 1983.

[41] T. E. Feuchtwang and P. H. Cutler, "Tunneling and scanning tunnel microscopy: a critical review," *Phys. Scr.*, vol. 35, no. 2, p. 132, 1987.

[42] L. E. C. van de Leemput and H. van Kempen, "Scanning tunnelling microscopy," *Rep. Prog. Phys.*, vol. 55, no. 8, p. 1165, 1992.

[43] J. Tersoff and D. R. Hamann, "Theory of the scanning tunneling microscope," *Phys. Rev. B*, vol. 31, pp. 805–813, Jan 1985.

[44] R. Wiesendanger, *Scanning Probe Microscopy and Spectroscopy.* Cambridge University Press, 1994.

[45] N. Yao and Z. L. Wang, eds., *Handbook of Microscopy for Nanotechnology.* Kluwer Academic Publishers, 2005.

[46] R. Gutzler, *Surface-Confined Molecular Self-Assembly.* PhD thesis, University of Munich, Germany, 2010.

[47] S. Schlögl, *Influence of Reaction Parameters on the Bottom-Up Synthesis of Two-Dimensional Polymers.* PhD thesis, Tech. Univ. Munich, Germany, 2013.

[48] H. Yamane, K. Kanai, Y. Ouchi, N. Ueno, and K. Seki, "Impact of interface geometric structure on organic-metal interface energetics and subsequent films electronic structure," *J. Electron. Spectrosc.*, vol. 174, pp. 28–34, 2009.

[49] J. Bardeen, "Tunnelling from a many-particle point of view," *Phys. Rev. Lett.*, vol. 6, pp. 57–59, Jan 1961.

[50] C. J. Chen, "Microscopic view of scanning tunneling microscopy," *Topical Conference on Nanometer Scale Properties of Surfaces and Interfaces*, vol. 9, no. 1, pp. 44–50, 1991.

[51] A. D. Gottlieb and L. Wesoloski, "Bardeen's tunnelling theory as applied to scanning tunnelling microscopy: a technical guide to the traditional interpretation," *Nanotechnology*, vol. 17, no. 8, p. R57, 2006.

[52] S. Ohnishi and M. Tsukada, "Molecular orbital theory for the scanning tunneling microscopy," *Solid State Commun.*, vol. 71, no. 5, pp. 391 – 394, 1989.

[53] W. A. Hofer, A. S. Foster, and A. L. Shluger, "Theories of scanning probe microscopes at the atomic scale," *Rev. Mod. Phys.*, vol. 75, pp. 1287–1331, 2003.

[54] G. Doyen, E. Koetter, J. Vigneron, and M. Scheffler, "Theory of scanning tunneling microscopy," *Appl. Phys. A*, vol. 51, no. 4, pp. 281–288, 1990.

[55] C. J. Chen, "Tunneling matrix elements in three-dimensional space: The derivative rule and the sum rule," *Phys. Rev. B*, vol. 42, pp. 8841–8857, Nov 1990.

[56] G. Heimel, S. Duhm, I. Salzmann, A. Gerlach, A. Strozecka, J. Niederhausen, C. Bürker, T. Hosokai, I. Fernandez Torrente, G. Schulze, S. Winkler, A. Wilke, R. Schlesinger, J. Frisch, B. Bröker, A. Vollmer, B. Detlefs, J. Pflaum, S. Kera, K. J. Franke, N. Ueno, J. I. Pascual, F. Schreiber, and N. Koch, "Charged and metallic molecular monolayers through surface-induced aromatic stabilization," *Nat. Chem.*, vol. 5, no. 3, pp. 187–194, 2013.

[57] P. Sautet and C. Joachim, "Calculation of the benzene on rhodium stm images," *Chem. Phys. Lett.*, vol. 185, pp. 23 – 30, 1991.

[58] G. Binnig, H. Rohrer, C. Gerber, and E. Weibel, "Tunneling through a controllable vacuum gap," *Appl. Phys. Lett.*, vol. 40, no. 2, pp. 178–180, 1982.

[59] F. F. Tao, L. Nguyen, and S. Zhang, "Design of a new reactor-like high temperature near ambient pressure scanning tunneling microscope for catalysis studies," *Rev. Sci. Instrum.*, vol. 84, no. 3, p. 034101, 2013.

[60] M. Assig, M. Etzkorn, A. Enders, W. Stiepany, C. R. Ast, and K. Kern, "A 10 mk scanning tunneling microscope operating in ultra high vacuum and high magnetic fields," *Rev. Sci. Instrum.*, vol. 84, no. 3, p. 033903, 2013.

[61] Y. I. Yanson, F. Schenkel, and M. J. Rost, "Design of a high-speed electrochemical scanning tunneling microscope," *Rev. Sci. Instrum.*, vol. 84, no. 2, p. 023702, 2013.

[62] G. Binnig, H. Rohrer, C. Gerber, and E. Weibel, "Surface studies by scanning tunneling microscopy," *Phys. Rev. Lett.*, vol. 49, pp. 57–61, Jul 1982.

[63] B. C. Stipe, M. A. Rezaei, and W. Ho, "A variable-temperature scanning tunneling microscope capable of single-molecule vibrational spectroscopy," *Rev. Sci. Instrum.*, vol. 70, no. 1, pp. 137–143, 1999.

[64] T. Sirtl, "Surface-mediated self-assembly vs. polymerization," Master's thesis, University of Munich, Germany, 2009.

[65] R. Gutzler, W. M. Heckl, and M. Lackinger, "Combination of a knudsen effusion cell with a quartz crystal microbalance: In situ measurement of molecular evaporation rates with a fully functional deposition source," *Rev. Sci. Instrum.*, vol. 81, no. 1, p. 015108, 2010.

[66] K. Besocke, "An easily operable scanning tunneling microscope," *Surf. Sci.*, vol. 181, pp. 145 – 153, 1987.

[67] G. Eder, *From building blocks to 2D networks*. PhD thesis, University of Munich, Germany, 2013.

[68] S. Kloft. PhD thesis, University of Munich, Germany. in preparation.

[69] C. Davisson and L. H. Germer, "Diffraction of electrons by a crystal of nickel," *Phys. Rev.*, vol. 30, pp. 705–740, Dec 1927.

[70] L. De Broglie, *Recherches sur la theorie des quanta*. PhD thesis, 1924.

[71] J. C. Riviere, "Auger electron spectroscopy," *Contemp. Phys.*, vol. 14, no. 6, pp. 513–539, 1973.

[72] L. J. Clarke, *Surface crystallography, an introduction to low energy electron diffraction*. John Wiley, Chichester, 1985.

[73] F. Jona, J. A. S. Jr, and W. S. Yang, "Low-energy electron diffraction for surface structure analysis," *Rep. Prog. Phys.*, vol. 45, no. 5, p. 527, 1982.

[74] N. W. Ashcroft and N. D. Mermin, *Solid State Physics*. Harcourt College Publishers, 1976.

[75] W. Moritz, "Effective calculation of leed intensities using symmetry-adapted functions," *J. Phys. C Solid State*, vol. 17, no. 2, p. 353, 1984.

[76] G. Kleinle, W. Moritz, and G. Ertl, "An efficient method for leed crystallography," *Surf. Sci.*, vol. 238, pp. 119 – 131, 1990.

[77] H. Over, U. Ketterl, W. Moritz, and G. Ertl, "Optimization methods and their use in low-energy electron-diffraction calculations," *Phys. Rev. B*, vol. 46, pp. 15438–15446, Dec 1992.

[78] J. C. Slater, "A simplification of the hartree-fock method," *Phys. Rev.*, vol. 81, pp. 385–390, Feb 1951.

[79] W. Kohn and L. J. Sham, "Self-consistent equations including exchange and correlation effects," *Phys. Rev.*, vol. 140, pp. A1133–A1138, Nov 1965.

[80] R. Gaspar, "Über eine approximation des hartree-fockschen potentials durch eine universelle potentialfunktion," *Acta Phys. Acad. Sci. Hung.*, vol. 3, no. 3-4, pp. 263–286, 1954.

[81] W. Moritz, J. Landskron, and M. Deschauer, "Perspectives for surface structure analysis with low energy electron diffraction," *Surf. Sci.*, vol. 603, pp. 1306 – 1314, 2009.

[82] J. B. Pendry, "Reliability factors for leed calculations," *J. Phys. C Solid State*, vol. 13, no. 5, p. 937, 1980.

[83] G. Kleinle, W. Moritz, D. Adams, and G. Ertl, "A novel procedure for fast surface structural analysis based on leed intensity data," *Surf. Sci.*, vol. 219, pp. L637 – L645, 1989.

[84] Omicron NanoTechnology GmbH, Taunusstein, Germany, *Spectaleed Optics and Electron gun User's Guide*, 4.0 ed., 1999.

[85] Specs GmbH, Berlin, Germany, *Optics and Power Supplies ErLEED UserManual*, 1.2 ed., 2002.

[86] S. Schloegl, T. Sirtl, J. Eichhorn, W. M. Heckl, and M. Lackinger, "Synthesis of two-dimensional phenylene-boroxine networks through in vacuo condensation and on-surface radical addition," *Chem. Commun.*, vol. 47, no. 45, pp. 12355–12357, 2011.

[87] H. Walch, R. Gutzler, T. Sirtl, G. Eder, and M. Lackinger, "Material- and orientation-dependent reactivity for heterogeneously catalyzed carbon-bromine bond homolysis," *J. Phys. Chem. C*, vol. 114, no. 29, pp. 12604–12609, 2010.

[88] R. Gutzler, T. Sirtl, J. F. Dienstmaier, K. Mahata, W. M. Heckl, M. Schmittel, and M. Lackinger, "Reversible phase transitions in self-assembled mono layers at the liquid-solid interface: Temperature-controlled opening and closing of nanopores," *J. Am. Chem. Soc.*, vol. 132, no. 14, pp. 5084–5090, 2010.

[89] S. Bauer, "Beugung niederenergetischer elektronen (leed) an guanin-monolagen auf ag(111)," project study, Tech. Univ. Munich, Germany, 2012.

[90] L.-g. Liu and W. A. Bassett, "Compression of ag and phase transformation of nacl," *J. Appl. Phys.*, vol. 44, no. 4, pp. 1475–1479, 1973.

[91] M. Winter, "Webelements: the periodic table on the www." http://www.webelements.com/ (effective 2013-05-24).

[92] M. E. Straumanis and L. S. Yu, "Lattice parameters, densities, expansion coefficients and perfection of structure of cu and of cu-in alpha phase," *Acta Crystallogr. A*, vol. 25, no. 6, pp. 676–682, 1969.

[93] P. Trucano and R. Chen, "Structure of graphite by neutron diffraction," *Nature*, vol. 258, p. 136, 1975.

[94] P. W. Atkins, *Physikalische Chemie*. WiILEY-VCH Verlag GmbH, Weinheim, Germany, 2004.

[95] E. Bosch and C. L. Barnes, "Triangular halogen-halogen-halogen interactions as a cohesive force in the structures of trihalomesitylenes," *Cryst. Growth Des.*, vol. 2, no. 4, pp. 299–302, 2002.

[96] E. Arras, A. P. Seitsonen, F. Klappenberger, and J. V. Barth, "Nature of the attractive interaction between proton acceptors and organic ring systems," *Phys. Chem. Chem. Phys.*, vol. 14, pp. 15995–16001, 2012.

[97] P. Messina, A. Dmitriev, N. Lin, H. Spillmann, M. Abel, J. V. Barth, and K. Kern, "Direct observation of chiral metal-organic complexes assembled on a cu(100) surface," *J. Am. Chem. Soc.*, vol. 124, no. 47, pp. 14000–14001, 2002.

[98] F. G. A. Stone, "Perspectives in organometallic chemistry," *Nature*, vol. 232, pp. 534–539, Aug. 1971.

[99] P. Seema, J. Behler, and D. Marx, "Adsorption of methanethiolate and atomic sulfur at the cu(111) surface: A computational study," *J. Phys. Chem. C*, vol. 117, no. 1, pp. 337–348, 2013.

[100] C. Meier, M. Roos, D. Künzel, A. Breitruck, H. E. Hoster, K. Landfester, A. Gross, R. J. Behm, and U. Ziener, "Concentration and coverage dependent adlayer structures: From two-dimensional networks to rotation in a bearing," *J. Phys. Chem. C*, vol. 114, no. 2, pp. 1268–1277, 2010.

[101] M. Lackinger and W. M. Heckl, "Carboxylic acids: Versatile building blocks and mediators for two-dimensional supramolecular self-assembly," *Langmuir*, vol. 25, no. 19, pp. 11307–11321, 2009. PMID: 19453128.

[102] Y. Ye, W. Sun, Y. Wang, X. Shao, X. Xu, F. Cheng, J. Li, and K. Wu, "A unified model: Self-assembly of trimesic acid on gold," *J. Phys. Chem. C*, vol. 111, no. 28, pp. 10138–10141, 2007.

[103] L. Grill, M. Dyer, L. Lafferentz, M. Persson, M. V. Peters, and S. Hecht, "Nano-architectures by covalent assembly of molecular building blocks," *Nat. Nano.*, vol. 2, pp. 687–691, Nov. 2007.

[104] W.-I. Lin, "Low energy electron diffraction - 3,3',5,5'-tetrabromobiphenyl adsorbed onto cu(111)," internship report, University of Munich, 2011.

[105] J. Domange and J. Oudar, "Structure et conditions de formation de la couche d'adsorption du soufre sur le cuivre," *Surf. Sci.*, vol. 11, pp. 124 – 142, 1968.

[106] N. Miyashita and D. G. Kurth, "Directing supramolecular assemblies on surfaces," *J. Mater. Chem.*, vol. 18, pp. 2636–2649, 2008.

[107] G. Pawin, K. Wong, D. Kim, D. Sun, L. Bartels, S. Hong, T. Rahman, R. Carp, and M. Marsella, "A surface coordination network based on substrate-derived metal adatoms with local charge excess," *Angew. Chem. Int. Edit.*, vol. 47, no. 44, pp. 8442–8445, 2008.

[108] N. Lin, S. Stepanow, F. Vidal, K. Kern, M. S. Alam, S. Stromsdorfer, V. Dremov, P. Muller, A. Landa, and M. Ruben, "Surface-assisted coordination chemistry and self-assembly," *Dalton Trans.*, vol. 0, pp. 2794–2800, 2006.

[109] M. Schütte, D. G. Kurth, M. R. Linford, H. Cölfen, and H. Möhwald, "Metallosupramolecular thin polyelectrolyte films," *Angew. Chem. Int. Edit.*, vol. 37, no. 20, pp. 2891–2893, 1998.

[110] D. Kühne, F. Klappenberger, R. Decker, U. Schlickum, H. Brune, S. Klyatskaya, M. Ruben, and J. V. Barth, "Self-assembly of nanoporous chiral networks with varying symmetry from sexiphenyl-dicarbonitrile on ag(111)," *J. Phys. Chem. C*, vol. 113, no. 41, pp. 17851–17859, 2009.

[111] S. Klyatskaya, F. Klappenberger, U. Schlickum, D. Kühne, M. Marschall, J. Reichert, R. Decker, W. Krenner, G. Zoppellaro, H. Brune, J. V. Barth, and M. Ruben, "Surface-confined self-assembly of di-carbonitrile polyphenyls," *Adv. Funct. Mater.*, vol. 21, no. 7, pp. 1230–1240, 2011.

[112] Y. Li and N. Lin, "Combined scanning tunneling microscopy and kinetic monte carlo study on kinetics of cu-coordinated pyridyl-porphyrin supramolecular self-assembly on a au(111) surface," *Phys. Rev. B*, vol. 84, p. 125418, Sep 2011.

[113] P. M. Agrawal, B. M. Rice, and D. L. Thompson, "Predicting trends in rate parameters for self-diffusion on fcc metal surfaces," *Surf. Sci.*, vol. 515, pp. 21 – 35, 2002.

[114] N. Lin, D. Payer, A. Dmitriev, T. Strunskus, C. Wöll, J. V. Barth, and K. Kern, "Two-dimensional adatom gas bestowing dynamic heterogeneity on surfaces," *Angew. Chem. Int. Edit.*, vol. 44, no. 10, pp. 1488–1491, 2005.

[115] T. Yokoyama, S. Yokoyama, T. Kamikado, Y. Okuno, and S. Mashiko, "Selective assembly on a surface of supramolecular aggregates with controlled size and shape," *Nature*, vol. 413, pp. 619–621, Oct. 2001.

[116] D. Döpp, C. Kruse, U. Flörke, and G. Henkel, "rel-(1r,4r,9r)-1-acetyl-9-(1-pyrrolidinyl)-1,4-dihydro-1,4-ethanonaphthalene-9-carbonitrile: the major [4+2]-photocycloadduct of 1-acetonaphthone with 2-(1-pyrrolidinyl)propenenitrile," *Acta Crystallogr., Sect. E*, vol. 62, no. 8, pp. o3245–o3246, 2006.

[117] S. Özbey, F. Kaynak, H. Göker, and C. Kus, "Synthesis and crystal structure elucidation of 1-(4-fluorobenzyl)-2-(4-cyanophenyl)-1h- benzimidazole-5-carbonitrile," *J. Chem. Crystallogr.*, vol. 34, no. 12, pp. 851–858, 2004.

[118] S. Griessl, M. Lackinger, M. Edelwirth, M. Hietschold, and W. M. Heckl, "Self-assembled two-dimensional molecular host-guest architectures from trimesic acid," *Single Mol.*, vol. 3, no. 1, pp. 25–31, 2002.

[119] M. Ruben, D. Payer, A. Landa, A. Comisso, C. Gattinoni, N. Lin, J.-P. Collin, J.-P. Sauvage, A. De Vita, and K. Kern, "2d supramolecular assemblies of benzene-1,3,5-triyl-tribenzoic acid: Temperature-induced phase transformations and hierarchical organization with macrocyclic molecules," *J. Am. Chem. Soc.*, vol. 128, no. 49, pp. 15644–15651, 2006. PMID: 17147373.

[120] R. Otero, M. Lukas, R. E. A. Kelly, W. Xu, E. Lægsgaard, I. Stensgaard, L. N. Kantorovich, and F. Besenbacher, "Elementary structural motifs in a random network of cytosine adsorbed on a gold(111) surface," *Science*, vol. 319, no. 5861, pp. 312–315, 2008.

[121] M. Stöhr, M. Wahl, C. H. Galka, T. Riehm, T. A. Jung, and L. H. Gade, "Controlling molecular assembly in two dimensions: The concentration dependence of thermally induced 2d aggregation of molecules on a metal surface," *Angew. Chem. Int. Edit.*, vol. 44, no. 45, pp. 7394–7398, 2005.

[122] T. Classen, M. Lingenfelder, Y. Wang, R. Chopra, C. Virojanadara, U. Starke, G. Costantini, G. Fratesi, S. Fabris, S. de Gironcoli, S. Baroni, S. Haq, R. Raval, and K. Kern, "Hydrogen and coordination bonding supramolecular structures of trimesic acid on cu(110)," *J. Phys. Chem. A*, vol. 111, no. 49, pp. 12589–12603, 2007. PMID: 17994713.

[123] D. Heim, D. Ecija, K. Seufert, W. Auwärter, C. Aurisicchio, C. Fabbro, D. Bonifazi, and J. V. Barth, "Self-assembly of flexible one-dimensional coordination polymers on metal surfaces," *J. Am. Chem. Soc.*, vol. 132, no. 19, pp. 6783–6790, 2010.

[124] S. L. Tait, A. Langner, N. Lin, S. Stepanow, C. Rajadurai, M. Ruben, and K. Kern, "One-dimensional self-assembled molecular chains on cu(100): Interplay between surface-assisted coordination chemistry and substrate commensurability," *J. Phys Chem. C*, vol. 111, no. 29, pp. 10982–10987, 2007.

[125] M. Matena, M. Stöhr, T. Riehm, J. Björk, S. Martens, M. S. Dyer, M. Persson, J. Lobo-Checa, K. Müller, M. Enache, H. Wadepohl, J. Zegenhagen, T. A. Jung, and L. H. Gade, "Aggregation and contingent metal/surface reactivity of 1,3,8,10-tetraazaperopyrene (tapp) on cu(111)," *Chem.-Eur. J.*, vol. 16, no. 7, pp. 2079–2091, 2010.

[126] Y. Wang, S. Fabris, T. W. White, F. Pagliuca, P. Moras, M. Papagno, D. Topwal, P. Sheverdyaeva, C. Carbone, M. Lingenfelder, T. Classen, K. Kern, and G. Costantini, "Varying molecular interactions by coverage in supramolecular surface chemistry," *Chem. Commun.*, vol. 48, pp. 534–536, 2012.

[127] J. Bjork, M. Matena, M. S. Dyer, M. Enache, J. Lobo-Checa, L. H. Gade, T. A. Jung, M. Stohr, and M. Persson, "Stm fingerprint of molecule-adatom interactions in a self-assembled metal-organic surface coordination network on cu(111)," *Phys. Chem. Chem. Phys.*, vol. 12, pp. 8815–8821, 2010.

[128] M. Matena, T. Riehm, M. Stöhr, T. A. Jung, and L. H. Gade, "Transforming surface coordination polymers into covalent surface polymers: Linked polycondensed aromatics through oligomerization of n-heterocyclic carbene intermediates," *Angew. Chem. Int. Edit.*, vol. 47, no. 13, pp. 2414–2417, 2008.

[129] U. Schlickum, R. Decker, F. Klappenberger, G. Zoppellaro, S. Klyatskaya, M. Ruben, I. Silanes, A. Arnau, K. Kern, H. Brune, and J. V. Barth, "Metal-organic honeycomb nanomeshes with tunable cavity size," *Nano Lett.*, vol. 7, no. 12, pp. 3813–3817, 2007. PMID: 18020476.

[130] T. Classen, G. Fratesi, G. Costantini, S. Fabris, F. L. Stadler, C. Kim, S. de Gironcoli, S. Baroni, and K. Kern, "Templated growth of metal-organic coordination chains at surfaces," *Angew. Chem. Int. Edit.*, vol. 44, no. 38, pp. 6142–6145, 2005.

[131] D. Dougherty, P. Maksymovych, and J. Y. Jr., "Direct stm evidence for cu-benzoate surface complexes on cu(110)," *Surf. Sci.*, vol. 600, pp. 4484 – 4491, 2006.

[132] S. Stepanow, N. Lin, D. Payer, U. Schlickum, F. Klappenberger, G. Zoppellaro, M. Ruben, H. Brune, J. V. Barth, and K. Kern, "Surface-assisted assembly of 2d metal-organic networks that exhibit unusual threefold coordination symmetry," *Angew. Chem. Int. Edit.*, vol. 46, no. 5, pp. 710–713, 2007.

[133] J. Brunel, O. Mongin, A. Jutand, I. Ledoux, J. Zyss, and M. Blanchard-Desce, "Propeller-shaped octupolar molecules derived from triphenylbenzene for nonlinear optics: Synthesis and optical studies," *Chem. Mat.*, vol. 15, no. 21, pp. 4139–4148, 2003.

[134] M. J. Frisch, G. W. Trucks, H. B. Schlegel, G. E. Scuseria, M. A. Robb, J. R. Cheeseman, J. A. Montgomery, Jr., T. Vreven, K. N. Kudin, J. C. Burant, J. M. Millam, S. S. Iyengar, J. Tomasi, V. Barone, B. Mennucci, M. Cossi, G. Scalmani, N. Rega, G. A. Petersson, H. Nakatsuji, M. Hada, M. Ehara, K. Toyota, R. Fukuda, J. Hasegawa, M. Ishida, T. Nakajima, Y. Honda, O. Kitao, H. Nakai, M. Klene, X. Li, J. E. Knox, H. P. Hratchian, J. B. Cross, V. Bakken, C. Adamo, J. Jaramillo, R. Gomperts, R. E. Stratmann, O. Yazyev, A. J. Austin, R. Cammi, C. Pomelli, J. W. Ochterski, P. Y. Ayala, K. Morokuma, G. A. Voth, P. Salvador, J. J. Dannenberg, V. G. Zakrzewski, S. Dapprich, A. D. Daniels, M. C. Strain, O. Farkas, D. K. Malick, A. D. Rabuck, K. Raghavachari, J. B. Foresman, J. V. Ortiz, Q. Cui, A. G. Baboul, S. Clifford, J. Cioslowski, B. B. Stefanov, G. Liu, A. Liashenko, P. Piskorz, I. Komaromi, R. L. Martin, D. J. Fox, T. Keith, M. A. Al-Laham, C. Y. Peng, A. Nanayakkara, M. Challacombe, P. M. W. Gill, B. Johnson, W. Chen, M. W. Wong, C. Gonzalez, and J. A. Pople, "Gaussian 03, Revision C.02." Gaussian, Inc., Wallingford, CT, 2004.

[135] A. D. Becke, "A new mixing of hartree-fock and local density-functional theories," *J. Chem. Phys.*, vol. 98, no. 2, pp. 1372–1377, 1993.

[136] W. Koch and M. C. Holthausen, *A Chemist's Guide to Density Functional Theory, 2nd Edition*. Wiley-VCH, 2001.

[137] S. J. Clark, M. D. Segall, C. J. Pickard, P. J. Hasnip, M. I. J. Probert, K. Refson, and M. C. Payne, "First principles methods using castep," *Z. Kristallogr.*, vol. 220, pp. 567–570, May 2005.

[138] J. P. Perdew, K. Burke, and M. Ernzerhof, "Generalized gradient approximation made simple," *Phys. Rev. Lett.*, vol. 77, pp. 3865–3868, Oct 1996.

[139] A. Tkatchenko and M. Scheffler, "Accurate molecular van der waals interactions from ground-state electron density and free-atom reference data," *Phys. Rev. Lett.*, vol. 102, p. 073005, Feb 2009.

[140] D. Vanderbilt, "Soft self-consistent pseudopotentials in a generalized eigenvalue formalism," *Phys. Rev. B*, vol. 41, pp. 7892–7895, Apr 1990.

[141] H. J. Monkhorst and J. D. Pack, "Special points for brillouin-zone integrations," *Phys. Rev. B*, vol. 13, pp. 5188–5192, Jun 1976.

[142] Y. Yang and C. Wang, "Solvent effects on two-dimensional molecular self-assemblies investigated by using scanning tunneling microscopy," *Curr. Opin. Colloid Interface Sci.*, vol. 14, no. 2, pp. 135 – 147, 2009.

[143] U. K. Weber, V. M. Burlakov, L. M. A. Perdigão, R. H. J. Fawcett, P. H. Beton, N. R. Champness, J. H. Jefferson, G. A. D. Briggs, and D. G. Pettifor, "Role of interaction anisotropy in the formation and stability of molecular templates," *Phys. Rev. Lett.*, vol. 100, p. 156101, Apr 2008.

[144] N. Martsinovich and A. Troisi, "Modeling the self-assembly of benzenedicarboxylic acids using monte carlo and molecular dynamics simulations," *J. Phys. Chem. C*, vol. 114, no. 10, pp. 4376–4388, 2010.

[145] J. Adisoejoso, K. Tahara, S. Lei, P. Szabelski, W. Rzysko, K. Inukai, M. O. Blunt, Y. Tobe, and S. De Feyter, "One building block, two different nanoporous self-assembled monolayers: A combined stm and monte carlo study," *ACS Nano*, vol. 6, no. 1, pp. 897–903, 2012.

[146] S. Lei, K. Tahara, K. Müllen, P. Szabelski, Y. Tobe, and S. De Feyter, "Mixing behavior of alkoxylated dehydrobenzo[12]annulenes at the solid-liquid interface: Scanning tunneling microscopy and monte carlo simulations," *ACS Nano*, vol. 5, no. 5, pp. 4145–4157, 2011.

[147] S. Uemura, R. Tanoue, N. Yilmaz, A. Ohira, and M. Kunitake, "Molecular dynamics in two-dimensional supramolecular systems observed by stm," *Materials*, vol. 3, no. 8, pp. 4252–4276, 2010.

[148] S. Lei, K. Tahara, F. C. De Schryver, M. Van der Auweraer, Y. Tobe, and S. De Feyter, "One building block, two different supramolecular surface-confined patterns: Concentration in control at the solid-liquid interface," *Angew. Chem. Int. Edit.*, vol. 47, no. 16, pp. 2964–2968, 2008.

[149] L. Kampschulte, T. L. Werblowsky, R. S. K. Kishore, M. Schmittel, W. M. Heckl, and M. Lackinger, "Thermodynamical equilibrium of binary supramolecular networks at the liquid-solid interface," *J. Am. Chem. Soc.*, vol. 130, no. 26, pp. 8502–8507, 2008. PMID: 18533654.

[150] A. Jahanbekam, S. Vorpahl, U. Mazur, and K. W. Hipps, "Temperature stability of three commensurate surface structures of coronene adsorbed on au(111) from heptanoic acid in the 0 to 60c range," *J. Phys. Chem. C*, vol. 117, no. 6, pp. 2914–2919, 2013.

[151] A. Bellec, C. Arrigoni, G. Schull, L. Douillard, C. Fiorini-Debuisschert, F. Mathevet, D. Kreher, A.-J. Attias, and F. Charra, "Solution-growth kinetics and thermodynamics of nanoporous self-assembled molecular monolayers," *J. Chem. Phys.*, vol. 134, no. 12, p. 124702, 2011.

[152] C. Marie, F. Silly, L. Tortech, K. Müllen, and D. Fichou, "Tuning the packing density of 2d supramolecular self-assemblies at the solid-liquid interface using variable temperature," *ACS Nano*, vol. 4, no. 3, pp. 1288–1292, 2010. PMID: 20155970.

[153] Y. Li, C. Liu, Y. Xie, X. Li, X. Li, X. Fan, K. Deng, Q. Zeng, and C. Wang, "Temperature-controlled self-assembling structure with selective guest-recognition at the liquid-solid interface," *Phys. Chem. Chem. Phys.*, vol. 15, pp. 125–128, 2013.

[154] B. J. Gyarfas, B. Wiggins, M. Zosel, and K. W. Hipps, "Supramolecular structures of coronene and alkane acids at the au(111)-solution interface: A scanning tunneling microscopy study," *Langmuir*, vol. 21, no. 3, pp. 919–923, 2005. PMID: 15667168.

[155] S. De Feyter, P. C. M. Grim, M. Rücker, P. Vanoppen, C. Meiners, M. Sieffert, S. Valiyaveettil, K. Müllen, and F. C. De Schryver, "Expression of chirality by achiral coadsorbed molecules in chiral monolayers observed by stm," *Angew. Chem. Int. Edit.*, vol. 37, no. 9, pp. 1223–1226, 1998.

[156] P. Vanoppen, P. C. M. Grim, M. Rücker, S. De Feyter, G. Moessner, S. Valiyaveettil, K. Müllen, and F. C. De Schryver, "Solvent codeposition and cis-trans isomerization of isophthalic acid derivatives studied by stm," *J. Phys. Chem.*, vol. 100, no. 50, pp. 19636–19641, 1996.

[157] P. C. M. Grim, P. Vanoppen, M. Rucker, S. D. Feyter, S. Valiyaveettil, G. Moessner, K. Mullen, and F. C. D. Schryver, "Molecular organization of azobenzene derivatives at the liquid/graphite interface observed with scanning tunneling microscopy," *J. Vac. Sci. Technol. B*, vol. 15, no. 4, pp. 1419–1424, 1997.

[158] H. Walch, A.-K. Maier, W. M. Heckl, and M. Lackinger, "Isotopological supramolecular networks from melamine and fatty acids," *J. Phys. Chem. C*, vol. 113, no. 3, pp. 1014–1019, 2009.

[159] J. Saiz-Poseu, A. Martinez-Otero, T. Roussel, J. K.-H. Hui, M. L. Montero, R. Urcuyo, M. J. MacLachlan, J. Faraudo, and D. Ruiz-Molina, "Self-assembly of a catechol-based macrocycle at the liquid-solid interface: experiments and molecular dynamics simulations," *Phys. Chem. Chem. Phys.*, vol. 14, pp. 11937–11943, 2012.

[160] Y. Kikkawa, H. Kihara, M. Takahashi, M. Kanesato, T. S. Balaban, and J.-M. Lehn, "Two-dimensional structures of anthracene derivatives: Photodimerization and host-guest chemistry," *J. Phys. Chem. B*, vol. 114, no. 50, pp. 16718–16722, 2010.

[161] Y. Kikkawa, K. Omori, M. Kanesato, and K. Hiratani, "Two-dimensional structures of isobutenyl ether compounds possessing dodecyl and tridecyl chains: Effects of solvent and tandem claisen rearrangement," *Chem. Lett.*, vol. 41, no. 10, pp. 1196–1198, 2012.

[162] Z. Ma, Y.-Y. Wang, P. Wang, W. Huang, Y.-B. Li, S.-B. Lei, Y.-L. Yang, X.-L. Fan, and C. Wang, "Star-shaped oligofluorenes end-capped with carboxylic groups: Syntheses and self-assembly at the liquid-solid interface," *ACS Nano*, vol. 1, no. 3, pp. 160–167, 2007.

[163] W. Mamdouh, H. Uji-i, J. S. Ladislaw, A. E. Dulcey, V. Percec, F. C. De Schryver, and S. De Feyter, "Solvent controlled self-assembly at the liquid-solid interface revealed by stm," *J. Am. Chem. Soc.*, vol. 128, no. 1, pp. 317–325, 2006.

[164] K. Tahara, S. Furukawa, H. Uji-i, T. Uchino, T. Ichikawa, J. Zhang, W. Mamdouh, M. Sonoda, F. C. De Schryver, S. De Feyter, and Y. Tobe, "Two-dimensional porous molecular networks of dehydrobenzo[12]annulene derivatives via alkyl chain interdigitation," *J. Am. Chem. Soc.*, vol. 128, no. 51, pp. 16613–16625, 2006.

[165] S. Y. Lee, J. Noh, E. Ito, H. Lee, and M. Hara, "Solvent effect on formation of cysteamine self-assembled monolayers on au(111)," *Jpn. J. Appl. Phys.*, vol. 42, no. Part 1, No. 1, pp. 236–241, 2003.

[166] M. Alemani, L. Gross, F. Moresco, K.-H. Rieder, C. Wang, X. Bouju, A. Gourdon, and C. Joachim, "Recording the intramolecular deformation of a 4-legs molecule during its stm manipulation on a cu(211) surface," *Chem. Phys. Lett.*, vol. 402, pp. 180 – 185, 2005.

[167] A. Hauschild, K. Karki, B. C. C. Cowie, M. Rohlfing, F. S. Tautz, and M. Sokolowski, "Molecular distortions and chemical bonding of a large pi-conjugated molecule on a metal surface," *Phys. Rev. Lett.*, vol. 94, p. 036106, Jan 2005.

[168] L. Kilian, W. Weigand, E. Umbach, A. Langner, M. Sokolowski, H. L. Meyerheim, H. Maltor, B. C. C. Cowie, T. Lee, and P. Bäuerle, "Adsorption site determination of a large pi-conjugated molecule by normal incidence x-ray standing waves: End-capped quaterthiophene on ag(111)," *Phys. Rev. B*, vol. 66, p. 075412, Aug 2002.

[169] G. Held, S. Uremovic, C. Stellwag, and D. Menzel, "A low-energy electron diffraction data acquisition system for very low electron doses based upon a slow scan charge coupled device camera," *Rev. Sci. Instrum.*, vol. 67, no. 2, pp. 378–383, 1996.

[170] J. Vogt, "The structure of n2 adsorbed on the rumpled nacl(100) surface - a combined leed and dft-d study," *J. Chem. Phys.*, vol. 137, no. 17, p. 174705, 2012.

[171] R. Lindsay, S. Tomic, A. Wander, M. Garcia-Mendez, and G. Thornton, "Low energy electron diffraction study of tio2(110)(2x1)-[hcoo]-," *J. Phys. Chem. C*, vol. 112, no. 36, pp. 14154–14157, 2008.

[172] C. Bittencourt, E. Soares, and D. Woodruff, "Low energy electron diffraction structure determination of the ni(110)c(2x2)-cn surface phase," *Surf. Sci.*, vol. 526, pp. 33 – 43, 2003.

[173] Z. V. Zheleva, T. Eralp, and G. Held, "Complete experimental structure determination of the p(3x2)pg phase of glycine on cu110," *J. Phys. Chem. C*, vol. 116, no. 1, pp. 618–625, 2012.

[174] K. Johnson, B. Sauerhammer, S. Titmuss, and D. A. King, "Benzene adsorption on ir(100) studied by low-energy electron diffraction i-v analysis: Evidence for formation of tilted benzyne," *J. Chem. Phys.*, vol. 114, no. 21, pp. 9539–9548, 2001.

[175] G. Held, W. Braun, H.-P. Steinrück, S. Yamagishi, S. J. Jenkins, and D. A. King, "Light-atom location in adsorbed benzene by experiment and theory," *Phys. Rev. Lett.*, vol. 87, p. 216102, Nov 2001.

[176] K. Pussi, M. Lindroos, J. Katainen, K. Habermehl-Cwirzen, J. Lahtinen, and A. Seitsonen, "The adsorption structure on co(0001): a combined tensor leed and dft study," *Surf. Sci.*, vol. 572, pp. 1 – 10, 2004.

[177] G. Held, M. P. Bessent, S. Titmuss, and D. A. King, "Realistic molecular distortions and strong substrate buckling induced by the chemisorption of benzene on ni(111)," *J. Chem. Phys.*, vol. 105, no. 24, pp. 11305–11312, 1996.

[178] K. Pussi, M. Lindroos, and C. Barnes, "A tensor leed study of an unusual cyclic hydrocarbon intermediate formed by benzene adsorption on co(10-10)," *Chem. Phys. Lett.*, vol. 341, pp. 7 – 15, 2001.

[179] W. Braun, G. Held, H.-P. Steinrück, C. Stellwag, and D. Menzel, "Coverage-dependent changes in the adsorption geometries of ordered benzene layers on ru(0001)," *Surf. Sci.*, vol. 475, pp. 18 – 36, 2001.

[180] C. Stellwag, G. Held, and D. Menzel, "The geometry of ordered benzene layers on ru(001)," *Surf. Sci.*, vol. 325, pp. L379 – L384, 1995.

[181] W. Moritz, B. Wang, M.-L. Bocquet, T. Brugger, T. Greber, J. Wintterlin, and S. Günther, "Structure determination of the coincidence phase of graphene on ru(0001)," *Phys. Rev. Lett.*, vol. 104, p. 136102, Apr 2010.

[182] H. I. Li, K. Pussi, K. J. Hanna, L.-L. Wang, D. D. Johnson, H.-P. Cheng, H. Shin, S. Curtarolo, W. Moritz, J. A. Smerdon, R. McGrath, and R. D. Diehl, "Surface geometry of c60 on ag(111)," *Phys. Rev. Lett.*, vol. 103, p. 056101, Jul 2009.

[183] V. G. Ruiz, W. Liu, E. Zojer, M. Scheffler, and A. Tkatchenko, "Density-functional theory with screened van der waals interactions for the modeling of hybrid inorganic-organic systems," *Phys. Rev. Lett.*, vol. 108, p. 146103, Apr 2012.

[184] S. Grimme, "Semiempirical gga-type density functional constructed with a long-range dispersion correction," *J. Comput. Chem.*, vol. 27, no. 15, pp. 1787–1799, 2006.

[185] A. Tkatchenko, L. Romaner, O. T. Hofmann, E. Zojer, C. Ambrosch-Draxl, and M. Scheffler, "Van der waals interactions between organic adsorbates and at organic/inorganic interfaces," *MRS Bull.*, vol. 35, pp. 435–442, 6 2010.

[186] N. Atodiresei, V. Caciuc, P. Lazić, and S. Blügel, "Chemical versus van der waals interaction: The role of the heteroatom in the flat absorption of aromatic molecules c6h6, c5nh5, and c4n2h4 on the cu(110) surface," *Phys. Rev. Lett.*, vol. 102, p. 136809, Apr 2009.

[187] D. Stradi, S. Barja, C. Diaz, M. Garnica, B. Borca, J. J. Hinarejos, D. Sanchez-Portal, M. Alcami, A. Arnau, A. L. Vazquez de Parga, R. Miranda, and F. Martin, "Role of dispersion forces in the structure of graphene monolayers on ru surfaces," *Phys. Rev. Lett.*, vol. 106, p. 186102, May 2011.

[188] M.-T. Nguyen, C. A. Pignedoli, M. Treier, R. Fasel, and D. Passerone, "The role of van der waals interactions in surface-supported supramolecular networks," *Phys. Chem. Chem. Phys.*, vol. 12, pp. 992–999, 2010.

[189] T. Olsen, J. Yan, J. J. Mortensen, and K. S. Thygesen, "Dispersive and covalent interactions between graphene and metal surfaces from the random phase approximation," *Phys. Rev. Lett.*, vol. 107, p. 156401, Oct 2011.

[190] E. McNellis, J. Meyer, A. D. Baghi, and K. Reuter, "Stabilizing a molecular switch at solid surfaces: A density functional theory study of azobenzene on cu(111), ag(111), and au(111)," *Phys. Rev. B*, vol. 80, p. 035414, Jul 2009.

[191] G. Mercurio, E. R. McNellis, I. Martin, S. Hagen, F. Leyssner, S. Soubatch, J. Meyer, M. Wolf, P. Tegeder, F. S. Tautz, and K. Reuter, "Structure and energetics of azobenzene on ag(111): Benchmarking semiempirical dispersion correction approaches," *Phys. Rev. Lett.*, vol. 104, p. 036102, Jan 2010.

[192] M. Konopka, R. Turansky, M. Dubecky, D. Marx, and I. Stich, "Molecular mechanochemistry understood at the nanoscale: Thiolate interfaces and junctions with copper surfaces and clusters," *J. Phys. Chem. C*, vol. 113, no. 20, pp. 8878–8887, 2009.

[193] A. Ferral, E. M. Patrito, and P. Paredes-Olivera, "Structure and bonding of alkanethiols on cu(111) and cu(100)," *J. Phys. Chem. B*, vol. 110, no. 34, pp. 17050–17062, 2006.

[194] J. Rundgren, "Optimized surface-slab excited-state muffin-tin potential and surface core level shifts," *Phys. Rev. B*, vol. 68, p. 125405, Sep 2003.

[195] J. Rundgren, "Elastic electron-atom scattering in amplitude-phase representation with application to electron diffraction and spectroscopy," *Phys. Rev. B*, vol. 76, p. 195441, Nov 2007.

[196] R. Pentcheva, W. Moritz, J. Rundgren, S. Frank, D. Schrupp, and M. Scheffler, "A combined dft/leed-approach for complex oxide surface structure determination: Fe3o4(001)," *Surf. Sci.*, vol. 602, pp. 1299 – 1305, 2008.

[197] V. B. Nascimento, R. G. Moore, J. Rundgren, J. Zhang, L. Cai, R. Jin, D. G. Mandrus, and E. W. Plummer, "Procedure for leed i-v structural analysis of metal oxide surfaces: Ca1.5sr0.5ruo4(001)," *Phys. Rev. B*, vol. 75, p. 035408, Jan 2007.

[198] W. Moritz and J. Landskron, "Anisotropic temperature factors in the calculation of low-energy electron diffraction intensities," *Surf. Sci.*, vol. 337, pp. 278 – 284, 1995.

[199] W. Meyer, K. Biedermann, M. Gubo, L. Hammer, and K. Heinz, "Superstructure in the termination of coo(111) surfaces: Low-energy electron diffraction and scanning tunneling microscopy," *Phys. Rev. B*, vol. 79, p. 121403, Mar 2009.

[200] O. Romanyuk, P. Jiricek, and T. Paskova, "Quantitative low-energy electron diffraction analysis of the gan(0001) (1x1) reconstruction," *Surf. Sci.*, vol. 606, pp. 740 – 743, 2012.

[201] V. B. Nascimento, A. Li, D. R. Jayasundara, Y. Xuan, J. O'Neal, S. Pan, T. Y. Chien, B. Hu, X. B. He, G. Li, A. S. Sefat, M. A. McGuire, B. C. Sales, D. Mandrus, M. H. Pan, J. Zhang, R. Jin, and E. W. Plummer, "Surface geometric and electronic structures of bafe2as2(001)," *Phys. Rev. Lett.*, vol. 103, p. 076104, Aug 2009.

[202] P. D. Quinn, C. Bittencourt, and D. P. Woodruff, "Tensor leed analysis of the ni(111)(r3xr3)r30°-pb surface," *Phys. Rev. B*, vol. 65, p. 233404, May 2002.

[203] P. D. Quinn, C. Bittencourt, D. Brown, D. P. Woodruff, T. C. Q. Noakes, and P. Bailey, "Tensor low energy electron diffraction and medium energy ion scattering determination of the ni(110)c(2x2)-sn surface structure," *J. Phys.: Condens. Matter*, vol. 14, no. 4, p. 665, 2002.

[204] E. Soares, C. Bittencourt, E. Lopes, V. de Carvalho, and D. Woodruff, "{LEED} structure determination of the ni(111)(r3xr3)r30 - sn surface," *Surf. Sci.*, vol. 550, pp. 127 – 132, 2004.

[205] K. Pussi, E. AlShamaileh, A. Cafolla, and M. Lindroos, "A tensor leed study of the c(2x2)-sb adsorption structure on cu(110)," *Surf. Sci.*, vol. 583, pp. 151 – 156, 2005.

[206] G. J. P. Abreu, R. Paniago, F. R. Negreiros, E. A. Soares, and H.-D. Pfannes, "Surface investigation of au monolayers on pd(100)," *Phys. Rev. B*, vol. 83, p. 165410, Apr 2011.

[207] D. Lerch, A. Klein, A. Schmidt, S. Müller, L. Hammer, K. Heinz, and M. Weinert, "Unusual adsorption site of hydrogen on the unreconstructed ir(100) surface," *Phys. Rev. B*, vol. 73, p. 075430, Feb 2006.

[208] J. P. Hofmann, S. F. Rohrlack, F. Hess, J. C. Goritzka, P. P. Krause, A. P. Seitsonen, W. Moritz, and H. Over, "Adsorption of chlorine on ru(0001) - a combined density functional theory and quantitative low energy electron diffraction study," *Surf. Sci.*, vol. 606, pp. 297 – 304, 2012.

[209] V. Blum, L. Hammer, K. Heinz, C. Franchini, J. Redinger, K. Swamy, C. Deisl, and E. Bertel, "Structure of the c(2x2)-br/pt(110) surface," *Phys. Rev. B*, vol. 65, p. 165408, Apr 2002.

[210] R. Koller, W. Bergermayer, G. Kresse, C. Konvicka, M. Schmid, J. Redinger, R. Podloucky, and P. Varga, "The structure of the oxygen-induced c(6x2) reconstruction of v(110)," *Surf. Sci.*, vol. 512, pp. 16 – 28, 2002.

[211] E. A. Soares, R. Paniago, V. E. de Carvalho, E. L. Lopes, G. J. P. Abreu, and H.-D. Pfannes, "Quantitative low-energy electron diffraction analysis of mno(100) films grown on ag(100)," *Phys. Rev. B*, vol. 73, p. 035419, Jan 2006.

[212] T. Lerotholi, G. Held, and D. King, "The adsorption geometry of sulphur on ir(100): A quantitative leed study," *Surf. Sci.*, vol. 600, no. 4, pp. 880 – 889, 2006.

[213] E. AlShamaileh, K. Pussi, H. Younis, C. Barnes, and M. Lindroos, "The structure of oxygen-induced reconstruction on cu(100)-c(2x2)-pt surface alloy: the pt/cu(100)-(2x2)-o," *Surf. Sci.*, vol. 548, pp. 231 – 238, 2004.

[214] C. Klein, G. Kresse, S. Surnev, F. P. Netzer, M. Schmid, and P. Varga, "Vanadium surface oxides on pd(111): A structural analysis," *Phys. Rev. B*, vol. 68, p. 235416, Dec 2003.

[215] M. Lahti, K. Pussi, M. Alatalo, S. Krasnikov, and A. Cafolla, "Sulphur adsorption on au110: Dft and leed study," *Surf. Sci.*, vol. 604, pp. 797 – 803, 2010.

[216] Y. P. Guo, K. C. Tan, H. Q. Wang, C. H. A. Huan, and A. T. S. Wee, "Low-energy electron diffraction study of oxygen-induced reconstructions on cu(210)," *Phys. Rev. B*, vol. 66, p. 165410, Oct 2002.

[217] M. Ohmasa, M. Suzuki, and Y. Takeuchi, "A refinement of the crystal structure of covellite, cus," *Mineral. J. (Japan)*, vol. 8, pp. 311–319, 1977.

[218] H. T. Evans, "Copper coordination in low chalcocite and djurleite and other copper-rich sulfides," *Am. Mineral.*, vol. 66, pp. 807–818, 1981.

[219] T.-C. Tseng, C. Urban, Y. Wang, R. Otero, S. L. Tait, M. Alcami, D. Ecija, M. Trelka, J. M. Gallego, N. Lin, M. Konuma, U. Starke, A. Nefedov, A. Langner, C. Wöll, M. A. Herranz, F. Martin, N. Martin, K. Kern, and R. Miranda, "Charge-transfer-induced structural rearrangements at both sides of organic/metal interfaces," *Nat. Chem.*, vol. 2, pp. 374–379, May 2010.

[220] M. K. Cyranski and T. M. Krygowski, "Two sources of the decrease of aromaticity: Bond length alternation and bond elongation. part i. an analysis based on benzene ring deformations," *Tetrahedron*, vol. 55, no. 19, pp. 6205 – 6210, 1999.

[221] O. V. Shishkin, I. V. Omelchenko, M. V. Krasovska, R. I. Zubatyuk, L. Gorb, and J. Leszczynski, "Aromaticity of monosubstituted derivatives of benzene. the application of out-of-plane ring deformation energy for a quantitative description of aromaticity," *J. Mol. Struc.*, vol. 791, pp. 158 – 164, 2006.

[222] M. Baba, Y. Kowaka, U. Nagashima, T. Ishimoto, H. Goto, and N. Nakayama, "Geometrical structure of benzene and naphthalene: Ultrahigh-resolution laser spectroscopy and ab initio calculation," *J. Chem. Phys.*, vol. 135, no. 5, p. 054305, 2011.

[223] Q. Meng, W. Zhang, J. Yu, and D. Huang, "Crystal structure of anthraquinone-1,5-dithiol," *Dyes Pigm.*, vol. 65, no. 3, pp. 281 – 283, 2005.

[224] D. P. Woodruff, "The interface structure of n-alkylthiolate self-assembled monolayers on coinage metal surfaces," *Phys. Chem. Chem. Phys.*, vol. 10, pp. 7211–7221, 2008.

[225] F. Schreiber, "Structure and growth of self-assembling monolayers," *Prog. Surf. Sci.*, vol. 65, pp. 151 – 257, 2000.

[226] T. Otsubo, Y. Aso, and K. Takimiya, "Functional oligothiophenes as advanced molecular electronic materials," *J. Mater. Chem.*, vol. 12, pp. 2565–2575, 2002.

[227] J. Scherer, M. R. Vogt, O. M. Magnussen, and R. J. Behm, "Corrosion of alkanethiol-covered cu(100) surfaces in hydrochloric acid solution studied by in-situ scanning tunneling microscopy," *Langmuir*, vol. 13, no. 26, pp. 7045–7051, 1997.

[228] K. Saha, S. S. Agasti, C. Kim, X. Li, and V. M. Rotello, "Gold nanoparticles in chemical and biological sensing," *Chem. Rev.*, vol. 112, no. 5, pp. 2739–2779, 2012.

[229] G. Ku, M. Zhou, S. Song, Q. Huang, J. Hazle, and C. Li, "Copper sulfide nanoparticles as a new class of photoacoustic contrast agent for deep tissue imaging at 1064 nm," *ACS Nano*, vol. 6, no. 8, pp. 7489–7496, 2012.

[230] G. J. Jackson, D. P. Woodruff, R. G. Jones, N. K. Singh, A. S. Y. Chan, B. C. C. Cowie, and V. Formoso, "Following local adsorption sites through a surface chemical reaction: Ch3sh on cu(111)," *Phys. Rev. Lett.*, vol. 84, pp. 119–122, Jan 2000.

[231] G. Rousseau, A. Mulligan, N. Bovet, M. Adams, V. Dhanak, and M. Kadodwala, "A structural study of disordered sulfur overlayers on cu(111)," *Surf. Sci.*, vol. 600, pp. 897 – 903, 2006.

[232] E. Wahlstrom, I. Ekvall, T. Kihlgren, H. Olin, S.-A. Lindgren, and L. Wallden, "Low-temperature structure of s/cu(111)," *Phys. Rev. B*, vol. 64, p. 155406, Sep 2001.

[233] E. Wahlstrom, I. Ekvall, H. Olin, S.-A. Lindgren, and L. Wallden, "Observation of ordered structures for s/cu(111) at low temperature and coverage," *Phys. Rev. B*, vol. 60, pp. 10699–10702, Oct 1999.

[234] F. Sirotti, M. De Santis, and G. Rossi, "Synchrotron-radiation photoemission and x-ray absorption of fe silicides," *Phys. Rev. B*, vol. 48, pp. 8299–8306, Sep 1993.

[235] F. Caprioli, A. Martinelli, D. Gazzoli, V. Di Castro, and F. Decker, "Enhanced protective properties and structural order of self-assembled monolayers of aromatic thiols on copper in contact with acidic aqueous solution," *J. Phys. Chem. C*, vol. 116, no. 7, pp. 4628–4636, 2012.

[236] F. Caprioli, M. Beccari, A. Martinelli, V. Di Castro, and F. Decker, "A multi-technique approach to the analysis of sams of aromatic thiols on copper," *Phys. Chem. Chem. Phys.*, vol. 11, pp. 11624–11630, 2009.

[237] J. Gebhardt, J. McCarron, P. Richardson, and A. Buckley, "The effect of cathodic treatment on the anodic polarization of copper sulfides," *Hydrometallurgy*, vol. 17, no. 1, pp. 27 – 38, 1986.

[238] M. Beccari, A. Kanjilal, M. G. Betti, C. Mariani, L. Floreano, A. Cossaro, and V. D. Castro, "Characterization of benzenethiolate self-assembled monolayer on cu(100) by xps and nexafs," *Journal of Electron Spectroscopy and Related Phenomena*, vol. 172, pp. 64 – 68, 2009.

[239] N. Prince, D. Seymour, M. Ashwin, C. McConville, D. Woodruff, and R. G. Jones, "A sexafs and x-ray standing wave study of the cu(111)(r7xr7)r19°-s surface: Adsorbate-substrate and adsorbate-adsorbate registry," *Surf. Sci.*, vol. 230, pp. 13 – 26, 1990.

[240] M. Saidy and K. Mitchell, "Tensor leed analysis for the cu(111)-(r7xr7)r19.1°-s surface structure," *Surf. Sci.*, vol. 441, pp. 425 – 435, 1999.

[241] M. Foss, R. Feidenhans'l, M. Nielsen, E. Findeisen, T. Buslaps, R. Johnson, and F. Besenbacher, "Sulfur induced cu4 tetramers on cu(111)," *Surf. Sci.*, vol. 388, pp. 5 – 14, 1997.

[242] Y. Taki and O. Takai, "Xps structural characterization of hydrogenated amorphous carbon thin films prepared by shielded arc ion plating," *Thin Solid Films*, vol. 316, pp. 45 – 50, 1998.

[243] P. H. Citrin, P. Eisenberger, and R. C. Hewitt, "Adsorption sites and bond lengths of iodine on cu(111) and cu(100) from surface extended x-ray-absorption fine structure," *Phys. Rev. Lett.*, vol. 45, pp. 1948–1951, Dec 1980.

[244] L. Ma, J. Zhang, and K. Xu, "Structural and electronic properties of atomic oxygen adsorption on cu(111) surface: A first-principles investigation," *Sci. China Ser. A*, vol. 56, no. 3, p. 573, 2013.

List of Publications

9. "From Benzenetrithiolate Self-Assembly to Copper-Sulfide Adlayers on Cu(111): Temperature-Induced Irreversible and Reversible Phase Transitions"

   Thomas Sirtl, Matthias Lischka, Johanna Eichhorn, Atena Rastgoo-Lahrood, Thomas Strunskus, Wolfgang M. Heckl, and Markus Lackinger

   The Journal of Physical Chemistry C, DOI:10.1021/jp411084k, **2014**

   Cf. page 113.

8. "Solvent-Dependent Stabilization of Metastable Monolayer Polymorphs at the Liquid-Solid Interface"

   Thomas Sirtl, Wentao Song, Georg Eder, Subhadip Neogi, Michael Schmittel, Wolfgang M. Heckl, and Markus Lackinger

   ACS Nano 7(8), 6711-6718, **2013**

   Cf. page 81.

7. "Adsorption Structure Determination of a Large Polyaromatic Trithiolate on Cu(111): Combination of LEED-I(V) and DFT-vdW"

   Thomas Sirtl, Jelena Jelic, Jörg Meyer, Kalpataru Das, Wolfgang M. Heckl, Wolfgang Moritz, John Rundgren, Michael Schmittel, Karsten Reuter, and Markus Lackinger

   Physical Chemistry Chemical Physics 15, 11054-11060, **2013**

   Cf. page 95.

6. "Control of Intermolecular Bonds by Deposition Rates at Room Temperature: Hydrogen Bonds vs. Metal-Coordination in Trinitrile Monolayers"

   Thomas Sirtl, Stefan Schlögl, Atena Rastgoo-Lahrood, Jelena Jelic, Subhadip Neogi, Michael Schmittel, Wolfgang M. Heckl, Karsten Reuter, and Markus Lackinger

   Journal of the American Chemical Society 135, 691-695, **2013**

   Cf. page 61.

5. "Synthesis of Two-Dimensional Phenylene-Boroxine Networks Through In-Vacuo Condensation and On-Surface Radical Addition"

   Stefan Schlögl, Thomas Sirtl, Johanna Eichhorn, Wolfgang M. Heckl, and Markus Lackinger

   Chemical Communications 47, 12355-12357, **2011**

4. "Extended Two-Dimensional Metal-Organic Frameworks Based on Thiolate-Copper Coordination Bonds"

   Hermann Walch, Jürgen F. Dienstmaier, Georg Eder, Rico Gutzler, Stefan Schlögl, Thomas Sirtl, Kalpataru Das, Michael Schmittel, and Markus Lackinger

   Journal of the American Chemical Society 133, 7909-7915, **2011**

3. "Phase Formation, Crystal Structures and Magnetic Properties of Perovskite-Type Phases in the System $La_2Co_{1+z}(Mg_xTi_{1-x})_{1-z}O_6$"

   Samrand Shafeie, Jekabs Grins, S.Y. Istomin, L. Karvonen, S. A. Chen, T.H. Chen, J.M. Chen, A. Weidenkaff, M. Karppinen, Thomas Sirtl, and Gunnar Svensson

   Journal of Solid State Chemistry 184, 177-190, **2011**

2. "Material- and Orientation-Dependent Reactivity for Heterogeneously Catalyzed Carbon-Bromine Bond Homolysis"

   Hermann Walch, Rico Gutzler, Thomas Sirtl, Georg Eder, and Markus Lackinger

   The Journal of Physical Chemistry C 114, 12604-12609, **2010**

1. "Reversible Phase Transitions in Self-Assembled Monolayers at the Liquid-Solid Interface: Temperature-Controlled Opening and Closing of Nanopores"

   Rico Gutzler, Thomas Sirtl, Jürgen F. Dienstmaier, Kingsuk Mahata, Wolfgang M. Heckl, Michael Schmittel, and Markus Lackinger

   Journal of the American Chemical Society 132, 5084-5090, **2010**

Danke,

Markus, für alles, was Du mir in den letzten Jahren beigebracht hast. Es hat viel Spaß gemacht, für Dich zu arbeiten und mit Dir zu forschen! Vielen Dank fürs Korrekturlesen.

Wolfgang, für das Vertrauen, das Du mir in den letzten Jahren entgegengebracht hast und nicht zuletzt danke für die finanzielle Unterstützung.

Johannes Barth, dafür, dass Sie sich so kurzfristig als erster Gutachter zur Verfügung gestellt haben.

liebe Büro- und Laborkollegen Jürgen, Stefan & Stefan, Atena, Matthias, Stephan, Johanna, Schorsch, Olli & Olli, Christoph und Wentao für die gute Arbeitsatmosphäre und die gegenseitige Unterstützung im harten Laboralltag. Nicht zu vergessen sind natürlich die vielen Anlässe zum Feiern (una cervecita).

Wolfgang Moritz, für die gute Zusammenarbeit, die viel Spaß gemacht hat und ohne die meine Doktorarbeit erheblich schmaler ausgefallen wäre. Vielen Dank fürs Korrekturlesen des Theorieteils.

liebe Ex-Kollegen Hermann, Rico, Marek, Schacki, Alex, Sophie und Anne-Kathrin für die unterhaltsame und lehrreiche Zeit vor der Promotion. Auch hier werden mir die vielen Abende in Erinnerung bleiben, an denen wir erfolgreiche Forschungswochen bei wohlverdienten Feierabendbierchen ausklingen ließen.

fleißige Praktikantinnen Stefanie und Paula. ¡Muchas Gracias!

Claudine, Susanne Bußmann (DM) und Barbara Jäger (LMU) für die zuverlässige Organisation, die freundliche Art und allgemeine Lebensweisheiten.

Karsten, Jelena, Jörg, Michael Schmittel, Kalpataru Das, Subhadip Neogi und John Rundgren. Thank you for the fruitful collaborations.

Feinmechanik- und Elektronikwerkstätten der LMU, besonders Günter und Max. Mit Eurer Hilfe konnte ich viele Probleme lösen und hab nebenbei eine Menge gelernt.

Werkstätten des Deutschen Museums. Ihr standet uns tatkräftig zur Seite, als wir nach dem Umzug die Labore wieder startklar gemacht haben. Auch danach wart Ihr hilfsbereit und zuverlässig.

Forum am Deutschen Museum, dass Du uns so freundlich aufgenommen hast, auch wenn Du zu später Stunde manchmal etwas unheimlich warst.

Registratur (Karl Bochsbichler, Josef Paul, ...), für die Hilfsbereitschaft und den Spaß, den wir hatten, z.B. beim Verschicken von Gasflaschen.

Herr Krapf, fürs tägliche Schlüssel- und Paketeausgeben sowie für Ihre Orientierungshilfen im Zuständigkeitsdschungel des DMs.

FCI, für die finanzielle Förderung.

Flip, Du bist der beste denkbare Grund dafür, sich mit dem Zusammenschreiben zu beeilen. Ich freu mich auf Dich.

liebe Familie, für alles.

Curriculum Vitae

since 10/10	**PhD Student (Physics)** *Technische Universität München (TUM)* *Center for NanoScience (CeNS)* *Deutsches Museum* Scholarship of the Fonds der Chemischen Industrie (FCI)
10/07-11/09	**Master of Science (Chemistry)** *Ludwig-Maximilians-Universität München (LMU)*
10/04-09/07	**Bachelor of Science (Chemistry & Biochemistry)** *Ludwig-Maximilians-Universität München (LMU)*
09/95-06/04	**Abitur / University Entrance Qualification** *Heinrich-Heine-Gymnasium München*

Munich, October 28, 2013

Thomas Sirtl